

Low-dimensional phase transitions in and outside equilibrium

Juliane Uta Klamser

▶ **To cite this version:**

Juliane Uta Klamser. Low-dimensional phase transitions in and outside equilibrium. Data Analysis, Statistics and Probability [physics.data-an]. Sorbonne Université, 2018. English. ⟨NNT : 2018SORUS333⟩. ⟨tel-02865332v2⟩

HAL Id: tel-02865332

https://theses.hal.science/tel-02865332v2

Submitted on 11 Jun 2020

HAL is a multi-disciplinary open access archive for the deposit and dissemination of scientific research documents, whether they are published or not. The documents may come from teaching and research institutions in France or abroad, or from public or private research centers.

L'archive ouverte pluridisciplinaire **HAL**, est destinée au dépôt et à la diffusion de documents scientifiques de niveau recherche, publiés ou non, émanant des établissements d'enseignement et de recherche français ou étrangers, des laboratoires publics ou privés.



HAL Authorization

SORBONNE UNIVERSITÉ
CRÉATEURS DE FUTURS DEPUIS 1257

Département de Physique
École normale supérieure

LPS

THÈSE DE DOCTORAT DE SORBONNE UNIVERSITÉ

Spécialité : Physique

École doctorale n°564: Physique en Île-de-France

réalisée

au Laboratoire de Physique Statistique de l'École normale supérieure de Paris

sous la direction de Werner KRAUTH

présentée par

Juliane Uta KLAMSER

pour obtenir le grade de :

DOCTEUR DE SORBONNE UNIVERSITÉ

Sujet de la thèse :

Transitions de phase en basse dimension à l'équilibre et hors d'équilibre

soutenue le 10 décembre 2018

devant le jury composé de :

M.	Ludovic BERTHIER	Rapporteur
M.	Thomas SPECK	Rapporteur
M^{me}	Silke HENKES	Examinatrice
M^{me}	Annie LEMARCHAND	Examinatrice
M.	Werner KRAUTH	Directeur de thèse

Version of Friday 1st March, 2019, 11:50

Contents

Introduction **x**

I Preparatory material **1**
I.1 Equilibrium phases and phase transitions . . . 1
I.2 Systems outside thermodynamic equilibrium . . . 6
I.2.1 Equilibrium steady state . . . 8
I.2.2 Non-equilibrium steady state . . . 9
I.2.3 Characteristic differences between equilibrium and non-equilibrium steady states . . . 9
I.3 Continuous Markov process, Fokker-Planck equation, and Langevin dynamics . . . 13
I.3.1 Continuous-time Markov process . . . 13
I.3.2 Fokker-Planck equation . . . 14
I.3.3 Langevin dynamics . . . 15
I.4 Active Matter . . . 16
I.4.1 Self-propelled particles with equilibrium interactions . . . 19
a) Models . . . 20
b) Motility-induced phase separation . . . 21
I.5 Thermodynamic phases in passive two-dimensional particle systems . . . 26
I.5.1 Two-dimensional solid . . . 27
I.5.2 Harmonic solid in two dimensions . . . 29
I.6 The Berezinskii-Kosterlitz-Thouless transition in the two-dimensional XY model . . . 31
I.6.1 Low-temperature ordered phase . . . 35
I.6.2 High-temperature disordered phase . . . 35
I.6.3 Few characteristics and robustness of the Berezinskii-Kosterlitz-Thouless transition . . . 36
I.7 The BKTHNY theory for the two-step melting . . . 38
I.7.1 Topological defects . . . 39
I.7.2 The harmonic approximation for the two-dimensional solid . . . 41
I.7.3 Solid-hexatic transition . . . 42
I.7.4 Hexatic-liquid transition . . . 43
I.8 Present day status of two-step melting scenario . . . 44

II Two-dimensional interacting particles in and out of equilibrium **49**
II.1 Persistent kinetic Monte Carlo . . . 50

II.1.1 Analytic characterization of the kinetic Monte Carlo dynamics 52
a) Probability distribution of the displacement ϵ in one dimension 52
b) Auto-correlation time of the displacements 52
c) Persistence length of a single free particle movement in two dimensions 53
II.2 One-dimensional results of the kinetic Monte Carlo algorithm 56
II.2.1 A single self-propelled trapped particle 56
II.2.2 Two self-propelled particles on a ring 58
II.2.3 Collective many-particle behavior on a ring 60
II.3 Collective behavior in two dimensions 62
II.3.1 Ensemble specification 63
II.3.2 Motility-induced phase separation 64
II.3.3 Two-step melting 69
II.3.4 The full phase diagram 74
II.3.5 MIPS under the influence of stiffer potentials 77
II.3.6 Anisotropic effects in two dimensions? 82
II.4 Dimensional reduction of the kinetic Monte Carlo dynamics 87
II.4.1 One-dimensional single particle: approximate dynamics 89
II.4.2 Exact analysis of the kinetic Monte Carlo dynamics 90
a) Discrete-time Master equation for a single particle 91
b) Passive limit 92
c) Dimensional reduction in the small-δ limit 92
d) Multi-particle continuous limit for small δ 96
II.4.3 Continuous limit following standard steps 99
II.4.4 Two other stochastic models of self-propelled dynamics 102
a) The active random acceleration process 102
b) The active Ornstein-Uhlenbeck process 106
II.4.5 Summary 108
II.5 Pressure in the kinetic Monte Carlo 110
II.5.1 Pressure in the passive limit of kinetic Monte Carlo 111
II.5.2 Pressure in the persistent limit of kinetic Monte Carlo 114
II.6 Pressure in the active Ornstein-Uhlenbeck process 117
II.7 Discussion 121

III Phase transitions in one dimension **125**
III.1 Introduction 125
III.2 Arguments for absence of phase transition 126
III.3 Examples of phase transitions 128
III.4 New example: a model of interacting rods 134
III.4.1 Simple case: nearest neighbor interaction 135
a) Singular free energy 135
b) Integral transfer operator 137
c) Origin of singularities 140
d) Structure of the transfer matrix 140
e) Precise nature of the singularities 142
f) Exact diagonalization for $\kappa = 1$ 145

III.4.2 Soft-core interaction . . . 147
III.4.3 Monte Carlo simulation of interacting rods . . . 150
III.5 Discussions . . . 151
a) Two dimensions . . . 153
b) Non-equilibrium steady state . . . 154

A Appendix **157**
A.1 Discrete-time probability distribution of the displacements . . . 157
A.2 Grid/cell scheme . . . 160
A.3 Orientational correlation function at the outer boundary of MIPS . . . 162
A.4 Convergence data for the activity-induced two-step melting . . . 162
A.5 MIPS under the influence of the potential stiffness . . . 165
A.6 Further evidence for negligible anisotropic effects in 2D . . . 169
A.7 Time evolution of fluctuating distribution function, passive case . . . 169
A.8 Time evolution of fluctuating distribution function, persistent case . . . 171
A.9 Continuity equation of the particle density . . . 173
A.10 Active Ornstein-Uhlenbeck process: Time evolution of the fluctuating distribution function . . . 174
A.11 Active Ornstein-Uhlenbeck process: Time evolution of the average velocity $m_t(x)$ . . . 175
A.12 Active Ornstein-Uhlenbeck process: recasting pressure . . . 176
A.13 Active Ornstein-Uhlenbeck process: $Q(\Lambda)$ . . . 177
A.14 Runtime information . . . 178
A.15 Publication 1:
Thermodynamic phases in two-dimensional active matter . . . 180
A.16 Publication 2:
Multiple singularities of the equilibrium free energy
in a one-dimensional model of soft rods . . . 199
A.17 Publication 3:
A kinetic-Monte Carlo perspective on active matter . . . 210

Bibliographie **211**

Introduction

Even though the fundamental laws of physics are simple, the surrounding nature on an everyday scale is full of amazing complexities, collective motions, and intricate structures [1]. The archetypal examples range from lifeless objects, like atmospheric activities, snowflecks, to living systems such as ant colonies, swarms of bees, to innate objects, like human social behavior, economics, social network, *etc*. It is baffling to see the intricacies of such collective structures and behaviors that emerge as a whole from the interplay of basic components which are simple. Understanding such emergent collective properties is one of the major avenues of modern day Physics[1].

These emergent properties are many-body effects. A single water molecule is neither fluid nor ice, but a collection of Avogadro number ($\sim 10^{23}$) of water molecules at room temperature is clearly liquid. Philippe W. Anderson articulates this eloquently as "*more is different*" [3]. Surely, the notions of liquidity, crystallinity, magnetism are macroscopic collective properties. The development of statistical physics in the past century offers a clear understanding of these collective properties of matter when it is in equilibrium. For example, there is a good understanding of how a collection of the same water molecules in different environmental conditions can manifest as water, ice or vapor. These are examples of phases in which matter can exist. Statistical physics connects the microscopic world of single particles to their macroscopic phases. One of the unifying concepts that have emerged from this theory is that macroscopic properties are usually governed by conservation laws and broken symmetries. For example, at high temperatures, water molecules are disordered with a full rotational and positional symmetry. As water freezes into ice, these symmetries are spontaneously broken. The subject matter of this thesis is about such macroscopic collective properties (phases) with an emphasis on their symmetry and how they emerge from interactions of microscopic constituents. The goal is to explore regimes (out-of-equilibrium systems) where concepts of equilibrium statistical mechanics are not directly applicable.

The primary focus of this thesis is about low-dimensional systems. Although nature around us is spatially three dimensional, there are many materials that behave as though they are either one or two dimensional. Films of liquid crystals, fluctuating interfaces, biological tissues, bacterial colony in a petri dish, surface transport in topological insulators, colloidal suspensions under confined conditions, magnetic and superconducting thin film, electrons trapped on liquid helium surfaces, transport of molecules inside porous medium or nanotubes, molecular motors on microtubules are only a few of such vast natural ex-

[1] Laughlin and Pines write [2] it as, "*The central task of theoretical physics in our time is no longer to write down the ultimate equations but rather catalog and understand emergent behavior in its many guises, including potential life itself.*"

amples of effective low-dimensional systems (see [4–6] and section I.8 for their references). Two-dimensional materials have also become increasingly important since the discovery of graphene [7], as such systems could be synthesized in the laboratory. Furthermore, theoretical models can be easily constructed in low dimensions, and it is instructive to do so. Importance of dimensionality on the collective properties of matter has been realized, especially in the context of critical phenomena. While much of Physics carries over straightforwardly from three-dimensions, some properties have a strong dependence on dimensionality, including aspects of phase behavior. This, as will be discussed in this thesis, can reveal new fundamental principles that are strikingly different from higher dimensions. Low-dimensional systems are also easier to study numerically than their higher-dimensional extensions. Over the past decades, studies of low-dimensional systems have grown to an extremely active field in Physics, especially in soft matter, fluid dynamics, condensed matter and even in quantum gases.

Perhaps the fundamentally new phenomenon that is revealed in the low-dimensional systems is about the presence of order. As spatial dimensions decrease, fluctuations become more important. In one dimension, fluctuations destroy order, unless the interactions are long-ranged [8–10]. Naively, this is related to connectivity. The way information is passed from one end of a one-dimensional system to the other end is directly along the chain. Then, in a large system, fluctuations can cut the flow of information and hence the lack of order. In two dimensions, there are many more connections from one point to the other, and it turns out that fluctuations can destroy long-range order, but not necessarily phase transitions. This is seen in the most common transition that occurs in condensed matter, *i.e.* melting from solid to liquid. In the two-dimensional world, melting can occur by a process in which the order is gradually destroyed, quite unlike the sharp change in three-dimensional melting. This transition is induced by topological defects, where symmetry plays a crucial role. Over the decades a substantial understanding is gained of these topological transitions, for which Kosterlitz and Thouless were awarded the 2016 Nobel Prize in Physics. Even though the modern day theory (discussed in section I.7) for two-dimensional melting was proposed several decades ago, a consensus on the precise nature of the transitions has been reached only recently. This is reached by numerical simulations [11–13], which emphasizes the importance of numerical studies for such many-body physics and it is the primary tool used in this thesis.

The question that will be pursued in the largest part of this thesis is how such two-dimensional melting scenario and the associated equilibrium phases get affected by non-equilibrium conditions. Do the equilibrium phases with their characteristic symmetries survive far beyond a linear-response regime, or/and what new collective behaviors emerge due to the non-equilibrium nature of the microscopic dynamics? All these are questions that merit understanding. Keeping this broad perspective in mind, this thesis presents numerical studies of a non-equilibrium extension of a celebrated model of interacting isotropic disks that played a pivotal role in concluding the long-standing debate on two-dimensional melting. The non-equilibrium component in this extension is introduced by a persistent self-propelled motion of individual disks that is a characteristic of active matter, which constitutes an important subclass of non-equilibrium systems.

The field of active matter is by itself a rapidly expanding research area of non-equilibrium physics that spans diverse disciplines, ranging from soft matter physics to cell biology, to material science, and to engineering (see the recent reviews [14, 15]). It is about natural

or artificial systems in which the individual components are themselves internally driven out of equilibrium by an energy injection at the microscopic scale which they convert into mechanical work. Living entities such as birds, fish or bacteria are typical examples. They transform the chemical content of their food into some form of mechanical work[2]. Similarly, artificial active matter can be designed to perform work driven by an energy input from light, chemical gradients or vibration [17–19].

An important feature that concerns studies of active matter is the emergence of self-organization, for example, collective motion in which a group of active agents moves together as a unit on scales that are significantly larger than the size of an individual. Every day examples are the intricate structures formed by airborne bird flocks or when a school of fish moves together to avoid a predator. Similar collective behavior exists even at small length scales, where bacterial suspensions, tissues, and molecular motors use their intrinsic activity to create motions or form structures on lengths larger than individual cells or proteins. A broad goal of the field of active matter is to understand the fundamental principles that govern such emergence of large-scale patterns and collective behaviors. From a theoretical perspective, these active systems provide a testing ground for theories of non-equilibrium statistical physics.

The two-dimensional model of self-propelled disks, that is at the center of this thesis, is one of the simplest possible theoretical examples of active matter. The conception of this model comes from a goal to mimic the behavior of natural active matter in a controlled manner by shredding unimportant details, to gain a better understanding of the collective phenomena at work. It is inspired by a physicists perspective that when faced with a complex physical phenomenon, the most useful approach often involves simplifying it drastically with the aim of distilling the essence of the problem. Once such simplified examples are clearly understood, eventually, it becomes a cornerstone on which a comprehensive theory can be build that incorporates more general cases.

The primary hurdle (what also makes it interesting) in this study of active matter comes from the lack of a universal theoretical framework similar to the equilibrium statistical mechanics. In equilibrium, there are state functions like free energies, Gibbs potentials which determine thermodynamic properties. However, outside equilibrium, there is no such analog. In fact, many thermodynamic concepts have to be reconsidered as they are not necessarily defined. For example, the definition of pressure and temperature (that appear in the equilibrium equation of state) do not obviously extend for active materials and even the mere existence of an equation of state becomes an issue in itself. Confronted with such difficulties of deriving analytic results for active many-body systems, numerical methods like the Monte Carlo methods are found to be very useful tools to understand several aspects of the collective behavior of active matter. On one hand such numerical experiments can predict macroscopic properties from microscopic dynamics and on the other hand, it can shed light on the fundamental principles of microscopic dynamics by exploring their macroscopic consequences, which can be tested experimentally. This is the guiding motivation behind the numerical work presented in this thesis. The study here implements Monte Carlo algorithms for the model of two-dimensional self-propelled disks, and charts out a quantitative phase diagram that includes the established equilibrium phases as well

[2]Nearly three centuries ago Leibniz [16] aptly emphasized the key difference between living and non-living entities: "*I define the organism, or natural machine, a machine in which each part is a machine [. . .], whereas the parts of our artificial machines are not machines*".

as their extension into regimes far from equilibrium. It also shows how new macroscopic phases appear due to the self-propulsion in the dynamics, and presents a quantitative characterization of the nature of these phases, emphasizing on their symmetries.

Besides this work about self-propelled particles, this thesis investigates another fundamental aspect of collective behavior for low-dimensional systems. For this, the discussion returns to the systems in equilibrium and delves into the question of order in one-dimensional systems. In fact, this topic is very nicely connected to the history of how the theory of two-dimensional melting developed (the topic that concerns the first part of this thesis). Kosterlitz recounts in a recent review [6] that his foray into the melting transition started with the question of phase transitions in the one-dimensional Ising model with a $\frac{1}{r^2}$ interaction. This question was posed to Kosterlitz and Thouless by Anderson who was able to map the famous Kondo problem [20] to this question of one-dimensional phase transitions.

The precise question that this second part of the thesis addresses is whether phase transitions can happen in one-dimensional systems with short-range interactions at finite non-zero temperature. There is a common belief that such transitions cannot happen. Indeed, the commonly studied models in graduate textbooks, like the Ising model, the Potts model or the XY model, do not undergo phase transitions in one dimension. In fact, Landau on the last page of his statistical physics book [8], gave an argument based on a free energy estimate, for the absence of long-range order in any finite-state one-dimensional model. Later, the work of van Hove [9], Peierls [21], Ruelle [22] and Frölich [23] also showed that for particle systems with sufficiently short-range pair interactions ($\frac{1}{r^n}$ with $n > 2$), the free energy does not have any singularities and therefore, there are no phase transitions. Even though these results are for specific models, it is often blindly generalized to all one-dimensional systems. However, there is no general theorem that forbids one-dimensional phase transitions [10]. The second part of this thesis confronts this particular issue. After citing a few existing counterexamples of quasi-one-dimensional systems, the thesis presents a clearly one-dimensional model that shows robust singularities in its thermodynamic free energy as the coupling constant is varied. The origin of these singularities are certain geometrical changes in the accessible phase space, and it is a mechanism that has not been emphasized earlier.

The content of this thesis is organized into three chapters, with their outline described as follows.

The first chapter I introduces the general concepts that are essential for understanding the results of this thesis. It starts with an introduction to the ideas of thermodynamic phases and their transitions in section I.1. Concepts of equilibrium and non-equilibrium steady states and their characteristic differences are discussed in section I.2 using the formalism of discrete-time Markov processes. The discussion also includes fundamental concepts like time reversibility and the fluctuation-dissipation relation. A few additional details of stochastic processes like the Fokker-Planck equation and the Langevin dynamics are also subsequently presented in section I.3. Following this primer, active matter is introduced in section I.4 as an important subclass of non-equilibrium processes, with a special focus on the active matter systems of self-propelled particles in subsection I.4.1. The latter section also introduces a set of well-known models of active matter and discusses one of the most commonly observed collective phenomenon of active matter, known as the motility-induced phase separation. The primary goal of this thesis is to understand

how the states of such self-propelled particles connect with the equilibrium phases in their passive limit. This is particularly addressed in two dimensions and therefore, an understanding of the equilibrium phases, especially of the two-dimensional melting is necessary. An abridged version of the melting scenario emphasizing the crucial theoretical concepts like the Berezinskii-Kosterlitz-Thouless transition and the Berezinskii-Kosterlitz-Thouless-Halperin-Nelson-Young (BKTHNY) melting scenario are presented in section I.5 to I.7. This chapter concludes with a discussion of the present-day status of the equilibrium two-step melting scenario in section I.8.

The second chapter II contains the main work of this thesis, which is the full phase diagram of a model of spherical self-propelled (active) particles with isotropic pair-wise interactions. The chapter begins with a microscopic definition of the concerned model and an algorithmic implementation of its microscopic dynamics in section II.1. The model is an active variant of the kinetic Monte Carlo dynamics of particles, which is different from usual continuous models of active matter. Characteristic properties that quantify the activity of a single particle following this dynamics are presented in the same section II.1. Before discussing the many-body collective phenomena in two dimensions, the simpler one-dimensional case is considered in section II.2. First, an instructive example of a single particle in a one-dimensional box is used to illustrate the characteristic effect that comes solely from the activity/self-propulsion. Even this simple case qualitatively captures the basic feature that results in the many-body collective phenomena such as motility-induced phase separation. This is illustrated using a single particle, then two particles, and subsequently by the density inhomogeneities in the many-particle case. The non-trivial case of many-particles in two dimensions is presented in section II.3. A complete quantitative phase diagram is presented that shows how the equilibrium two-step melting scenario (including the hexatic phase) extends far inside the non-equilibrium regime of high activity. Moreover, it is shown how the melting transitions (non-)interact with the motility-induced phase separation observed within the here studied model. This is established with a detailed discussion of the finer quantitative details of the phase diagram, anisotropic effects of the dynamics, and especially the effect of the stiffness of particles with the comparison of earlier studies. This brings the discussion to the question of relevant control parameters and the universality of the phase diagram. This is discussed at length in section II.4, where different aspects of the Monte Carlo dynamics, as well as other models of active matter, are analyzed in details. The question of the precise nature of the melting transitions far from equilibrium is an open question and has not been resolved in this thesis. A prospective approach requires thermodynamic state variables like pressure, which can be used to identify the nature of the transitions. However, even such questions of thermodynamic state variables outside equilibrium are non-trivial to answer. In this direction, the analysis in section II.5 presents an approach to define pressure. Relying on recent studies, an expression for pressure is obtained for the concerned model, as well as for another stochastic model of active matter (section II.6). This work on pressure is incomplete, but still, it achieves a crucial step which paves the way for future investigations on the nature of the non-equilibrium phase transitions in this thesis.

The third chapter III comes back to the question of order in low-dimensional systems in equilibrium. The introduction in section III.1, is followed by a discussion of a common belief that one-dimensional systems with short-range interactions cannot exhibit phase transitions in section III.2. The latter section delves into the literature searching for the origin

of such folklore. Later in the section III.3 a few already existing counterexamples are presented. However, these examples are quasi-one-dimensional. In section III.4 a new clearly one-dimensional model is presented which exhibits phase transitions at a finite temperature even though the interaction is short-range. The phase transitions are analytically established as singularities in the free energy which appears due to a new geometrical mechanism. This is discussed in details. The chapter concludes in section III.5 with a discussion about the nature of these transitions and its general applicability.

I – Preparatory material

I.1 Equilibrium phases and phase transitions

This section I.1 presents a few essential details about equilibrium phase transitions which are relevant for the discussion about phases in active matter.

In general, the word "phase" describes a macroscopic homogeneous state of matter where, under fixed external conditions, the material usually has unique values of thermostatic properties. For example, depending on the pressure and the temperature a collection of water molecules can be either in one of its various solid states or in the fluid state (gas or liquid). There is no fundamental difference between a liquid or a gas state and they can be smoothly transformed from one into the other. There are situations, where some thermostatic properties may take two or even more values. For example, at $T = 373$ Kelvin and one atmospheric pressure, water can be in both the liquid phase and the gas phase. This means, that in a constant volume ensemble, the two phases coexist[1], where the gas phase becomes distinguishable from the liquid due to its much smaller density. More importantly, as the external conditions change, the water molecules can rearrange themselves to move between phases, which results in sharp changes in the macroscopic properties. These correspond to phase transitions which are non-trivial collective phenomena arising in the thermodynamic limit.

Phase diagrams are used as a visual representation to identify the thermodynamic phases as the external conditions change. Usually, a phase diagram is given on the space of thermodynamic control parameters, which depend on the thermodynamic ensemble. For example, the phase diagram of water can be in the P-T plane in the constant pressure-temperature ensemble ((N, P, T) ensemble), or it can be on the T-V (equivalently density) plane in a constant temperature-volume ensemble ((N, V, T) ensemble), as shown in Fig. I.1. The lines mark the boundary between stable thermodynamic phases, where the fluid undergoes a phase transition as the parameters are varied. In this example, the liquid-gas line stops at a point. This means, the transformation form liquid to gas is possible without passing through a phase transition. This is related to the same symmetry in the liquid and gas phase. In comparison, when the liquid freezes to a solid, it breaks translational symmetry, and there is no smooth (transition free) way for it to happen. A coexistence line between phases of different symmetry cannot end in a critical point. It must either extend to infinity or else cross another line. Such a breakdown of symmetries at the thermodynamic scale is often an important feature of phase transitions and also plays a crucial role in this thesis.

[1] For fluids, the phase coexistence is governed by the equality of three quantities, the pressure, the temperature and the chemical potential.

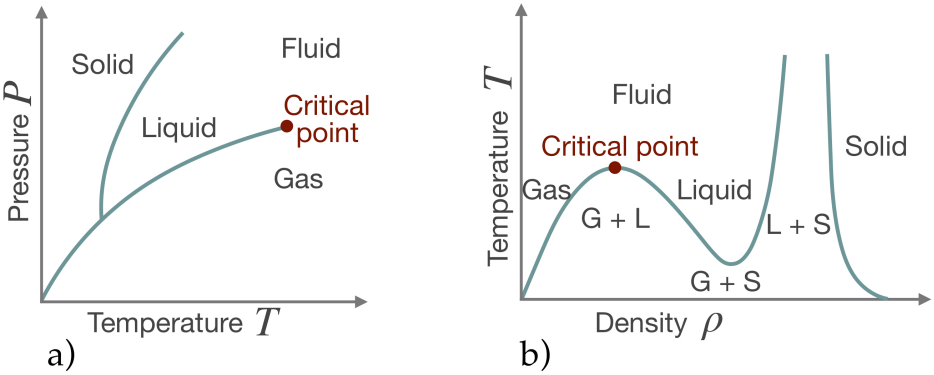


Figure I.1: **Phase diagram of a typical fluid.** (a) Phase diagram in the pressure-temperature plane and (b) in the temperature-density plane. Solid lines are phase boundaries separating regions of stable phases. The lines denote a first-order transition except at the critical point where the transition is of second order. Source: Inspired by the web article http://soft-matter.seas.harvard.edu

In the thermodynamic description, a phase transition point is specified by a non-analytic change in the free energy in the thermodynamic limit. Following the Ehrenfest definition [24–26], phase transitions are classified according to the nature of this non-analyticity. A phase transition is referred as a k^{th} order transition, if the Gibbs free energy[2] has up to $(k-1)^{\text{th}}$ continuous derivatives, but the k^{th} derivative is discontinuous. Therefore, according to this classification, if the first derivative of the Gibbs free energy has a jump discontinuity, the phase transition is of first order. Whereas, at a second-order transition, the first derivative of the Gibbs free energy changes continuously, but the second derivative is singular.

A schematic of such a non-analyticity in a first-order transition is illustrated in Fig. I.2. The Gibbs free energy $G(T,P)$ in the (N,P,T) ensemble has a jump discontinuity in its first derivative, which means that at the transition the volume of the system changes sharply from one phase to the other. However, in the (N,V,T) ensemble thermodynamics is described by the Helmholtz free energy $F(T,V)$, which is related by a Legendre transformation to $G(T,P)$

$$G(T,P) = PV + F(T,V)\,, \quad \text{with pressure } P = -\frac{\partial F(T,V)}{\partial V} \quad \text{and volume } V = -\frac{\partial G(T,P)}{\partial P}\,.$$

Therefore, in the (N,P,T) ensemble, the volume jumps, which corresponds to a constant pressure in the (N,V,T) ensemble, as illustrated in Fig. I.2. The way a system typically manages this constant pressure is by forming a coexistence between two phases and by changing their relative volume fraction as the total volume is changed externally. This shows that a first-order transition in the (N,P,T) ensemble shows coexistence in the (N,V,T) ensemble. This is one of the basic principles used to identify first-order transitions in the two-dimensional melting scenario of interacting particles [12, 13].

Clearly, the Ehrenfest scheme could be inadequate. A more modern accepted classification is given by Landau [8, 25] in terms of order parameters, which are generically defined

[2]The Gibbs free energy (also free enthalpy) is defined in the constant (N,P,T) ensemble and defined as $G(P,T) = H - TS$ (T is the temperature, S the entropy, H is the enthalpy $H = U + PV$, with U the internal energy, P the pressure and V the volume). In contrast, the (N,V,T) ensemble is described by the Helmholtz free energy $F(V,T) = U - TS$.

as macroscopic quantities (typically, the thermodynamic average of an observable) that take characteristically different values in different phases. For example, the density difference between a liquid and a gas could be considered as an order parameter at the liquid-gas transition[3]. If the order parameter changes discontinuously at the transition point, the transition is identified as a first-order transition. On the other hand, if the order parameter changes continuously but non-analytically at the transition point it is called a second-order transition or more appropriately a continuous transition.

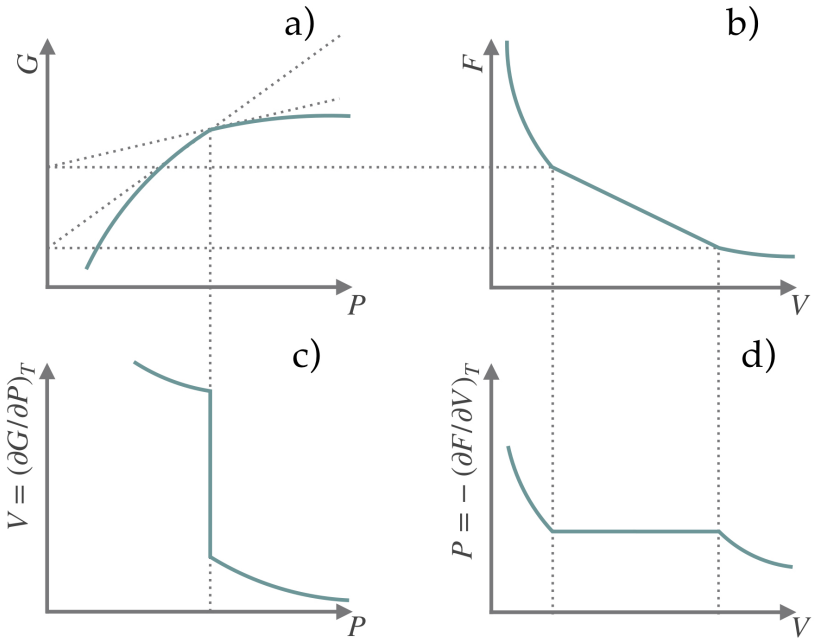


Figure I.2: **Non-analyticity in a first-order transition.** a) The Gibbs free energy G over the pressure P. b) The Helmholtz free energy F over the volume V. c) V over P at constant temperature T. d) P over V at constant T. The jump in V (equivalently density) in the (N, P, T) ensemble in c) corresponds to an invariant pressure in the (N, V, T) ensemble in d) which the system manages by changing the volume fraction of the coexisting phases. Source: Inspired by Fig. 2.15 in D. Chowdhury and D. Stauffer, *Principles of Equilibrium Statistical Mechanics* → [24]

In the following, a few important characteristics of typical phase transitions are given.

First-order transition: Usually, the jump discontinuities lead to a Latent heat for the transition. For example, when water freezes at 273 Kelvin to ice, around 334.72 Joule of heat is released per gram of water. The correlation length, which characterizes correlations of the fluctuations of the order parameter with respect to its average, remains finite. Usually, a phase that is stable in one side of the transition becomes first meta-stable on the other side before it becomes unstable against microscopic fluctuations as illustrated in the schematics

[3] In some cases, finding a suitable order parameter could itself be tricky and the choice may not be unique (any power of an order parameter is itself an order parameter). In fact, in some cases, transitions are not described by thermodynamic order parameters (in the sense of global averages of some quantity) but own other non-obvious phase-defining characteristic properties as the case in the topological Berezinskii-Kosterlitz-Thouless transition in the two-dimensional XY model which is described later.

in Fig. I.3a (an example is supercooled water).

Second-order transition: In a second-order transition, a state that is stable on one side of the transition becomes unstable on the other side of it (see Fig. I.3b). The order parameter changes continuously at the transition and the correlation length of the spatial fluctuations of the order parameter diverges algebraically[4] while approaching the transition point and becomes infinite at the transition point. In consequence, the macroscopic state at the transition point is scale-free, even when microscopic interactions are short-ranged. Most of the microscopic details become unimportant for the thermodynamic properties at the phase transition. This has led to the idea of universality, where systems with very different physical properties have a similar macroscopic behavior at the transition point. For example, fluids and magnets could have similar critical properties at the transition point. This is quantified by thermodynamic scaling laws, where different universality classes are defined according to critical exponents which are usually determined by the symmetry, space dimension, and dimension of the order parameter. Within the same universality class, a transition point can be different but the critical exponents are the same. An effort to understand this has culminated in the theory of renormalization group [25–27].

Infinite-order transition: There are cases where the discontinuity is characterized by an essential singularity[5], where the non-analyticity is seen only at infinite order. Such singularities appear in the Berezinskii-Kosterlitz-Thouless transition in the two-dimensional XY model or in the melting of a two-dimensional solid (both are discussed later). In these examples, there is no obvious thermodynamic order parameter[6], and the transition is between a phase with a finite correlation length and a phase with a power-law correlation of some system depending correlation function (*e.g.* the spatial correlation of rotors in the two-dimensional XY model).

An intuitive picture, illustrating the fundamental differences between types of phase transition can be seen in Landau's phenomenological theory. An equilibrium state corresponds to the minimum of the Landau free energy as a function of the order parameter. Without getting into the details of the Landau description of phase transitions, the basic idea is illustrated in Fig. I.3 for first- and second-order transitions. Even though Landau's original phenomenological theory did not take spatial fluctuations of the order parameter into account, it provides an adequate description of phase transitions. The phenomenological description of superconductivity is considered as one of the most accomplishments of this theory, which emphasized by the Nobel Prize, awarded in 2003 to Abrikosov and Ginzburg. Shortly thereafter, the importance of fluctuations was recognized. The respective theory developed by Kadanoff, Fisher, Wilson, Patashinkii [28–36] culminated in the idea of renormalization.

[4] The correlation length follows $\xi \sim \frac{1}{|T-T_c|}^{\nu}$, where ν is the critical exponent. Even systems which are microscopically different can have the same set of critical exponents, which defines the universality class of the transition.

[5] An essential singularity is different from a pole, as the discontinuity is seen only at the infinite order derivative. For example, $f(x) = e^{-1/x^2}$ for $x \neq 0$ and $f(0) = 0$ looks smooth near $x = 0$. However, $f(x)$ is non-analytic as there is no Taylor series expansion around this point as all order derivatives of the function are zero at $x = 0$.

[6] For the two-dimensional melting which undergoes a similar defect-mediated transition as in the two-dimensional XY model, there have been attempts for a Landau theory using Fourier coefficients of the density as an order parameter. See [5].

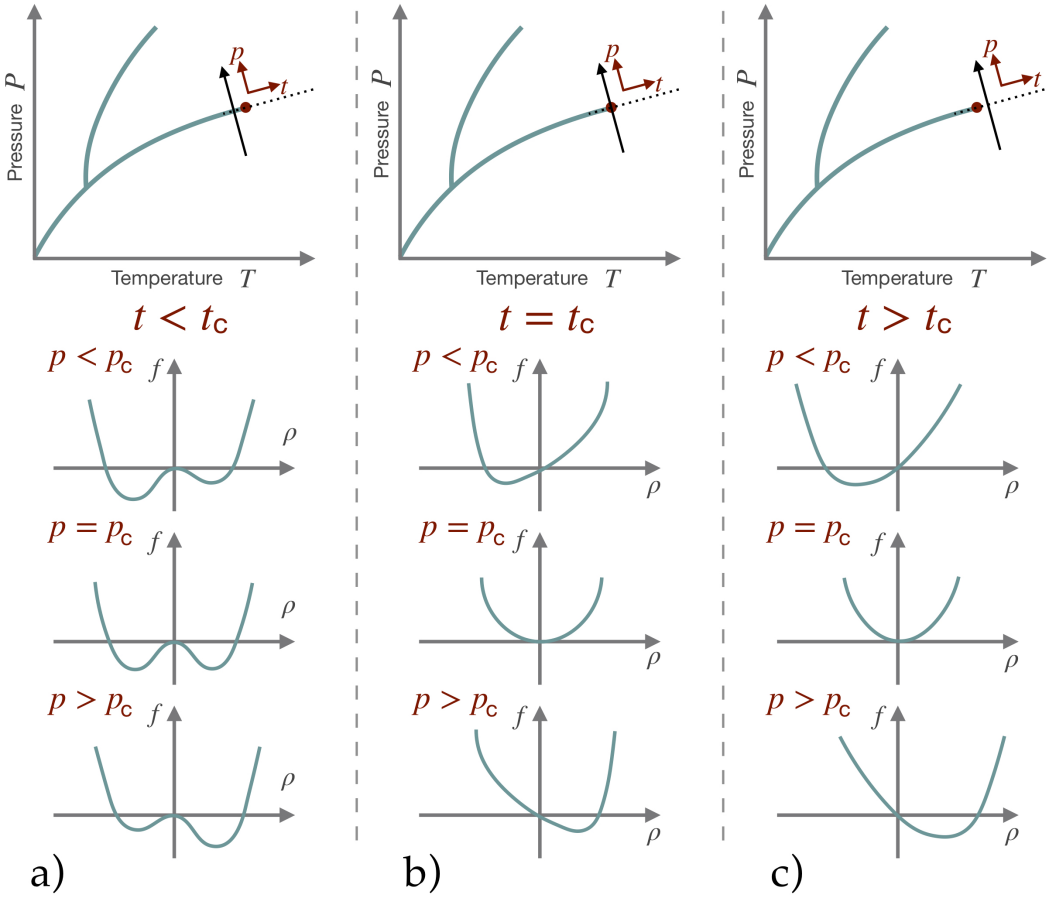


Figure I.3: **Landau picture of phase transitions.** The figures show the evolution of the shape of the Landau free-energy density $f(\rho)$ in paths around the critical point, indicated in the top panel. New thermodynamic parameters (p, t) are defined for paths moving perpendicular and parallel to the liquid-gas transition line near the critical point $(P_c, T_c) = (p_c, t_c)$. In column a), as p is changed while keeping $t < t_c$ fixed the fluid undergoes a first-order transition from the gas phase to the liquid phase. Similarly, column b) follows a path at $t = t_c$ passing through the critical point, column c) follows a path at $t > t_c$ without passing through a phase transition. The columns illustrate how the Landau free energy density changes along these paths. The value $\rho = \rho_{\text{min}}$ at the global minimum of $f(\rho)$ gives the equilibrium value of the order parameter. In column a), ρ_{min} jumps as p is varied across p_c. The local minima in the free energy represent a metastable state. In column b), as p is varied ρ_{min} changes smoothly while crossing the second-order transition point (p_c, t_c). If a path is followed varying t while keeping $p = p_c$, the free energy evolves as shown in the middle row, where the system undergoes a spontaneous symmetry breaking. Source: Inspired by Fig. 12.2 in D. Chowdhury and D. Stauffer, *Principles of Equilibrium Statistical Mechanics* → [24].

Remark: The non-analyticity of the free energy[7] at a phase transition is only seen at the thermodynamic limit. For a finite system, the partition function (and thus the free energy)

[7] Helmholtz or Gibbs free energy, depending on the ensemble.

is a finite degree polynomial in the control parameters (for example, in e^{β}, fugacity, *etc.*) and therefore, the free energy is always analytic. Only in the thermodynamic limit, when the partition function becomes an infinite degree polynomial, a non-analyticity in the free energy can appear. How this happens in theoretical analyses is illustrated by Yang-Lee zeros [37], where for finite size systems, the singularities appear on the complex parameter space, and they converge to a real parameter value as the thermodynamic limit is reached.

I.2 Systems outside thermodynamic equilibrium

Feynman [38] emphasizes[8] that the concept of equilibrium is a theoretical one and as such only effectively realized in real world experiments. The equilibrium picture requisites vanishing (microscopic) fluxes of all quantities (*e.g.* energy, matter, temperature, *etc.*) in the system. In the real-world, this is achievable within a certain time and length scales only. Outside these scales, a system is in a non-equilibrium state. Such non-equilibrium situations are found in a large variety of physical systems, in fact, they are more common in nature than systems in equilibrium. Such systems often exchange fluxes of matter or energy with the surrounding or undergo chemical reactions. Living systems are one of the prominent examples. In the literature, also glasses may be described as non-equilibrium systems, which are in the transient before reaching equilibrium [39].

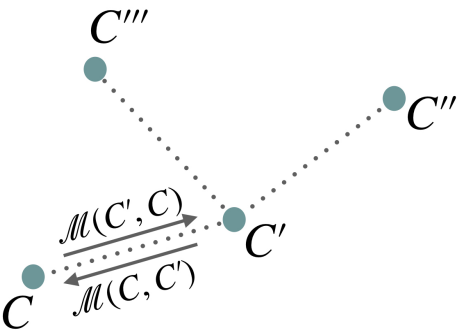


Figure I.4: **Transitions in a discrete-time Markov process.** An illustration of transition probabilities $\mathcal{M}(C', C)$ of a discrete-time Markov process on a *finite* configuration space.

An interesting non-equilibrium situation is the steady state in which there is no time dependence, but there is a constant flow of some quantity. Such flow can be maintained by injection at one boundary and subtraction at another, as, for example, in a conducting rod between two baths, or the flow can be driven by an external field such as the electric field driving an electric current around a conducting loop. Driving could also come from an internal engine of the microscopic agents, as often the case for active media like bacteria, molecular motors, *etc*. Such non-equilibrium systems have characteristic properties like the break down of time reversibility, the violation of the fluctuation-dissipation relation, *etc.*.

Many of these concepts, namely, the steady state, detailed balance, time reversibility, *etc.*, can be clearly described using a stochastic description of the time evolution of a system on its configuration space. Such an example is a discrete-time (n) Markov process[9] given

[8] [38]: "*If a system is very weakly coupled to a heat bath at a given 'temperature', if the coupling is indefinite or not known precisely, if the coupling has been on for a long time, and if all the 'fast' things have happened and all the 'slow' things not, the system is said to be in thermal equilibrium.*"

[9] The Markov property implies that the dynamics of a system depends only on the present state and not on the past. This is often a reasonable description as systems typically have a finite correlation over time. Moreover, it often happens that a non-Markovian problem can be embedded into a larger Markovian system by taking supplementary degrees of freedom into account. This is the case for the persistent kinetic Monte

in terms of the transition probability $\mathcal{M}(C', C)$ for a jump from configuration C to C' (see Fig. I.4). To keep the presentation simple, only a **finite configuration space** is considered. The dynamics is given in terms of the time evolution of the probability $P_n(C)$ for the system to be at a configuration C at time n, which follows a Master equation

$$P_{n+1}(C') = \sum_C \mathcal{M}(C', C) P_n(C)\,, \tag{I.1}$$

with a probability conserving condition

$$\sum_{C'} \mathcal{M}(C', C) = 1\,. \tag{I.2}$$

The transition matrix $\mathcal{M}$ is also known as the Markov matrix.

Given an initial probability distribution $P_0(C)$, the solution of (I.1) is formally written as

$$P_n(C) = \left[\mathcal{M}^n \cdot P_0\right](C)\,,$$

where the dot $(\cdot)$ denotes a matrix product. In general $\mathcal{M}$ is not symmetric, and therefore it has distinct left eigenvectors ($\mathcal{L}_k(C)$) and right eigenvectors ($\mathcal{R}_k(C)$) associated to the eigenvalues μ_k. Then, using a normalization $\sum_k \mathcal{L}_k(C)\mathcal{R}_k(C') = \delta_{C,C'}$ the probability

$$P_n(C) = \mu_0^n\, \mathcal{R}_0(C) A_0 + \mu_1^n \mathcal{R}_1(C) A_1 + \cdots$$

where $A_k = \sum_C \mathcal{L}_k(C) P_0(C)$.

On a finite configuration space, as long as all entries in $\mathcal{M}$ are positive and non-zero, the Perron-Frobenius theorem[10] [40] ensures that the largest eigenvalue (say μ_0) is non-degenerate, with non-vanishing spectral gap $\Delta\mu = \mu_0 - |\mu_1|$. In addition, due to the condition (I.2), $\mu_0 = 1$ and $\mathcal{L}_0(C) = 1$. In combination with the finite configuration space, this means: at large time, the probability reaches a steady-state (time-independent) distribution given by

$$P_{\text{steady}}(C) = \mathcal{R}_0(C)$$

and the system relaxes to the steady state in a time scale $1/\Delta\mu$.

Clearly, the steady state does not depend on the initial state and it is solely decided by the transition probabilities. The probability $P_{\text{steady}}(C)$ is time-independent, and then (I.1) gives

$$P_{\text{steady}}(C') = \sum_C \mathcal{M}(C', C) P_{\text{steady}}(C)\,.$$

This is the **global-balance condition**. Better sense can be made out of this by using (I.2) which gives

$$\sum_C \mathcal{M}(C, C') P_{\text{steady}}(C') = \sum_C \mathcal{M}(C', C) P_{\text{steady}}(C)\,. \tag{I.3}$$

The left hand side is the net outgoing probability current (probability flow per unit time) from C', and the right hand side is the net incoming probability current. This means, in the steady state, the outgoing and incoming probability currents are the same.

Carlo dynamics presented later in this thesis.

[10] The same theorem becomes crucial in discussion of phase transitions in one-dimensional equilibrium systems (see chapter III).

I.2.1 Equilibrium steady state

The equilibrium state is "only" a subclass of possible steady states (see Fig. I.5) and appears when for each edge-connected configurations C-C' (see Fig. I.4), the outgoing and incoming currents cancel, resulting in vanishing local net currents (and hence also in a vanishing global net current). This condition, written as

$$\mathcal{M}(C,C')P_{\text{eq}}(C') = \mathcal{M}(C',C)P_{\text{eq}}(C) \qquad \text{(I.4)}$$

where the notation $P_{\text{steady}}(C) = P_{\text{eq}}(C)$ is chosen, is known as the **detailed-balance condition** and can be considered as a microscopic definition of the equilibrium state [11]. This says that a steady state is in equilibrium if the probability current vanishes everywhere in the configuration space.

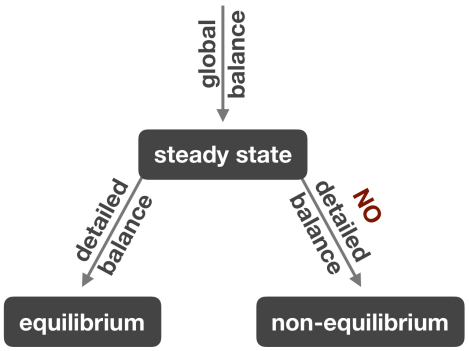


Figure I.5: **Classification of steady states.** When the global-balance condition (I.3) is fulfilled, the system reaches a steady state. The equilibrium state is only a subclass of steady states where the additional condition of detailed balance is satisfied. Otherwise, the steady state is out-of-equilibrium.

For a system in thermal equilibrium at the inverse temperature β, knowing that the equilibrium probability is a Gibbs-Boltzmann distribution $P_{\text{steady}}(C) \sim e^{-\beta E(C)}$ with $E(C)$ being the energy of a configuration C, the detailed-balance condition gives

$$\frac{\mathcal{M}(C,C')}{\mathcal{M}(C',C)} = \frac{P_{\text{eq}}(C)}{P_{\text{eq}}(C')} = e^{-\beta[E(C)-E(C')]} .$$

There are several possible choices of transition rates which lead to the same equilibrium state, as long as the above condition is satisfied. This freedom is often utilized in the literature for efficient numerical sampling of the equilibrium distribution, and this led to several variations like the Glauber dynamics, the Kawasaki spin exchange algorithm for Ising model, the Swendsen-Wang cluster algorithm, the Metropolis algorithm, *etc.* [42]. One of the popular implementations, which is also used extensively in this thesis, is the **Metropolis filter**, where the transition probability is given by

$$\mathcal{M}(C,C') = \min\left\{1, \frac{P_{\text{eq}}(C)}{P_{\text{eq}}(C')}\right\} = \min\left\{1, e^{-\beta[E(C)-E(C')]}\right\} .$$

It is straightforward to verify that (I.4) is satisfied with the Gibbs equilibrium distribution.

Another form that is often used is the Suzuki-Kubo [43] transition probability

$$\mathcal{M}(C,C') = \frac{1}{2}\left\{1 - \tanh\left[\frac{\beta(E(C)-E(C'))}{2}\right]\right\} .$$

[11] The detailed-balance condition (I.4) requires the prior knowledge about the equilibrium probability $P_{\text{steady}}(C)$. Is it possible to say, just from the transition rates, whether a Markov process leads to an equilibrium steady state? The answer is given by the Kolmogorov criterion [41] which states that for every loop on the configuration space if the product of transition rates in clock-wise direction is the same as the product in the anti-clockwise direction, then it is a necessary and sufficient condition for the steady state to be in equilibrium.

I.2.2 Non-equilibrium steady state

This freedom in choices of the transition probabilities for equilibrium dynamics breaks down when the detailed-balance condition is not fulfilled. This is the non-equilibrium situation which is characterized by non-zero probability currents in at least one edge on the configuration space. One of the simplest examples of a non-equilibrium dynamics is when for each incoming path to a configuration there is one outgoing path and their currents are equal. More precisely,

$$\mathcal{M}(C'', C')P_{\text{steady}}(C') = \mathcal{M}(C', C)P_{\text{steady}}(C)$$

which, in analogy with (I.4), is sometimes referred as **pairwise balance** (see Fig. I.4 for illustration). Clearly, the global-balance condition (I.3) is satisfied, but the probability current is non-zero, and therefore the steady state is out of equilibrium. A trivial example is a biased random walker on a periodic one-dimensional lattice with unequal right and left rates. The bias drives a non-zero current and the steady state is out of equilibrium. The popular examples of out-of-equilibrium models, like the asymmetric exclusion process, the Katz–Lebowitz–Spohn model of driven Ising chains, follow this pairwise balance of the probability currents.

Clearly, there are innumerable possibilities of transition rates that do fulfill the global-balance condition but that do not fulfill the detailed-balance condition. This identifies non-equilibrium steady states as the most general case and the equilibrium state as a non-typical (but without doubt an important) subclass.

I.2.3 Characteristic differences between equilibrium and non-equilibrium steady states

Non-equilibrium systems often display novel and unexpected features that are in striking contrast to equilibrium properties. This subsection I.2.3 discusses some of these important characteristic differences.

The detailed-balance condition is a strong microscopic symmetry which introduces many thermodynamic properties that are characteristics of equilibrium. An obvious characteristic is the vanishing current of any quantity. However, there are examples of non-equilibrium steady states which have vanishing currents in many observables. For example, in a Kawasaki spin exchange Ising model on a square lattice, if the vertical and horizontal exchanges are done at different temperatures, the steady state has a zero average current of spins [44]. However, the steady state is out-of-equilibrium, as energy flows between the two temperature reservoirs. In another example, relevant to this thesis, an active self-propelled particle in a one-dimensional confining potential has a vanishing particle current. But again, this is a non-equilibrium steady state and the non-vanishing probability current can be seen in the position-velocity phase-space. In this very same example, the probability distribution of the particle position can be written in a Gibbs form with an effective potential. This is to emphasize that an equilibrium-like Gibbs probability is not unique to equilibrium. Another, very well known example is the previously mentioned Katz–Lebowitz–Spohn model of Ising spins on a one-dimensional circular lattice under a driving field, such that nearest-neighbor spins are exchanged following a dynamics that favors "up" spins to move rightward. It was

shown [45, 46] that the steady state has the same probability distribution as the equilibrium Ising model, but with an effective temperature.

For a system in equilibrium, there is a well-developed thermodynamic description [8]. Even though the microscopic configuration space is made of a number of degrees of freedom on the order of the Avogadro number, there are only a handful number of relevant thermodynamic variables, like, pressure, volume, temperature, entropy, to describe the macroscopic properties of a system. There is a notion of thermodynamic conjugate variables, like pressure to volume, temperature to entropy, chemical potential to density, *etc.*, which introduce concepts of thermodynamic ensembles. Moreover, the macroscopic statistical properties *i.e.* the entire spectrum of fluctuations of thermodynamic variables can be characterized in terms of thermodynamic potentials, like the free energy, the enthalpy, and the Gibbs potential, depending on the ensemble. There is no such equivalence for systems outside equilibrium. In fact, even the basic idea of well-defined thermodynamic variables seems not possible in general (see *e.g.* [47, 48]).

There has been an effort in the past to extend the concepts of thermodynamic variables outside equilibrium, like the effective-temperature description of glasses [49, 50], and a thermodynamic pressure can exist in certain active media [51]. For systems near equilibrium, one may describe dynamics in an effective free-energy landscape. However, these are constructed rather phenomenologically and are not solidly founded on statistical mechanics. Even in cases where an effective equilibrium-type description is possible for static quantities (single-time properties), the dynamical fluctuations are fundamentally different in non-equilibrium. For example, at first glance, a glass may appear like an amorphous solid in equilibrium. Likewise, in cellular processes, it is often unclear whether particular stochastic fluctuations of cellular components (*e.g.*, proteins, membranes, organelles) are driven by thermal or non-thermal processes [52]. What truly reveals the non-equilibrium nature in these systems are the dynamical properties. Two ideas that have been extensively used to identify non-equilibrium states are the time reversibility and the fluctuation-dissipation relation. They are described below.

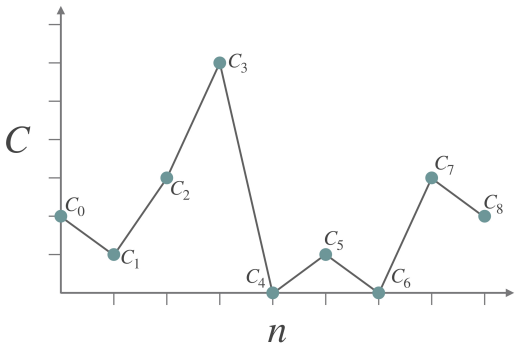


Figure I.6: **Discrete stochastic time evolution.** Schematic of a stochastic path on the configuration (C) space of a discrete-time (n) Markov process.

A dynamics which is **symmetric under time reversal**, is in equilibrium. More precisely, in equilibrium, the probability of a particular time evolution (path) is the same as the probability of the time reversal of that path. A path is given by the set of configurations that the system passes through in a discrete-time window from 0 to N. Such a path is denoted by $\mathcal{T}_N \equiv \{C_0, C_1, \ldots, C_N\}$, and its time reversal by $\mathcal{RT}_N \equiv \{C_N, C_{N-1}, \ldots, C_0\}$, as illustrated in Fig. I.6. The probability of seeing such a path when the system is in its steady state is given by

$$P(\mathcal{T}_N) = \mathcal{M}(C_N, C_{N-1}) \cdots \mathcal{M}(C_2, C_1)\mathcal{M}(C_1, C_0)P_{\text{steady}}(C_0)$$

and similarly for $P(\mathcal{RT}_N)$. Using the detailed-balance condition (I.4) for an equilibrium

system, this gives

$$\frac{P(\mathcal{R}\mathcal{T}_N)}{P(\mathcal{T}_N)} = \frac{\mathcal{M}(C_0,C_1)\mathcal{M}(C_1,C_2)\cdots\mathcal{M}(C_{N-1},C_N)P_{\text{steady}}(C_N)}{\mathcal{M}(C_N,C_{N-1})\cdots\mathcal{M}(C_2,C_1)\mathcal{M}(C_1,C_0)P_{\text{steady}}(C_0)} = 1\,,$$

which means that both probabilities are identical. Therefore, stochastic time reversibility is a simple consequence of the detailed-balance condition. In consequence, this also means that the way a spontaneous fluctuation gets created in equilibrium is the same as how the system relaxes from this fluctuation [53]. This is the characteristic of equilibrium and this breaks down outside equilibrium.

The second dynamical property, which is a characteristic of equilibrium is the **fluctuation-dissipation relation**. This appears in the context of the linear response of an equilibrium state to a small change of a thermodynamic condition. For example, how much does the volume of a gas changes under a small change in the pressure. For a precise statement, consider B (*e.g.*, internal energy or volume) as a fluctuating thermodynamic variable in a constant h ensemble (*e.g.*, the (N,P,T) ensemble). If h is changed by a tiny amount in the past over time $\delta h(t)$, the system readjusts to a new equilibrium steady state, and say $\langle\delta B\rangle$ is the associated change in the average of B. Then, as long as δh is small,

$$\langle\delta B\rangle \simeq \int_{-\infty}^{0} dt\,\delta h(t)R(t)\,,$$

where the response function is expressed in terms of the dynamical correlation of B and the variable A (conjugate to h) as

$$R(t) = \beta\frac{d\langle B(0)A(t)\rangle_c}{dt}\,,$$

where the subscript c denotes the connected correlation. This is the fluctuation-dissipation relation and is a consequence of the detailed-balance symmetry in the dynamics. To appreciate the relation, δh can be considered constant and $B\equiv A$. In this case, assuming a finite correlation time, the above result gives

$$\frac{1}{\beta}\left\langle\frac{\delta A}{\delta h}\right\rangle = \langle A^2\rangle_c\,,$$

thus the response and the fluctuations are related. For instance, if A is the total energy and h is the temperature, then the response $\left\langle\frac{\delta A}{\delta h}\right\rangle$ is the specific heat and it is related to the fluctuation of energy. Similarly, the compressibility is related to volume fluctuations.

Outside equilibrium such fluctuation-dissipation relations break down. For systems like active matter, they are broken by the injection of energy even at the microscopic level. In recent years there have been developments on extending the fluctuation-dissipation relation far from equilibrium. These proposals (*e.g.* [54, 55]) predict correction terms to the relation. However, normally, these terms are expressed in terms of microscopic details which are not easily accessible to measurements.

The success of statistical mechanics is to bridge the gap between microscopic dynamics and the thermodynamic measurable properties when the system is in equilibrium. The formalism has provided a strong microscopic basis for the laws of thermodynamics. It provided tools to describe equilibrium phases of matter and led to a deep understanding of

phase transitions, which culminated in the renormalization group theory. In contrast, there is no such general framework outside equilibrium capable of predicting the macroscopic behavior in terms of microscopic physics. There is no analog of the universal Boltzmann-Gibbs distribution and presumably it does not exists. It is still very difficult to define thermodynamic state variables, or thermodynamic potentials similar to the free energy, from which the statistical properties of non-equilibrium systems can be computed and which provide an intuition for how these systems behave. Some of these important characteristic differences between an equilibrium and a non-equilibrium steady state are summarized in Tab. I.1.

Equilibrium	**Out-of-equilibrium**
Zero probability current.	Non-zero probability current.
One-time statistical properties do not depend on specific details of the dynamics.	Details of the dynamics are important.
Relevant state variables like pressure and temperature exist.	Not available.
Thermodynamic potentials like the free energy and the enthalpy exist and are well-defined.	Not available.
Universal microscopic distributions like the Gibbs-Boltzmann distribution $P_{\text{eq}} \propto e^{-\beta E(C)}$.	Not available.
Linear response and fluctuation-dissipation relation.	Breaks down.
Time-reversal symmetry of fluctuations.	Not symmetric.
Universal properties like, $\Delta S \leq 0$.	Fluctuation theorem like Gallavotti-Cohen relation, Jarzynski equation.

Table I.1: **A list of basic characteristic differences between an equilibrium and a non-equilibrium steady state.** Some of these are briefly discussed in subsection I.2.3 .

Nevertheless, the field of non-equilibrium has seen much progress and a few strikingly universal results have come out in the past few decades. Fluctuation theorems, like the Jarzynski equality [56, 57] and the Gallavotti-Cohen relation [58, 59], allowed for the extension of universal thermodynamic results like the second law to regimes far from equilibrium. Even with the lack of a clear classification of thermodynamic variables, distinct macroscopic phases are clearly seen outside equilibrium [41, 60–62]. There are indeed non-equilibrium phase transitions. Collective behavior in active matter, glass transitions, tran-

sitions in contact processes, epidemic spreading are only a few of such examples. Even the concept of universality exists [62] outside equilibrium, *e.g.* in directed percolation, or in interface fluctuations [63]. However, their understanding is far from complete.

The subject of non-equilibrium collective behavior is one of the challenging directions in modern Physics. A global theory akin to equilibrium thermodynamics that would describe general non-equilibrium behavior still remains to be found. In the absence of a well-defined framework, most of the studies of non-equilibrium systems resort to detailed microscopic analysis of low-dimensional models and their computer simulations. The systems of active matter are such examples where many non-equilibrium collective properties, distinct phases, spontaneous symmetry breaking, *etc.* emerge from relatively simple interactions. Naturally, active matter has attracted a tremendous amount of attention in recent years [14, 64–67]. Studies in these systems are expected to improve the understanding of non-equilibrium that may someday solve this long-standing problem.

I.3 Continuous Markov process, Fokker-Planck equation, and Langevin dynamics

In this section I.3, a few of the archetypal stochastic dynamics are introduced which are essential for understanding this thesis. For this mostly the presentation from the book of van Kampen [40] is followed.

I.3.1 Continuous-time Markov process

A systematic approach to go to the continuous-time limit from (I.1) is by writing $t = n\,\epsilon$ and taking $\epsilon \to 0$. In this small-ϵ limit, the transition probability becomes

$$\mathcal{M}(C', C) = \delta_{C',C} + dt\,\mathcal{W}(C', C) + \cdots\,,$$

where $\delta_{C',C}$ captures the situation that when zero time has passed by the system is in its initial configuration. $\mathcal{W}(C', C)$ is the transition rate from C to C'. Using this in (I.1) and taking the $\epsilon \to 0$ limit gives

$$\frac{dP_t(C')}{dt} = \sum_C \mathcal{W}(C', C) P_t(C)\,, \tag{I.5}$$

where $P_t(C)$ is the probability for the systems to be at C at the continuous time t. This is the continuous-time Master equation. In this case, the condition (I.2) translates to

$$\sum_{C'} \mathcal{W}(C', C) = 0\,. \tag{I.6}$$

Writing this condition as $\mathcal{W}(C, C) = -\sum_{C' \neq C} \mathcal{W}(C', C)$, the Master equation is often written in a convenient form as

$$\frac{dP_t(C')}{dt} = \sum_C \left[\mathcal{W}(C', C) P_t(C) - \mathcal{W}(C, C') P_t(C')\right]\,. \tag{I.7}$$

Then, for this case, the global-balance condition (I.3) becomes

$$\sum_C \left[\mathcal{W}(C', C)P_t(C) - \mathcal{W}(C, C')P_t(C')\right] = 0$$

and the detailed-balance condition (I.4) becomes

$$\mathcal{W}(C', C)P_t(C) = \mathcal{W}(C, C')P_t(C') \,.$$

The largest eigenvalue of $\mathcal{W}$ is 1 and the associated right eigenvector is the steady-state probability distribution.

I.3.2 Fokker-Planck equation

When the configuration space is continuous $C \equiv x$, the sum in (I.7) becomes an integral, leading to

$$\frac{dP_t(x)}{dt} = \int dy \left[\mathcal{W}(x, y)P_t(y) - \mathcal{W}(y, x)P_t(x)\right] \,. \tag{I.8}$$

For simplicity, it is assumed that the configuration space is one-dimensional. This is the Master equation when both time and configuration space are continuous, as for example in Brownian motion.

In most natural examples, the system can move only small distances in a small time. Therefore a reasonable assumption is that $\mathcal{W}(x, y)$ decays fast with the distance between x and y. This is equivalent of writing $\mathcal{W}(y, x) = g(y - x, x)$ such that $g(\epsilon, x)$ is a fast varying function of ϵ, but has a smooth dependence on x. This property can be used to write the continuous Master equation (I.8) as a Fokker-Planck equation. This systematic approach is known as the Kramers-Moyal expansion [40] and is described below.

Writing $y = x - r$ in (I.8) gives

$$\frac{dP_t(x)}{dt} = -\int dr \left[g(r, x - r)P_t(x - r) - g(-r, x)P_t(x)\right] \,.$$

Because the function $g(y, x)$ has a smooth dependence on the second argument x, a Taylor expansion in the second argument is well-defined, but may not be in the first argument y. Using this,

$$\frac{dP_t(x)}{dt} = -\int dr \left[g(r, x)P_t(x) - r\frac{d}{dx}(g(r, x)P_t(x)) + \frac{r^2}{2}\frac{d^2}{dx^2}(g(r, x)P_t(x)) + \cdots - g(-r, x)P_t(x)\right] \,.$$

The first and last term on the right hand side vanish as $\int dr g(r, x) = 0 = \int dr g(-r, x)$ due to (I.6). Then, defining

$$a_n(x) = -\int dr\, r^n g(r, x) = -\int dy\, (y - x)^n \mathcal{W}(y, x)$$

gives

$$\frac{dP_t(x)}{dt} = -\frac{d}{dx}[a_1(x)P_t(x)] + \frac{1}{2}\frac{d^2}{dx^2}[a_2(x)P_t(x)] + \cdots \,. \tag{I.9}$$

This is known as the Fokker-Planck equation.

Remarks:

- In typical examples, the transition rate $\mathcal{W}(x+r,x)$ is a sharply peaked function of r, and one can stop at the second order in (I.9). This is the case for the Langevin dynamics discussed next. However, there are examples where it is essential to keep higher order terms, and the Fokker-Planck equation may not have a Langevin description. One such case is the continuous limit of the persistent kinetic Monte Carlo model in this thesis (see subsection II.4.3).

- Drawing similarity with the Master equation (I.5), the Fokker-Planck equation is often written as $\partial_t P_t(x) = \mathbb{L} \cdot P_t(x)$, where the role of the Markov matrix is played by the differential operator $\mathbb{L}$. However, from the mathematical point of view, things are more difficult. For instance, the statement of the Perron-Frobenius theorem requires more stringent assumptions and its proof is much more involved than in the discrete case [10].

I.3.3 Langevin dynamics

This dynamics was originally proposed by P. Langevin as a mechanical model for the Brownian motion. The basic idea is to incorporate thermal noise as a random force in the classical Newtonian dynamics of a particle. The position $x(t)$ of a particle of mass m under an external force $F(x)$ follows Newton's equation

$$m\ddot{x}(t) = F(x) + \eta(t) - \gamma\dot{x}(t)\,,$$

where $\eta(t)$ is a random force due to the thermal noise of the surrounding medium. Such a noise is assumed to be delta correlated in time

$$\langle \eta(t) \rangle = 0, \qquad \text{and} \qquad \langle \eta(t)\eta(t') \rangle = 2D\,\delta(t-t')\,.$$

The term $\gamma\dot{x}$ is due to the viscous drag of the medium. The inertial term $m\ddot{x}(t)$ can be ignored, if the medium is highly viscous, leading to

$$\dot{x}(t) = \frac{1}{\gamma}F(x) + \frac{1}{\gamma}\eta(t)\,. \tag{I.10}$$

This is known as the over-damped limit. In many practical examples, particularly for small objects, like pollen grains, colloids, this is a reasonable limit. Even the simple models of active matter are usually defined in this limit and typically referred to as "dry" active matter [14]. In contrast, $m\ddot{x}(t)$ cannot be ignored, if the fluid flow is important in the system. This class of momentum conserving systems are refereed to as "wet" active matter [14]. To keep the presentation simple, the dry limit is used for the rest of the discussion.

It can be shown that such an over-damped Langevin equation corresponds to a Fokker-Planck equation

$$\frac{dP_t(x)}{dt} = -\frac{1}{\gamma}\frac{d}{dx}[F(x)P_t(x)] + \frac{D}{\gamma^2}\frac{d^2}{dx^2}[P_t(x)]\,.$$

In the steady state, $\partial_t P_{\text{steady}}(x) = 0$, and thus

$$F(x)P_{\text{steady}}(x) - \frac{D}{\gamma}\frac{d}{dx}[P_{\text{steady}}(x)] = J = \text{constant}.$$

J is the probability current, and similar to the discrete Markov process, the steady state is in equilibrium when $J = 0$. This happens when the force due to a potential $U(x)$ is such that $F(x) = -U'(x)$. Then, $D\partial_x P_{\text{steady}}(x) = -\gamma U'(x)P_{\text{steady}}(x)$, and the solution is

$$P_{\text{steady}}(x) = P_{\text{eq}}(x) \propto e^{-\frac{\gamma U(x)}{D}} .$$

If the Langevin equation models a particle in contact with a thermal bath at temperature T, it must follow that

$$D = \gamma k_{\text{B}} T .$$

This is the **fluctuation-dissipation relation** for the Langevin dynamics which relates the strength of fluctuations (D) to the viscous dissipation (γ). This is an energy balance condition between the injection of energy from the surrounding bath in the form of thermal noise, and dissipation into the bath due to viscosity. This is an essential condition for the system to be in equilibrium. In systems outside equilibrium, *e.g.* for active particles, the energy source originates from internal degrees of freedom of the particles and the energy is not returned to it. As a result the fluctuation-dissipation relation breaks down.

In such non-equilibrium situations, the force $F(x)$ cannot necessarily be expressed as the gradient of a potential. Such forces are called **non-gradient forces**. A simple example is a Brownian particle on a ring under a circular constant driving force f in addition to a periodic potential,

$$F(x) = -U'(x) + f .$$

Because of the periodicity, such a force cannot be written in a gradient form. The system reaches a steady state which is not in equilibrium, and the current J is non-zero. In fact, in this case, the steady-state probability has an explicit form. If the perimeter of the ring is of unit length such that $0 \leq x \leq 1$, then

$$P_{\text{steady}}(x) = \mathcal{N}\left\{\int_0^x dy\, e^{\frac{2}{k_{\text{B}}T}\int_y^x dz F(z)} + e^{\frac{2}{k_{\text{B}}T}\int_0^1 dz F(z)} \int_x^1 dy\, e^{\frac{2}{k_{\text{B}}T}\int_y^x dz F(z)}\right\} .$$

Clearly, the probability distribution does not have a Gibbs-Boltzmann form.

I.4 Active Matter

Thermodynamic phases exist even outside equilibrium. As described above, one does not have the tools of statistical mechanics for an analytical understanding. Thermodynamic concepts, such as the one of a free energy are not guaranteed to exist outside equilibrium, thus new paths need to be explored to gain understanding. The main focus of this thesis lies on one important class of non-equilibrium systems, the active matter. "*Active particles contain internal degrees of freedom with the ability to take in and dissipate energy and, in the process, execute systematic movement* [65]." This definition captures a large variety of natural and artificial examples, such as large animal groups [68] (*e.g.* school of fish [69], flock

of birds [70]), bacteria swarming [71], actin filaments [72], microtubules in motility assays [73], autophoretic colloids [18, 74, 75], colloidal rollers [76], *etc.*. The local energy input adds complexity and increases the diversity of the collective behavior of active particles, which, in contrast to equilibrium systems, is not restricted by rules like time-reversal symmetry. Equilibrium theorems, which *e.g.* forbid crystalline order in two dimensions, do not hold a priori outside equilibrium, thus it is legitimate to ask whether crystalline structures might be favored in two-dimensional active systems under certain conditions, or whether it is possible to at all identify all phases known at equilibrium.

Active Matter systems have been primarily studied in low-density regimes, far away from the equilibrium melting densities. Analytical approaches, such as hydrodynamic, or mean-field descriptions, but also numerical investigations have broadened the understanding of active matter in the dilute limit. New interesting phenomena have been observed and intensely investigated, such as collective motion [77], giant density fluctuations [19, 71, 78, 79] and motility-induced phase separation [80].

The number of studies including the high-density limit, on the contrary, is much fewer. The aim of this thesis is to draw a full phase diagram of a particular active-particle model, which covers both the high- and the low-density limit in one picture. Facing the complexity of analytical approaches for high-density many-body systems, with the additional complications introduced by activity, this thesis exploits a numerical approach to address fundamental questions, such as the question of the existence of a partially ordered hexatic phase outside equilibrium.

The goal to understand the complex phenomena emerging out of equilibrium from numerical simulations raises the question about the "right" technique. Fundamental concepts in equilibrium provide a clear distinction in whether a numerical approach is correct or wrong. Basic guidelines are provided by concepts, such as detailed balance, the fluctuation-dissipation theorem, and time-reversal symmetry (see section I.2). Given that the sole subject of interest are the steady-state properties, the choice is free to either follow individual particle trajectories by using Molecular dynamic simulations or Langevin simulations (Brownian dynamics simulations) or, in contrast, it is equally justified to use Monte Carlo approaches, which, commonly, do not relate to the underlying real-world microscopic movements of the particles. Either of the approaches leads to the same equilibrium steady state obeying the same Gibbs-Boltzmann distribution. Out of equilibrium, systems lack this kind of basic guidelines. However, using the above definition of active particles, it appears that an essential criterion for numerical approaches for such systems is a local dynamics. Clearly this criterion is matched by the numerical integration of the constructed dynamical equation, however, also a kinetic Monte Carlo approach can be designed in a way, such that it captures this and other essential features of active matter.

The long-term and ambitious objective of scientists working in the field of active matter is a fundamental theory describing the living world, including processes such as the movement of cells, transport processes in cells, the stability of the shape of cells and how they divide, but also the leaderless collective motion of, *e.g.*, huge flock of birds, bacteria colonies or cytoskeleton components [64]. If the only available transport mechanism in living organisms would be restricted to passive diffusion processes, the complex structures and functions of the life around us would not have developed. Living matter bases on **self-propelled entities**, which self-organize into large-scale structures and movements. The complexity arises not from the self-propulsion itself, but only in combination with in-

teractions of individual agents. In addition, interactions with the medium the particles are immersed in can be considered, or, for example also, the form and dimension of the confining space.

The choice of the precise kind of interactions depends on the posed question. A model, capturing basic features of the coherent movements observed in flocks of birds may consist of point particles only, which interact solely through the alignment of their velocity to the average direction of motion of their neighbors. When adding a certain amount of random error to the alignment, the famous Vicsek model [77] is recovered. However, this kind of model assumes some kind of visual sensing and complex adaptation mechanisms of the individual agents. The modeling of the collective behavior of bacteria, as for example *Escherichia coli*, requires a different approach.

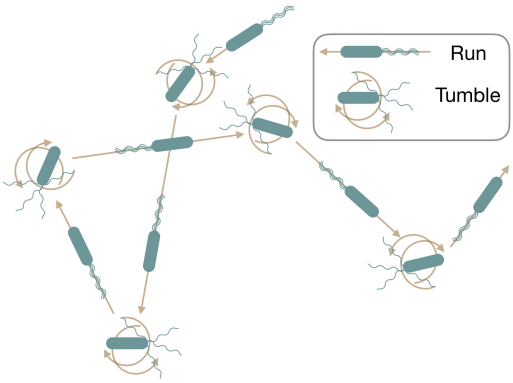


Figure I.7: **Run-and-tumble motion of *Escherichia coli*.** The self-propelled motion is composed of runs, where all flagella rotate in the same sense, and tumbles, where one or more flagella change the rotation direction. During a tumble the bundle of flagella breaks apart, thus the persistent motion stops, and the bacterium rotates randomly around, thus its orientation changes before the next run starts.

Escherichia coli is a rod-shaped bacterium with about four filaments arising at random from the sides of the cell body. This filaments, called flagella, bundle near one end of the rod-shaped cell and equip the bacterium with a self-propulsion mechanism. The flagella are able to rotate in two directions, say in plus- and in minus-direction. In case all flagella rotate in plus-direction, the flagella form an ordered bundle, whose rotation self-propels the bacterium along its major axis. The coherent plus-rotation of all flagella is regularly interrupted by a transient transition to a minus-rotation of one or more flagella. This state, called tumble, brings the flagella bundle in disorder and thus stops the persistent run. During the tumble, the orientation of the major axis changes randomly, thus as soon as all flagella return in the state of a plus-rotation, which reorders the bundle, the bacterium moves in a new direction, dictated by its major axis' orientation. In consequence, the motion consists of persistent runs in a certain direction, interrupted by tumbles, after which the persistent run follows a new direction (see Fig. I.7). [81]

Clearly, a model describing the collective phenomena of *Escherichia coli* must be different from the Vicsek model designed to capture essential features of the collective motion of birds. Firstly the introduction of persistent motion must be different, as a bacterium does not have the same possibilities of sensing its environment and its neighbors like a bird. Furthermore, observing single agents, the persistent trajectories of a bid and of a bacterium look clearly different (see Fig. I.7). Even though bacteria are not able to visually detect their neighbors, they are able to measure the population density via a local chemical communication mechanism called Quorum sensing. Last but not least, the rod shape introduces torques when bacteria collide either with each other or for example with a wall, thus the shape of particles can generally be an essential ingredient. In the case of Bacteria, the com-

bination between self-propulsion and the rod-like shape leads to alignment interactions, which is further supported by a hydrodynamic coupling to the medium the bacteria are immersed in [82].

There has been much progress in the development of synthetic active systems. An example are vibrated polar disks [19]. Individual particles are made of symmetric hard-core disks, which stand on a pair of asymmetric feet. Essentially, the experimental setup then consists of this disks vertically confined between two plates, of which the upper one is transparent to allow for visual observation. Energy is injected into the system by a strictly vertical vibration of the entire system. Due to the asymmetric feet, the disks can transform the vibration energy into a directed (persistent) motion, which looks significantly different from the run-and-tumble motion of bacteria (compare Fig. I.8a and Fig. I.7). As shown in Fig. I.8a, the motion consists of rather straight trajectories, which smoothly change the direction after a certain time. At coarse-grained time and length scales, this persistent random motion of a single particle converges to a normal passive random walk (as shown in Fig. I.8b for the same experimental setup, but with nonpolar disks standing on symmetric feet) with a mean square displacement $\propto t$. However, at small time scales, the single particle performs a ballistic motion with the mean square displacement $\propto t^2$. This is due to memory effects of the velocity, which are absent in the passive case. This type of memory effects can be achieved in various ways. Other examples of synthetic active particle systems are diffusiophoresis driven [18], or light activated [17] Janus particles, or colloidal surfers [75].

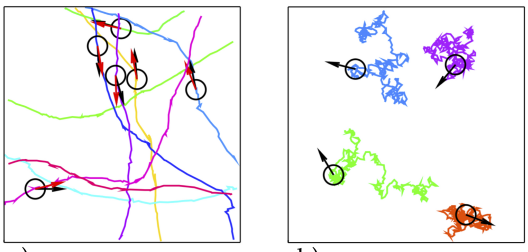


Figure I.8: **Active vs. passive Brownian motion**. a) shows the typical particle trajectories of the vibrated disks with asymmetric feet. The black arrows indicate the direction of motion and the red arrows the polarity of the disks. In contrast, b) shows trajectories of disks with symmetric feet (nonpolar). Source: Fig. 2 in J. Deseigne *et al.*, *PRL* **105**, 098001 (2010) → [19].

I.4.1 Self-propelled particles with equilibrium interactions

Facing the large variety of active systems, the important subclass of self-propelled, persistently moving particles, which otherwise interact only via standard equilibrium forces (attraction, repulsion, alignment, *etc.*) has emerged. Approaching the goal of a common theoretical framework for this class [80], the dilute limit, where inter-particle interactions can essentially be neglected, has drawn attention. Dilute active suspensions already show a nontrivial collective behavior, which, for example, manifests in the density profiles of sedimentation processes [83–85] and in their interplay with ratchets illustrating the loss of time-reversal symmetry [83, 86–89].

The next stage of complexity is reached by considering **self-propelled, persistently moving spherical particles with only isotropic interactions and explicitly without any kind of alignment interactions**. One may ask the "simple" question of how the equilibrium phase diagram changes under the influence of a persistent motion of individual particles. Are all the equilibrium phases preserved under finite persistence? Do new phases appear?

Does the precise choice of how self-propulsion is introduced in the model changes the overall picture of the phase diagram? Below, three possibilities for self-propelled dynamics are given.

a) Models

Active Brownian particles [90, 91]: This model is inspired by the motion of synthetic active swimmers and consists of (spherical) particles interacting only via excluded-volume interactions. As depicted in Fig. I.8, the trajectory of individual particles is smooth and the direction of motion changes after a characteristic average persistence length is covered. The active Brownian model basis on the over-damped Langevin description in (I.10). Persistence is introduced by an additional force term. It is assumed that each particle i moves with a velocity of constant amplitude v. The direction of the velocity $\boldsymbol{q}_i(t) = (\cos[\theta_i(t)], \sin[\theta_i(t)])$ (θ_i angle to a fixed axis) decorrelates smoothly via rotational diffusion, thus the behavior of N particles interacting via a pairwise inter-particle potential $U(r_{ij})$ (r_{ij} distance between the particles i and j) is described by

$$\begin{aligned} \gamma\dot{\boldsymbol{r}}_i(t) &= v\boldsymbol{q}_i(t) - \nabla_i \sum_{j\neq i} U(r_{ij}(t)) + \boldsymbol{\eta}_i(t)\,, \\ \dot{\theta}_i(t) &= \xi_i(t)\,. \end{aligned} \tag{I.11}$$

Here, the noise terms, $\boldsymbol{\eta}_i(t)$ and $\xi_i(t)$, are Gaussians with zero mean and

$$\begin{aligned} \left\langle \eta_i^{(a)}(t)\eta_j^{(b)}(t')\right\rangle &= 2D_{\mathrm{t}}\,\delta_{ab}\delta_{ij}\delta(t-t')\,, \\ \langle \xi_i(t)\xi_j(t)\rangle &= 2D_{\mathrm{r}}\,\delta_{ij}\delta(t-t')\,, \end{aligned}$$

where spatial components are denoted by the superscripts, D_{t} is the passive Brownian translational diffusivity and D_{r} is the angular diffusivity.

The motion of a single particle is ballistic at small time scales and becomes diffusive at large time scales with the diffusivity $D = \frac{v^2}{2D_{\mathrm{r}}} + D_{\mathrm{t}}$ (in two dimensions).

Active Ornstein-Uhlenbeck process [92]: In contrast to the active Brownian model, particles of the active Ornstein-Uhlenbeck process do not move with a constant velocity. The velocity of each particle evolves as a random walk in a harmonic potential, thus the particle positions follow

$$\begin{aligned} \gamma\dot{\boldsymbol{r}}_i(t) &= v_0\boldsymbol{v}_i(t) - \nabla_i \sum_{j\neq i} U(r_{ij}(t)) + \boldsymbol{\eta}_i(t) \quad \text{with} \\ \dot{\boldsymbol{v}}_i(t) &= -\alpha\boldsymbol{v}_i(t) + \boldsymbol{\xi}_j(t)\,. \end{aligned}$$

The noise term $\boldsymbol{\eta}_i(t)$ is the same as in the active Brownian model and

$$\left\langle \xi_i^{(a)}(t)\right\rangle = 0 \quad \text{and} \quad \left\langle \xi_i^{(a)}(t)\xi_j^{(b)}(t')\right\rangle = 2D_{\mathrm{a}}\,\delta_{ab}\delta_{ij}\delta(t-t')\,.$$

Run-and-tumble model for Bacteria [93]: As described above, the motion of bacteria such

as *Escherichia coli* consists of straight runs interrupted by tumbles during which the direction of motion reorientates (see Fig. I.7). During a run of a single particle, the amplitude of the velocity v can be considered as constant and the tumbles occur at a random rate α [81, 94]. Also the motion of a single run-and-tumble particle is diffusive at large length and time scales with a diffusivity of $D = \frac{v^2}{2\alpha}$ (in two dimensions). It was shown [95] that run-and-tumble particles and active Brownian particles can be described by the general large-scale diffusivity

$$D = \frac{v^2\tau}{d} + D_\mathrm{t} \quad \text{with} \quad \tau^{-1} = \alpha + (d-1)D_\mathrm{r}\,,$$

with d indicating the dimension.

All three mentioned models vary in the choice of how self-propulsion/persistence is introduced (compare Fig. I.8a and Fig. I.7). However, in the run-and-tumble model, the velocity explicitly depends on the local density [93].

b) Motility-induced phase separation

Much progress has been achieved in the dilute limit of self-propelled particles, where the novel phenomenon of motility-induced phase separation (MIPS) appears [93]. Although it can be connected to the process of phase separation, for example within the Van-der-Waals theory, MIPS is a purely non-equilibrium phenomenon and describes the macroscopic phase separation into a dilute gas phase and a denser cluster, particularly also for particles with purely repulsive pair potentials [96–99]. Within the van-der-Waals theory, attractive particle interactions are required to produce a comparable phase separation (although the two-dimensional melting provides another example of first-order transitions with purely repulsive interactions).

The phenomenon of MIPS has been reported in various numerical models, as for example in one-dimensional[12] and two-dimensional run-and-tumble models of bacteria [96], but also in simulations of active Brownian particles. In active Brownian particle simulations, MIPS has been reported in two dimensions for a variety of hard-sphere potentials [98–102], for soft spheres [97, 103], and in three dimensions [101]. MIPS was equally observed in the the active Ornstein-Uhlenbeck process [92, 104].

A kinetic approach to MIPS

A kinetic mechanism to capture MIPS was presented for the active Brownian model in [98]. The phase-separated state is described by the functional dependence of the fraction of particles in the dense phase (cluster) f_c on the Péclet number Pe and the packing fraction ϕ. The Péclet number is a measure for the ratio of advective transport to diffusive transport, and as such often used [51, 66, 80, 101, 102, 105, 106] to quantify activity. The model builds on the assumption that the steady-state macroscopic cluster is close-packed so that particles inside the cluster do not move but only change their orientation θ_i diffusively. The cluster is then held together by the surface particles with an orientation $\boldsymbol{q}$ (see (I.11)) that satisfies $\boldsymbol{n}\cdot\boldsymbol{q} < 0$, where $\boldsymbol{n}$ is normal to the cluster surface. The surrounding gas is supposed homogeneous and isotropic.

[12] In one dimension, MIPS occurs as alternating sequences of high- and low-density domains.

It is assumed that a collision event between a gas particle and the cluster leads to an immediate absorption of the gas particle into the cluster. Then the kinetic absorption rate of gas particles with orientation θ can be written as

$$k_{\text{in}}(\theta) = \frac{1}{2\pi}\rho_{\text{g}} v \cos(\theta)\,,$$

where v is the constant velocity in (I.11) and ρ_{g} is the gas number density. If the cluster is large enough to assume the interface as flat, the total incoming flux per unit length is given by

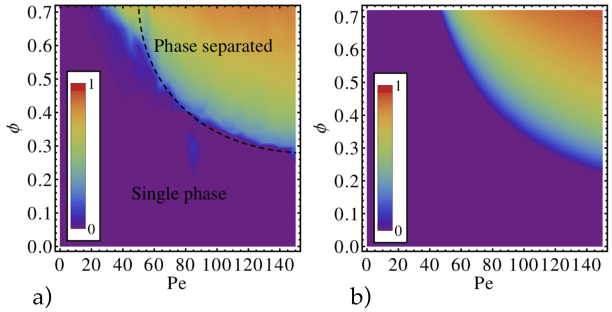


Figure I.9: **MIPS in active Brownian particles**. a) simulation results of cluster fraction $f_{\text{c}}(Pe, \phi)$. Dashed line is the approximate binodal. b) predicted result from (I.12). Source: Fig. 3 in G. S. Redner *et al.*, *Phys. Rev. Lett.* **110**, 055701 (2013) → [98].

$$k_{\text{in}} = \int_{-\pi/2}^{\pi/2} d\theta\, k_{\text{in}}(\theta) = \frac{\rho_{\text{g}} v}{\pi}\,.$$

On the other hand, it is assumed that a surface particle escapes the cluster as soon as its orientation satisfies $\boldsymbol{n}\cdot\boldsymbol{q} > 0$. The escape rate results from the solution of the diffusion equation in angular space $\partial_t P(\theta,t) = D_{\text{r}}\partial_\theta^2 P(\theta,t)$ with absorbing boundaries at $P(\pm\frac{\pi}{2},t) = 0$ and an initial condition $P(\theta,0) = \frac{1}{2}\cos(\theta)$ taking care of the distribution of incoming particles.

However, an escaping particle leaves a hole in the chain of surface particles, thus close-by particles from the cluster interior can escape if their orientation points outwards at the time of the escape event. If κ is the average total number of particles leaving the cluster during one escape event, the total outgoing rate can then be written as

$$k_{\text{out}} = \frac{\kappa D_{\text{r}}}{\sigma}\,,$$

with σ being a length scale set by the interaction potential. The steady state must satisfy $k_{\text{in}} = k_{\text{out}}$, which results in

$$\rho_{\text{g}} = \frac{\pi\kappa D_{\text{r}}}{\sigma v}\,,$$

and thus finally in

$$f_{\text{c}}(\phi, \text{Pe}) = \frac{4\phi\text{Pe} - 3\pi^2\kappa}{4\phi\text{Pe} - 6\sqrt{3}\pi\kappa\phi}\,. \tag{I.12}$$

With $f_{\text{c}} = 0$, this equation leads to a condition for the onset of MIPS

$$\phi\sigma v \sim D_{\text{r}}\,.$$

The comparison with numerical data [98] is shown in Fig. I.9 revealing a good agreement.

This picture assumes that the cluster has always the same close-packed density and that the effect of activity is to let this cluster grow until it contains all particles of the system. However, the real behavior is more complex [98]. Fig. I.10a shows the distribution of local densities under the influence of self-propulsion for a fixed global packing fraction. The system shows a homogeneous, unimodal density distribution at small Pe. When overcoming a certain value of Pe, the density distribution shows a clear double peak, indicating the

MIPS region. The separation between the peaks grows with increasing Pe, and the cluster becomes denser, whereas the gas becomes more dilute with increasing activity. Fig. I.10b demonstrates clearly that the positions of the double peaks do not depend on the global packing fraction of the system, but solely on the activity quantified by Pe.

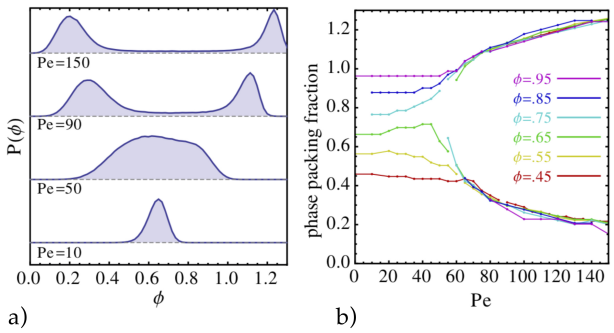


Figure I.10: **Local densities in MIPS**. a) Distribution of the local density at $\phi = 0.65$ for different Pe. It shows the transition from a unimodal distribution to a bimodal distribution. b) Phase densities as function of Pe for various global packing fractions ϕ. The system consists of a single phase at small Pe, and it phase-separates at high Pe. Source: Fig. 2 in G. S. Redner *et al.*, *Phys. Rev. Lett.* **110**, 055701 (2013) → [98].

Clearly, this kinetic description relies on certain strong assumptions, as for example that the cluster is at closed-packed density such that bulk particles are immobile. In reality, the particles inside the cluster are not immobile and even there are debates on the exact nature of the cluster phase, which is certainly not commensurate with a close-packing arrangement. Even though this kinetic approach provides a qualitative picture of the origin of MIPS, it does not give a quantitative description (see Fig. I.10).

Mapping to equilibrium by coarse-graining

This following discussion is largely motivated by [80]. Another approach to theoretically explain MIPS is based on the observation that active particles generically accumulate in regions where they move more slowly (first observed in run-and-tumble bacteria [94]). As mentioned in paragraph a) of subsection I.4.1, in the case of run-and-tumble particles, the velocity is a priori density-dependent. For active Brownian particles, on the other hand, the collisions between particles result in a slowdown at high densities, which is confirmed by measurements of an emergent v, defined as the average of the true particle velocity projected along the propulsion direction [97, 98, 100, 101].



Figure I.11: **Feedback loop leading to MIPS**.

The steady-state solution of the master equation for self-propelled particles with a spatially varying speed $v(\boldsymbol{r})$

$$\dot{P}(\boldsymbol{r},\boldsymbol{u}) = -\nabla\cdot[v(\boldsymbol{r})\boldsymbol{u}P(\boldsymbol{r},\boldsymbol{u})] + \Theta[P(\boldsymbol{r},\boldsymbol{u})]\,,$$

where $\boldsymbol{u}$ is the particle orientation and $\Theta[P]$ is responsible for changes of the orientation, is

$$P_s(\boldsymbol{r},\boldsymbol{u}) \propto \frac{1}{v(\boldsymbol{r})}$$

for an isotropic process [80]. In combination with a propulsion speed depending on the local density, this can lead to a positive feedback loop (see Fig. I.11) leading finally to MIPS.

The condition of this feedback loop can be understood by a linear instability analysis [80]. If $\rho_0 \equiv \frac{c}{v(\rho_0)}$ is an initially homogeneous density, a small perturbation $\delta\rho(\boldsymbol{r})$ leads to a spatially varying speed $v[\rho_0 + \delta\rho(\boldsymbol{r})] = v(\rho_0) + v'(\rho_0)\delta\rho(\boldsymbol{r})$, where $\delta\rho(\boldsymbol{r})$ and $\delta v(\boldsymbol{r})$ are in anti-phase if the velocity decreases with increasing density. The new steady-state density for this velocity is $\rho_0 + \delta\rho'$, with

$$\rho_0 + \delta\rho' = \frac{c}{v(\rho_0) + v'(\rho_0)\delta\rho(\boldsymbol{r})} \simeq \frac{c}{v(\rho_0)}\left(1 - \frac{v'(\rho_0)}{v(\rho_0)}\delta\rho(\boldsymbol{r})\right) = \rho_0 - \rho_0\frac{v'(\rho_0)}{v(\rho_0)}\delta\rho(\boldsymbol{r})\,.$$

A linear instability occurs if $\delta\rho' > \delta\rho$, which leads to the condition

$$\frac{v'(\rho_0)}{v(\rho_0)} < -\frac{1}{\rho_0}\,. \tag{I.13}$$

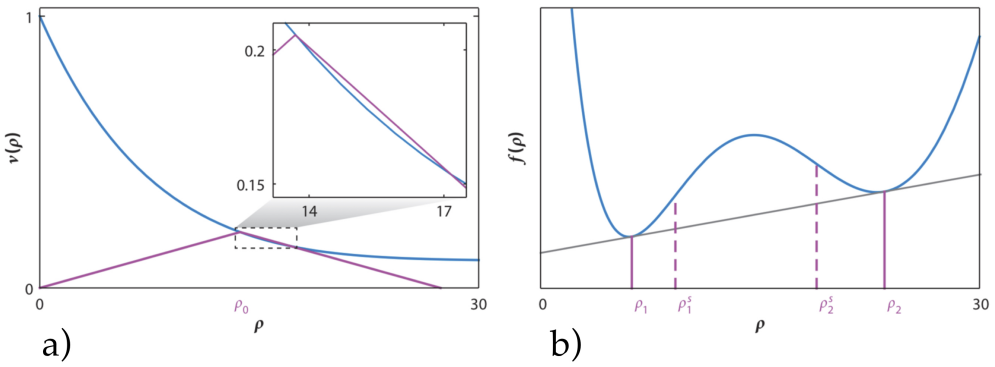


Figure I.12: **Effective free-energy construction for active particles with only local motility interaction via a mapping onto a passive simple fluid of interacting Brownian particles**. a) shows a functional dependence of $v(\rho)$, decreasing rapidly enough at ρ_0 to satisfy (I.13), which can be checked by the depicted geometric construction (see [80] for details). b) the corresponding free energy density $f(\rho)$ has a region of negative curvature (spinodal), in which two phases at the binodal densities ρ_1 and ρ_2 coexist. Source: Fig. 3 in M. E. Cates and J. Tailleur, *Annu. Rev. Conden. Matter Phys.* **6**, 219-44 (2015) → [80].

It is possible to extend this linear instability analysis by mapping the coarse-grained dynamics of active simple fluids onto the equilibrium dynamics of passive simple fluids with attractive interactions, which is only possible if the coarse-grained active dynamics do not violate the detailed-balance condition. In a local mean-field approximation of the many-body system, where the swim-speed is considered to depend only on the density, but not its gradients [80], it might be possible to map the coarse-grained density of active particles onto the coarse-grained density of isothermal passive Brownian particles in the presence of an effective potential, which leads to some additional drift velocity in the system. Within this mapping, a free-energy functional $F[\rho]$ might be defined (where $[\rho]$ is an arbitrary functional dependence on the coarse-grained density field $\rho(\boldsymbol{r})$), which then specifies the most probable configuration $\rho(\boldsymbol{r})$, but also all moments of the fluctuating density. In the local approximation, where $v(\boldsymbol{r}) = v[\rho(\boldsymbol{r})]$, thus gradients of ρ are neglected, the free-energy density $f(\rho)$ offers then a tool to explicitly search for (*e.g.*) a two-phase coexistence in a constant (N, V, T) ensemble, which appears if $f(\rho)$ is concave (if $f''(\rho) < 0$). It so

turns out that the condition for a concave free energy is the same as obtained in the linear instability analysis given in (I.13). Fig. I.12a shows a case, where (I.13) is fulfilled and the corresponding concave free energy density in Fig. I.12b, which is minimized by the common tangent construction. The common tangent construction recovers the two coexisting densities ρ_1 and ρ_2, with equal chemical potentials $\mu = \frac{df}{d\rho}$ (equal slope for the tangents at ρ_1 and ρ_2) and equal pressure $p = \mu\rho - f$ (equal intercept of the tangent), thus the same tangent connects both coexisting densities. The two points ρ_1^s and ρ_2^s mark the boundaries of the spinodal region, where $f''(\rho) < 0$. In this region, a uniform system is unstable under small fluctuations, thus infinitesimal fluctuations lead to phase separation. Due to the lack of a nucleation barrier, small clusters start to form throughout the whole system, they grow and merge until two coexisting domains are left. Outside the spinodal, the initial formation of microscopic clusters is hindered by a large free-energy barrier, thus the cluster formation happens rarely and the final phase-separated steady state might origin from a single nucleation event. Starting from this nucleation event, the microscopic cluster grows leading to the coexisting steady state determined by the common tangent construction.

In fact, the condition (I.13) holds for a system, where the passive Brownian diffusion was set to zero ($D_\mathrm{t} = 0$), thus diffusion is a process entirely determined by the self-propulsion. When additional thermal diffusion is not neglected, the concavity condition changes to [80]

$$f''(\rho) < 0 \quad \Leftrightarrow \quad v^2\tau \underbrace{(1 + \rho\frac{v'}{v})}_{q} < -dD_\mathrm{t}\,, \tag{I.14}$$

with d the dimension and τ the orientational relaxation time, determining how fast particles change their direction of motion. The case of additional thermal diffusion shows firstly that if D_t is finite and at the same time $v \to 0$, the concavity condition is never fulfilled. On the other hand it also says that for any given $v(\rho)$, there is a minimal ratio $\frac{v^2\tau}{dD_\mathrm{t}}$ of active to thermal diffusion, for which $\frac{v^2\tau}{dD_\mathrm{t}}q < -1$ cannot be satisfied anymore. With other words, a too strong thermal diffusion can prevent motility-induced phase separation.

This description of MIPS relies on a coarse-grained hydrodynamics description that is based on a non-rigorous ground. It relies on some equilibrium-like assumptions, which has its range of validity. It is thus not surprising that predictions from this theory do not characterize the full quantitative phase diagram. Nevertheless, this coarse-grained hydrodynamic picture captures the qualitative picture of MIPS establishing it on an intuitive reasoning. However, this is not a complete theory, which can, for example, be seen by comparing the theoretical predictions for active Brownian particles with the numerical data. Simulations have shown that MIPS disappears below a certain Péclet number. Following (I.14), this disappearance could be explained by an overpowering thermal diffusion, however, in contrast to experiments, it is possible to set the thermal (passive) diffusion to zero in simulations [97, 103]. These simulations show that a dominating thermal diffusion cannot be the only reason for the loss of MIPS as their result is similar to those which include an additional thermal (passive) diffusion [98, 100, 101].

Improvement was achieved [107] by going beyond the local approximation. This approximation does not include spatial features like the interfacial tension. This means, if a free-energy-landscape-evolution description is possible, as used for phase separation in passive systems, the local approximation above does not account for any gradient term in

the free-energy functional. Clearly, such terms would be essential to fully understand the dynamics of phase separation. This is precisely done in [107] for active Brownian particles, which (using a type of simplified kinetic theory) argues for an additional square gradient term to the free-energy functional. Such a free-energy functional led to an effective dynamics governed by the Cahn-Hilliard-Cook equation, which allows for a mapping between MIPS and phase separation in passive systems. Surely, this approach has the great benefit of simplicity, which gives a more accurate description of the phase boundaries and the nature of the phase transition and compares very well with numerical simulation results.

However, there are additional issues. For example, this coarse-grained description considers the free energy as a function of the local density, which can only describe MIPS as a coexistence between a liquid and a gas. These two are essentially the same phase. Clearly, this description does not include other phases with larger degrees of order, as for example the solid or the hexatic phase in two dimensions (defined later). In contrast, the statements about the precise nature of the coexisting phases observed in numerical simulations vary from descriptions as a coexistence between a "*solid-like and gas state*" [97], or between a "*dense large cluster and a dilute gas phase*" [18] , or a coexistence between a "*dense and dilute phase*", where the dense phase "*exhibits structural properties consistent with a two-dimensional colloidal crystal near the crystal-hexatic transition point*" [98] and it was lately described as coexistence, where the dense phase "*can be either disordered (liquid) or ordered (hexatic or solid)*" [108]. The above sketched theory is not able to distinguish between different degrees of order in the particle arrangements in denser regions and thus does not allow for any theoretical predictions on the degree of order.

I.5 Thermodynamic phases in passive two-dimensional particle systems

In this section I.5, the main aspects of the theory of melting transition in two-dimensional systems (Berezinskii–Kosterlitz–Thouless-Halperin-Nelson-Young (BKTHNY) scenario) are reviewed, including most recent updates on the theory. Materials in this section and in the following sections I.6, I.7, and I.8 are largely influenced by the thesis of Etienne P. Bernard [11], and also by lecture notes of Leticia F. Cugliandolo *et al.* [109, 110], a recent review by Valentin N. Ryzhov *et al.* [5] and another recent review by J. M. Kosterlitz [6].

Arguably the most prominent equilibrium collective behavior in two dimensions is the melting of solids in interacting particle systems. Because of an increasing dominance/impact of fluctuations with the loss of dimensions, a crystalline order is not possible in two dimensions (and below), as shown by Mermin and Wagner [111] and by Mermin [112]. Instead, at sufficiently low temperature and high enough pressure, a solid can be formed, where positional correlations extend over infinite distances but without a global translational order in the system. In similarity to the behavior of correlations at a critical point, positional correlations decay as a power-law in the solid and are thus scale-free.

What is even more fascinating is that this two-dimensional solid melts into a disordered liquid following a melting scenario which is distinct from the melting in higher dimensions. For example, three-dimensional water at ambient pressure freezes to form ice as the temperature is reduced below zero degree Celsius. This transition from a disordered liquid into

an ordered ice (ignoring the numerous possible manifestations of ice), where molecules are more correlated, is a first-order phase transition where the density jumps in the (N, P, T) ensemble. When the same water molecules are confined in a plane, the transition from liquid to solid may not be of first order anymore. Not only the type of the phase transition changes when lowering the dimension, but the transition may happen in multiple steps with new intermediate thermodynamic phases. In the system of interacting planar discs, it is now clearly established that the melting transition is very different from the melting scenario in three dimensions. On one hand there is the theory of BKTHNY building on the universality of the Berezinskii-Kosterlitz-Thouless transition which is a characteristic of a large class of two-dimensional phase transitions, and at the same time there is now clear numerical evidence [11, 12] that this theory is not fully applicable as a first-order transition can preempt a Berezinskii-Kosterlitz-Thouless transition under certain conditions.

The goal of this chapter is to summarize the phenomenon of melting transitions in two-dimensional particle systems in equilibrium which is the passive limit of the system of focus of this thesis. The universality of the Berezinskii-Kosterlitz-Thouless transition, which is crucial to understand the melting transition, is presented through the example of the two-dimensional XY model. This idea is then extended to two-dimensional particle systems to show how a solid melts into a liquid through an intermediate hexatic phase. This is the famous BKTHNY theory of defect-mediated melting. Predictions from this theory and its comparison with numerical results are discussed towards the end.

Remark: In the literature, it is often wrongly mentioned that the Mermin-Wagner theorem forbids spontaneously broken continuous symmetries in two-dimensional systems at finite temperature and sufficiently short-ranged interactions. However, this is not true in general and it was not claimed by these authors either. Their result is for a number of particular cases, but not necessarily in complete generality. The spontaneous breaking of orientational order in a two-dimensional solid is a counterexample.

I.5.1 Two-dimensional solid

Two-dimensional particle systems can form a solid at sufficiently low temperature or high enough density, yet with weaker ordering than three-dimensional solids. It was proven long ago that the two-dimensional crystalline state is thermodynamically unstable [111, 112]. Following the works of Alder and Wainwright [113], it was understood that a solid state nevertheless exists. Its existence is firmly established through numerical simulations [11–13], although the existence of the solid state has not yet been proven mathematically.

A characteristic feature of a solid is the non-zero shear modulus which offers a clear distinction from a liquid[13]. In many systems, particularly in three dimensions, a solid has a crystalline order where particles are located at the nodes of a lattice. The thermal fluctuations of the particles around these lattice points are small such that "positional order" is long-ranged. A quantitative measure of this positional order is the structure factor defined

[13] A shear modulus quantifies the rigidity of a material under a tangential force. In a two-dimensional material of $L \times L$ aspect ratio, if Δx is the displacement of a boundary under F amount of force applied parallel to the boundary, the shear modulus is $\frac{F}{\Delta x}$. A liquid has vanishing shear modulus.

as

$$S(\boldsymbol{q}) = \left\langle \frac{1}{N} \left| \int d^{\mathrm{d}}\boldsymbol{r}\, e^{\mathbb{i}\,\boldsymbol{q}\cdot\mathbf{r}} \rho(\boldsymbol{r}) \right|^2 \right\rangle = \frac{1}{N} \left\langle \sum_i \sum_j e^{\mathbb{i}\,\boldsymbol{q}\cdot(\boldsymbol{r}_i - \boldsymbol{r}_j)} \right\rangle$$

where $\mathbb{i}$ is the imaginary unit, $\boldsymbol{q}$ is the momentum vector, and $\rho(\boldsymbol{r}) = \sum_{i=1}^{N} \delta(\boldsymbol{r} - \boldsymbol{r}_i)$ is the density with $\boldsymbol{r}_i$ being the position of the i^{th} particle in the system of in total N particles in d dimensions. For a crystalline solid $S(\boldsymbol{q})$ shows peaks around the reciprocal lattice points $\boldsymbol{q} = \boldsymbol{Q}$. These are known as Bragg peaks and can be observed in the diffraction patterns of scattering experiments [4].

In high dimensions, like three dimensions, crystalline order is thermodynamically stable, particularly, because of high connectivity structures which make the translational long-range order robust against thermal fluctuations. However, in one dimension, this connectivity is less and thermal fluctuations destroy long-range order which was proven rigorously [9, 114]. This is argued heuristically by Landau and Lifshitz [115] using competition between energy and entropy. Two-dimensional systems represent the marginal case where the energy and the entropy could be comparable which thus makes the question of translational long-range order non-trivial.

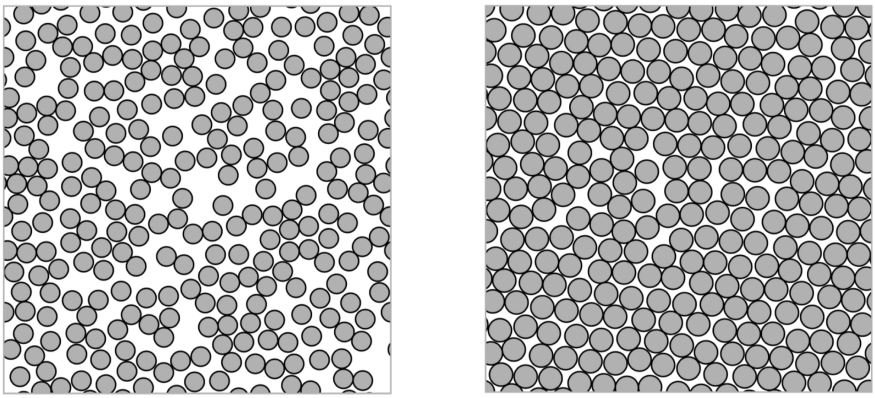


Figure I.13: **Appearance of a two-dimensional liquid and solid.** Sample configurations of two-dimensional interacting hard discs of radius σ in a square periodic box of volume V. a) A disordered liquid state at packing fraction $\mu = \frac{N\pi\sigma^2}{V} = 0.5$. b) A translational quasi-long-ranged ordered solid state for $\mu = 0.72$, where particles are almost arranged in a hexagonal order. In a large system, this positional order breaks up, but the orientational order remains long-ranged. Source: Fig. 1.3 in E. Bernard, Algorithms and applications of the Monte Carlo method: Two-dimensional melting and perfect sampling, (2011). → [11].

This marginal behavior can be seen in two-dimensional interacting particle systems. Peierls, in 1934, argued [21, 116] that the positional correlations decay logarithmically in a two-dimensional harmonic solid (connected harmonic strings) and therefore long-range positional order is not possible. However, decades later Alder and Wainwright [113] found numerical evidence that the two-dimensional hard-disk system undergoes a phase transition. Around the same time, Mermin and Wagner [111, 112] rigorously proved that particles interacting with any finite ranged continuous potential cannot show long-range positional order in two dimensions and thus extended the work of Peierls [21, 116] and Landau [117].

Nevertheless, the observation of Alder and Wainwright is correct. The two-dimensional hard discs can freeze to a solid (see Fig. I.13) with quasi-long-range positional order and long-range orientational order, as the Mermin-Wagner theorem does not exclude such a solid. In fact, Mermin noted [112] that the two-dimensional harmonic solid can show a long-range orientational order. The existence of two-dimensional solids is now convincingly established, both in computer simulations [11–13, 113] and in experiments [118, 119].

I.5.2 Harmonic solid in two dimensions

The fact that a non-crystalline solid with quasi-long-range positional order and long-range orientational order can exist in two dimensions can be seen in a simple model system: the harmonic solid. In this system, particles are connected by harmonic springs and arranged such that at zero deformation the particle positions form a lattice, as shown in Fig. I.14. The positions of the lattice sites are denoted by a planar lattice vector $\boldsymbol{R}$. At finite temperature, the particle positions $\boldsymbol{r}_{\boldsymbol{R}}(t)$, each associated to an individual $\boldsymbol{R}$, fluctuate with time and they can be expressed as

$$\boldsymbol{r}_{\boldsymbol{R}}(t) = \boldsymbol{R} + \boldsymbol{u}_{\boldsymbol{R}}(t)\,, \tag{I.15}$$

where $\boldsymbol{u}_{\boldsymbol{R}}(t)$ denotes the fluctuations of a particle around the lattice site.

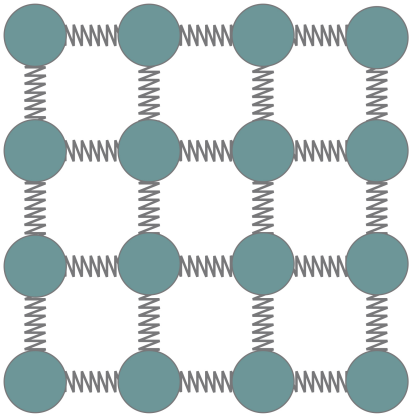


Figure I.14: **The harmonic solid.** A schematic example of the two-dimensional harmonic solid model where particles are connected by harmonic springs with the connectivity of a lattice.

The displacement field $\boldsymbol{u}_{\boldsymbol{R}}(t)$ can be written in terms of plane waves (phonons)

$$\boldsymbol{u}_{\boldsymbol{R}}(t) = \int d^2q\, e^{\mathrm{i}\boldsymbol{q}\cdot\boldsymbol{R}} \widehat{\boldsymbol{u}}_{\boldsymbol{q}}(t)\,.$$

For the harmonic solid, the interaction potential is quadratic in the displacement field $\boldsymbol{u}_{\boldsymbol{R}}(t)$ and thus the effective Hamiltonian is quadratic. Therefore, the phonon modes are independent [4], and one can write

$$\widehat{\boldsymbol{u}}_{\boldsymbol{q}}(t) = \boldsymbol{a}_{\boldsymbol{q}} e^{\mathrm{i}\omega_{\boldsymbol{q}} t} + \boldsymbol{b}_{\boldsymbol{q}} e^{-\mathrm{i}\omega_{\boldsymbol{q}} t}\,,$$

where $\boldsymbol{a}_{\boldsymbol{q}}$ and $\boldsymbol{b}_{\boldsymbol{q}}$ are the amplitudes associated to the wave vector $\omega_{\boldsymbol{q}}$. As the phonon modes are uncoupled, the harmonic solid can be seen as a gas of non-interacting phonons, for which thermodynamics is simple. For example, due to the equipartition theorem the thermal average of the q-phonon mode is

$$\left\langle |\widehat{\boldsymbol{u}}_{\boldsymbol{q}}(t)|^2 \right\rangle \simeq \frac{k_{\mathrm{B}}T}{\omega_{\boldsymbol{q}}^2}\,.$$

Using this, the correlation of the displacement vector is

$$\langle \Delta \boldsymbol{u}^2 \rangle := \langle [\boldsymbol{u}_{\boldsymbol{R}} - \boldsymbol{u}_{\boldsymbol{0}}]^2 \rangle \sim k_{\mathrm{B}}T \int d^2q\, \frac{1-\cos(\boldsymbol{q}\cdot\boldsymbol{R})}{\omega_{\boldsymbol{q}}^2}\,. \tag{I.16}$$

For large $\boldsymbol{R}$, the integral is dominated by small $\boldsymbol{q}$ modes for which $\omega_{\boldsymbol{q}} \propto q$ (because of constant sound velocity) and this leads to

$$\langle \Delta \boldsymbol{u}^2 \rangle \sim k_{\mathrm{B}} T \int_{1/R} dq \, \frac{q}{q^2} \sim k_{\mathrm{B}} T \log R \,, \tag{I.17}$$

with R being the amplitude of the vector $\boldsymbol{R}$. Therefore, fluctuations of the particle positions around their mean are correlated even at large distances which rules out the possibility of thermally stable crystalline order that is defined through finite fluctuations[14]. A more general proof for the absence of a crystalline solid in two dimensions, which does not rely on the harmonic approximation, was given by Mermin [112].

At the same time, all positions are on average centered around lattice points which means a non-zero shear modulus and this is thus consistent with an interpretation as a solid. A diffraction pattern shows Bragg peaks arranged in a lattice structure, although they are not δ-functions as in crystals. It can be shown [120–122] that for the first Bragg peak $\boldsymbol{Q}$, the correlation

$$C_{\boldsymbol{Q}}(r) = \left\langle e^{i \boldsymbol{Q} \cdot \Delta \boldsymbol{r}} \right\rangle_{|\Delta \boldsymbol{r}| = r} \sim r^{-\nu_{\boldsymbol{Q}}} \,, \qquad \text{with } \nu_{\boldsymbol{Q}} \propto k_{\mathrm{B}} T \,. \tag{I.18}$$

This indicates a power-law decay of the positional correlation for the harmonic solid.

Following a very similar analysis, it can be argued that a harmonic solid can have long-range orientational order. A definition of orientational order was given by Mermin [112] in terms of the vector field

$$\boldsymbol{\phi}_{\boldsymbol{R}} = \boldsymbol{r}_{\boldsymbol{R}+\boldsymbol{a}} - \boldsymbol{r}_{\boldsymbol{R}} \,,$$

where $\boldsymbol{r}_{\boldsymbol{R}}$ denotes the position of the particle associated to the lattice point $\boldsymbol{R}$ and $\boldsymbol{a}$ is the lattice unit vector. This field corresponds to the relative position of two neighboring particles and can define a local orientation in the system. Using (I.15) gives the correlation of this orientation field as

$$\langle \boldsymbol{\phi}_{\boldsymbol{R}} \cdot \boldsymbol{\phi}_{\boldsymbol{0}} \rangle = a^2 + \langle [\boldsymbol{u}_{\boldsymbol{R}+\boldsymbol{a}} - \boldsymbol{u}_{\boldsymbol{R}}] \cdot [\boldsymbol{u}_{\boldsymbol{a}} - \boldsymbol{u}_{\boldsymbol{0}}] \rangle + \cdots \,,$$

where the linear order term in $\boldsymbol{a}$ vanish as $\langle \boldsymbol{u} \rangle$ is uniform. For large R the correlation of the displacement field $\boldsymbol{u}$ vanishes, leading to

$$\langle \boldsymbol{\phi}_{\boldsymbol{R}} \cdot \boldsymbol{\phi}_{\boldsymbol{0}} \rangle \to a^2 \,, \qquad \text{for } R \to \infty \,.$$

The correlation is non-zero even when the distance is infinite, and therefore the orientations are correlated over the entire system which means that the two-dimensional harmonic solid is characterized by a long-ranged orientational correlation. For references to earlier studies of orientational order in two-dimensional systems see [5, 6].

The analysis of the harmonic solid shows that it is characterized by quasi-long-range positional order and long-range orientational order in two dimensions. In a two-dimensional

[14] A similar calculation in three dimensions shows that $\langle \Delta \boldsymbol{u}^2 \rangle$ is constant and thus **includes** the possibility of crystalline order. It is noteworthy that the logarithmic divergence is very slow. For instance, according to the estimates in [11], a fluctuation displacement of the order of 10 interatomic distances emerges in a system in which the number of particles exceeds the number of atoms in the observable Universe. Therefore, in reality, two-dimensional solids can be treated as two-dimensional crystals with a rather high degree of accuracy.

particle system, at low enough temperature, or high density, relative deformations of particle positions are small and the harmonic solid description is reasonable (although without rigorous proof). However, as the temperature becomes large, the fluctuations in the particle positions increases and the system can no longer be described by a harmonic solid. In fact, the system melts into a disordered liquid via a non-trivial melting transition in two dimensions.

Due to the high degree of ordering of a two-dimensional solid, topological defects like dislocations and disclinations are well-defined, despite the absence of the long-range translational order. This is particularly important because in the current theories (explained later) the two-dimensional melting is induced by these topological defects.

Indications of a solid in two dimensions first came from the work of Alder and Wainwright, who performed molecular dynamics simulations of hard discs in a (N, V, T) ensemble [113]. For this very small systems, it was found that at a certain rescaled density ($\phi = 0.7$ with the definition (II.11)) the pressure curve (equation of state) follows a Mayer-Woods loop, which indicates a first-order transition. This hinted at the existence of a transition from liquid to solid. It is now clearly established that a two-dimensional solid with quasi-long-range positional order and long-range orientational order exists in systems of interacting discs even with only hard-core interactions. The nature of the transition is partly governed by the idea of the Berezinskii-Kosterlitz-Thouless transition which is mediated by topological defects. This is discussed in the next section I.6.

Remark: It may be surprising to think of a hard-disk system which does not have any energy to be described as a harmonic solid, even at high density. However, this can be understood by thinking of an effective interaction due to caging effects. If two discs get separated, thus the empty space in between increases, the discs get hit harder from other discs, thus pushing them closer together again. Therefore, the two discs see an effective elastic interaction created by the rest of the system. Alternatively, when the two discs get closer, the available phase space for other discs increases leading to higher entropy. Therefore, even the hard-disk system can show elastic behavior, with the origin of elasticity being only entropic. This so-called depletion interaction and its possible relevance to biological systems, macromolecules, and proteins was first described by Asakura and Oosawa [123].

I.6 The Berezinskii-Kosterlitz-Thouless transition in the two-dimensional XY model

Here, the concept of the Berezinskii-Kosterlitz-Thouless transition, which is pivotal in understanding the two-dimensional equilibrium melting in interacting particle systems, is discussed using the two-dimensional XY model, which was shown [124] to exhibit a Berezinskii-Kosterlitz-Thouless transition. It is shown later how the basic ideas of a defect-mediated transition in the XY model can be translated to understand melting in the system of interacting particles.

The two-dimensional XY model consists of a system of interacting rotors pinned at the sites of a two-dimensional lattice. The state of a rotor at the i^{th} site is defined by an angular variable θ_i, such that a unit vector $\boldsymbol{S}(\boldsymbol{r}_i) \equiv (\cos\theta_i, \sin\theta_i)$ can be assigned to the site i. In the

simplest version of the model, only the nearest-neighbor rotors interact with an interaction strength J such that the Hamiltonian is given by

$$H = -J \sum_{\langle i,j \rangle} \boldsymbol{S}(\boldsymbol{r}_i) \cdot \boldsymbol{S}(\boldsymbol{r}_j) \,. \tag{I.19}$$

For the XY model, the description of the low-temperature phase through the harmonic approximation was proven mathematically [125]. At this low temperature, the correlation of the rotors $\langle \boldsymbol{S}(\boldsymbol{r}) \cdot \boldsymbol{S}((\boldsymbol{0})) \rangle$ decays as a power-law which is consistent with the Mermin-Wagner theorem, as the system lacks long-range order. This means that the correlation length is infinite, similar to that in the critical state of a second-order phase transition. Such a state shows a critical slowing down and required new numerical approaches like the cluster algorithm by Wolff [126].

At high temperature, the power-law correlation is destroyed by thermal fluctuations and the system is thus in a disordered phase with a finite correlation length. These two phases are separated by a phase transition at a non-zero temperature T_{KT}. Kosterlitz and Thouless [127, 128], as well as Berezinskii [129, 130], showed independently that the transition is continuous, with a new universality markedly different from transitions in higher dimensions. This transition is now referred to as the Berezinskii-Kosterlitz-Thouless transition which governs the universality of a large class of two-dimensional phase transitions.

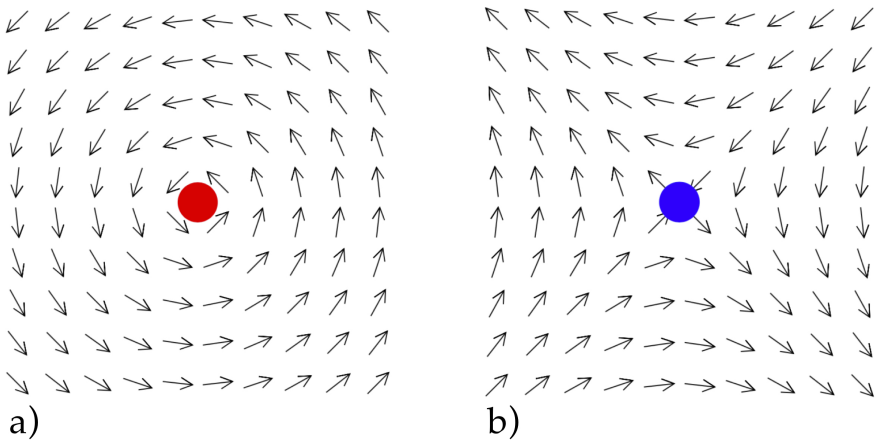


Figure I.15: **Two relevant vortices in the two-dimensional XY model.** The arrows in the sketch indicate the orientation of the rotors. a) A vortex with a positive winding number $q = 1$. b) A vortex with a negative winding number $q = -1$. When two such vortices with opposite winding numbers form pairs, the total winding number vanishes and the pair does not disrupt the orientational order at large distances. Source: Fig. 1.4 in E. Bernard, Algorithms and applications of the Monte Carlo method: Two-dimensional melting and perfect sampling, (2011). → [11].

The transition is mediated by the formation of vortices in the XY model. The qualitative picture is the following. In the two-dimensional XY model, there could be simple vortices as given in Fig. I.15. At low temperatures, these vortices are not thermodynamically favorable and therefore $\langle \boldsymbol{S}(\boldsymbol{r}) \cdot \boldsymbol{S}(\boldsymbol{0}) \rangle$ can extend over the system size having quasi-long-range order in accordance with the Mermin-Wagner theorem. Above the transition temperature, vortices are thermodynamically stable and destroy the quasi-long-range order, thus $\langle \boldsymbol{S}(\boldsymbol{r}) \cdot \boldsymbol{S}(\boldsymbol{0}) \rangle$

decays exponentially beyond a finite correlation length. In more general cases of two-dimensional systems, a Berezinskii-Kosterlitz-Thouless transition is ruled by topological defects. For example, in two-dimensional particle systems, dislocations and disclinations are topological defects. This is the basis of the Berezinskii-Kosterlitz-Thouless-Halperin-Nelson-Young (BKTHNY) theory for the melting in two-dimensional particle systems.

The large-scale properties in the two-dimensional XY model can be understood using a coarse-grained orientational field $\theta(\boldsymbol{r})$. At low temperature, similar to the harmonic solid, the system can be described by an effective Gaussian Hamiltonian

$$H_{\text{eff}} = \frac{1}{2} J_{\text{eff}} \int d^2 r \, (\nabla \theta(\boldsymbol{r}))^2 \,, \tag{I.20}$$

defined with a small scale cutoff (a coarse-grain length) and J_{eff} is the renormalized interaction strength (spin stiffness). Similar to ((I.16), (I.17)) the variance is

$$\begin{aligned} \left\langle [\theta(\boldsymbol{r}) - \theta(\boldsymbol{0})]^2 \right\rangle =& \frac{k_{\text{B}} T}{J_{\text{eff}}} \int_{1/r}^{1/a} d^2 q \, \frac{1 - \cos(\boldsymbol{q} \cdot \boldsymbol{r})}{(2\pi q)^2} \\ \sim& \frac{k_{\text{B}} T}{\pi J_{\text{eff}}} \log \frac{a}{r} \,, \end{aligned}$$

where a is the microscopic cutoff scale for the hydrodynamic description (I.20). The correlation of rotors can be expressed in terms of the macroscopic field as [11, 127, 128]

$$\langle \boldsymbol{S}(\boldsymbol{r}) \cdot \boldsymbol{S}(\boldsymbol{0}) \rangle \sim e^{-\frac{1}{2} \left\langle [\theta(\boldsymbol{r}) - \theta(\boldsymbol{0})]^2 \right\rangle}$$

which leads to an algebraic decay in the low-temperature phase (quasi-long-range order)

$$\langle \boldsymbol{S}(\boldsymbol{r}) \cdot \boldsymbol{S}(\boldsymbol{0}) \rangle \sim r^{-\nu_{XY}} \,, \qquad \text{with } \nu_{XY} = \frac{k_{\text{B}} T}{2\pi J_{\text{eff}}} \,. \tag{I.21}$$

The absence of vortices at low temperatures can be argued using the well-known free energy argument of Kosterlitz and Thouless [127, 128]. This starts with an estimate of the energy cost for a single vertex. Using $|\nabla \theta(\boldsymbol{r})| \sim \frac{1}{r}$ for large r around a vortex in a system of size L, the energy of a single vortex can be estimated from (I.20) and is given by

$$\begin{aligned} E_{\text{vortex}} \simeq& \frac{1}{2} J_{\text{eff}} \int_a^L dr \, 2\pi r \, \frac{1}{r^2} + E_0 \\ =& \pi J_{\text{eff}} \log \frac{L}{a} + E_0 \,, \end{aligned}$$

where E_0 is the core energy of the vortex. At a zeroth level approximation, the vortices can be assumed to be independent. Then, the entropy associated to placing of a single vortex anywhere in the system is

$$S_{\text{vortex}} \simeq k_{\text{B}} T \log \frac{L^2}{a^2} .$$

Then, the free energy cost for the presence of a single vortex is

$$F_{\text{vortex}} = E_{\text{vortex}} - S_{\text{vortex}} \simeq (\pi J_{\text{eff}} - 2 k_{\text{B}} T) \log \frac{L}{a} \,.$$

This means, for $T < \frac{\pi J_{\text{eff}}}{2k_{\text{B}}}$, the presence of a vortex increases the free energy, and is therefore thermodynamically unstable. When $T > \frac{\pi J_{\text{eff}}}{2k_{\text{B}}}$, the presence of a vortex decreases the free energy, and is therefore thermodynamically stable. The presence of free vortices disrupt the orientational order and the high temperature phase shows short-ranged correlations. Therefore, at the temperature

$$T_{\text{KT}} = \frac{\pi J_{\text{eff}}}{2k_{\text{B}}} \tag{I.22}$$

there is a phase transition between a quasi-long-range ordered state to a disordered state.

This heuristic analysis does not determine T_{KT} as the effective J_{eff} is not calculated. However, the analysis correctly predicts the exponent ν_{KT} in (I.21) which is

$$\nu_{\text{KT}} = \frac{1}{4} \qquad \text{at} \qquad T = T_{\text{KT}}.$$

Unlike J_{eff}, this value of the exponent is universal for the Berezinskii-Kosterlitz-Thouless transition, as it does not depend on specific microscopic details of the model. The value of the exponent is confirmed, *e.g.*, for the two-dimensional XY model [131], but was also found in superfluid transitions of two-dimensional ^{4}He films [132], and in simulations of interacting two-dimensional particles systems [13] and is playing again a role later in this thesis.

Remark: It should be stressed that this result ideally applies only in the thermodynamic limit. At short distances, there are logarithmic corrections [133].

To be precise, below T_{KT}, the vortices are predicted, but they unbind only above T_{KT}. To see this, the interaction energy between vortices must be included in the effective Hamiltonian (I.20). The effective interaction between two vortices is expressed in terms of their winding number q which is defined by

$$q = \frac{1}{2\pi} \oint_c \nabla\theta(\boldsymbol{r}) \cdot d\boldsymbol{l}\,,$$

where c is any closed path around the vortex. For example, in the vortex in Fig. I.15a, $q = 1$ whereas in Fig. I.15b, $q = -1$. Looking at the flow of the orientation fields, it can be seen that vortices of opposite signs in the winding number decrease the elastic energy if they are close, and therefore attract each other. Similarly, vortices with winding numbers of the same sign repel each other. The effective interaction energy between two vortices of winding number q_i and q_j separated by a distance r_{ij} is given by [127, 128]

$$U_{ij}(r_{ij}) = -\pi J_{\text{eff}}\, q_i q_j \log \frac{r_{ij}}{a} + 2E_0\,.$$

Including this pairwise interactions between vortices, the effective Hamiltonian can be written as

$$H_{\text{eff}} = \frac{1}{2} J_{\text{eff}} \int d^2 r\, (\nabla\theta(\boldsymbol{r}))^2 + \sum_{i,j} U_{ij}(r_{ij})\,.$$

This is similar to the energy of a system of charged particles in two dimensions which is known as the Coulomb gas.

Kosterlitz and Thouless used [127, 128] the renormalization-group method to analyze this effective Hamiltonian. Their main results, which are relevant for this thesis, are given below.

I.6.1 Low-temperature ordered phase

When interactions between vortices are neglected, it was argued (using the free energy estimates) that vortices are thermodynamically unstable. However, in the Hamiltonian, a pair of vortices with opposite winding number decrease the energy. Therefore, such pairs can get created by thermal fluctuations with a finite average intermediate distance between the vortices in a pair. At length scales above this distance, the presence of such paired vortices does not disrupt the orientational field and the system can be described by the effective vortex free Hamiltonian (I.20). The presence of these thermally created vortices only changes the effective interaction strength J_{eff}. Using a renormalization group analysis it was shown that near the Berezinskii-Kosterlitz-Thouless transition the effective interaction shows a cusp and is given by

$$J_{\text{eff}}(T) = J_{\text{eff}}(T_{\text{KT}}) \left[1 + \text{const}\sqrt{T_{\text{KT}} - T}\right] , \qquad \text{for } T \leq T_{\text{KT}} .$$

Then, using (I.21), gives the exponent for the correlation decay

$$\langle \boldsymbol{S}(\boldsymbol{r}) \cdot \boldsymbol{S}(\boldsymbol{0}) \rangle \sim r^{-\nu_{\text{KT}}} , \qquad \text{with} \qquad \nu_{\text{KT}} = \frac{1}{4} \left[1 + \text{const}\sqrt{T_{\text{KT}} - T}\right] . \tag{I.23}$$

This result for the exponent has been confirmed in numerical simulations [131].

I.6.2 High-temperature disordered phase

The transition at T_{KT} happens as the vortices are not paired anymore. The average number of unbound vortices increases from zero at T_{KT} to a finite value at high temperatures. The presence of such free vortices destroys the orientational order, thus the orientational correlation decays exponentially with a finite correlation length which is the typical distance between free vortices

$$\langle \boldsymbol{S}(\boldsymbol{r}) \cdot \boldsymbol{S}(\boldsymbol{0}) \rangle \sim e^{-r/\xi} .$$

A renormalization group analysis [127, 128] gives the correlation length as

$$\xi \sim e^{\frac{\text{const}}{\sqrt{T - T_{\text{KT}}}}} . \tag{I.24}$$

This shows that the correlation decays faster than for any second-order transition [134]. This behavior has been observed in simulations [131, 135] as well as in experiments.

Remark: In the disordered phase, the system is uncorrelated beyond the finite correlation length. Therefore, the effective interaction J_{eff} of the coarse-grained field $\theta(\boldsymbol{r})$ in (I.20) which is defined beyond ξ, must vanish in the high temperature phase. This means that J_{eff} changes discontinuously at T_{KT} from $J_{\text{eff}} = \frac{2k_{\text{B}}T_{\text{TK}}}{\pi}$ to $J_{\text{eff}} = 0$. However, at the transition point, the correlation length is infinite, and therefore it cannot be interpreted as a first-order transition.

I.6.3 Few characteristics and robustness of the Berezinskii-Kosterlitz-Thouless transition

Unlike in first- or second-order phase transitions, Berezinskii-Kosterlitz-Thouless transitions are usually not associated to a sharp change in the thermodynamic order parameters (like density or magnetization). In general, the transition is characterized by essential singularities in the thermodynamic functions (for example (I.24)). Because of this, a Berezinskii-Kosterlitz-Thouless transition is often referred to as an infinite order transition (following the Ehrenfest classification). These are transitions mediated by the unbinding of topological defects, separating a phase where defects are free from a phase where these defects form bound pairs. The transition separates a phase with a finite correlation length form a phase with a power-law correlation similar to a critical state. Usually, the dynamics at the transition point is associated to the growth of a quasi-long-range order and annihilation of topological defects [136].

The analysis of the Berezinskii-Kosterlitz-Thouless transition relies on the assumption that the low-temperature phase stays ordered up to the unbinding of vortices. In practice, unbinding may happen earlier and T_{KT} in (I.22) only gives an upper bound for the transition from the ordered phase to the disordered phase. For example, the Berezinskii-Kosterlitz-Thouless transition may get preempted by a first-order transition. In fact, it was initially predicted [137] that the transition in the two-dimensional XY model could be of first order rather than a Berezinskii-Kosterlitz-Thouless transition. In a first-order transition, the correlation length remains finite whereas in a Berezinskii-Kosterlitz-Thouless transition (or in a second-order transition) the correlation length is infinite. In numerical simulations of finite systems, it often gets difficult to distinguish a finite but large correlation from a truly infinite one, as it was the case in the two-dimensional melting.

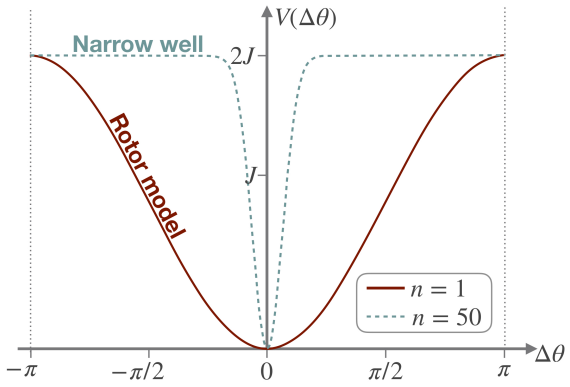


Figure I.16: **Two rotor models.** pairwise interaction potential $V(\theta_i - \theta_j)$ between nearest-neighbor rotors with angles θ_i and θ_j. For the potential (I.25) (red curve) the ordered low-temperature phase remains stable up to the vortex unbinding and therefore the melting transition is of Berezinskii-Kosterlitz-Thouless type. For the dashed curve with a narrow well, the Berezinskii-Kosterlitz-Thouless transition is preempted by a first-order transition. Source: inspired by Fig. 1.9 in E. Bernard, Algorithms and applications of the Monte Carlo method: Two-dimensional melting and perfect sampling, (2011) → [11]

This point, particularly that the Berezinskii-Kosterlitz-Thouless transition could be preempted by a first-order transition, is important to understand when studying the melting of two-dimensional particle systems in this thesis. For this, a careful study of the analysis presented for the Berezinskii-Kosterlitz-Thouless transition is needed, to see how it can break down. The Berezinskii-Kosterlitz-Thouless theory is built on the assumption that the harmonic approximation for the low-temperature phase remains valid up to the vortex-unbinding transition. This means that T_{KT} only gives an upper limit for the thermodynamic stability of the quasi-long-range order in the low-temperature phase. It can happen that

another type of transition at a temperature $T < T_{\mathrm{KT}}$ preempts the Berezinskii-Kosterlitz-Thouless transition.

Precisely this was shown to happen by Domany *et al.* [138] in the two-dimensional XY model with modified interactions. In the model in (I.19) the interaction between nearest-neighbor rotors i and j can be written as an interaction potential

$$V(\theta_i - \theta_j) = 2J\left[1 - \cos^{2n}\left(\frac{\theta_i - \theta_j}{2}\right)\right], \qquad \text{with } n = 1\,. \tag{I.25}$$

This potential has a wide valley near $\Delta\theta = 0$ as shown in Fig. I.16. Instead, if n is a large positive integer, the interaction potential has a sharp well near $\Delta\theta = 0$ and in this case, it was found [138] in numerical simulations that the transition is of first order and not of Berezinskii-Kosterlitz-Thouless type anymore. For a more recent analysis see [139]. This is precisely the result of the Berezinskii-Kosterlitz-Thouless transition being preempted by a first-order transition. This can be qualitatively seen as follows. The depth of the potential fixes an energy scale $\sim 2J$. If the temperature $T \gg \frac{J}{k_{\mathrm{B}}}$, the thermal fluctuations of the rotors destroy order. This means, if at $T_{1\mathrm{st}} \simeq \frac{J}{k_{\mathrm{B}}}$ the system is still in an algebraically ordered phase, and not yet destroyed by vortex-unbinding, then the system undergoes a discontinuous (first-order) transition to the disordered phase. On the other hand, if $T_{1\mathrm{st}}$ is higher than $T_{\mathrm{KT}} = \frac{J_{\mathrm{eff}}\pi}{2k_{\mathrm{B}}}$, then vortex-unbinding destroys the order and the transition is of Berezinskii-Kosterlitz-Thouless type. This competition between $T_{1\mathrm{st}}$ and T_{KT} can be tuned by adjusting the narrowness of the interaction potential $V(\Delta\theta)$. The more the potential well becomes narrow, the stronger the fluctuations of the rotors are coupled and as a result, the effective interaction strength J_{eff} grows, which in turn increase T_{KT}. This is why for a narrow well potential the transition is of first order.

A similar behavior is known in other examples, like in the q-state Potts model, where the order of transitions can be changed by varying the number of states q, or in the two-dimensional Coulomb gas, where the Berezinskii-Kosterlitz-Thouless transition at low density changes towards a first-order phase transition at higher density [140].

This example indicates a possible scenario where a low-temperature ordered phase moves to a disordered high-temperature phase via two successive transitions: first, a Berezinskii-Kosterlitz-Thouless transition where the quasi-long-range ordered phase changes to a short ranged ordered phase. Then, this short-ranged ordered phase changes into another short-ranged ordered phase by a first-order (discontinuous) transition as in the liquid-gas transition. This is precisely the scenario in the melting of two-dimensional particle systems. The two-dimensional solid with quasi-long-range positional order melts to a hexatic state with short-range positional order. This is a Berezinskii-Kosterlitz-Thouless transition. This is then followed by a second transition in which the hexatic phase melts into a disordered liquid. The nature of this second transition could either be of Berezinskii-Kosterlitz-Thouless type or a first-order transition and this can be tuned by changing the steepness of the interaction potential similar to that in the XY model. This is discussed in the next section I.7.

Remark: The fact that the nature of transitions can be changed by simply changing the interaction potential appears to contradict the idea of universality which is usually conceived as that the symmetry and dimensionality govern the transition and the critical exponents.

Nevertheless, it is now rigorously established [141] that by making the interaction potential sufficiently narrow the transition can be indeed changed to be of first order.

I.7 The BKTHNY theory for the two-step melting

The melting transition in two-dimensional particle systems is more complex than that for the two-dimensional XY model. In fact, the exact nature of the transition has been debated for long [142, 143]. Here, mostly the basic concepts are discussed drawing a comparison with the XY model. Details of numerical results are presented afterwards, following earlier results of [11–13].

It is now established [11–13] that in two-dimensional particle systems the quasi-long-range ordered solid melts through an intermediate hexatic phase. In this, the role of the vortices in the XY model is played by topological defects in the particle arrangement. Kosterlitz and Thouless originally developed the theory for melting of two-dimensional solids. This was later completed by Nelson and Halperin, as well as Young [144–146]. The combined theory is now referred to as the Berezinskii-Kosterlitz-Thouless-Halperin-Nelson-Young (BKTHNY) theory. According to this theory, a two-dimensional solid melts first into a translational disordered hexatic phase where the positional order is short-ranged but orientational order (defined in (II.12)) is quasi-long-ranged. The hexatic phase subsequently melts into a disordered liquid where both positional and orientational correlations are short ranged. A table summarizing these characteristics of the positional and orientational order in the two-dimensional phases is given in Tab. I.2.

	Solid	Hexatic	Liquid
Positional order	Quasi-long-range (power-law decay)	Short-range (exponential decay)	Short-range (exponential decay)
Orientational order	Long-range (constant)	Quasi-long-range (power-law decay)	Short-range (exponential decay)

Table I.2: **Characterizing properties of two-dimensional phases.** A summary of characteristic positional and orientational orders in the three thermodynamic phases in two-dimensional particle systems. [144–146]

Within the BKTHNY theory, both transitions are predicted to be of Berezinskii-Kosterlitz-Thouless type and they are mediated by the unbinding of topological defects: dislocations and disclinations. Later, various other scenarios were proposed which were based on the unbinding of grain boundaries, the condensation of vacancies, or the simultaneous unbinding of both dislocations and disclinations [147–151]. It is now confirmed by numerical simulations [11–13] that the solid-hexatic transition is a Berezinskii-Kosterlitz-Thouless transition in agreement with the BKTHNY theory. However, the hexatic-liquid transition can either be a Berezinskii-Kosterlitz-Thouless or a first-order transition depending on the softness of the interaction potential. Below we present this using the BKTHNY theory for interacting discs.

I.7.1 Topological defects

The basic idea of the BKTHNY theory is that the low-temperature solid phase (see Tab. I.2) melts through the unbinding of topological defects. Although there are many types of topological defects possible, the most relevant ones for melting are the disclinations and dislocations. In a perfectly ordered solid in two dimensions, the particles are arranged in a hexagonal arrangement as shown in Fig. I.17. The indicated Voronoi construction[15] allows for the identification of nearest neighbors. Two particles are defined as nearest neighbors if their Voronoi cells share an edge. In the perfect ordered arrangement in Fig. I.17 the Voronoi construction is made of perfect hexagons, thus each particle has 6 nearest neighbors. The arrows in the figure characterize the local orientation which can be quantified with the ψ_6 order parameter defined as

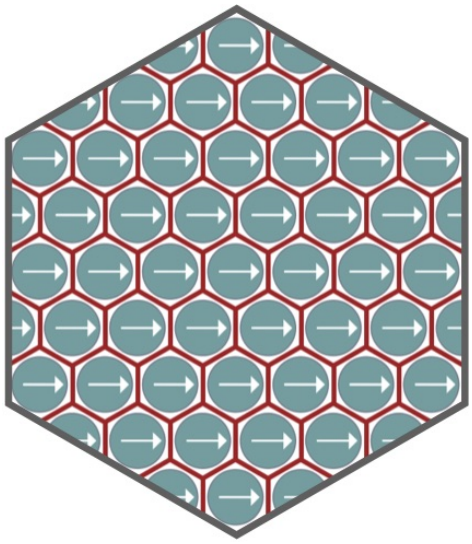


Figure I.17: **Perfect order.** A sample construction of a perfect hexagonal ordering of discs without defects. The red hexagons show the Voronoi construction and the white arrows denote the local orientation of each particle defined by ψ_6 in (I.26).

$$\psi_6(\boldsymbol{r}_i) = \frac{1}{\text{number of neighbors } k \text{ of } i} \sum_k e^{\mathbb{i}\, 6\theta_k(\boldsymbol{r}_i)}, \tag{I.26}$$

where $\theta_k(\boldsymbol{r}_i)$ is the angle enclosed by the line connecting the particle i at position $\boldsymbol{r}_i$ with its k^{th} nearest neighbor and a chosen reference axis[16]. In the perfect hexagonal order, the reference axis can be always chosen such that $\theta_k(\boldsymbol{r}_i) = \frac{2\pi k}{6}$, leading to $\psi_6(\boldsymbol{r}_i) = 1$ for all particles. Deviations from this value can appear due to disorder and topological defects.

The disclination is the simplest kind of topological defect in this hexagonal arrangement caused by a single particle with either 5 or 7 nearest neighbors, as shown in Fig. I.18. Similar to the vortices in the XY model they can be assigned a "charge" depending on how much the local orientational order parameter ψ_6 winds for a closed path around a defect. The orientation ψ_6 winds by -2π for a disclination caused by a particle with 7 neighbors, it is a disclination with a negative charge (Fig. I.18a). For the disclination with 5 nearest neighbors the winding is 2π and it has a positive charge (Fig. I.18b). This defect is similar to a vortex in the two-dimensional XY model. The presence of free disclinations causes

[15] The Voronoi diagram is the dual graph of the Delaunay triangulation. The Delaunay triangulation connects points (particle positions) in two dimensions. The result is a grid of triangles, where a circle, connecting all points (particle centers) of one triangle does not contain another point. Starting from the Delaunay triangulation, the Voronoi diagram can be constructed by drawing the perpendicular bisector (p_i) for all existing triangle sites (s_i). Starting from the intersect of a p_i-s_i-pair, p_i is only drawn until it is intersected by another p_j in the diagram. This way the p_i form cells, containing only a single point (particle center) as shown in Fig. I.17. The nearest neighbors of a particle are either those directly connect by one site in the Delaunay triangulation, or equivalently those in a neighboring Voronoi cell (see also Fig. II.17b).

[16] A similar observable $e^{i2\theta_k(\boldsymbol{r})}$ is used in two-dimensional nematic liquid crystals [152]. The observable is chosen considering the two-fold symmetry of the liquid crystal.

disruptions in both positional and orientational order, therefore if such free disclinations are thermodynamically stable, the system is in the disordered liquid phase.

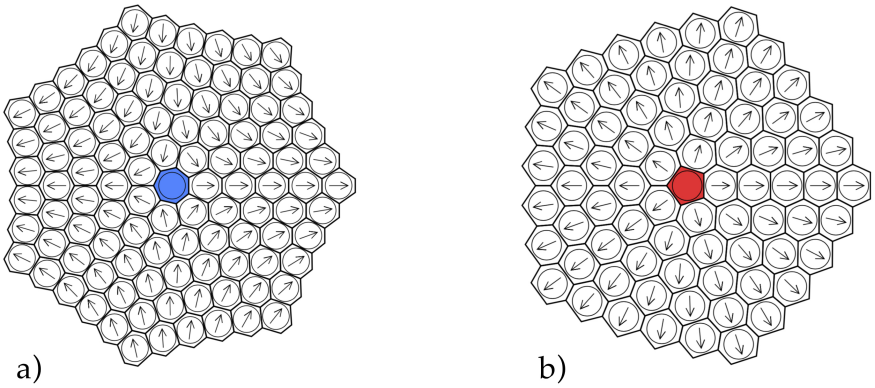


Figure I.18: **Schematics of disclination defects in a hard-disk system.** The polygons denote the Voronoi construction, where the blue color highlights a heptagon and the red color a pentagon. The arrows denote the local orientation field ψ_6 in (I.26). a) A disclination caused by a single particle with seven nearest neighbors. The orientation winds by -2π around the defect. b) A disclination caused by a single particle with five nearest neighbors. The orientation winds by 2π around the defect. These are similar to vertices with negative and positive winding numbers in the two-dimensional XY model. Individual disclinations disrupt orientational order around them, but if they form pairs consisting of two disclinations of an opposite winding number the orientational order remains unperturbed at large distances. Paired disclinations are called dislocations (see Fig. I.19). Source: Fig. 1.12 in E. Bernard, Algorithms and applications of the Monte Carlo method: Two-dimensional melting and perfect sampling, (2011) → [11].

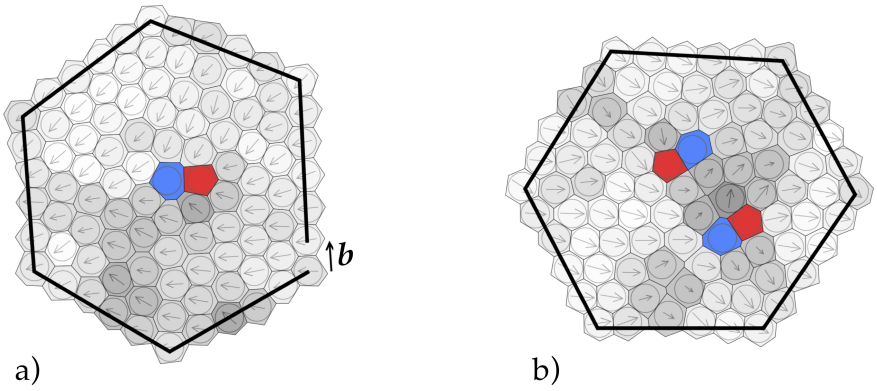


Figure I.19: **Schematics of dislocations in a hard-disk system.** The polygons denote the Voronoi construction and (as in Fig. I.18) blue heptagons highlight disks with seven neighbors, whereas red pentagons have five neighbors. The arrows denote the local orientation field ψ_6 in (I.26). a) A path around a free dislocation. The path would be closed on a perfect lattice, here it leaves a gap characterized by the Burgers vector $\boldsymbol{b}$. The resulting disturbance of the positional order infects the whole system. The creation of a single dislocation requires an infinite elastic energy. b) A path around a bound pair of dislocations. The resulting stress due to the pair remains local, thus also the positional order is disturbed only locally. The creation of a paired dislocation requires a finite elastic energy. Source: Fig. 1.11 in E. Bernard, Algorithms and applications of the Monte Carlo method: Two-dimensional melting and perfect sampling, (2011) → [11].

In comparison, when disclinations of opposite "charge" are paired, the orientation field around such a pair can be ordered, but positional order is still disturbed. Such paired disclinations are called dislocations and are shown in Fig. I.19. Such defects can be seen as a missing or an extra row of particles. A dislocation can be characterized in terms of the Burgers vector. This is defined as the vector $\boldsymbol{b}$ (see Fig. I.19a) by which a path around the defect fails to close, which would have closed on a perfect lattice. A free dislocation disrupts positional order. However, when two dislocations form a pair, a path around the pair could close as in a perfect lattice (see Fig. I.19b), and therefore does not destroy positional order at large distance. This means a two-dimensional solid can have paired dislocations.

The basic idea of the BKTHNY theory deals with the thermal stability of bound dislocations and bound disclinations. In the two-dimensional solid pairs of dislocations are bound together with a finite distance between them such that at large distances (quasi-long-ranged) positional order can survive. At the melting temperature, dislocations unbind and the solid turns into a hexatic phase where the presence of free dislocations does not allow positional order but orientational order can be quasi-long-ranged. As the temperature is raised, the dislocations unbind into free disclinations which melts the hexatic phase into a disordered liquid. This is similar to the Berezinskii-Kosterlitz-Thouless transition in the XY model due to the unbinding of vortices, and one would naturally expect that the melting transitions in two-dimensional particle system are Berezinskii-Kosterlitz-Thouless transitions. Further quantitative details to this two-step melting are presented below.

I.7.2 The harmonic approximation for the two-dimensional solid

The existence of a two-dimensional solid at low temperature is argued in this subsection I.7.2 using the harmonic approximation. This solid phase has the same properties as the harmonic solid: quasi-long-range positional order and long-range orientational order. This can be even quantitatively analyzed with the theory of elasticity assuming hexagonal order in the arrangement of particle positions which is the stable arrangement for ordered packings of isotropic discs in two dimensions [4, 144]. For this low-temperature phase a displacement field $\boldsymbol{u}(\boldsymbol{r})$ (similar to that in the harmonic solid) of particle positions can be defined around the perfect lattice arrangement. The strain tensor $\boldsymbol{v}$ caused due to the displacement is a 2×2 matrix in two dimensions and is given by

$$v_{ij}(\boldsymbol{r}) = \frac{1}{2}\left(\partial_{x_i} u_j + \partial_{x_j} u_i\right) , \qquad \text{with } i,j \in \{1,2\} .$$

Within the harmonic approximation, the effective Hamiltonian is expressed in terms of the strain tensor, giving

$$H_{\text{eff}} = \frac{1}{2}\int d^2r \sum_{ij} \left(\lambda\, \delta_{ij} v_{ij}(\boldsymbol{r})^2 + 2\mu\, v_{ij}(\boldsymbol{r})^2\right) , \tag{I.27}$$

where λ is the Lamé elastic coefficient, δ_{ij} is the Kronecker delta and μ is the shear modulus. The Hamiltonian is quadratic, just like in the harmonic solid or in the XY model (I.20), and similar to them it can be analyzed exactly. For example, the positional correlation (I.18) gives [144]

$$C_{\boldsymbol{Q}}(r) \sim r^{-\nu_{\boldsymbol{Q}}} , \qquad \text{with } \nu_{\boldsymbol{Q}} = \frac{k_{\text{B}} T \boldsymbol{Q}^2}{4\pi} \frac{3\mu+\lambda}{\mu(2\mu+\lambda)} , \tag{I.28}$$

where $\boldsymbol{Q}$ is the reciprocal lattice vector. Similar to the harmonic solid, for a system of linear size L, the structure factor $S(\boldsymbol{q})$ at the Bragg peaks $\boldsymbol{Q}$ depends as $S(\boldsymbol{q}) \sim L^{2-\nu_{\boldsymbol{Q}}}$ and the shape of the peaks is $\sim |\boldsymbol{q}-\boldsymbol{Q}|^{\nu_{\boldsymbol{Q}}-2}$. This means the diffraction pattern forms a lattice whose shape is a power-law instead of δ-functions found in a crystalline solid.

I.7.3 Solid-hexatic transition

The harmonic description (I.27) of the two-dimensional solid is a macroscopic description at large length scales. The presence of bound pairs of dislocations is permitted in this description as such defects do not disrupt order at distances larger than the intermediate distance between the two dislocations forming a pair. This distance is finite until the melting temperature T_m of the solid and becomes of the order of the system size at T_m when the pairs start to unbind. This unbinding can be argued using a heuristic estimation for the free energy of the Hamiltonian (I.27). A free dislocation costs an elastic energy which can be estimated using the strain tensor $v_{ij}(\boldsymbol{r}) \sim \frac{1}{r}$ in (I.27) for deformations at distance r from a free dislocation. Then, for a system of size L, the elastic energy cost from (I.27) due to a single defect is

$$E_{\text{disloc}} = \frac{b^2}{8\pi} Y \log \frac{L}{b} + E_0 \,,$$

where Y is the Young's modulus and E_0 is the core energy of the defect. The entropy for placing the defect anywhere in the system is

$$S_{\text{disloc}} \simeq 2k_{\text{B}} T \log \frac{L}{b}$$

and the free energy cost for the presence of a single defect is

$$F_{\text{disloc}} = \left(\frac{b^2}{8\pi} Y - 2k_{\text{B}} T \right) \log \frac{L}{b} \,.$$

Clearly, this heuristic argument gives a temperature

$$T_m = \frac{b^2 Y}{16\pi k_{\text{B}}}$$

such that for temperatures $T < T_m$ defects are unstable, whereas for $T > T_m$ they are stable, thus disrupting the order and hence melting the solid. Clearly, this means, below the melting temperature T_m, the dislocations form bound pairs (or generally any other kind of defects with zero Burgers vector) which do not disturb positional order. Above T_m, the dislocations are free, and thus disrupt positional order [17].

A more detailed analysis requires to include interactions between dislocations which (similar to vortices in the XY model) are logarithmic. A detailed renormalization group study gives [144–146] a normalized shear modulus and the power-law (I.28) of the positional correlation. Unlike in the XY model, the exponential $\nu_{\boldsymbol{Q}}$ is not universal at T_m. However, it was found [153] that its value is bounded $\frac{1}{4} \leq \nu_{\boldsymbol{Q}} \leq \frac{1}{3}$ which is supported by

[17] The argument can be extended to hard-discs, even though there is no energy scale. In this case, two competing forces are entropic.

experiments [154]. For a temperature $T > T_m$, the positional correlation is short-ranged with a finite correlation length [144–146]

$$\xi \sim e^{\frac{const}{|T-T_m|^{0.36963}}} .$$

As discussed earlier in the context of the XY model (see section I.6), this defect-mediated melting could get preempted by a first-order transition. It is only recently confirmed [11–13] that the solid-hexatic transition is indeed a Berezinskii-Kosterlitz-Thouless type transition for systems of interacting particles.

I.7.4 Hexatic-liquid transition

One of the major findings of the BKTHNY theory [144–146] is the existence of a hexatic phase where the positional order of the solid phase is lost but orientational order is still quasi-long-ranged. Inside this phase dislocations are free which destroys the positional order, and as a result the shear modulus vanishes [146]. The orientational order is not fully lost and can be characterized by the local orientation of the neighboring particles around a particle. The corresponding microscopic local order parameter is ψ_6 defined in (I.26). At a macroscopic effective description the system can be described [144, 146] by an effective Hamiltonian

$$H_{\text{hex}} = \frac{1}{2} I_{\text{eff}} \int d^2 r (\nabla \theta(\boldsymbol{r}))^2 ,$$

where I_{eff} is the effective stiffness (also known as the Frank constant) of the macroscopic orientational field $\theta(\boldsymbol{r})$. As the underlying stable arrangement (solid phase) has a hexagonal ordering, the macroscopic field should have a $\frac{\pi}{3}$ rotational symmetry. This makes it easy to compare with the macroscopic description (I.20) of the XY model with $J_{\text{eff}} = \frac{I_{\text{eff}}}{36}$. This comparison leads to an algebraic decay of the orientational correlation function at the melting temperature T_{hl}:

$$g_6(r) \propto \left\langle \sum_{i,j}^{N} \psi_6^\star(\boldsymbol{r}_i) \psi_6(\boldsymbol{r}_j) \delta(r - r_{ij}) \right\rangle \sim r^{-\nu_{\text{hl}}} .$$

Remarks:

1. In the elastic description in terms of the displacement field $\boldsymbol{u}(\boldsymbol{r})$, the elastic constants vanish [146] when the system turns into the hexatic phase making $H_{\text{sol}} = 0$. The effective Hamiltonian H_{hex} becomes the leading term with the orientational field $\theta(\boldsymbol{r})$ being connected to the displacement field by

$$\theta(\boldsymbol{r}) = \frac{1}{2} \sum_{i,j} \left(\partial_{x_i} u_j - \partial_{x_j} u_i \right) , \qquad \text{with } i, j \in \{1, 2\} .$$

2. As the orientational correlation decays algebraically to zero, there is no net orientation for thermodynamically large systems. Therefore, its diffraction pattern is made of isotropic rings, just like for a liquid. However, because the decay is algebraic (and not exponential), on a finite system the diffraction ring is modulated and shows reminiscence of six brighter spots from the solid.

The hexatic melts into a disordered liquid as the dislocations split into free disclinations. Extending the comparison with the vortex unbinding in the XY model, the hexatic-liquid transition temperature T_{hl} can be found by substituting $J_{\text{eff}} = \frac{I_{\text{eff}}}{36}$ in (I.22) leading to

$$T_{\text{hl}} = \frac{\pi I_{\text{eff}}}{72 k_{\text{B}}} .$$

This comparison also gives the exponent ν_{hl} for the power-law decay of the orientational correlation (using (I.21))

$$\nu_{\text{hl}} = \frac{18 k_{\text{B}} T_{\text{hl}}}{\pi I_{\text{eff}}} = \frac{1}{4} \qquad \text{at } T = T_{\text{hl}}.$$

More generally, for $T \leq T_{\text{hl}}$ inside the hexatic phase, the exponent has a cusp singularity and is given by (using (I.23))

$$\nu_{\text{hl}} = \frac{1}{4} \left(1 - \text{const} \sqrt{T_{\text{hl}} - T} \right) .$$

For $T \geq T_{\text{hl}}$, in the liquid phase, the orientational correlation function decays exponentially

$$g_6(r) \sim e^{-r/\xi}$$

with the correlation length

$$\xi \sim e^{\frac{\text{const}}{\sqrt{T - T_{\text{hl}}}}} .$$

In the liquid phase, both the positional and the orientational correlation are short ranged and the diffraction pattern consists of an isotropic ring. In this state free disclinations are thermally stable.

The BKTHNY theory predicts that both transitions are Berezinskii-Kosterlitz-Thouless type and their behavior is governed by the unbinding of dislocations and disclinations. There are also other types of defects like vacancies and interstices but they do not change the qualitative behavior of the system.

I.8 Present day status of two-step melting scenario

The BKTHNY theory predicts a two-step melting scenario with both melting transitions of Berezinskii-Kosterlitz-Thouless type. Primarily, these results were derived from a renormalization group analysis [144–146] of the continuous elastic model of a solid (particularly, assuming a hexagonal arrangement in the solid phase). In reality, this elastic description may break down or different arrangements of a solid could exist, and therefore, other melting scenarios may emerge. Hence, even though the theory appears to be universal, it is reasonable to ask whether all two-dimensional systems melt in accordance with this scenario. Since the theory was proposed, its universality has been strongly debated. Even convincing evidence for the hexatic phase was tough to get (see, however, [155]). Due to finite system sizes, short-range correlations were difficult to distinguish from power-law correlations. For reference to these earlier studies see [5, 6, 156, 157].

A number of experimental and numerical attempts have been made to verify the predictions of the BKTHNY scenario. Experiments on quasi-two-dimensional systems (*e.g.* on a monolayer of gas molecules on a graphite substrate [142, 158], or electrons confined at the surface of liquid Helium [118, 159–161], or simulations on dipole-dipole interactions [155]) confirm the melting of a solid phase, but they do not verify the existence of the hexatic phase [5]. A clear experimental evidence of the hexatic phase and the two-step melting comes from studies on thin single-crystal films [162, 163], charged polystyrene spheres confined in two dimensions [119, 164–166], and particularly the recent works on colloidal particles [167–169]. However, the nature of the transition is still ambiguous in most experimental results (existing exceptions like [170] discussed below). In fact, some conclusions from these experiments do not fully agree with results from computer simulations [5]. For example, the continuous transition claimed in the experiment in the Xenon monolayer on graphite [171, 172] is in contradiction with the first-order transition seen in molecular dynamics simulation of the system [173, 174]. A further indication for a first-order melting transition comes [175, 176] from the behavior of the heat capacity which does not coincide with predictions of the BKTHNY theory. These experimental results suggest that there are multiple possible scenarios of melting in two dimensions and they are not necessarily the precise mechanism of the BKTHNY theory [5]. This is further confirmed by computer simulations.

A huge amount of studies has been done using computer simulations, beginning with the first study of two-dimensional melting in a system of hard disks by Alder and Wainwright [113]. Based on an analysis of the pressure-density curve it was concluded that the melting is a conventional first-order transition, which was later supported by Hoover and Ree [177]. These studies were done on merely 900 particles and their conclusion about the nature of the transition is now known to be incorrect. Later simulations often suffered from insufficient run times and these have been done either using Markov-chain Monte Carlo, Molecular dynamics, or even hybrid Monte Carlo [178–183]. Many variants of particles and interactions are studied, like Lenard-Jones, Coulomb repulsion, soft disks and especially the hard-disk model [113, 135, 142, 184–186]. Most of these studies added to conflicting results about the melting scenario, sometimes even for the same system. For example, in a system of hard disks, [185] reported a first-order transition and later [187] described the transition to be a continuous transition without a hexatic phase, both of these are now established to be incorrect. The situation turned out to be more complicated for systems with soft interactions. Even though there was an understanding [142] that a long-range potential leads to the BKTHNY scenario, and a short-range potential leads to a first-order transition, there were already conflicting claims to this picture. On one hand [188] reported a first-order transition for the $\frac{1}{r^3}$ potential, and on the other hand [153] reported a two-step continuous transition for the $\frac{1}{r^{12}}$ potential.

All these discrepancies are possibly due to the natural consequence of being in the vicinity of phase transitions, where correlation lengths of fluctuations can exceed the system size, making simulations prone to erroneous results. These errors are especially prominent in two dimensions due to increased fluctuations. In addition, two-dimensional solids have power-law correlations, and similar to a critical state, these simulations take extremely long times to thermalize the system as the system size grows. Therefore, these simulations often analyzed systems that were too large for the used algorithms, but which are required for a convincing study of the melting transition. It was shown [189] that the finite-system-size results are highly sensitive to the choice of the boundary. The finite-size scaling, which is

typically used to overcome these difficulties [190], are also tricky to apply because of the two diverging correlation lengths corresponding to the orientational and the positional order. In addition, the hexatic phase turns out to be very narrow, and this can lead to incorrect conclusions about the melting scenario.

These difficulties were recently overcome [11–13]. A novel algorithm (Event-chain Monte Carlo) allowed the authors to reach the thermalization much faster even in large systems (up to 1024^2 disks). Together with robust criteria indicating the steady state, this works finally provided convincing results. Based on a thorough data analysis using a Mayer-Wood loop of isotherms and a detailed consideration of positional and orientational order, their result gave an unambiguously picture: for sufficiently hard repulsive inter-particle interactions, the melting transition between the hexatic and liquid phases is of first order, although the transition between the solid and the hexatic remains a Berezinskii-Kosterlitz-Thouless transition as predicted within the BKTHNY theory. A possible picture is that the Berezinskii-Kosterlitz-Thouless transition predicted for the hexatic-liquid transition gets preempted by a first-order transition. The situation is similar to the competition between a first-order and a Berezinskii-Kosterlitz-Thouless transition in the two-dimensional XY model discussed in section I.6, where the nature of the transition can be changed by tuning the sharpness of the interaction potential. Indeed, their numerical simulations confirm [13, 191] that for sufficiently soft interactions between particles ($\frac{1}{r^n}$ pair potential with $n \lesssim 6$), the transition between the hexatic and liquid is a Berezinskii-Kosterlitz-Thouless transition in accordance with the BKTHNY theory. On the other hand, for $n \gtrsim 6$, the transition is of first order[18]. More specifically, for purely hard-core interactions ($n \to \infty$), there is clear evidence for two-step melting with an intermediate hexatic phase and a first-order liquid-hexatic transition [11, 12, 192, 193]. The first-order liquid-hexatic transition even persists in quasi-two dimensions [193]. On the other hand, the hexatic phase tends to disappear in a system of binary mixtures [194]. This melting scenario proposed in [11, 12, 192], is now confirmed in experiments [170] on a monolayer of colloidal particles in a water-ethanol mixture, where even a quantitative agreement with the simulation results [12] is obtained. For a soft-sphere interaction, using an extension of the event-chain algorithm, it was shown by Kapfer and Krauth [13, 191], that the intermediate hexatic phase is stable for all n up to at least $n = 3$. This work also supports that for $n > 6$, the liquid-hexatic transition is of first order, but for $n = 6$ the coexistence between the liquid and the hexatic is undetectable. However, for $n < 6$ the BKTHNY scenario holds, with a clear numerical confirmation for $n = 3$ by Lin *et al.* [155]. A similar effect, where a first-order transition could preempt the Berezinskii-Kosterlitz-Thouless transition of the BKTHNY scenario is claimed to be achieved by changing the form of the particles [195] or by random pinning [196, 197].

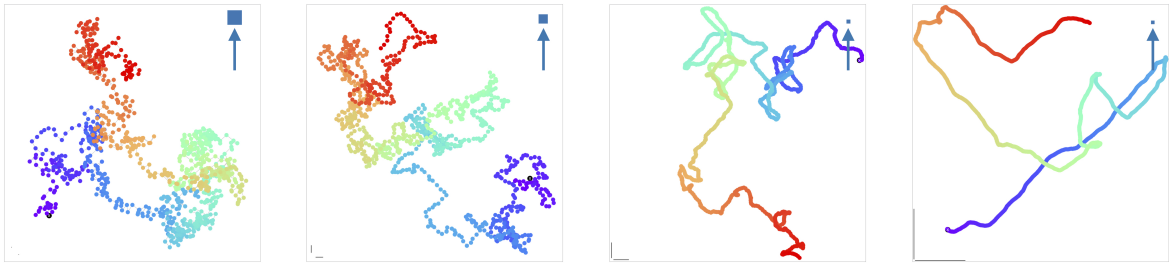
In general, from these results of experiments and computer simulations, it is now realized [5] that the two-dimensional melting can take place following multiple scenarios. The most important ones among them are the following. It is most likely that the two-step melting in accordance with BKTHNY scenario (two Berezinskii-Kosterlitz-Thouless transitions), is realized for systems with slowly decaying pair potentials (for example, power-law $\frac{1}{r^n}$ with $n \lesssim 6$). If the interaction potential decays sharply enough, the hexatic-liquid transition becomes a first-order transition. In a third scenario, melting can happen in a single step following a conventional first-order transition. However, to date, there is no clear theoret-

[18] There have been theoretical attempts by Chui *et al.* [148, 149] to connect a first-order transition to the formation of grain boundaries.

ical criterion that could predict the melting scenario based on the shape of the interaction potential [5] and this remains an open problem to be unambiguously solved.

II – Collective behavior of two-dimensional interacting particles in and out of equilibrium

This chapter contains the main part of this thesis. The goal here is to understand how the two-dimensional equilibrium phase diagram of interacting particles is affected as persistence is introduced in the dynamics of individual particles. Fig. II.1 illustrates the change in the particle motion as the persistence is smoothly increased, leading to the characteristic trajectory of active self-propelled particles (see subsection I.4.1 in introduction) with a finite persistence length. There have been several earlier studies of the collective behavior of self-propelled particles, but primarily using Brownian and molecular dynamics simulations [97, 98, 107, 198, 199] (also see subsection I.4.1). The model studied here, which uses a kinetic Monte Carlo dynamics, is an atypical approach to numerically study active matter. The model was first discussed in a system of hard disks [200]. It consists of a modified Metropolis algorithm with a memory term in the update rule, allowing for a smooth tuning from a passive to a self-propelled/persistent particle motion as shown in Fig. II.1.



a) b) c) d)

Figure II.1: **Random persistent walks.** The persistence of the motion increases from left to right. a) Brownian motion. b), c) and d) persistent random motion. The edge length of the blue square in the upper right corner of each figure corresponds to twice the maximum jump length and serves as a scale for the unit spatial length in this figures. Each walk contains 100 jumps.

The discussion in this chapter is arranged in the following order. The first section II.1 contains a detailed description of the persistent kinetic Monte Carlo algorithm and a quantitative characterization of self-propulsion (section II.1). This is followed by results in one dimension, which illustrate the effect of persistence/self-propulsion within this Monte Carlo approach (section II.2). Section II.3 contains the main result of this thesis, namely the full

phase diagram of self-propelled interacting particles including the two-step melting scenario outside equilibrium and its (non-existing) interplay with MIPS. The following section II.4 discusses the continuum limit of the kinetic Monte Carlo dynamics and answers the question of the number of relevant parameters within this dynamics. The last two sections II.5 and II.6 address the question of the existence of pressure in the kinetic Monte Carlo dynamics and in a closely related active Ornstein-Uhlenbeck process.

II.1 Persistent kinetic Monte Carlo

The goal of this section II.1 is the introduction of a minimal algorithm as a tool to investigate how self-propulsion could influence the thermodynamic equilibrium phases in two dimensions. For this, a system of N interacting particles in a box of volume V is considered. Each particle follows a dynamics closely related to the active Ornstein-Uhlenbeck process [92]. The dynamics is simulated by a modified Metropolis algorithm which breaks detailed balance [200].

In each Monte Carlo step, a displacement by an amount $\boldsymbol{\epsilon}_i$ is proposed for a single randomly chosen particle i. The move is accepted with the Metropolis probability

$$P(E' \to E) = \min\left[1, e^{-\beta \Delta E}\right] , \tag{II.1}$$

where $\Delta E = E - E'$ is the change in the total energy $E = \sum_{i<j} U(\boldsymbol{r}_i - \boldsymbol{r}_j)$ caused by the displacement and $\beta = (k_\mathrm{B} T)^{-1}$ is the inverse temperature in the equilibrium limit.

Self-propelled/persistent motion is introduced into the dynamics by choosing the proposed displacement $\boldsymbol{\epsilon}_i$ of particle i based on the previously proposed displacement $\boldsymbol{\epsilon}'_i$ of the same particle. The correlation is introduced in two stages. First, a random vector $\boldsymbol{\eta}$ is sampled from a bivariate normal distribution $\propto \exp[-(\boldsymbol{\eta} - \boldsymbol{\epsilon}'_i)^2/2\sigma^2]$, where σ is the standard deviation. In the second stage, $\boldsymbol{\epsilon}_i$ is generated from $\boldsymbol{\eta}$ using the folding scheme

$$\epsilon_{i,z} = \begin{cases} q_{i,z} - \delta & \text{if } q_{i,z} < 2\delta \\ 3\delta - q_{i,z} & \text{if } q_{i,z} \geq 2\delta \,, \end{cases} \tag{II.2}$$

with $z \in \{\mathrm{x}, \mathrm{y}\}$ and $q_{i,z} = (\eta_z + \delta) \bmod 4\delta$, with $a \bmod b = a - b \left\lfloor \frac{a}{b} \right\rfloor$, i. e., $0 \leq q_{i,z} < 4\delta$, where $\lfloor a \rfloor$ is the floor function. The folding scheme sets a cutoff for the size of the proposed displacements. The scheme is equivalent to a random walk of the displacement variables $\boldsymbol{\epsilon}_i$ in a $[-\delta, \delta]^2$ box with reflecting boundary conditions, see Fig. II.2a. A sufficiently small δ keeps the dynamics local.

In this algorithm, the ratio $\frac{\sigma}{\delta}$ controls the persistence, allowing for a smooth transition from passive to self-propelled dynamics. In the case $\sigma \lesssim \delta$, the proposed displacement $\boldsymbol{\epsilon}_i$ of particle i is close to the previously proposed displacement $\boldsymbol{\epsilon}'_i$, and reflections happen only if $\boldsymbol{\epsilon}'_i$ is near the boundary (see Fig. II.2a). This translates in a particle motion with an average number of τ displacements in the same direction, before the direction of motion changes (see Fig. II.2b). For the case $\sigma > \delta$, on the other hand, almost each ϵ results from multiple reflections in the $[-\delta, \delta]^2$ displacement box (see Fig. II.2c), uncorrelating the corresponding particle motion (see Fig. II.2d). The moderate ratio $\frac{\sigma}{\delta} \approx 2$ in Fig. II.2c was chosen for a

clear presentation. However before going into the analytic analysis it is simple to imagine that for $\sigma \gg \delta$ the sampled ϵ_i are, due to the large number of multiple reflections, entirely uncorrelated, thus the passive limit of a random walk is recovered.

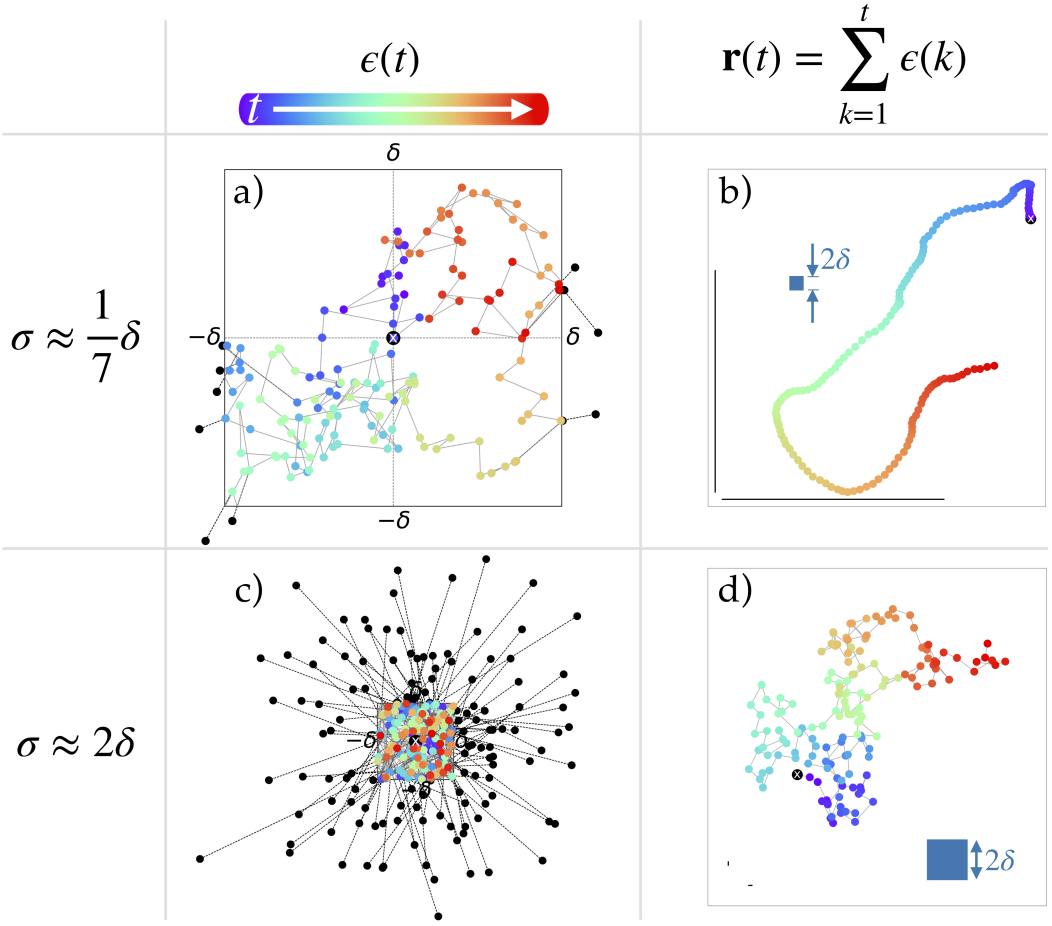


Figure II.2: **Translation of a random walk into particle motion.** a) and c) show random walks of the displacement $\boldsymbol{\epsilon}$ in a $[-\delta, \delta]^2$ box with reflective boundary conditions. b) and d) show the resulting particle motion. The color gradient shown above a) indicates the time evolution. Following the scheme of the $\boldsymbol{\epsilon}$ sampling, the intermediate random vector $\boldsymbol{\eta}$ is indicated by black data point only, if $\boldsymbol{\eta}$ was sampled outside the δ-box. The attached black line draws the connection to the corresponding previous displacement $\boldsymbol{\epsilon}'$. The sampled displacements for the first case $\sigma \approx \frac{1}{7}\delta$ in a) clearly result in a persistent particle motion in b). The color gradient allows for a direct connection between a) and b). The large standard deviation in the second case $\sigma \approx 2\delta$ leads to largely uncorrelated displacements, thus the resulting particle walk in d) is visually indistinguishable from a passive random walk.

In the many-particle case, each particle is performing its proper random $\boldsymbol{\epsilon}$-walk, independent from the other particles and of the positions of the particles. The $\boldsymbol{\epsilon}$-sampling scheme persists whether the displacement was accepted or not, thus leaving the system entirely free of alignment interactions.

II.1.1 Analytic characterization of the kinetic Monte Carlo dynamics

a) Probability distribution of the displacement ϵ in one dimension

In one dimension the displacement $\epsilon(t)$ is chosen from a reflected random walker (of variance σ^2) inside a $[-\delta, \delta]$ box. Without the reflecting walls, $\epsilon(t)$ would simply perform a random walk on an infinite line with

$$P(\epsilon, t) = \frac{1}{\sqrt{2\pi\sigma^2 t}} e^{-\frac{\epsilon^2}{2\sigma^2 t}} .$$

This is a solution of the diffusion equation $\partial_t P(\epsilon, t) = D\partial_\epsilon^2 P(\epsilon, t)$ with $D = \frac{\sigma^2}{2}$. However, the random walker inside the δ-box must follow the same diffusion equation, as long as the walker is not close to the walls. The reflecting walls impose the boundary condition of a vanishing probability current at $\epsilon = \pm\delta$

$$\partial_\epsilon P(\epsilon, t)|_{\epsilon=\pm\delta} = 0 . \tag{II.3}$$

Assuming that the walker starts at ϵ_0 at $t = 0$, the probability must also satisfy ($\boldsymbol{\delta}(x)$ is the Dirac delta function)

$$P(\epsilon, 0|\epsilon_0, 0) = \boldsymbol{\delta}(\epsilon_0 - \epsilon) . \tag{II.4}$$

Choosing the ansatz $P(\epsilon, t|\epsilon_0, 0) = W(t)V(\epsilon|\epsilon_0)$, the solution of the diffusion equation with (II.3) and (II.4) is

$$P(\epsilon, t|\epsilon_0, 0) = \frac{1}{2\delta} + \frac{1}{\delta}\sum_{n=1}^{\infty}\left(A_n(\epsilon_0)\sin\left(\frac{(2n-1)\pi\epsilon}{2\delta}\right) e^{-\frac{(2n-1)^2\pi^2\sigma^2 t}{8\delta^2}} + B_n(\epsilon_0)\cos\left(\frac{(2n)\pi\epsilon}{2\delta}\right) e^{-\frac{(2n)^2\pi^2\sigma^2 t}{8\delta^2}}\right) , \tag{II.5}$$

with the coefficients resulting from the comparison of $P(\epsilon, 0|\epsilon_0, 0)$ with the Fourier series of the δ-function

$$\sum_{n=1}^{\infty}\sin\left(\frac{\pi n\epsilon_0}{\delta}\right)\sin\left(\frac{\pi n\epsilon}{\delta}\right) = \sum_{n=1}^{\infty} A_n(\epsilon_0)\sin\left(\frac{\pi(2n-1)\epsilon}{2\delta}\right) , \tag{II.6}$$

and

$$B_n(\epsilon_0) = \cos\left(\frac{\pi(2n)\epsilon_0}{2\delta}\right) .$$

b) Auto-correlation time of the displacements

The displacement auto-correlation time τ is one measure of persistence. In the case of a single free particle, τ corresponds to the average number of steps of persistent motion in the same direction. In the many-particle case, τ is the number of attempted moves in the same direction (accepted or not accepted by the Metropolis filter in (II.1)).

The auto-correlation time results from the displacement's auto-correlation function. For $t_2 > t_1$ this is

$$\begin{aligned}\langle \epsilon_2(t_2)\epsilon_1(t_1)\rangle &= \int_{-\delta}^{\delta}\int_{-\delta}^{\delta} \epsilon_2\epsilon_1 P\left(\epsilon_2, t_2|\epsilon_1, t_1\right) P\left(\epsilon_1,\, t_1|\, 0, 0\right) d\epsilon_1 d\epsilon_2 \\ &= \int_{-\delta}^{\delta}\int_{-\delta}^{\delta} \epsilon_2\epsilon_1 P\left(\epsilon_2, t_2 - t_1|\epsilon_1, 0\right) P\left(\epsilon_1,\, t_1|\, 0, 0\right) d\epsilon_1 d\epsilon_2\,.\end{aligned}$$

The auto-correlation time is a steady-state property, which is reached for $t_1, t_2 \to \infty$. For $t_1 \to \infty$, it follows from (II.5) that $P\left(\epsilon_1,\, t_1|\, 0, 0\right) = \frac{1}{2\delta}$, thus in the steady state $\langle \epsilon_2(t_2)\epsilon_1(t_1)\rangle \approx C(t_2 - t_1)$. To determine the leading time dependence of the auto-correlation function, the case $(t_2 - t_1) \gg 1$ but finite is of interest. In this case, the leading time dependence of $P\left(\epsilon_2, t_2 - t_1|\epsilon_1, 0\right)$ is given by the sin-term with $n = 1$ in equation (II.5). This leads to

$$\begin{aligned}C(t_2 - t_1) &= \int_{-\delta}^{\delta}\int_{-\delta}^{\delta} \epsilon_2\epsilon_1 A_1(\epsilon_1) \sin\left(\frac{\pi\epsilon_2}{2\delta}\right) e^{-\frac{\pi^2\sigma^2(t_2-t_1)}{8\delta^2}} \frac{1}{2\delta} d\epsilon_1 d\epsilon_2 \\ &\propto \exp(-\frac{t_2 - t_1}{\tau})\,,\end{aligned}$$

with

$$\tau = \frac{8}{\pi^2}\frac{\delta^2}{\sigma^2}\,. \tag{II.7}$$

The integration over $A_1(\epsilon_1)$ does not lead to zero as $A_1(\epsilon)$ is an odd function (see (II.6)).

In two dimensions, the sampling of the x- and y-component of $\boldsymbol{\epsilon}$ are independent, thus leaving the exponential time dependence, in particular the form of τ, unchanged. The numerical confirmation of the theoretical result is shown in Fig. II.3.

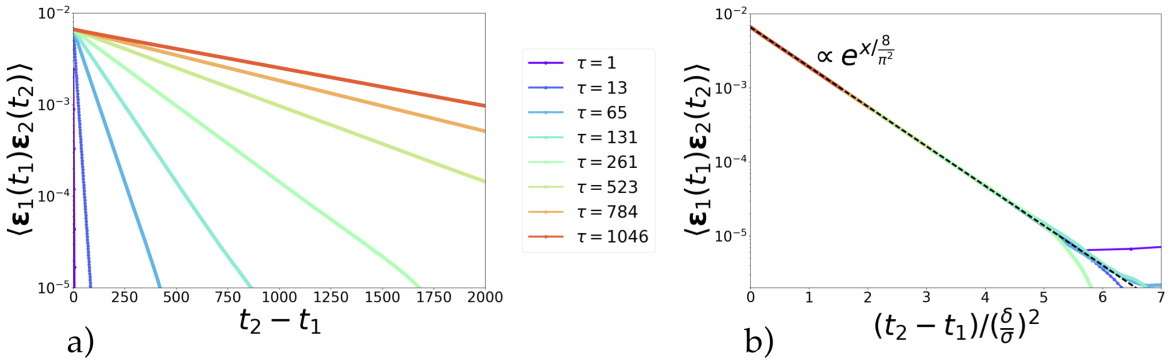


Figure II.3: **Displacement auto-correlation function in two dimensions for a set of different correlation times** τ. a) the exponential decay of the auto-correlation function is apparent. b) shows the scaling collapse of the data in a), confirming the analytic result for τ in (II.7). The data is for $\delta = 0.1$.

c) Persistence length of a single free particle movement in two dimensions

Another measure for the persistence is the average distance a particle moves persistently. This persistence length λ depends on the dimension. Here the two-dimensional case is considered.

The average absolute displacement of the particle is defined as

$$\langle r(t)\rangle = \left\langle \sqrt{(x_{t+t_0}-x_{t_0})^2+(y_{t+t_0}-y_{t_0})^2} \right\rangle .$$

The actual particle position is given by the integral $\int_0^t \boldsymbol{\epsilon}(s)ds$, thus writing the above equation in terms of the displacement $\boldsymbol{\epsilon}$ leads to

$$\langle r(t)\rangle = \left\langle \left\langle \sqrt{\left(\int_{t_0}^{t+t_0}\epsilon_x(s)\,ds\right)^2+\left(\int_{t_0}^{t+t_0}\epsilon_y(s)\,ds\right)^2} \right\rangle_{H(\epsilon_x,\epsilon_y)} \right\rangle_{\epsilon_x(t_0),\epsilon_y(t_0)} ,$$

where the ensemble average is decomposed into the average over the History $(H(\epsilon_x,\epsilon_y))$ and the average over the initial displacements $(\epsilon_x(t_0),\epsilon_y(t_0))$. In a time scale less than the auto-correlation time τ, the leading-order contribution comes from the initial values $(\epsilon_x(t_0),\epsilon_y(t_0))$

$$\langle r(t)\rangle = tv + \mathcal{O}(\sqrt{t}) ,$$

where

$$\begin{aligned} v &= \left\langle \sqrt{(\epsilon_x(t_0))^2+(\epsilon_y(t_0))^2} \right\rangle_{\epsilon_x(t_0),\epsilon_y(t_0)} \\ &= \int_{-\delta}^{\delta}\int_{-\delta}^{\delta}\sqrt{\epsilon_x(t_0)^2+\epsilon_y(t_0)^2}\,P(\epsilon_x(t_0))\,P(\epsilon_y(t_0))d\epsilon_x(t_0)d\epsilon_y(t_0) \\ &= \int_{-\delta}^{\delta}\int_{-\delta}^{\delta}\sqrt{\epsilon_x(t_0)^2+\epsilon_y(t_0)^2}\frac{1}{4\delta^2}d\epsilon_x(t_0)d\epsilon_y(t_0) \\ &= \frac{1}{3}\left(\sqrt{2}+\operatorname{arsinh}(1)\right)\delta . \end{aligned}$$

With $C(t)\sim e^{-t/\tau}=e^{-\langle r(t)\rangle/v\tau}=e^{-\langle r(t)\rangle/\lambda}$, the persistence length is[1]

$$\lambda = v\tau \approx 0.62\frac{\delta^3}{\sigma^2} , \tag{II.8}$$

and the auto-correlation function can be expressed in terms of $\langle r\rangle$. Using this definition of λ, Fig. II.4 shows the collapse of data for the displacment auto-correlation $C(\langle r\rangle=\lambda x)\propto \mathrm{e}^{-(x+c_1x^2+c_2x^3)}$ at widely different persistence lengths. The prefactors of the superexponential terms c_1, c_2 are obtained from a numerical fit.

The persistence length λ separates ballistic from diffusive motion in the single-particle case (see also section I.4, where this behavior was described for other active materials). This is shown in Fig. II.5 for a set of different λ. In Fig. II.5a, the particle motion becomes purely diffusive for $\lambda\to 0$ (see the $\sqrt{t}$ dependence for $\lambda=0.0$). For finite λ, the average particle motion is ballistic for τ steps covering a distance λ (see $\langle r(t)\rangle\propto t$ dependence), before transitioning into a diffusive motion. Rescaling the time units by τ and the spatial units by λ as in Fig. II.5b further confirms the theoretical analysis.

[1]The corresponding persistence length in one dimension is $\lambda = v_{1\mathrm{d}}\tau = \frac{1}{2}\delta\tau = \frac{4}{\pi^2}\frac{\delta^3}{\sigma^2}$.

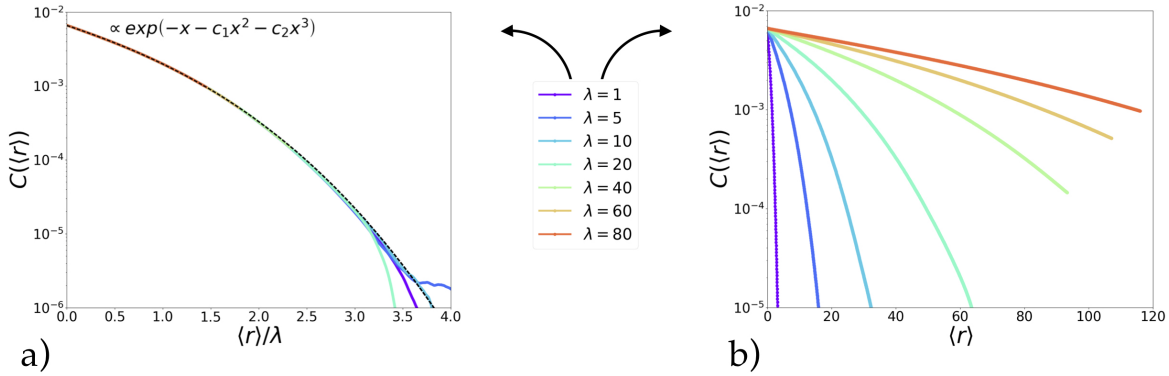


Figure II.4: **Auto-correlation of proposed displacements as a function of the covered distance for a single two-dimensional self-propelled particle for different values of λ.** a) shows the scaling collapse of the raw data in b) confirming the theoretical result of the correlation length in (II.8). The data is for $\delta = 0.1$. [201]

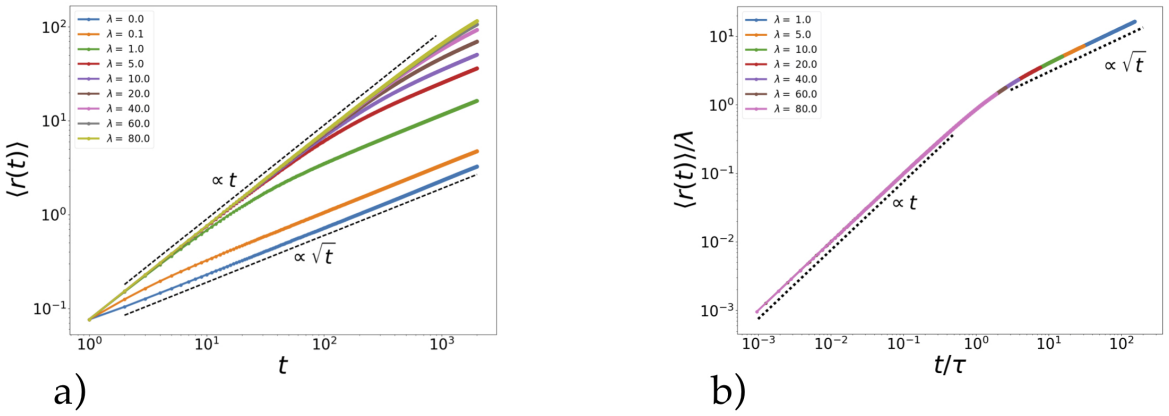


Figure II.5: **Time dependence of the average absolute displacement $\langle r(t) \rangle$ for a range of different λ.** a) shows the transition from diffusive motion ($\propto t^{1/2}$) for $\lambda \to 0$ to a motion composed of a ballistic component ($\propto t$) for $t < \tau$ and a diffusive component for $t > \tau$. b) Rescaling the time and spatial units by τ and λ respectively confirms the theoretical identification of the correlation time and length. The data is for $\delta = 0.1$.

II.2 One-dimensional results of the kinetic Monte Carlo algorithm

II.2.1 A single self-propelled trapped particle

The behavior of a self-propelled (persistently moving) point particle, trapped in a potential, is the simplest starting point to understand how persistent motion changes the steady-state properties in Monte Carlo. The point particle is confined in a potential of the form

$$U(x) = u_0\left(\left(\frac{\gamma}{L+x}\right)^n + \left(\frac{\gamma}{L-x}\right)^n\right), \tag{II.9}$$

with e.g. $n = 6$ (see Fig. II.6a). This potential is purely repulsive. If δ, the maximum jump length, is chosen appropriate, the particle is confined on the interval $[-L, L]$. In the passive $\lambda \to 0$ limit, the steady-state probability distribution of the particle position must follow $P(x) \propto \exp(-\beta U(x))$ (β is the inverse temperature in equilibrium), as shown in Fig. II.6b. This probability distribution has a maximum at $x = 0$ and decays to zero when moving closer to the potential walls. Increasing the persistence changes this behavior drastically. Fig. II.6b shows that the effect of small λ is to widen the passive probability distribution. When overcoming a certain threshold, $P(x)$ starts to from a double peak, with the peak positions shifting closer to the walls with increasing λ. With other words, persistent motion leads to an effective attraction to the purely repulsive walls. It is possible to reproduce the probability distributions in Fig. II.6b with an equilibrium model, by choosing appropriate attractive potentials for each λ.

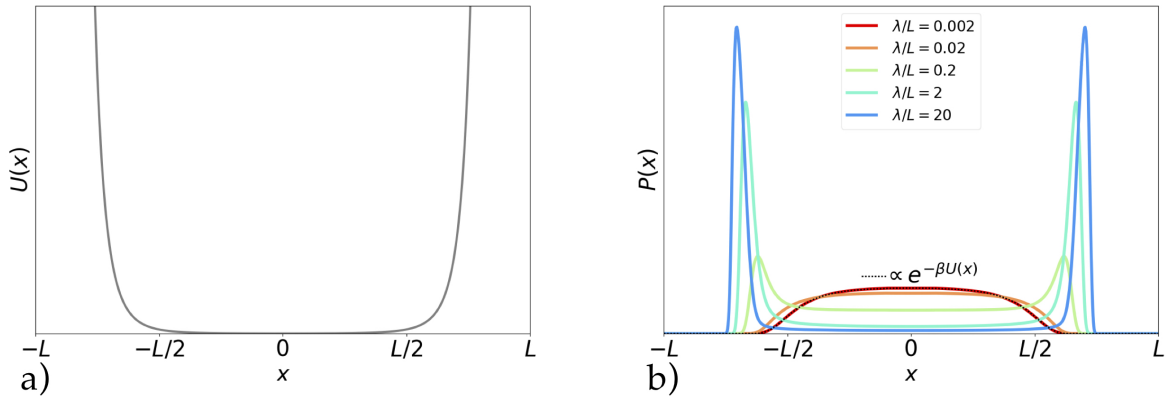


Figure II.6: **Effect of persistent motion for a point particle confined in a potential.** a) shows the confining potential $U(r)$ as in (II.9). b) shows the probability distribution of the particle position for a set of different persistent lengths λ. For small λ, the passive case $P(x) \propto \exp(-\beta U(x))$ is recovered. Increasing λ leads to the formation of a bimodal distribution. The peak positions shift closer to the wall with increasing λ. In the simulations, the λ is varied by changing σ, while keeping δ constant.

In this model, the non-equilibrium character of the steady state becomes visible only when the ϵ-space is taken into account as mentioned in subsection I.2.3. Fig. II.7 shows the joint steady-state probability $P(x, \epsilon)$. If the particles is at position x, then ϵ is the displacement which leads to the new configuration ($x \xrightarrow{\epsilon} x'$).

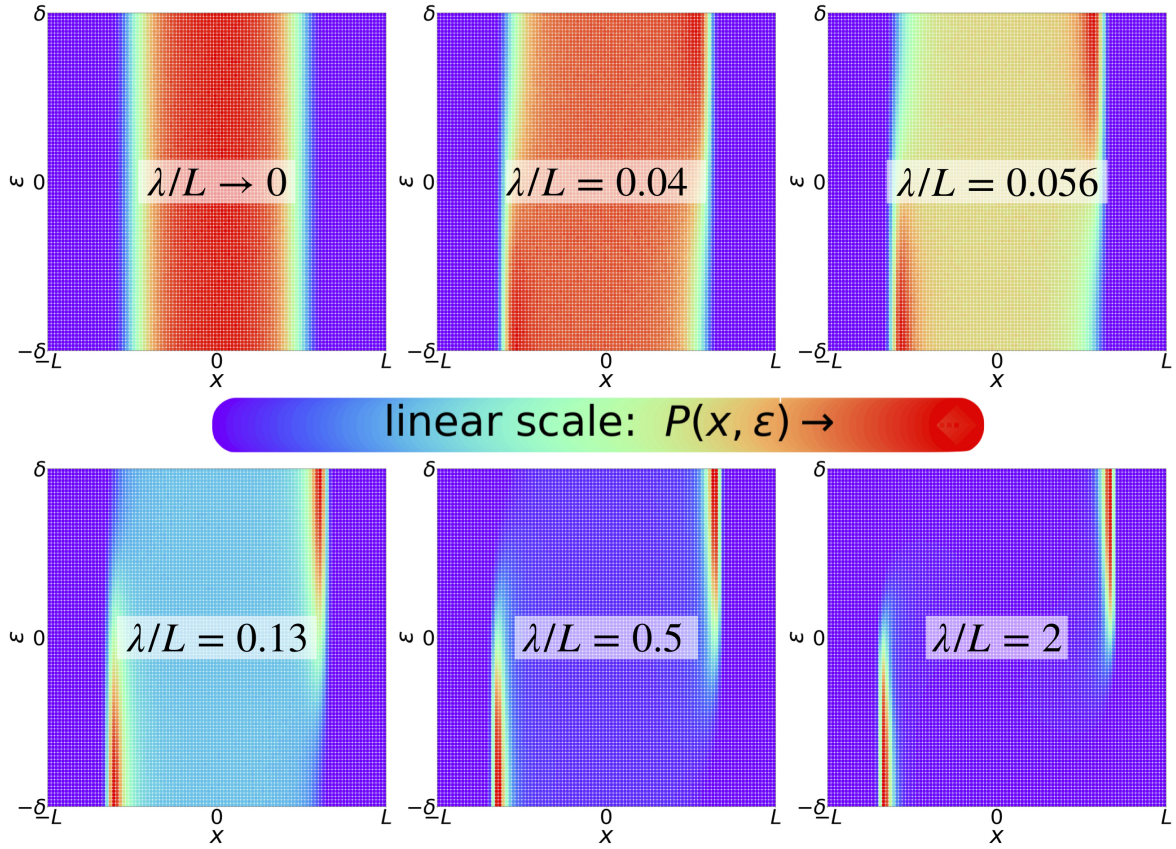


Figure II.7: **Non-equilibrium steady-state probability of a confined self-propelled particle.** Shown are two-dimensional histograms of the joint steady-state probability $P(x, \epsilon)$ for a confined self-propelled point particle in a repulsive potential (II.9). Here ϵ is the displacement leading to a new configuration $x \xrightarrow{\epsilon} x'$. Again, λ is varied by changing σ, and keeping δ constant.

For $\lambda \to 0$, $P(x, \epsilon)$ does not depend on ϵ (or equivalently the proposed move does not depend on x) as required for equilibrium. For finite λ/L, this is not the case anymore. For small λ/L, the distribution $P(x, \epsilon)$ develops an asymmetry with a tendency that larger positive ϵ are more likely at the $+L$ potential wall. Large negative ϵ, on the other hand, are more likely to be found at the potential wall at $-L$. As the ϵ dynamics is purely diffusive, the gradient in ϵ-direction clearly indicates a non-zero probability current in the vertical direction[2]. The probability current in ϵ-direction imposes a current in x-direction. As the probability must be conserved, the total current must form a loop on the ϵ-x-space.

The asymmetry grows with increasing λ/L, leading to a state where positive (negative) ϵ can almost only be found at the $+L$ ($-L$) potential wall. However, the peaks (*e.g.* at $\lambda/L = 2$) cross $\epsilon = 0$ and the tip of the peaks consists of a light shadows, which bent towards the center ($x = 0$). This indicates that the particle travels between the walls (a necessary feature for the steady state). However, at high persistence, the particle departs

[2]To see a gradient in x-direction is not sufficient to indicate a non-vanishing probability current as the particle dynamics is not purely diffusive due to the interaction of the particle with the potential controlled by the Metropolis filter.

from a wall with small ϵ pointing in the direction of the opposite wall only.

This example illustrates clearly that a non-equilibrium steady state is not always easily distinguishable from an equilibrium steady state. The particle current vanishes in this example and the non-vanishing probability current can be identified in the position-velocity phase-space only.

II.2.2 Two self-propelled particles on a ring

The model of two self-propelled particles on a ring reveals another interesting phenomena of persistence, leading to a probability distribution $P(r)$ (with r being the distance between the two particles) that cannot be easily reproduced with an effective equilibrium attraction. As shown in Fig. II.8, the model consists of two interacting particles on a ring with perimeter L. The pair potential is chosen as

$$U(r) = u_0 \left(\frac{\gamma}{r}\right)^n, \tag{II.10}$$

with $n = 6$ and r being the inter-particle distance.

As shown in Fig. II.8c the system recovers the passive dynamics for small λ (bright red curve), with uncorrelated successive displacements of individual particles, which results in the equilibrium probability distribution of the inter-particle distance $P(r) \propto \exp(\beta U(r))$, with a maximum at $L/2$ and vanishing probability for small r. This behavior changes drastically for finite λ. In this case the system can be in two states: 1) the two particles are moving persistently in opposite direction (see Fig. II.8a) and 2) the two particles are moving persistently in the same direction (see Fig. II.8b). The first state results in the same behavior, as described in the previous subsection II.2.1 for the single-particle case; the two particles stay close to each other and the mean inter-particle distance decreases with increasing λ. This effect of persistence might be described by an effective attraction. However, the second state of the self-propelled two-particle system cannot be easily captured under an effective equilibrium description. The second state in Fig. II.8b consists of a hunting situation, where the displacement vectors of both particles have the same sign, though not the same norm. Because the sampling of ϵ_1 and ϵ_2 is independent, one of the particles is always faster than the other one and thus plays the role of the hunter, whereas the slower particle is the hunted one. Moves of the hunted particle are always accepted, as they lead to an increase in r and thus decreasing the total energy, whereas the moves of the hunting particle increase the total energy and have thus a finite rejection probability. On average, each of the two particles tries to move in every alternate Monte Carlo step. The resulting competition, where the slower particle increases r in every attempt, and the faster particle tries to decreases r, but does not succeed in every attempt, leads to an average "hunting distance", which is independent of λ. This "hunting distance" is highlighted in Fig. II.8c with a black dashed line. The hunting phenomena is clearly detectable in $P(r)$ only at relatively large λ, as it requires not only $\mathrm{sgn}(\epsilon_1) = \mathrm{sgn}(\epsilon_2)$ but also a finite time in which the order $|\epsilon_i| > |\epsilon_j|$ $(j \neq i)$ does not reverse between the two particles. This is only given if the change between successive ϵ_i is small. This is the case if $\sigma \ll \delta$ which equivalently means large λ.

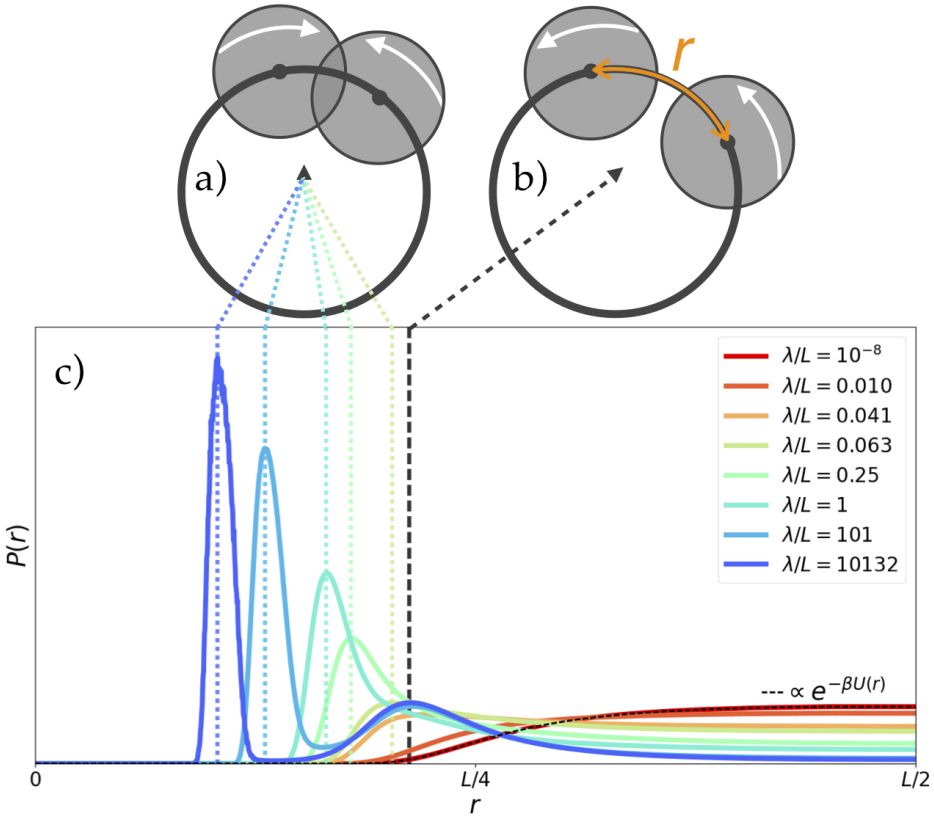


Figure II.8: **Effect of persistent motion for two particles on a ring.** a) and b) show the two possible states of the system. The white arrows indicate the sign of ϵ_i, thus the direction of the persistent motion. c) shows the probability of the inter-particle distance for a range of different λ indicated in the legend. The inter-particle distance r is the shortest distance between the two particles on the ring (see b), thus the x-range in c) is truncated at $L/2$. The maximum jump length δ is kept constant and was chosen such that the two particles cannot jump over each other. λ is varied by changing σ.

In conclusion, the two possible states shown in Fig. II.8a and b fully explain the behavior of $P(r)$ in Fig. II.8c. A small but finite persistence leads first to a widening of the equilibrium distribution function. Further increasing λ leads to the formation of a dominant peak at small inter-particle distances, with the peak position shifting to smaller r with increasing λ (state 1 shown in Fig. II.8a). An even further increase leads to a second sub-dominant peak at constant r (state 2 shown in Fig. II.8b).

In this two-particle model, it is simple to demonstrate the loss of time reversibility within the persistent kinetic Monte Carlo. Following the discussion in subsection I.2.3, time reversibility demands that the probability of a trajectory and its time reversal are the same. To construct the argument it is sufficient to consider hard disks and that the hunting and the hunted particle have fixed jump lengths with ϵ_1 and ϵ_2, respectively. A typical trajectory is sketched in Fig. II.9a where the hunted particle always moves, whereas the hunting particle moves only when the inter-particle distance is larger than ϵ_1. In the time-reversed trajectory (see in Fig. II.9b) the role of hunted and hunting particle exchanges. Clearly, the now hunted particle does not move at certain time steps in spite of the available empty space in its front. However, the probability for that to happen is zero because the acceptance rate is

strictly one for the hunted particle. This shows that the probability of this trajectory and its time-reversed trajectory are not equal and therefore break time-reversal symmetry.

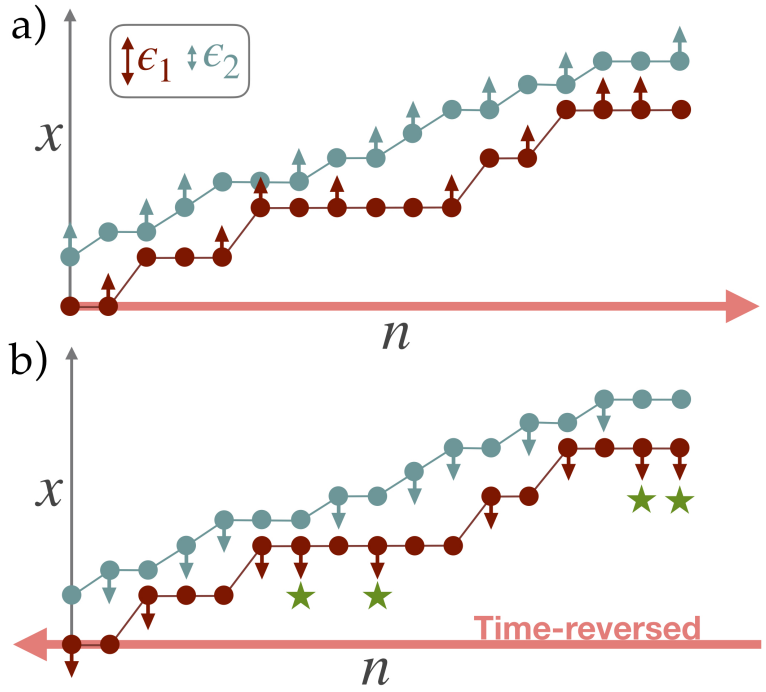


Figure II.9: **Breaking time-reversal symmetry.** a) shows a possible path of two hard disks in one dimension with fixed jump lengths ϵ_1 and ϵ_2. In each time step, one of the particles tries to move, which is indicated by the arrows. The proposed moves of the hunted particle with ϵ_2, are always accepted, as its moves cannot lead to overlaps. The moves of the hunting particle are rejected if the move would lead to an overlap, and thus the particle does not always changes its position after an attempted move. b) shows the same path in time reversal. The green stars indicate events which have zero probability to happen. In consequence, the whole time-reversed path has zero probability to occur.

II.2.3 Collective many-particle behavior on a ring

This subsection II.2.3 discusses the collective behavior of a system of N interacting particles on a ring of perimeter L. The particles again interact via the power-law potential in (II.10). The result is shown in Fig. II.10 for different persistent lengths λ. Here, λ is indicated in units of d, the mean global inter-particle distance defined as $d = L/N$.

The left column of Fig. II.10 shows that the passive limit ($\lambda/d = 10^{-8}$) preserves a homogeneous particle distribution throughout the whole simulation. Increasing λ leads to the formation of density inhomogeneities, which become more stable with increasing λ. Within this thesis, a macroscopic phase separation into one dense cluster, surrounded by a dilute phase could not be observed in one dimension. The observed clusters, *e.g.* at $\lambda/d = 128$, do not merge into one big cluster, they rather form, merge, break apart and dissolve throughout the simulation. However, they are an example of motility-induced phase separation [80] in one dimension as discussed in paragraph b) in subsection I.4.1.

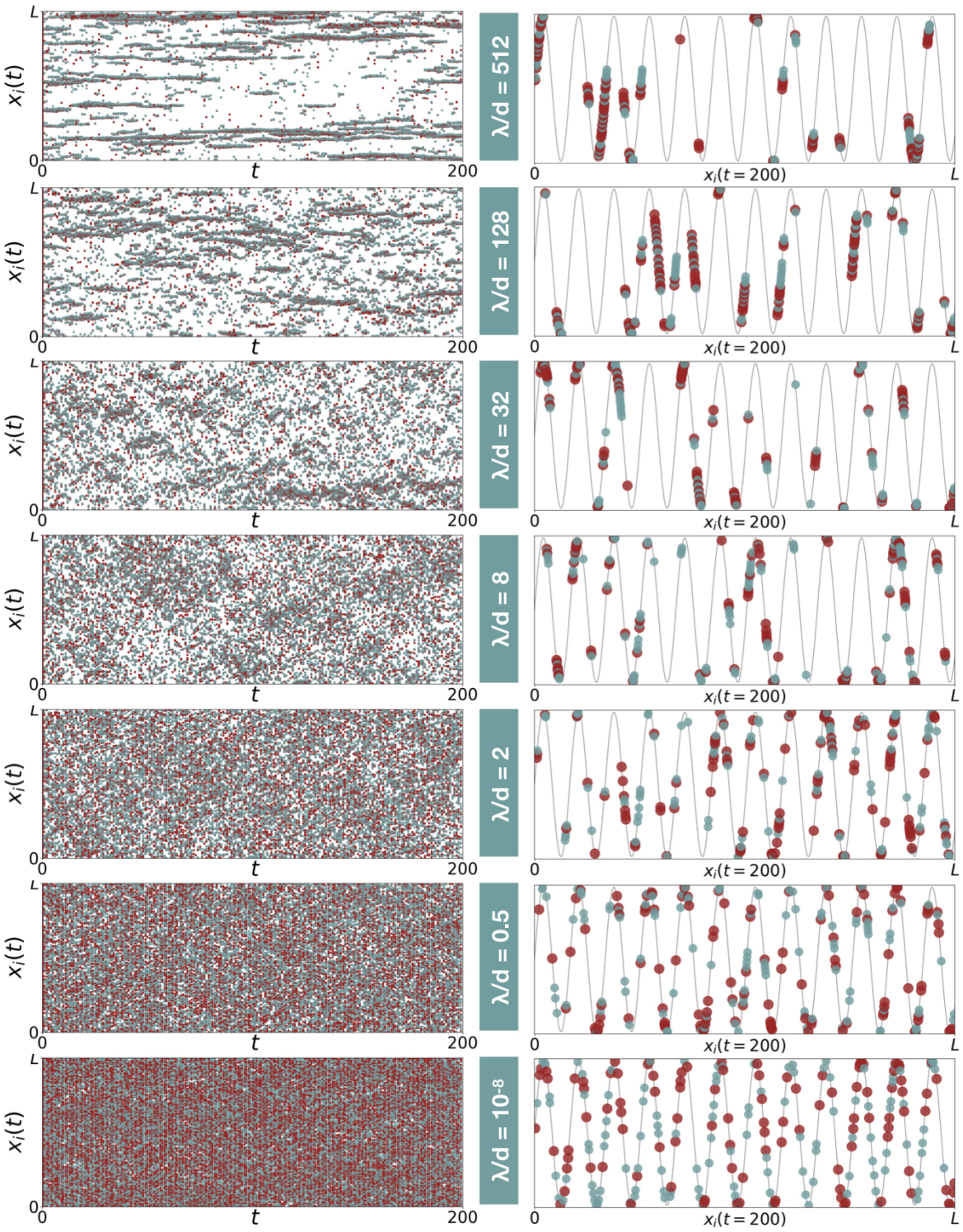


Figure II.10: **Collective behavior of self-propelled/persistent particles on a one-dimensional ring.** The left column shows the time evolution of the position of each particle, starting at $t = 0$ from an equidistant particle distribution. Particles with $\epsilon_i(t) > 0$ are red, particles with $\epsilon_i(t) < 0$ are blue. The right column shows the corresponding exemplary particle configuration at $t = 200$ (for a clear presentation, particle positions were plotted on a $\sin$-function). The persistence length λ increases from the bottom to the top and is given in units of the mean global inter-particle distance $d = L/N$. (One time unit are $\approx 8.9 \cdot 10^4$ Monte Carlo sweeps, with each sweep containing $N = 224$ Monte Carlo steps. Keeping δ fixed, the persistence was varied with σ.)

The origin of the cluster formation in a system with purely repulsive particle interactions (compare potential in (II.10)) can be understood by the right column of Fig. II.10, together with the phenomena discussed in the two previous subsections II.2.1 and II.2.2. The right column of Fig. II.10 shows exemplary particle configurations at $t = 200$, where particles with $\epsilon_i(t) > 0$ are colored in red and particles with $\epsilon_i(t) < 0$ are blue. At high persistence, a cluster is held together by precisely one particle at the small x end of the cluster with $\epsilon_i(t) > 0$ and one particle at the large x end with $\epsilon_i(t) < 0$. Particles within a cluster (between this two border particles) may alternate in their direction of motion (fighting state in subsection II.2.2) or they may try to move in the same direction (hunting state in subsection II.2.2). One possibility for a cluster to change is when the ϵ of one of the border particles decorrelates in the direction with the result that it moves away from the cluster, which allows the new surface particle to equally leave the cluster if its ϵ points away from the cluster. Therefore, an escaping surface particle may be followed by one or more particles from the cluster interior, as described in paragraph b) in subsection I.4.1 in the context of the kinetic approach to explain motility-induced phase separation in active Brownian particle systems. In further agreement to the kinetic approach, a cluster grows if a particle from the gas phase hits the cluster. However, the approach assumed that the particles inside the cluster do not move thus it does not offer an explanation for a cluster breaking apart into two clusters *etc.*.

The one-dimensional case illustrates persistence in the kinetic Monte Carlo dynamics. Simple examples were presented to demonstrate the non-equilibrium character of the dynamics due to the introduction of Probability currents (subsection II.2.1) and the loss of time-reversal symmetry (subsection II.2.2). The last example of many persistent interacting particles on a one-dimensional ring introduced the much-discussed non-equilibrium phenomenon in active systems, the motility-induced phase separation (MIPS) and revealed its origin within the kinetic Monte Carlo dynamics. The non-equilibrium mechanism leading to the formation of dense clusters (in a system of particles with purely repulsive pair-wise interactions) stays the same in higher dimensions, though the quantitative picture changes, which is discussed in the following section II.3.

II.3 Collective behavior in two dimensions

In this section II.3, the main results of this thesis are presented. First, the two-dimensional ensemble is specified in subsection II.3.1. Subsection II.3.2 presents motility-induced phase separation (MIPS) within the two-dimensional kinetic Monte Carlo dynamics as macroscopic phase separation. Based on numerical observations, the phase properties are specified, including the precise order of the two coexisting phases. The MIPS region is then located in a density-persistence phase diagram. Subsection II.3.3 focuses on the high-density limit. Being provided with the equilibrium melting densities [13], the departure from equilibrium is studied at small persistence lengths. Then, it is first shown that small persistence does not destroy the two-step melting scenario described in section I.7 and evidence for a non-equilibrium hexatic phase is provided using standard tools. The validity of this picture is extended to densities and persistence far from the equilibrium melting transitions. Subsection II.3.4 presents the phenomenon of MIPS and the two-step melting in a full quantitative phase diagram. It discusses that MIPS and the order-disorder transitions are two separated phenomena. The influence of the particle stiffness on the phase diagram is dis-

cussed at the end of this subsection II.3.4. Furthermore, subsection II.3.5 is dedicated to a combined discussion on the effect of the maximum jump length δ and the stiffness of the inter-particle potential on MIPS within the kinetic Monte Carlo dynamics. The last subsection II.3.6 presents evidence that the anisotropic effects introduced by the square-shaped ϵ-space (in the two-dimensional version of the kinetic Monte Carlo dynamics) do not influence the presented results.

II.3.1 Ensemble specification

The collective behavior of two- dimensional self-propelled/persistent particles is studied in an ensemble of N interacting point particles in a rectangular box with periodic boundary conditions. The particles interact via the repulsive power-law pair potential of (II.10), where the intensity parameter γ reduces to the particle diameter in the hard-disk limit $n \to \infty$. The dimensionless density

$$\phi = \gamma^2 N/V \qquad \text{(II.11)}$$

is varied by changing the volume V of the simulation box, while keeping the number of particles N and the intensity parameter γ fixed. In order to allow for crystallization into a hexagonal packing without defects, the aspect ratio of the periodic box is chosen as $(7 : 4\sqrt{3})$, together with the number of particles as $N = 7\nu \times 8\nu$, with $\nu \in \mathbb{N}$ as in [13]. This choice is to ensure that the two hexagonal orientations shown in Fig. II.11 have almost the same lattice unite vector, thus making the potential energy almost the same and thereby also making both orientations almost equally probable. An alternative choice was made in [12], where an exact square box assured that the two possible arrangements in Fig. II.11 were equally likely.

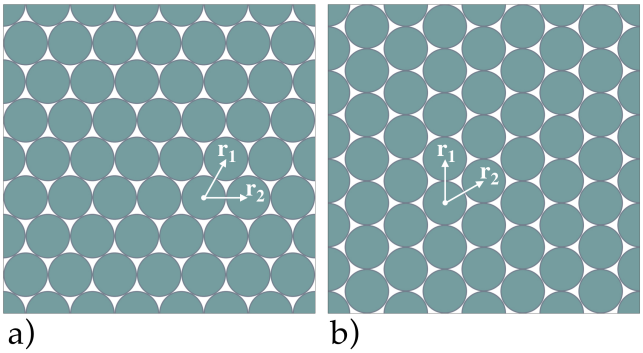


Figure II.11: **Illustration of the boundary conditions.** The number of particles is $N = 56$ and the aspect ratio of the periodic box is $(7 : 4\sqrt{3}) = 1.01036$. a) Perfect hexagonal packing with $|\boldsymbol{r}_1| = |\boldsymbol{r}_2|$. b) Rotating the orientation in a) by $90°$ leads to a packing with $|\boldsymbol{r}_2| = 1.0157|\boldsymbol{r}_1|$.

If not mentioned differently, the data presented in the following is for $\gamma = 1$, $u_0 = 1$, $n = 6$, $\beta = 1$, where γ also serves as the spatial unit length scale, thus the simulations are performed in the (N, V, T) ensemble. The consequences of this particular choice of n in the pair potential (II.10) is discussed later in the subsections II.3.4 and II.3.5. The soft-sphere potential (II.10) is furthermore truncated as [13]

$$\tilde{U}(r) = U(\min[r, r_c = 1.8]) \,,$$

thus the scaling behavior of the algorithm can be reduced from $\mathcal{O}(N)$ to $\mathcal{O}(1)$. This makes it possible to reach the steady state for system sizes large enough to allow for predictions in the thermodynamic limit. For details see section A.2.

II.3.2 Motility-induced phase separation

In one dimension, the effect of persistent motion is restricted to the formation of microscopic density inhomogeneities (see subsection II.2.3 and also subsection I.4.1) and does not lead to a macroscopic phase separation between two homogeneous phases. In contrast, the two-dimensional case shows a more complex behavior. In a certain parameter range of the density ϕ and the persistence length λ, the kinetic Monte Carlo dynamics leads to such a macroscopic phase separation into a dense cluster surrounded by a dilute gas phase, see Fig. II.12. (Information about the simulation run time and details about ensemble averages in the following figures can be found in the appendix A.14.)

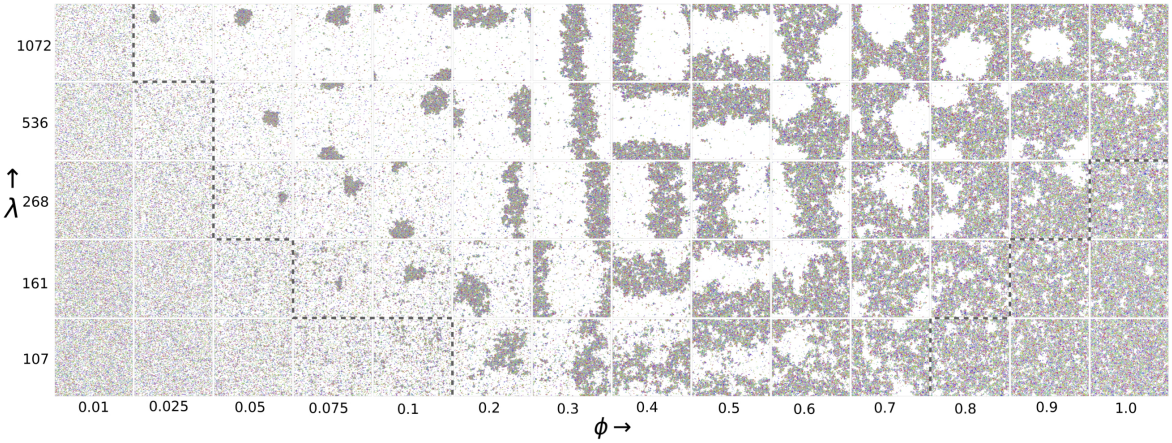


Figure II.12: **MIPS in two dimensions.** Configuration snapshots of a $N = 10976$ particle system in the density-persistence parameter space. The dashed lines indicate the visual boundary of MIPS. For a clear presentation, particles are plotted in arbitrary sizes, which is constant at fixed density. The non-evident but existing color code for particles is explained later (in electronic version, please zoom). Data corresponds to $\delta = 0.7$. [201]

The configuration snapshots in Fig. II.12 illustrate MIPS within the persistent kinetic Monte Carlo dynamics. Fig. II.13 shows that the mechanism leading to MIPS in two dimensions has the same origin as discussed in the one-dimensional many-particle case (see subsection II.2.3). Particles may get kinetically arrested by other particles, as shown in the zoom in Fig. II.13b. The particles in the bulk of the dense cluster are walled in by particles which try to move persistently towards the cluster. Along the border of the agglomeration in Fig. II.13b, almost all displacement vectors point inside the bulk, whereas the distribution of the displacement vectors is uncorrelated inside the bulk (similar mechanisms are also observed in experiments [18]).

Starting from an initially homogeneous distribution of particles, the minimal condition for the formation of small particle agglomerations due to kinetic arrest is a persistence length λ, which is larger than the mean free path ℓ between particles. In a homogeneous system ℓ increases with decreasing density ϕ and thus the formation of particle agglomerations requires larger λ. This simple argument offers access to understand why small ϕ require larger λ to induce phase separation (see Fig. II.12). However, a better understanding of the shape of the phase boundary of MIPS indicated in Fig. II.12 comes from the investigation of local densities. For this, two directions are chosen: 1) the vertical direction in

Fig. II.12, means λ varies as ϕ is kept constant, and 2) the horizontal direction in Fig. II.12, where ϕ is varied while λ is kept constant.

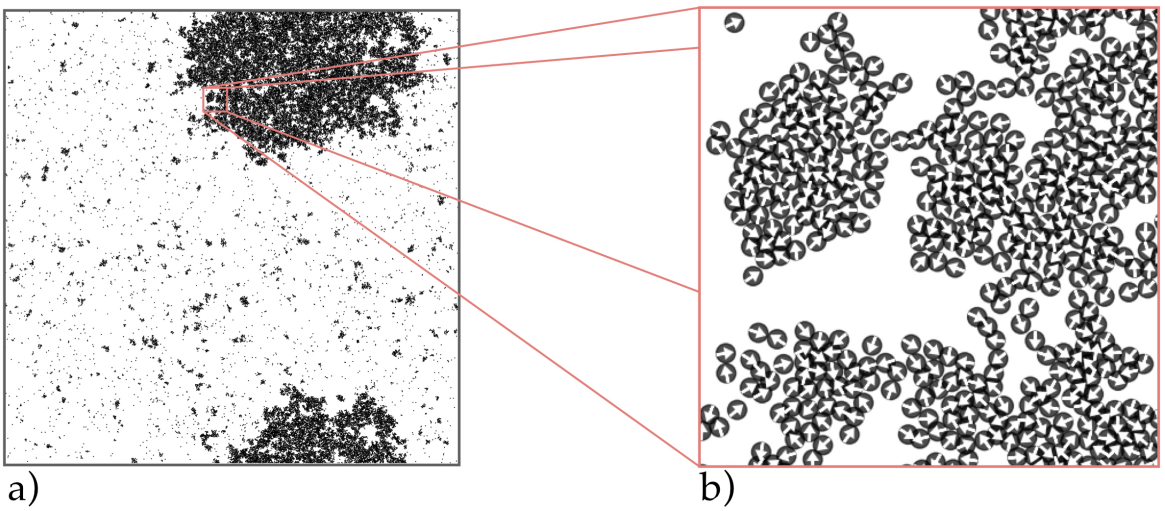


Figure II.13: **MIPS as result of kinetic arrest.** a) Configuration snapshot of a $N = 43904$ particle system at $\phi = 0.2$ and $\lambda = 214$. b) Zoom at a section of the interface between the coexisting phases in a). The arrows indicate the displacement vectors $\boldsymbol{\epsilon}_i(t)$ of each particle at the time of the snapshot. Data corresponds to $\delta = 0.7$. [201]

Vertical direction (ϕ = const.): Choosing any density ϕ within the MIPS region in Fig. II.12, the number of particles per area unit within the gas phase decreases when λ increases (*e.g.* compare configurations at $\lambda = 161$ and at $\lambda = 1072$ for $\phi = 0.1$). At the same time, the clusters at $\lambda = 107$ visually look less compact than the corresponding cluster at *e.g.* $\lambda = 1072$ at the same ϕ. Thus the configuration snapshots indicate that the local density of the cluster increases with λ, whereas the gas density decreases.

A quantitative picture is gained by the measurements of local densities. This is done by covering a configuration with randomly placed test circles of a certain radius. The local dimensionless density of the test circles is

$$\phi_{\mathrm{loc}} = \gamma^2 N_{\mathrm{loc}}/V_{\mathrm{loc}}\,,$$

where N_{loc} is the number of particle centers located within a circle of area V_{loc}. V_{loc} must be chosen large enough such that the test circles in the dilute gas phase contain a sufficient number

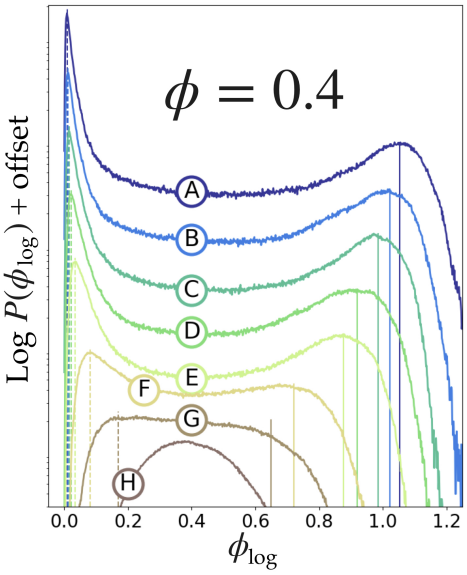


Figure II.14: **Local-density histogram for MIPS.** Histograms of local densities for a variation of persistence lengths at constant $\phi = 0.4$ (A: $\lambda = 450$; B: $\lambda = 359$; C: $\lambda = 268$; D: $\lambda = 214$; E: $\lambda = 161$; F: $\lambda = 107$; G: $\lambda = 80$; H: $\lambda = 54$). The histograms are shifted along the y-axis with increasing λ for a better presentation. Data is for $\delta = 0.7$. [201]

of particles and at the same time small enough to reduce the influence of the interface on the measurement. The presented data results from a test circle of radius 7.5.

The resulting histograms of the local density for a range of different λ at $\phi = 0.4$ are shown in Fig. II.14. At λ below the onset of MIPS (point H), the local-density distribution has a single peak at ϕ. Increasing λ leads to the formation of a bimodal distribution, with the peak position at small ϕ_{loc} corresponding to the density of the dilute gas phase ϕ_{Gas} in the coexistence, whereas the peak at high ϕ_{loc} indicates the density of the cluster ϕ_{Cluster}. The separation between the peaks increases with λ in a way that the cluster gets denser with increasing λ, while the gas phase becomes more dilute (see Fig. II.12 for an illustration).

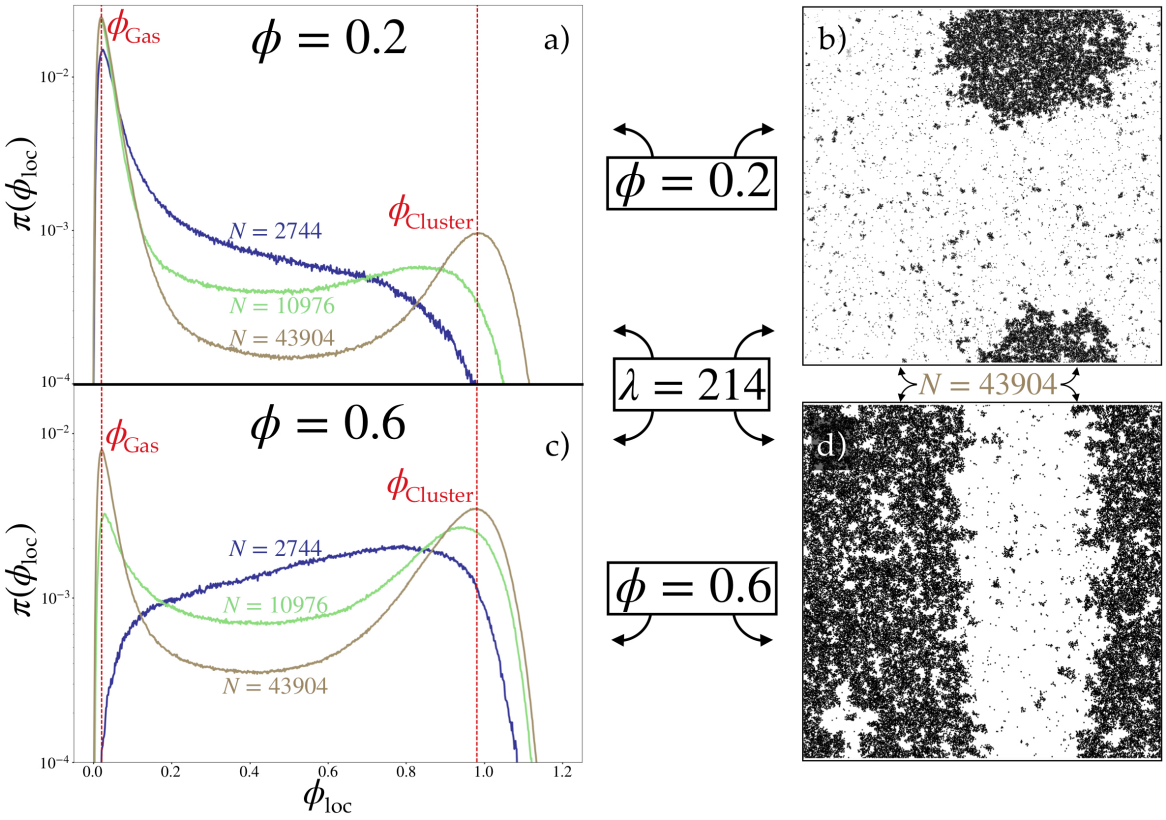


Figure II.15: **Finite-size scaling of local-density histograms.** a) and c) show the local-density histograms for different system sizes (indicated in the plots) for the global densities $\phi = 0.2$ and $\phi = 0.6$ at $\lambda = 214$ (identical x-axis used). b) and d) show the corresponding configuration snapshots for $N = 43904$. Data is for $\delta = 0.7$. [201]

Horizontal direction (λ = const.): Choosing any fixed λ in Fig. II.12 and moving from small to high densities, the system enters into the MIPS region with an approximate circular dense cluster surrounded by the gas phase. This cluster grows with increasing ϕ and also changes its form to a stripe that winds around the periodic boundary condition. At a certain ϕ the dense cluster becomes the majority phase and the gas phase exists as a bubble within the dense cluster. Increasing the density further leads to a shrinking of the gas bubble until it eventually disappears, resulting in a macroscopic homogeneous density distribution. A comparable behavior can be observed in equilibrium coexistence phases of finite (N, V, T)

ensembles, where this complex behavior is caused by the interface free energy [202, 203].

Furthermore, while crossing the coexistence region along an isotherm in an (N, V, T) ensemble, *e.g.* in the Van-der-Waals gas, the volume fractions of the coexisting liquid and gas adapt to the global density, while their local densities remain unchanged. The coexisting phases in the MIPS show the same behavior: for constant λ the positions of the two peaks in the local-density histogram are independent of the global density ϕ, which is shown in Fig. II.15. The local-density histograms are measured at constant λ, but for two different ϕ, thus the role of the minority and majority phase (by area fraction) is inverted (see Fig. II.15b and d). This inversion is reflected in the height of the corresponding peaks in Fig. II.15a and c, but it leaves the peak positions unchanged when approaching the thermodynamic limit.

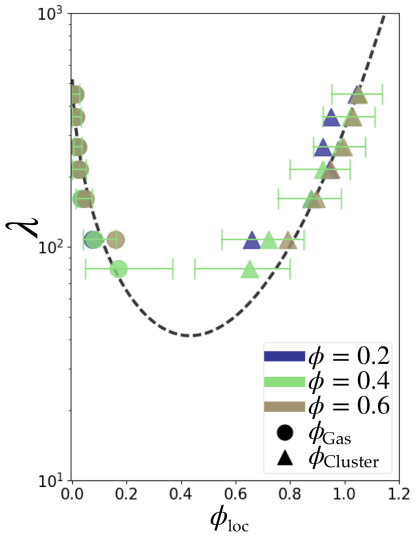


Figure II.16: **U-shaped boundary of MIPS.** Densities of the coexisting cluster and gas, identified through the peak positions as in Fig. II.14 for three wildly different global densities. Exemplifying error bars are plotted for $\phi = 0.4$ only, which were obtained from the width of the corresponding peak in Fig. II.14. Data is for $N = 10976$ and $\delta = 0.7$. [201]

In conclusion, the high-density boundary of the MIPS region is determined by $\phi = \phi_{\text{Cluster}}$, whereas the low-density boundary is determined by $\phi = \phi_{\text{Gas}}$. As described before in Fig. II.14, both, ϕ_{Cluster} and ϕ_{Gas}, are functions of λ. This λ-dependence is shown in Fig. II.16 and suggest an approximate U-shaped phase boundary of the MIPS region, which is in agreement with the configuration snapshots in Fig. II.12.

Nature of coexisting phases: It remains to identify the nature of the two coexisting phases in the MIPS region. While the dilute phase can be identified as disordered gas from the presented configuration snapshots (Fig. II.12, Fig. II.13, Fig. II.15), a classification of the cluster phase, requires a quantitative characterization of the precise degree of order. As described in subsection I.7.1, a possible manifestation of spatial order in two dimensions is the orientational order which quantifies the spatial correlation of the local sixfold orientational order. Fig. II.17 illustrates three different orientations of the local sixfold order, which can be quantified by the local bond-orientational order parameter (first defined in (I.26))

$$\psi_6(\boldsymbol{r}_i) = \frac{1}{\text{number of neighbors } j \text{ of } i} \sum_j \exp(6\mathrm{i}\theta_{ij}) \,,$$

with i being the imaginary unit and θ_{ij} is the angle enclosed by the x-axis and the connection line between particle i and its neighbor j. As described in subsection I.7.1, the Voronoi construction allows for the identification of the nearest neighbors of a particle. The construction of one Voronoi cell is illustrated in Fig. II.17b, whereas Fig. I.17 demonstrates the Voronoi construction on a perfect lattice. Particles are defined as neighbors if their Voronoi cells share an edge.

The neighbor definition by the Voronoi construction is not unique. An alternative is to define particles as neighbors if their inter-particle distance is smaller than a certain value.

It has been shown [204] that the choice of the neighborhood definition can influence the numerical values of $\psi_6(\boldsymbol{r}_i)$ and their trends. A robust result can be achieved by calculating the bond-orientational order parameter $\psi_6(\boldsymbol{r}_i)$ with Voronoi weights as described in [204]. The basic idea is to weight each bond ij by the length of the associated Voronoi edge (see Fig. II.17b). All here presented data involving $\psi_6(\boldsymbol{r}_i)$ is calculated following this weighted approach described in [204].

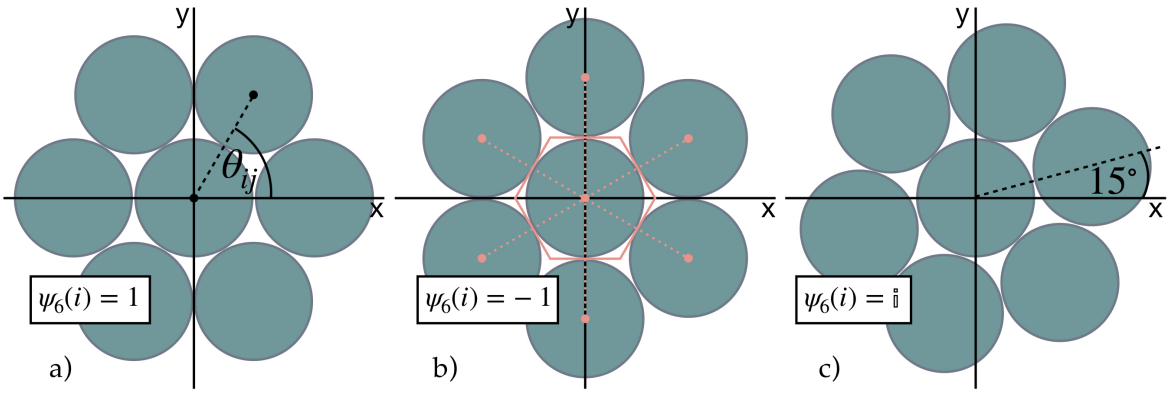


Figure II.17: **Illustration of local sixfold order.** Shown are three examples of the local sixfold orientation, with particle i positioned in the center. b) shows the Voronoi cell (bold orange hexagon) for the center particle.

In a N-particle system, the function

$$g_6(r) \propto \left\langle \sum_{i,j}^{N} \psi_6^{\star}(\boldsymbol{r}_i)\psi_6(\boldsymbol{r}_j)\boldsymbol{\delta}(r - r_{ij}) \right\rangle \tag{II.12}$$

(with $\boldsymbol{\delta}(x)$ being the Dirac delta function) is a measure of the correlation of the local sixfold orientational order at distance r. As already mentioned in the introduction subsection I.7.4, an exponential decay of $g_6(r)$ corresponds to short-range orientational order, an algebraic decay of $g_6(r)$ to orientational quasi-long-range order and a constant $g_6(r)$ to long-range orientational order. An exponential decay in $g_6(r)$ restricts also the pair-correlation function to an exponential decay. This is because positional order cannot exist in absence of orientational order. Therefore, the identification of an exponential decay in $g_6(r)$ unambiguously identifies a disordered fluid phase, characterized by a short-ranged orientational order and a short-ranged positional order.

Spatial correlation functions, such as $g_6(r)$, cannot be defined within coexistence regions. However, one illustrative way to analyze the orientational order within the MIPS region is shown in Fig. II.18. The figure shows configuration snapshots with each particle color-coded according to its local bond-orientational order parameter ψ_6. The color-coded snapshots illustrate the short-ranged orientational order within the cluster phase, thus MIPS can be identified here as **liquid-gas coexistence**. Particles in Fig. II.12 are plotted with the same color code. However, the snapshots may appear gray, due to the extremely short-ranged orientational correlations within the whole presented parameter range.

Further evidence for the fluid (spatially disordered) nature of the cluster phase, can be obtained from the decay of $g_6(r)$ in the homogeneous configurations at the outer boundary of the MIPS region. For the sake of completeness, a plot of $g_6(r)$ at $\phi = 1.0$ for $\lambda = 107, 161, 268$ can be found in the appendix (see Fig. A.5). $g_6(r)$ is short-ranged with a correlation length of less than $2d$ with

$$d = (\pi N/V)^{-1/2}$$

the global mean inter-particle distances.

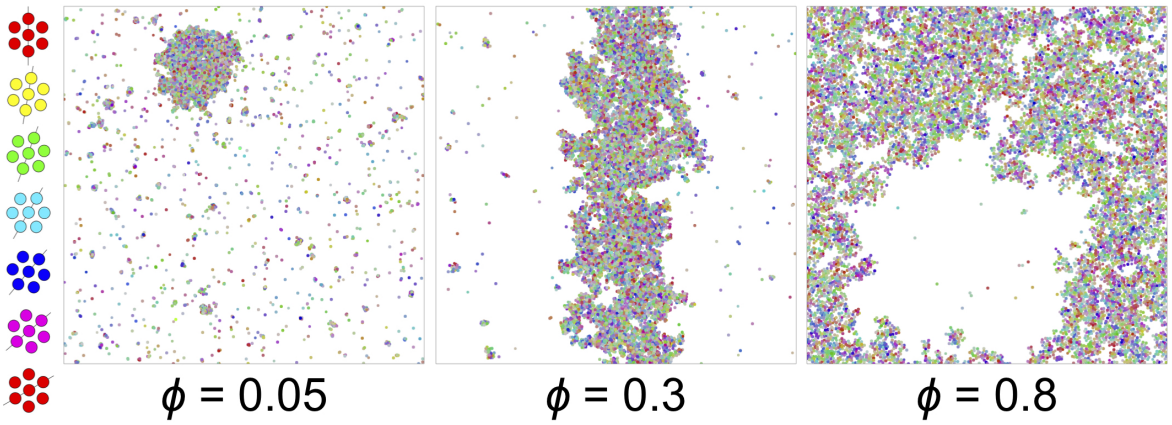


Figure II.18: **MIPS as liquid-gas coexistence.** Shown are configuration snapshots for $N = 10976$ particles at different densities for $\lambda = 1072$ (compare with Fig. II.12). The particles are color-coded according to their local bond-orientational order parameter ψ_6, as indicated on the left. Particles are plotted in arbitrary size which decreases with increasing ϕ. Data for $\delta = 0.7$.

In conclusion, this subsection II.3.2 has shown that MIPS emerges within the kinetic Monte Carlo dynamics as a liquid-gas coexistence within a U-shaped phase boundary. The onset of the U is located at high persistence and, compared to the equilibrium melting transitions, at relatively low densities. The MIPS region is surrounded by a fluid phase, which is homogeneous on macroscopic length scales. Data was presented, to provide evidence that the phase densities of the coexisting liquid and gas (ϕ_{Liquid} and ϕ_{Gas}) are independent of the global density ϕ. They solely depend on the persistence parameter λ, thus the phase boundary of MIPS is determined by $\phi_{\text{Gas}}(\lambda) = \phi$ and $\phi_{\text{Liquid}}(\lambda) = \phi$.

II.3.3 Two-step melting

The previous subsection II.3.2 concentrated on a region in the (ϕ, λ) phase space at relatively small ϕ and large λ. The present subsection II.3.3 concentrates on densities around and above the density range of the equilibrium two-step melting. The kinetic Monte Carlo dynamics permits access to the equilibrium dynamics with the ability to smoothly transit to the non-equilibrium state by tuning λ. As described in section I.5, crystals, the manifestation of perfect spatial order in nature, cannot exist in two dimensions, as this would require a spontaneous breaking of the continuous positional symmetry. Following the Mermin-

Wagner theorem, this is not possible in dimensions ≤ 2 for sufficiently short-ranged interactions. However, as discussed in section I.7, it is possible to define three distinct phases in two-dimensional particle systems, which are namely the liquid, hexatic and solid phase. They are characterized by different degrees of orientational and positional order. The **liquid phase** is short-ranged in both positional and orientational order, the **hexatic phase** shows short-ranged positional order, yet quasi-long-ranged orientational order, and the **solid phase** is characterized by quasi-long-ranged positional order, in combination with long-range orientational order.

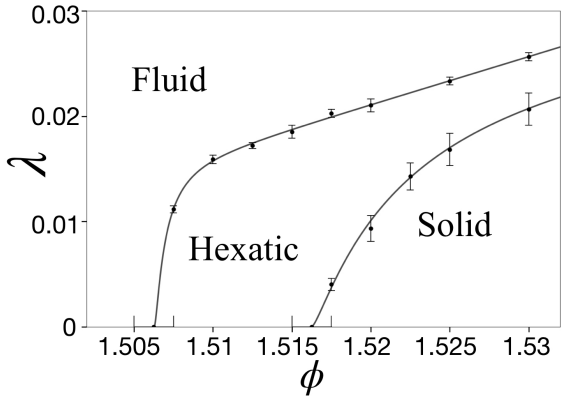


Figure II.19: **Two-step melting at small persistence lengths.** Phase diagram for small λ around the equilibrium melting densities. The transition lines shift to higher values with increasing λ. All equilibrium phases are preserved. The two-step melting is induced by a density reduction (as in equilibrium) but also by an increase in λ. [201]

In the equilibrium (N, V, T) ensemble, melting is induced by a density reduction. One main result of this thesis is that the non-equilibrium persistent counterpart has two parameters, which can induce melting, the density, and the persistence length. Fig. II.19 shows the region in the (ϕ, λ) phase space at small λ around the densities of the equilibrium melting transitions. The effect of persistent particle motions is to shift the melting transitions to higher densities, but all three phases survive the finite λ. Before providing data for the survival of the two-step melting scenario (with its intermediate hexatic phase) under the influence of persistent motion, the characterizing properties for the liquid, hexatic and solid phases are summarized for a clear overview.

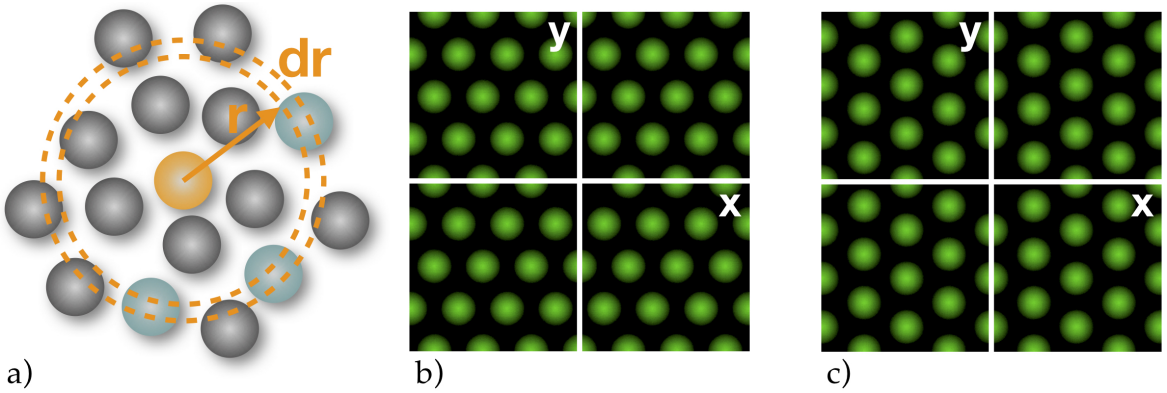


Figure II.20: **Pair-correlation function.** a) Scheme for the calculation of the radial distribution function $g(r)$. b) Zoom of a two-dimensional pair-correlation function $g(x, y)$ of a single (spatially ordered) configuration aligned as in Fig. II.11a. c) shows the corresponding zoom of a configuration aligned as in Fig. II.11b.

The identification of the three phases requires two measures, one for the orientational order and one for the positional order. Here, orientational order is quantified by $g_6(r)$, the

correlation function of the local bond-orientational order parameter defined in the previous subsection II.3.2 (see (II.12)). The positional order is determined by the pair-correlation function

$$g(\boldsymbol{r}) = g(x,y) = \frac{V}{N^2}\left\langle \sum_{i\neq j} \boldsymbol{\delta}(\boldsymbol{r} - (\boldsymbol{r}_i - \boldsymbol{r}_j)) \right\rangle$$

with $\boldsymbol{\delta}(x)$ being the Dirac delta function. In contrast to the radial distribution function $g(r)$, a measure of how density varies as a function of the distance r from a reference particle (see Fig. II.20a), the pair-correlation function $g(x,y)$ is a two-dimensional histogram and is thus depending on the global orientation $\Psi_6 = \sum_i^N \psi_6(\boldsymbol{r}_i)$ of the configuration. Fig. II.20b and c show zooms of $g(x,y)$ for two spatially ordered configurations with the two different orientations (the ones shown in Fig. II.11). An conclusive ensemble average of the two-dimensional histogram of $g(x,y)$ requires the realignment of each configuration, *e.g.* such that the Δx axis points in the direction of the global orientation parameter Ψ_6 [12]. This means in practice that the configuration in Fig. II.20c must be rotated by $90°$, before averaging over $g(x,y)$ in Fig. II.20b and c.

With this above definitions of the positional correlation function $g(x,y)$ and the orientational correlation function $g_6(r)$, the phases can be distinguished with the properties summarized in Tab. II.1.

	liquid phase	hexatic phase	solid phase
$g_6(r)$	$\propto e^{-r/\xi_6}$ short-ranged	$\propto r^{-\alpha_6}$ quasi-long-ranged	$\propto const$ long-ranged
$g(x, y=0)$	$\propto e^{-x/\xi_p}$ short-ranged	$\propto e^{-x/\xi_p}$ short-ranged	$\propto x^{-\alpha_p}$ quasi-long-ranged

Table II.1: **Definition of the two-dimensional phases.**

For equilibrium systems, the KTHNY-theory defines the limiting exponents $\alpha_6 = \frac{1}{4}$ and $\alpha_p = \frac{1}{3}$: algebraic decays of $g(x,0)$ with $\alpha_p \leq \frac{1}{3}$ identify the solid phase, whereas a decay of $g_6(r)$ with $\alpha_6 \leq \frac{1}{4}$ together with an exponentially decaying $g(x,0)$ identifies the hexatic phase. This determines the equilibrium melting transitions at $\lambda \to 0$ (see Fig. II.19). At finite λ, however, no comparable theory is available, thus only leaving the criterion of exponential *vs.* algebraic decay for the distinction of the phases.

With the definitions in Tab. II.1, Fig. II.21 illustrates the melting at a fixed density $\phi = 1.53$ induced by an increase in λ. This density corresponds to an equilibrium solid state point (compare Fig. II.19 or [13]). **Point A** in the figure corresponds to the finite persistence $\lambda = 0.0191$ and shows clearly the characteristic of the solid phase, namely: a clear power-law decay in $g(x,0)$, in combination with a long-raged $g_6(r)$. The uniform color in the configuration snapshot in Fig. II.21c confirms the orientational order throughout the system. At higher λ, the **points B to E** are characteristic for the hexatic phase. With increasing λ (from B to E) the hexatic phase "softens": the correlation length of the exponentially decaying $g(x,0)$ decreases, whereas the exponent α_6 of the algebraic $g_6(r)$ increases while moving closer to the hexatic-liquid transition. The behavior of the latter is reflected also in the color-coded configuration snapshots in Fig. II.21c: the disturbance of the uniform bluish

color, by purple, yellow and red patches increases from B to E. However, the appearance is clearly different from the configuration snapshots for **F and G**, where local orientations change within short length scales. For this points (F and G), Fig. II.21a and b show the characteristic exponential decay in $g(x,0)$ and $g_6(r)$ for the liquid phase.

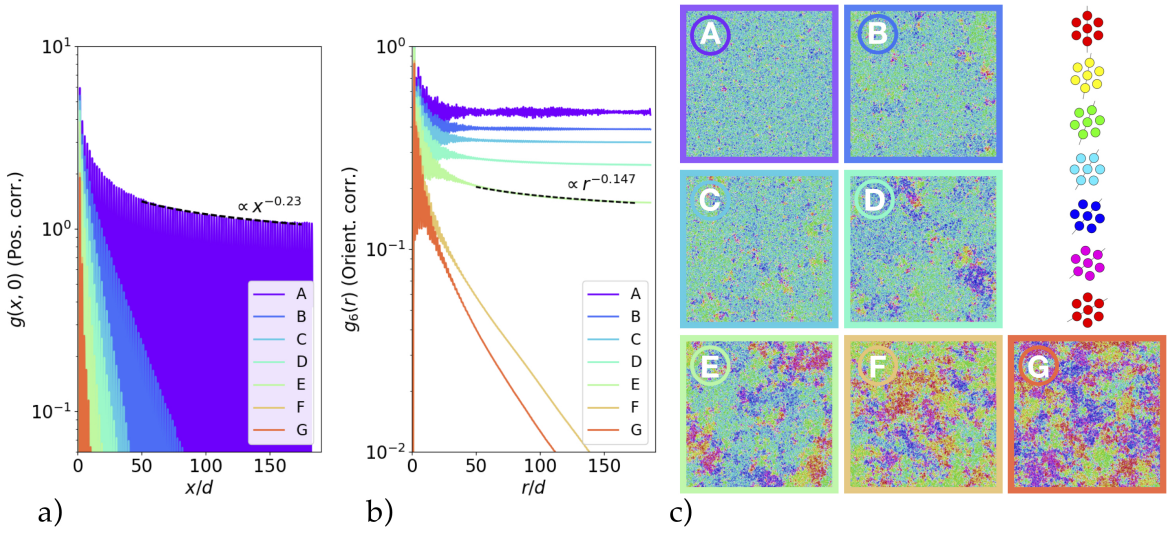


Figure II.21: **Activity-induced two-step melting.** Data is for $\phi = 1.53$ and a fixed set of λ. a) positional correlation function $g(x,0)$. b) orientational correlation function $g_6(r)$. c) configuration snapshots color coded according to the local bond-orientational order parameter $\psi_6(\boldsymbol{r}_i)$. (A: $\lambda = 0.0191$, B: $\lambda = 0.023$, C: $\lambda = 0.0237$, D: $\lambda = 0.0245$, E: $\lambda = 0.0253$, F: $\lambda = 0.0268$, G: $\lambda = 0.0276$, $\delta = 0.1$, $N = 43904$)

The phase diagram in Fig. II.19 results from the evaluation of $g(x,0)$ and $g_6(r)$ as in Fig. II.21. The error bars were obtained from the behavior of short-time ensemble averages, as the sole interpretation of long-time ensemble averages can be misleading in systems of finite size. Fig. II.22 shows an example at small λ, close to the hexatic-solid transition for a configuration that initially started from an arrangement of particles on a perfect hexagonal lattice. The long-time average (black solid curve, with the dashed gray curve as the corresponding fit) suggests that this state point is still in the solid phase. However, some of the short-time averages decay exponentially, indicating that a larger N would most likely characterize the state point as hexatic (algebraic $g_6(r)$ not shown) even in the long-time behavior. Therefore the lower-persistence error-bar of the solid-hexatic transition is determined by a state point with all short-

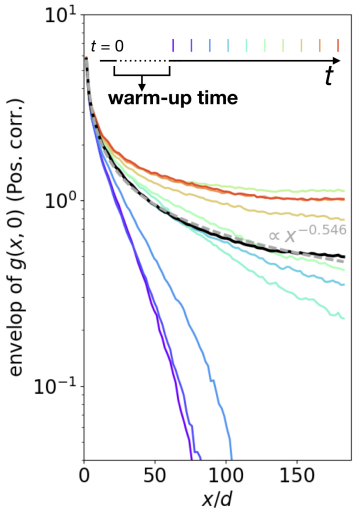


Figure II.22: **Short-time averages.** Time evolution (see legend) of the short-time averages of $g(x,0)$. The solid black curve is the long-time average including all shown short-time averages and the dashed gray line is the corresponding fit. ($\phi = 1.5175$, $\lambda = 4.59 \cdot 10^{-3}$, $N = 43904$, $\delta = 0.1$)

time averages of $g(x,0)$ having a clear power-law dependence. The high-persistence error bar is determined by state points with short-time averages decaying exponentially. The same criterion applied to $g_6(r)$ was used for the error bars of the liquid–hexatic transitions.

Having demonstrated that the two-step melting scenario, comprising the hexatic phase, survives close to the equilibrium melting transitions at small λ (see Fig. II.19) the following Fig. II.23 shows that this behavior is not only an artifact of the equilibrium melting within a perturbation regime but an autonomous property of the non-equilibrium system itself. The constant density $\phi = 2.4$ in Fig. II.23 is far inside the equilibrium solid phase and the persistence length λ is of the same order as the intensity parameter γ. **Points A and B** are solid state points, **points C to E** are hexatic state points and **points F and G** are liquid state points. For comparison, an algebraic decaying curve with the equilibrium limiting exponent $\alpha_p = \frac{1}{3}$ is plotted next to the last solid state point in $g(x,0)$ and respectively a curve with $\alpha_6 = \frac{1}{4}$ next to the last hexatic state point in $g_6(r)$.

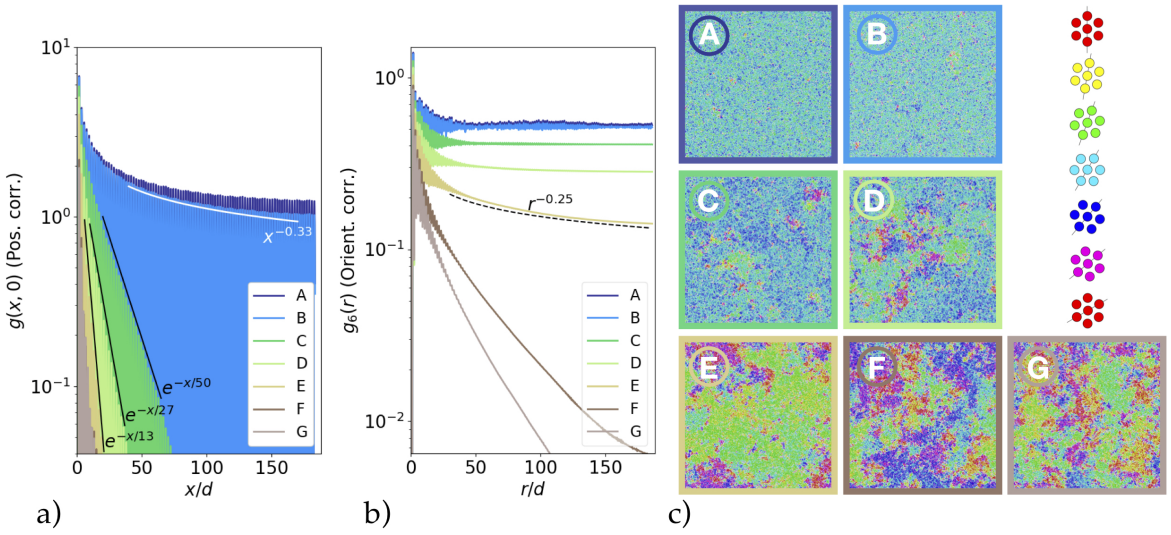


Figure II.23: **Activity-induced two-step melting far from equilibrium.** Data is for $\phi = 2.4$ and a fixed set of λ. a) positional correlation function $g(x,0)$. b) orientational correlation function $g_6(r)$. c) configuration snapshots color coded according to the local bond-orientational order parameter $\psi_6(\boldsymbol{r}_i)$. (A: $\lambda = 0.9874$, B: $\lambda = 0.9989$, C: $\lambda = 1.018$, D: $\lambda = 1.0333$, E: $\lambda = 1.0448$, F: $\lambda = 1.0639$, G: $\lambda = 1.0793$, $\delta = 0.1$, $N = 43904$)

To ensure that the steady state has been reached, simulations are performed from two structurally different initial particle configurations. For the hexatic phase, the two initial configurations are: 1) a random distribution of particle positions and 2) particles are arranged on a perfect hexagonal lattice. Fig. II.24 shows the time evolution of the positional and orientational correlation function, with both initial configurations converging to the same steady state. Fig. II.24 shows data for a hexatic state point at finite λ and high ϕ beyond the perturbation regime and thus providing further evidence for the existence of the hexatic phase outside equilibrium. Fig. A.6 in the appendix shows further data for a hexatic state point close to the liquid-hexatic transition. Fig. A.7 in the appendix shows convergence data for the solid phase close to the hexatic-solid transition.

Having discussed the phase space of MIPS (subsection II.3.2) and the two-step melting

(subsection II.3.3) separately, both phenomena are discussed in the same phase diagram in the next subsection II.3.4 together with the influence of the inter-particle potential strength.

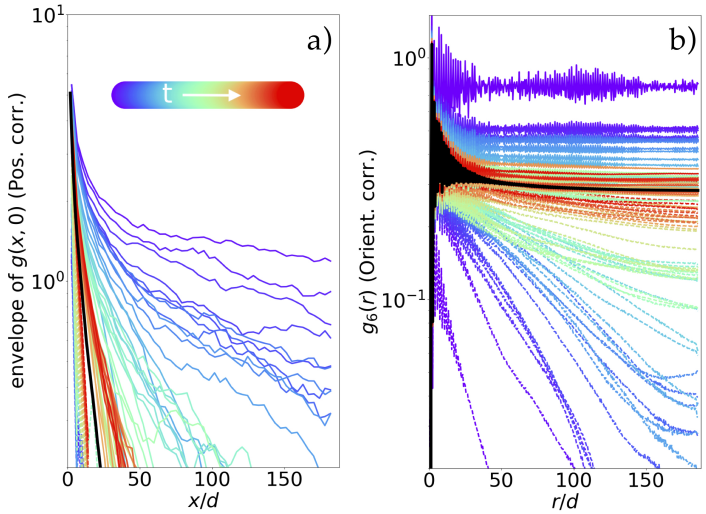


Figure II.24: **Convergence from two different initial conditions as a function of run time t.** a) Positional correlation function $g(x, y)$ along the x axis, in units of the global mean inter-particle distance d. b) Orientational correlation function $g_6(r)$. Both panels show the evolution with run time t (see color code for run-time ordering in a) starting from a random initial configuration (dashed lines) and from an initial configuration with particles arranged on a perfect hexagonal lattice (solid lines). Both initial configurations approach the same hexatic steady state (black solid line). Data at $\phi = 2.4$ with $\lambda = 1.0333$ and $\delta = 0.1$. [201]

II.3.4 The full phase diagram

Although MIPS [80] has been frequently reported in two-dimensional active systems [18, 97, 98, 106] (also see paragraph b) in subsection I.4), it has remained unclear of how MIPS is connected with all phases appearing in the equilibrium phase diagram. Recent works on an active dumbbell system [106, 205] proposes that MIPS continuously extends from the equilibrium liquid-hexatic transition region and that one of the separated phases preserves some degree of order. Other works with symmetric particles describe MIPS as a coexistence between a "*solid-like and gas state*" [97], or as a coexistence between a "*dense large cluster and a dilute gas phase*" [18], or referred to MIPS as a coexistence between a "*dense and dilute phase*", where the dense phase "*exhibits structural properties consistent with a 2D colloidal crystal near the crystal-hexatic transition point*" [98]. The latest closely related work (of an active Brownian particle system) [108] describes MIPS as coexistence, where the dense phase "*can be either disordered (liquid) or ordered (hexatic or solid)*".

Clearly, the resulting steady state in a non-equilibrium system, in general, depends on the underlying microscopic dynamics, thus here it is not possible to make a conclusive statement on a "general nature" of the coexisting phases in MIPS, however, a strength of the results in this thesis is the unambiguous characterization of MIPS as liquid-gas coexistence within the kinetic Monte Carlo dynamics. In consequence of the described properties of MIPS in subsection II.3.2, this must mean that (here) MIPS and the melting are two

disconnected phenomena, which is shown in the full phase diagram in Fig. II.25. The onset of MIPS is at relatively high λ and small ϕ, whereas the two-step melting transitions extend continuously from the equilibrium scenario and shift to higher ϕ with increasing λ without losing the hexatic phase in between the liquid and the solid. Within the accessed parameter space, the melting transitions and the phase boundary of the MIPS are always separated by the disordered fluid phase.

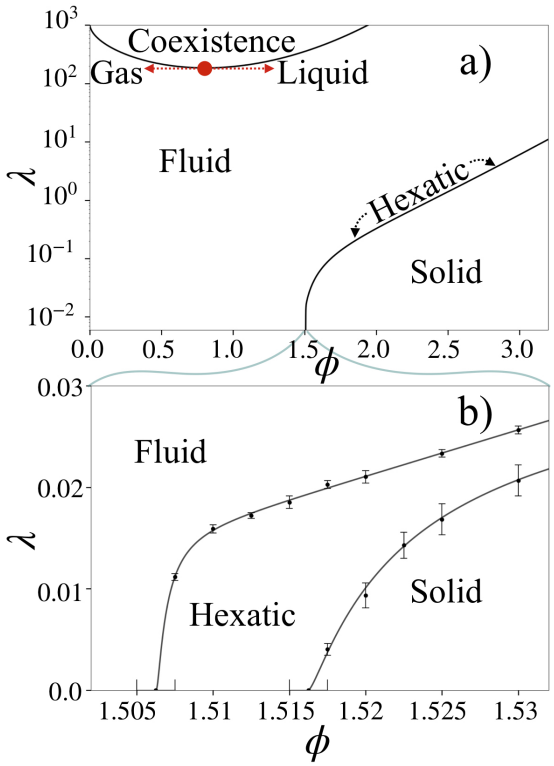


Figure II.25: **Full phase diagram.** a) Persistence length λ vs. density ϕ phase diagram. MIPS between a liquid and a gas, at high λ, is situated far above the solid-hexatic-liquid melting transitions. The red dot indicates a possible critical point. b) Zoom at small λ around the equilibrium melting densities as in Fig. II.19. Data for $\delta = 0.1$ and $N = 43904$.[201]

Being provided with the full phase diagram of the repulsive power-law potential $\propto r^{-n}$ for $n = 6$, the question arises how the phase diagram changes under stiffer potentials, corresponding to larger n. Numerical studies [13] on the equilibrium two-step melting of the same power-law model show that the two-step melting transitions change with n (also see the introduction section I.8). Not only the transition densities change but also the order of the liquid-hexatic transition [191]. For very soft particles ($n \lesssim 6$) the two-step melting scenario comprises two continuous transitions, while for harder particles with ($n \gtrsim 6$) the liquid–hexatic transition is of first order. Therefore a stiffer potential introduces an intermediate liquid-hexatic coexistence phase in the (N, V, T) ensemble which was explicitly verified by the analysis of the equation of state in [11–13]. However, the existence of a thermodynamic pressure in non-equilibrium active systems is a substantial question [47, 48, 51, 102, 105, 206]. Its answer within the kinetic Monte Carlo dynamics is not straight-forward and is discussed in section II.5. The question about the precise kind of phase transitions is not addressed in this subsection II.3.4.

Tab. II.2 summarizes the equilibrium results [13] for $n = 6$, $n = 16$ and the hard-disk case ($n \to \infty$). Firstly, the stiffer potential shifts the transitions to smaller densities and secondly, it increases the positional correlation length ξ_p. The large correlation lengths for large n, especially the large ξ_p in the hard-disk case, prevented conclusive numerical statements about the precise nature of the equilibrium phases and their transitions. Only the development of innovative and unconventional algorithms [12, 207] offered access to the steady state of system sizes large enough to clearly distinguish the hexatic and solid phase. Remarkably, the positional correlation length drops to the order of a view global mean interparticle distances d for $n = 6$, thus the phases can be clearly distinguished for much smaller system sizes. The identification of all three thermodynamic phases is far more difficult for the hard-disk model ($n \to \infty$) than for softer potentials.

n	ϕ_{liquid}	ξ_6/d	ϕ_{hexatic}	ξ_p/d	ϕ_{solid}
6	1.506	180	1.507	2.6	> 1.516
16	0.937	95	0.949	27	> 0.96
∞	0.892	62	0.913	51	> 0.919

Table II.2: **Equilibrium two-step melting transitions.** Density phase boundary of the liquid ϕ_{liquid} and orientational correlation length ξ_6 of the liquid at the transition. Lower density phase boundary of the hexatic phase ϕ_{hexatic} and the positional correlation length ξ_p of the hexatic at coexistence. The last column indicates the lower bound for the solid-hexatic melting density. Source: Table 1 in [13].

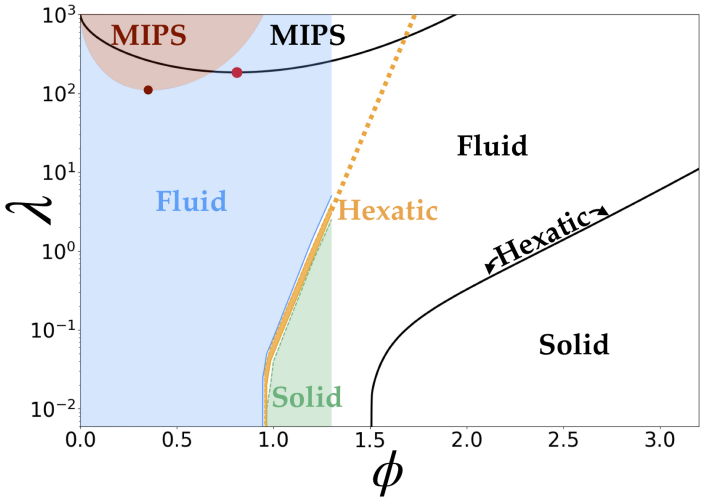


Figure II.26: **Effect of particle stiffness on the phase diagram.** Black lines correspond to the phase diagram for the soft $n = 6$ pair potential shown in Fig. II.25a. The colored areas correspond to $n = 16$: The green region is the solid phase, the orange region corresponds to the hexatic phase, the blue region is the homogeneous fluid phase and the MIPS region is indicated in red. The dashed-dotted line is an approximation. Measurements end at $\phi = 1.2$ for $n = 16$. All data for $\delta = 0.1$.

In comparison to conventional equilibrium Monte Carlo algorithms, the kinetic Monte Carlo algorithm suffers from a slow-down of the mixing times at finite λ due to kinetic arrest. This phenomenon, eventually leading to MIPS, is a critical factor at the high-density regime of the two-step melting. The correlation of individual particle displacements increases the rejection rate of proposed moves and thus reduces the efficiency of the algorithm. In consequence, the $n = 6$ pair potential (with its particularly small positional correlation length) becomes a strategic starting point to investigate the principal phase behavior of persistently moving many-particle systems.

Next to the clear evidence for the two-step melting scenario far from equilibrium for the $n = 6$ potential in subsection II.3.3, the present subsection II.3.4 also provides preliminary results for the stiffer $n = 16$ potential. Fig. II.26 shows the full phase diagram for both potentials ($n = 6$ and $n = 16$).

Reproducing and confirming the equilibrium results in [13], the stiffer potential shifts the equilibrium melting transitions to smaller densities, while the impact of λ on the transition densities decreases. For both potentials, a significant shift of the melting transitions sets in after overcoming a threshold λ^* which is of the same order. The MIPS region for $n = 16$ becomes narrower and the onset shifts to smaller densities. However, both phase diagrams share the same qualitative behavior: MIPS appears as a liquid-gas coexistence, with its onset at relatively low densities and high persistence lengths and the two-step melting scenario, with its intermediate hexatic phase is robust under the influence of persistent motion beyond the linear-response regime (which is below λ^*).

Fig. II.27 shows preliminary data of the orientational and positional correlation functions around the two-step melting for the $n = 16$ pair potential at $\phi = 1.2$ which is far above the equilibrium melting transitions (see Tab. II.2). This preliminary data is obtained from an initial configuration where particle positions are arranged on a hexagonal lattice. The black stars indicate that the steady state has been reached, which is tested by the convergence of a random initial configuration towards the same steady state (see Fig. A.8 for the hexatic state points). Therefore, $\lambda = 1.4$ and $\lambda = 1.1$ set a range for the liquid-hexatic transition. At this point of the simulation, it cannot be excluded that the solid state points in Fig. II.27 will melt into a hexatic phase.

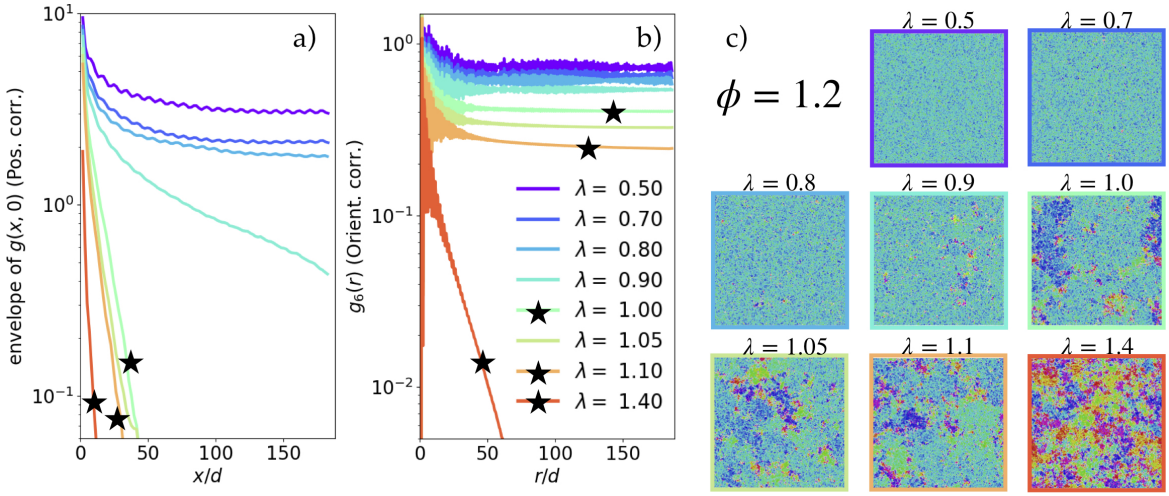


Figure II.27: **Activity-induced two-step melting far from equilibrium for $n = 16$.** Preliminary data is for $N = 43904$ at $\phi = 1.2$ for a fixed set of λ indicated in the legend in b). a) envelope of the positional correlation function $g(x, 0)$. b) orientational correlation function $g_6(r)$. c) configuration snapshots color-coded according to the local bond-orientational order parameter $\psi_6(\boldsymbol{r}_i)$ as in Fig. II.23. The black stars denote two hexatic state points converged to the steady state (see Fig. A.8).

II.3.5 MIPS under the influence of stiffer potentials

The previous subsection II.3.4 discussed the full phase diagram for particles interacting via the pair potential $\propto r^{-n}$ with $n = 6$ and $n = 16$. Both potentials resulted in the same qualitative phase diagram, where the two-step melting and MIPS are separated by a fluid phase. However, an earlier work [200] reports that MIPS does not appear for hard disks

within the kinetic Monte Carlo approach discussed here[3]. This suggests that the phase diagram must change drastically when approaching the hard-disk limit. Motivated by this result, a systematic study of the influence of the stiffness of the potential on MIPS within the kinetic Monte Carlo dynamics is presented in the present subsection II.3.5.

The simulation results show that the formation of MIPS is not hindered by the stiffness of the pair potential if the maximum jump length δ is comparably large. Fig. A.9 in the appendix shows configuration snapshots, which (partly) may still be in the coarsening process, but do not leave doubt on the existence for MIPS for potentials within the range $6 \leq n \leq 1024$.

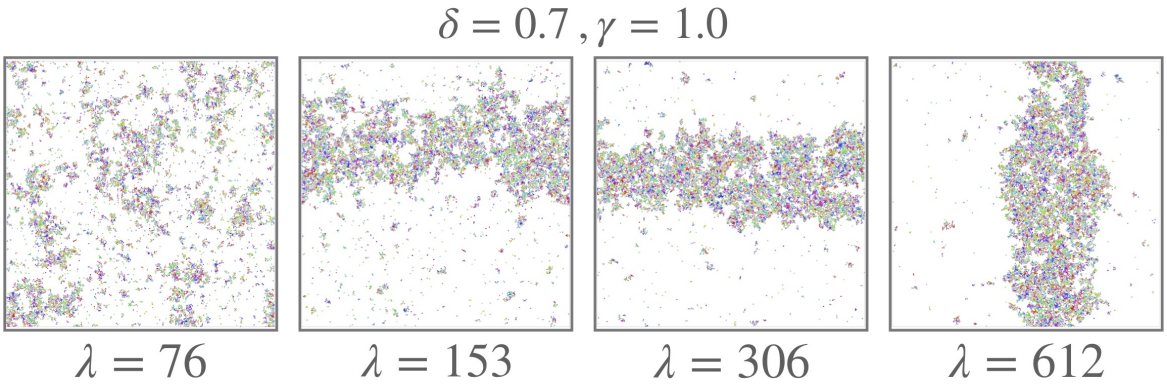


Figure II.28: **MIPS in the hard-disk system.** Configuration snapshots for $N = 10976$ hard disks of diameter $\gamma = 1.0$. The simulations were performed at $\phi = 0.2$ with $\delta = 0.7$. The particles are colored with the ψ_6 color code (indicated *e.g.* in Fig. II.23c).

In fact, MIPS can be easily recovered even for hard disks, if δ is sufficiently large but still smaller than the particle diameter. Fig. II.28 shows MIPS in the hard-disk system after a runtime of $3 \cdot 10^7$ Monte Carlo sweeps[4], with each sweep comprising N Monte Carlo steps. Interestingly, the dense phase does not show any orientational order (particles plotted in ψ_6 color code), just like for all other potentials in Fig. A.9. Without having investigated the melting in the hard-disk scenario, this observation leads to the immediate conclusion that MIPS and the two-step melting must also be separated by a fluid phase in this case (at least in a certain parameter range).

However, within the work [200], a smaller δ was chosen, leading to the question of whether MIPS could disappear in the hard-disk case if δ is small. Furthermore, it raises the question about the number of independent parameters within the kinetic Monte Carlo dynamics, which is addressed in section II.4.

In order to detect possible causes for the disappearance of MIPS reported in [200], a systematic study on the influence of δ is presented for a rather hard potential ($n = 256$). Fig. II.29 shows the coarsening process leading to MIPS for $\delta = 0.1$ and $\delta = 0.7$ at $\phi = 0.4$ and $\lambda = 800$. The first configuration snapshot is taken after $\approx 10^6$ Monte Carlo sweeps.

[3]The algorithm described in [200] is slightly different in the sampling scheme of the displacement described in section II.1. The implementation used in this thesis samples the ϵ from a random walk from a bivariate normal distribution. In contrast, the implementation in [200] samples the displacement random walk from a flat distribution. However, this difference is not expected to result in substantial differences.

[4]Approximately, this corresponds to 4 days CPU time for $N = 10976$.

The coarsening process for the larger δ is almost completed at this stage, leaving the system with two big gas bubbles only, which merge within the time interval leading to the following snapshot taken after $\approx 10^7$ Monte Carlo sweeps. The first configuration snapshot for $\delta = 0.1$, on the other hand, consists of many dense patches surrounded by a dilute phase. Nevertheless, the time evolution clearly shows a coarsening process to a state, which might not be the steady state yet[5], but which shows clear features of a liquid-gas phase coexistence.

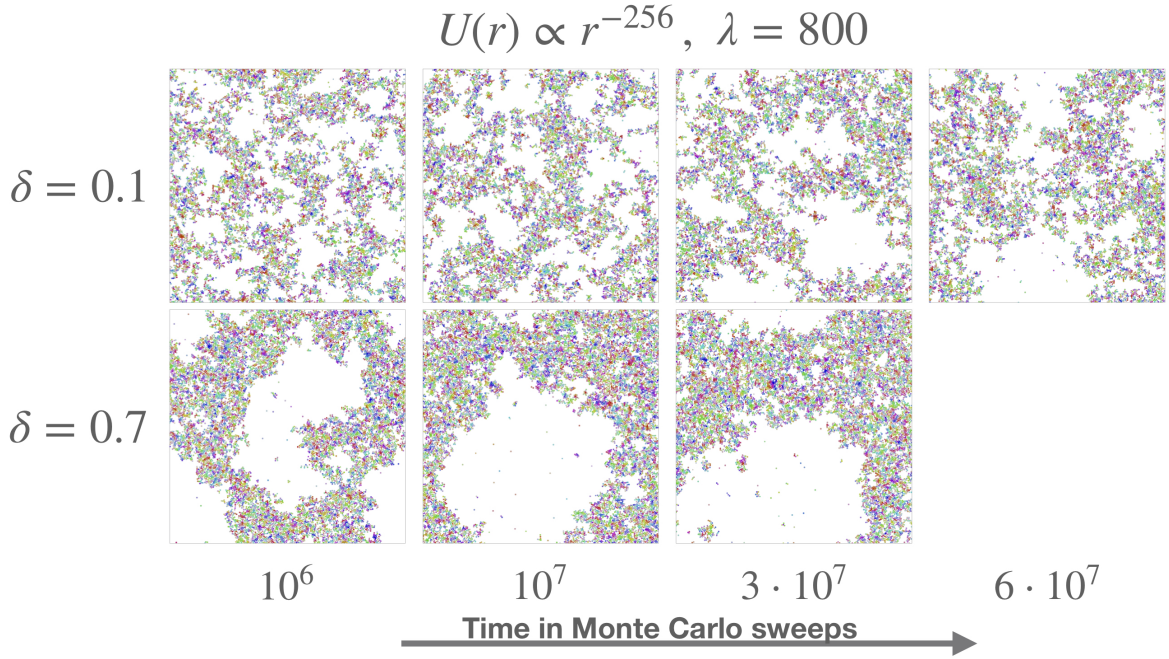


Figure II.29: **Coarsening process for MIPS under the influence of δ.** Configuration snapshots, with ψ_6 color-coded particles (indicated *e.g.* in Fig. II.23c) for $N = 10976$.

The appendix contains an equivalent figure (see Fig. A.10) for $\lambda = 1.6 \cdot 10^3$, where the liquid-gas coexistence for $\delta = 0.1$ is more pronounced. Additionally, a summary of a systematic decrease in δ is provided for the same potential and various λ in Fig. A.11. In this last figure, it can be clearly seen that the coarsening process slows down with increasing λ. For example, the configuration snapshot for $\delta = 0.7$ and $\lambda = 2.56 \cdot 10^4$ in Fig. A.11 still consists of two gas bubbles and the interface is rather rough, whereas the configuration for $\lambda = 1.6 \cdot 10^3$ shows a single, circular gas bubble surrounded by a largely homogeneous liquid. Especially systems with a large persistence and small δ suffer from a slow coarsening process (compare with Fig. II.29). This slow-down of the coarsening process with increasing λ is due to the equivalently increased auto-correlation time τ of the particle displacements. As described in the paragraphs b) and c) of subsection II.1.1

$$\lambda \propto \frac{\delta^3}{\sigma^2} \quad \text{and} \quad \tau \propto \frac{\delta^2}{\sigma^2}\,. \tag{II.13}$$

[5] $6 \cdot 10^7$ Monte Carlo sweeps correspond to appropriately 35 days in CPU time. The simulation was terminated at a stage where a macroscopic phase separation became apparent.

The persistence length $\lambda = 2.56 \cdot 10^4$ corresponds to a auto-correlation time $\tau \approx 4.8 \cdot 10^4$ Monte Carlo steps. This means each particle attempts to move for $4.8 \cdot 10^4$ Monte Carlo steps in a similar direction, before the displacement decorrelates. A major part of this attempts are rejected by the Metropolis filter, especially for particles inside the dense patches. In consequence, large λ slow down the dynamics and thus increase the time to reach the steady state.

The same argument of increased τ explains the slower coarsening process at constant λ for smaller δ shown in Fig. II.29. Smaller δ require larger persistence times τ, in order to gain the same persistence length λ (see (II.13)). In the example in Fig. II.29, the correlation time for $\delta = 0.1$ is $3.1 \cdot 10^5$ times larger than for $\delta = 0.7$. With the assumption that λ is a relevant parameter for the observation of MIPS (see section II.4), the large time scales of coarsening processes for small δ could in principle prevent the identification of MIPS.

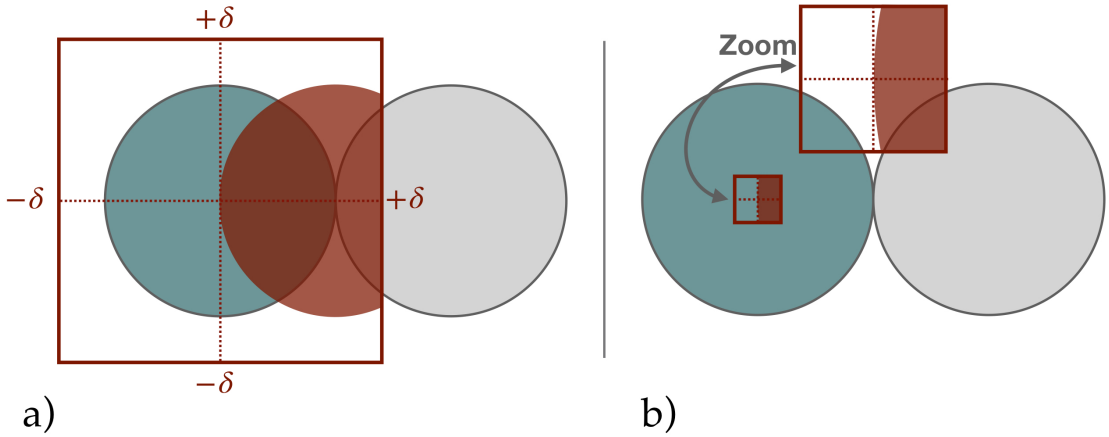


Figure II.30: **Forbidden zones in the δ space.** Shown are two hard disks (gray and green) during a collision. For the green disk, the displacement box is drawn in red. Displacements inside the red, shaded region within the δ-box would cause an overlap between the disks and would thus be rejected by the Metropolis filter. In a), the ratio between $\frac{\delta}{\gamma} = 0.7$, whereas in b), $\frac{\delta}{\gamma} = 0.1$. This ratios correspond to the ratios in Fig. II.29.

However, the large correlation times are not the only reason for the slow-down of coarsening when δ is small. Another inhibitor can be identified by questioning what precisely happens in a "collision event" and how δ influences this process. An understanding arises from the case where two hard disks move persistently towards each other until they "collide". Fig. II.30 shows this collision for two different δ. For the green particle, the displacement box is drawn in red. All trial moves with displacements sampled within the red shaded area are rejected by the Metropolis filter as they would lead to an overlap with the gray disks. The figure illustrates that the area fraction of the red forbidden region is much larger in the small-δ case. More precisely, the green disk in Fig. II.30b can almost not move in $+x$ direction to escape the collision event. The situation is clearly different for the larger δ in Fig. II.30a.

The role of this different area fractions occupied by the forbidden zone becomes clear when considering the situation of a particle joining a cluster. Fig. II.31 shows a schematic for hard disks. The green particles represent a small cluster and the gray and the red particles are in the process of joining the cluster. If δ is small, as shown in Fig. II.30b, the red particle

can hardly be integrated in the cluster, because: 1) All displacements in the direction of the cluster interior are rejected (see Fig. II.30b). Once the displacement moves outside of the forbidden zone, it points away from the cluster (red arrows symbolize the range of allowed directions), thus it is very unlikely that the particle stays close to the cluster due to the persistence. 2) Even if another particle blocks the red particle from behind, it can still escape to the right and left. The situation is clearly different for the gray particle. If another incoming particle blocks the gray particle from behind, it is not able to escape the cluster anymore.

In summary, if δ is small, a particle must hit the cluster as a gray particle to have a non-negligible chance to be sufficiently blocked by other incoming particles. Incoming red particles leave the cluster with a high probability as soon as the displacement's random walk moves out of the forbidden zone.

Clearly, the situation changes, if δ is chosen sufficiently large, as in Fig. II.30b. An incoming red disk would still have the chance to move closer to the cluster and to "transform into a gray disk".

Another way to bypass this large forbidden zones for small δ is to choose a soft inter-particle potential, where displacements inside the forbidden zones are simply accepted with the Metropolis probability [6].

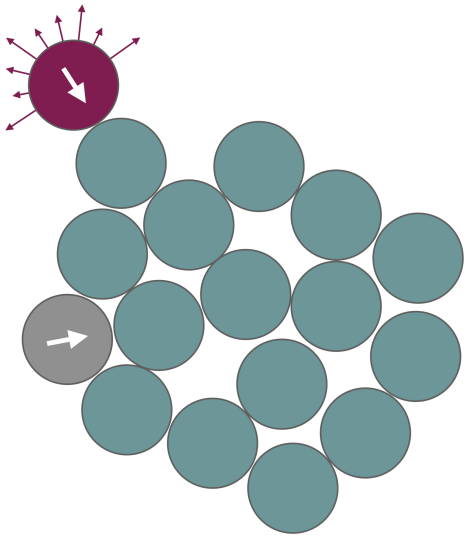


Figure II.31: **How to join a cluster?** Schematic of two hard disks (red and gray) joining a small cluster (green). For the red disk: If δ is small, as in Fig. II.30b, the red arrows symbolize the directions of motions which would **not** lead to an overlap. All displacements with a component pointing towards the cluster would lead to overlaps and would thus be rejected.

This subsection gave a qualitative argument for the deceleration of coarsening leading to MIPS with 1) decreasing δ and 2) with increasing stiffness of the inter-particle potential. However, one important aspect has been left out. Fixing the potential, the effect of a smaller δ is not only to slow down the coarsening process, but it also shifts the phase boundary of MIPS to higher persistence lengths. The specific effect of δ on the whole phase diagram is discussed in detail in section II.4. To conclude the discussion in this subsection II.3.5 it is sufficient to again consult Fig. A.11 in the appendix. The figure clearly indicates that the onset of the phase-separated region at this density shifts to higher λ with decreasing δ. Moreover, Fig. II.28 shows clearly that MIPS exists for $\lambda \geq 153$ in the hard-disk case for $\delta = 0.7$. Motivated by the observation that the onset of MIPS shifts to higher densities with decreasing δ, hard-disk simulations were performed for $\lambda \gg 153$ and the result is presented in Fig. II.32.

The steady state in Fig. II.32 might not have been reached yet (holes in the cluster might still coarsen), nonetheless, Fig. II.32 provides evidence for MIPS in the hard-disk case as a liquid-gas coexistence even for small δ within the kinetic Monte Carlo dynamics[7].

[6] Considering a situation as shown in Fig. II.30: Even if particles are able to overlap, the forbidden zone can never cover the entire displacement box. Displacements with components pointing away from the collision partner's center lead to an energy decrease and have thus an acceptance probability of 1.

[7] The maximum persistence length covered in [200] should be roughly comparable to $\lambda \approx 620$ for $\delta = 0.1$.

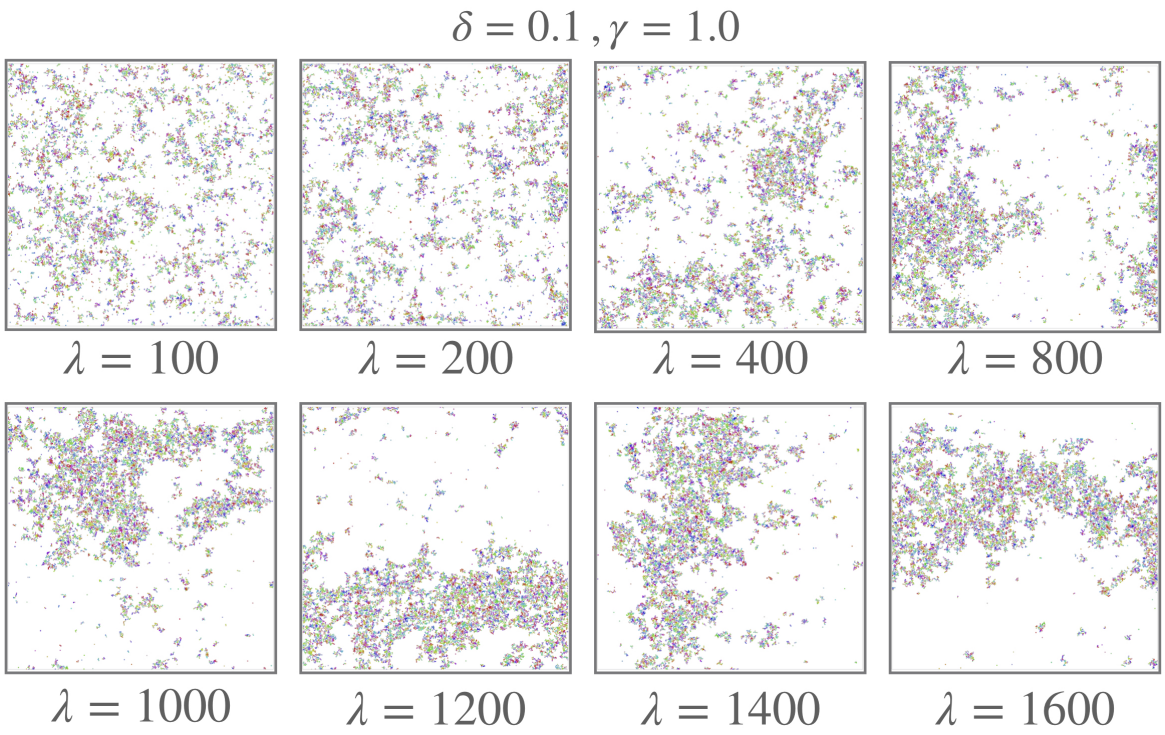


Figure II.32: **Hard-disk MIPS for small δ.** Configuration snapshots for $N = 10976$ hard disks of diameter $\gamma = 1.0$. The simulations were performed at $\phi = 0.2$ with $\delta = 0.1$. The particles are colored with the ψ_6 color code (indicated *e.g.* in Fig. II.23c). The run time is $1.1 \cdot 10^8$ Monte Carlo sweeps, which corresponds to roughly 16 days of CPU time.

II.3.6 Anisotropic effects in two dimensions?

An essential part of the particle dynamics has not been discussed yet: the influence of the $[-\delta, \delta]^2$ **square shape** of the reflecting boundary conditions for the sampling of the displacements $\boldsymbol{\epsilon}_i(t)$. The influence of different values of δ is discussed in detail in the next section II.4. This subsection II.3.6 is dedicated to the influence of the choice of a square-shaped box, instead of an isotropic, *i.g.*, circular one.

For a Monte Carlo approach, the choice of a square-shaped sampling box seems to be a natural one at the first glance. Common equilibrium Monte Carlo algorithms involve statistically independent sampling schemes for $\epsilon_{\mathrm{x}}(t)$ and $\epsilon_{\mathrm{y}}(t)$, *e.g.* in the most simple case from two independent uniform distributions such that $P(\epsilon_{\mathrm{z}}) = 1/(2\delta)$ for $\epsilon_z \in [-\delta, \delta]$ and $P(\epsilon_{\mathrm{z}}) = 0$ otherwise, where $\mathrm{z} = \mathrm{x}, \mathrm{y}$. This means that the particles can make larger jumps in the diagonal directions than in the directions parallel to the ϵ_{x}- or ϵ_{y}-axis. This angular anisotropy in the maximum jump length does not effect the equilibrium steady state. As discussed in subsection I.2.1, the equilibrium steady state relies on the microscopic symmetry of detailed balance. As long as the detailed balance condition is satisfied, any sampling scheme for $\boldsymbol{\epsilon}$ leads to the same steady state. Generalized Metropolis filters (Metropolis-Hastings algorithm) allow for, *e.g.*, triangular-shaped sampling boxes (see chapter 1.1.6 in [42]).

As further discussed in section I.2, non-equilibrium systems are not subject to strict rules like the detailed balance condition. Therefore, special attention must be paid to the choice of the sampling scheme. The square-shaped displacement box in the kinetic Monte Carlo algorithm leads to some degree of anisotropy in the dynamics for $\lambda > 0$. This subsection II.3.6 contains the explicit verification that the resulting many-body steady state is unaffected for the collective properties concerning the results in this thesis.

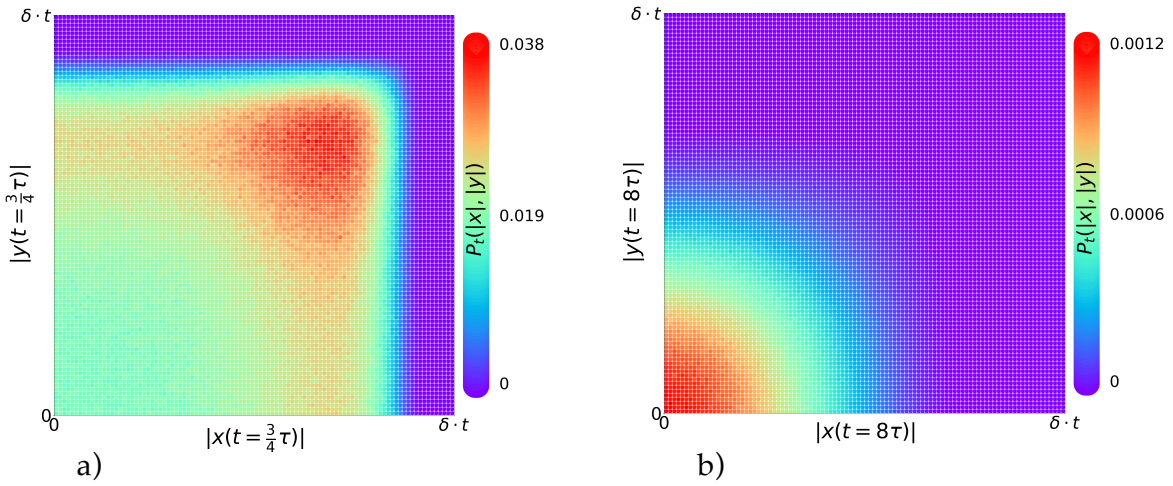


Figure II.33: **Angular anisotropic effects in the single particle case.** At $t = 0$ the particle is at the origin. Shown is the two-dimensional probability distribution $P_t(|x|, |y|)$ of the absolute values of the particle position at time $t = \frac{3}{4}\tau$ in a) and at $t = 8\tau$ in b) resulting from the persistent kinetic Monte Carlo dynamics with a $[-\delta, \delta]^2$ square-shaped sampling box for the displacement.

Fig. II.33 illustrates the angular anisotropic effects for the persistent random walk of a single particle (on an infinite space) introduced by the $[-\delta, \delta]^2$ square shape of the $\boldsymbol{\epsilon}$-sampling box. The particle is located at the origin at time $t = 0$ and performs a persistent random walk with a correlation time τ. As the square-shaped sampling box has four-fold symmetry, it is sufficient to compute the probability distribution of the absolute coordinates $(|x|, |y|)$ after a certain time t. Fig. II.33a shows $P_t(|x|, |y|)$ for $t < \tau$ with an angular anisotropy clearly originating from the square-shaped $\boldsymbol{\epsilon}$-space. This anisotropy is not the result of some effective dependence between the two displacement components $\epsilon_x(t)$ and $\epsilon_y(t)$ due to the reflective boundary conditions. The two $\boldsymbol{\epsilon}$-components are statistically independent at all times and for all τ. Fig. II.33b shows the angular isotropic result for times much larger than the persistence time τ. In this limit, the particle motion returns to the diffusive passive particle behavior, resulting in a Gaussian distributed $P_t(|x|, |y|)$.

This anisotropic effects for times $t < \tau$ could be easily overcome by choosing a circular sampling box of radius δ with reflective boundary conditions for the displacements (nothing else is changed otherwise). The resulting distribution $P_t(|x|, |y|)$ for the two time regimes[8] is shown in Fig. II.34. Fig. II.34a, for $t < \tau$, does not show any angular anisotropy. However, the sampling scheme for the reflective boundaries in the square-shaped box in (II.2) needs at most four calculation steps per dimension, whereas the circular boundary

[8]For simplicity τ is the same as in the "square" kinetic Monte Carlo approach, as it provides the correct order of magnitude to distinguish between the ballistic and the diffusive regime.

condition is computationally disproportionately more expensive. Furthermore, the reflection in the circle introduces a correlation between the two components $\epsilon_x(t)$ and $\epsilon_y(t)$, which makes the transition to the equilibrium dynamics more difficult compared to the square-shaped box [9].

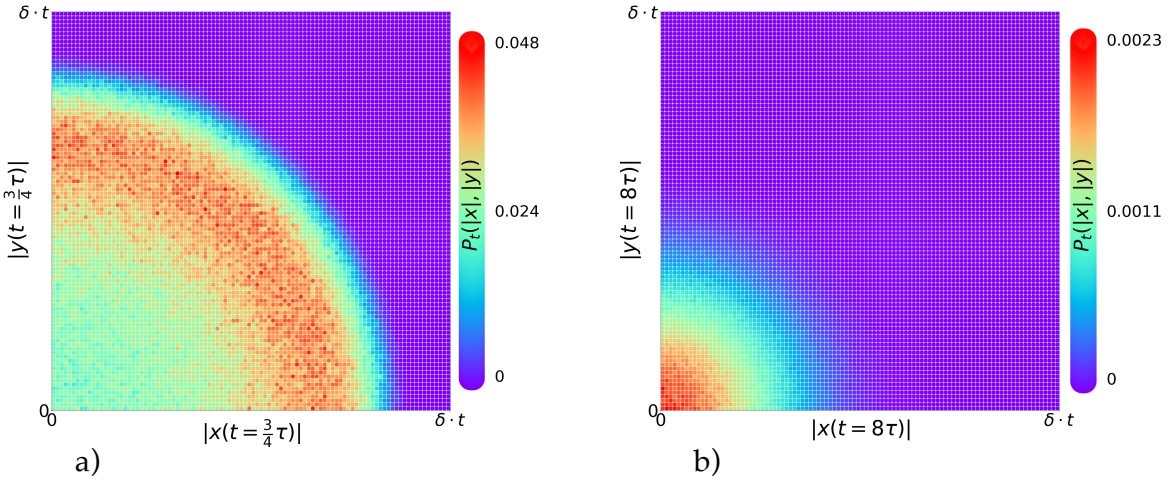


Figure II.34: **Angular isotropic results for circular displacement box.** Histograms as in Fig. II.33, but the displacement $\boldsymbol{\epsilon}(t)$ performs now a random walk in a circular box with reflective boundary conditions of radius δ.

The presented data in Fig. II.33 and Fig. II.34 result from the single particle behavior. However, the main result of this thesis concern the collective behavior of interacting persistent particles in two dimensions, thus the question is how and if this angular anisotropy in Fig. II.33a influences these many-particle results[10].

In the dilute case, where λ is much smaller than the mean free path, the kinetic Monte Carlo dynamics effectively reverts to the detailed-balance dynamics as interactions between particles happen at the diffusive time scale. At higher densities, anisotropic effects in the many-body properties can arise, if the probability distribution of the accepted displacements is anisotropic. Fig. II.35 shows that this is not the case. At higher densities, all large proposed displacements have a vanishing probability to be accepted by the Metropolis filter, thus leading to an effectively isotropic dynamics. So to say, the Metropolis does the job of an a priori circular reflecting $\boldsymbol{\epsilon}$-sampling box without additional computational cost.

Further evidence for the negligible influence of the square-shaped reflecting boundary is presented in the three figures, Fig. II.36, Fig. II.37 and Fig. A.12, each focusing on a different region in the phase diagram. The figures show in the first column measurements of the pair-correlation function in polar coordinates $g(\boldsymbol{r}) = g(r, \theta)$ averaged over different config-

[9] In the square-shaped box, the passive case is recovered due to the multiple reflections (when σ is large compared to δ), which decorrelates two successive $\boldsymbol{\epsilon}$. In a circular box, the angle of reflection of the first reflection within one time step $\boldsymbol{\epsilon}_i \to \boldsymbol{\epsilon}_{i+1}$ is the same as for all following reflections within this time step. This leads to the formation of traveling waves and for certain angles to the formation of standing waves (*e.g.* if the angle of reflection is $15°$). Angles close to the standing wave condition need a large number of reflections to decorrelate. (The phenomenon of standing waves is well-known in the context of whispering galleries as for example in the St Paul's Cathedral in London.)

[10] Clearly, the one-dimensional results do not suffer from any anisotropic effects

urations[11]. The representation in polar coordinates offers a clear detection tool for angular anisotropy.

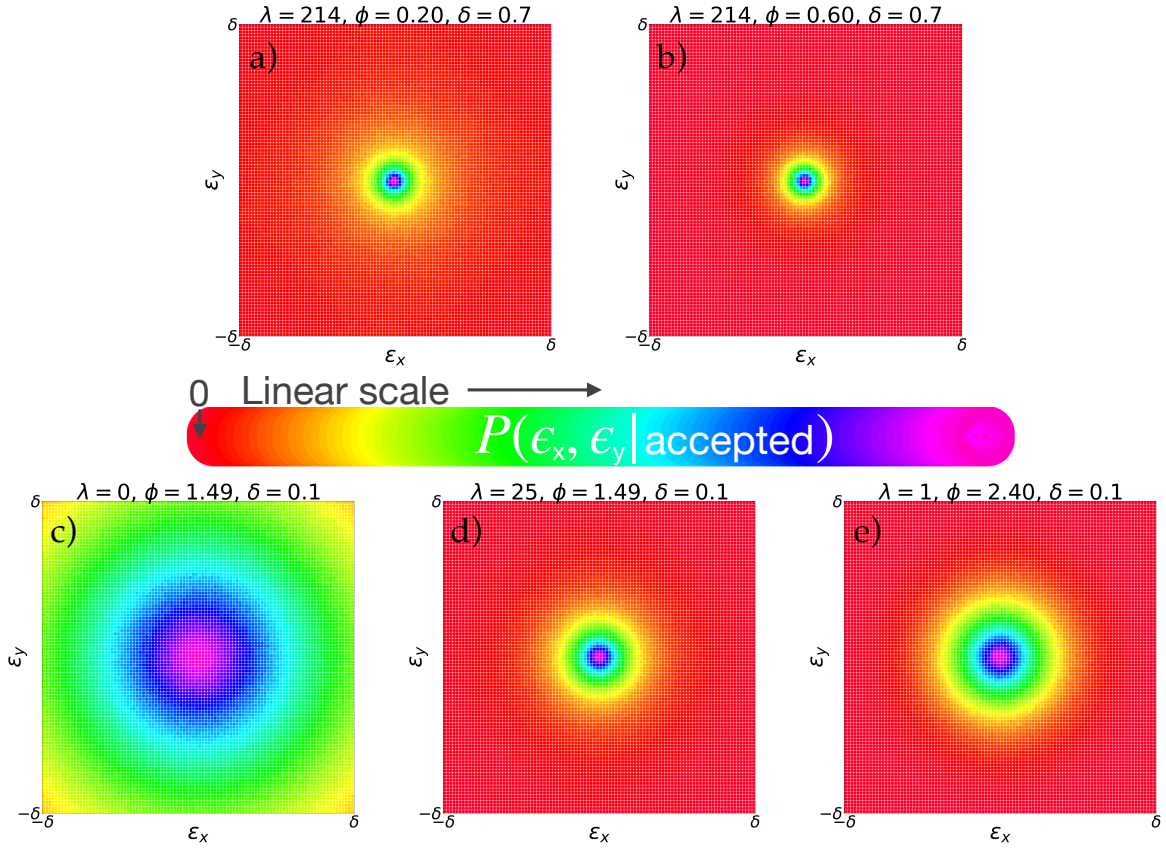


Figure II.35: **Histogram of accepted displacements.** Two-dimensional probability distribution of the accepted displacements $P(\epsilon_x, \epsilon_y|\text{accepted})$ with a linear color scale. a) and b) for displacements in the MIPS region (compare with Fig. II.15 and Fig. II.12). c) (for comparison) for the passive case in the liquid phase close to the liquid-hexatic transition. d) in the persistent case at the same density as c). e) in the solid close to the activity-induced solid-hexatic transition at a density far above the equilibrium melting transitions (compare Fig. II.23).

In order to show the effect of angular anisotropy in $g(\boldsymbol{r})$ in this representation, Fig. II.36 contains data for the solid, hexatic and liquid phase around the activity-induced melting high above the equilibrium melting transitions (compare Fig. II.23). The solid and hexatic phase show a clear six-fold rotational symmetry in $g(r, \theta)$, which is due to the hexagonal packing. In contrast, the liquid phase does not show any angular dependence in the pair-correlation function. An angular anisotropy introduced by the square shape of the reflecting boundaries in the $\boldsymbol{\epsilon}$-space should manifest in a four-fold rotational symmetry in $g(r, \theta)$, which is indicated by the red arrows. Clearly $g(r, \theta)$ does not show any four-fold rotational symmetry. To exclude also small angular asymmetries, the middle column shows the difference between $g(r, \theta)$ and its angular average $g(r)$. Neither of the phases shows a four-fold

[11]The configurations were **not** realigned according to their global orientation Ψ_6 as described in subsection II.3.3 for the configuration average of $g(x, y)$.

rotational symmetry.

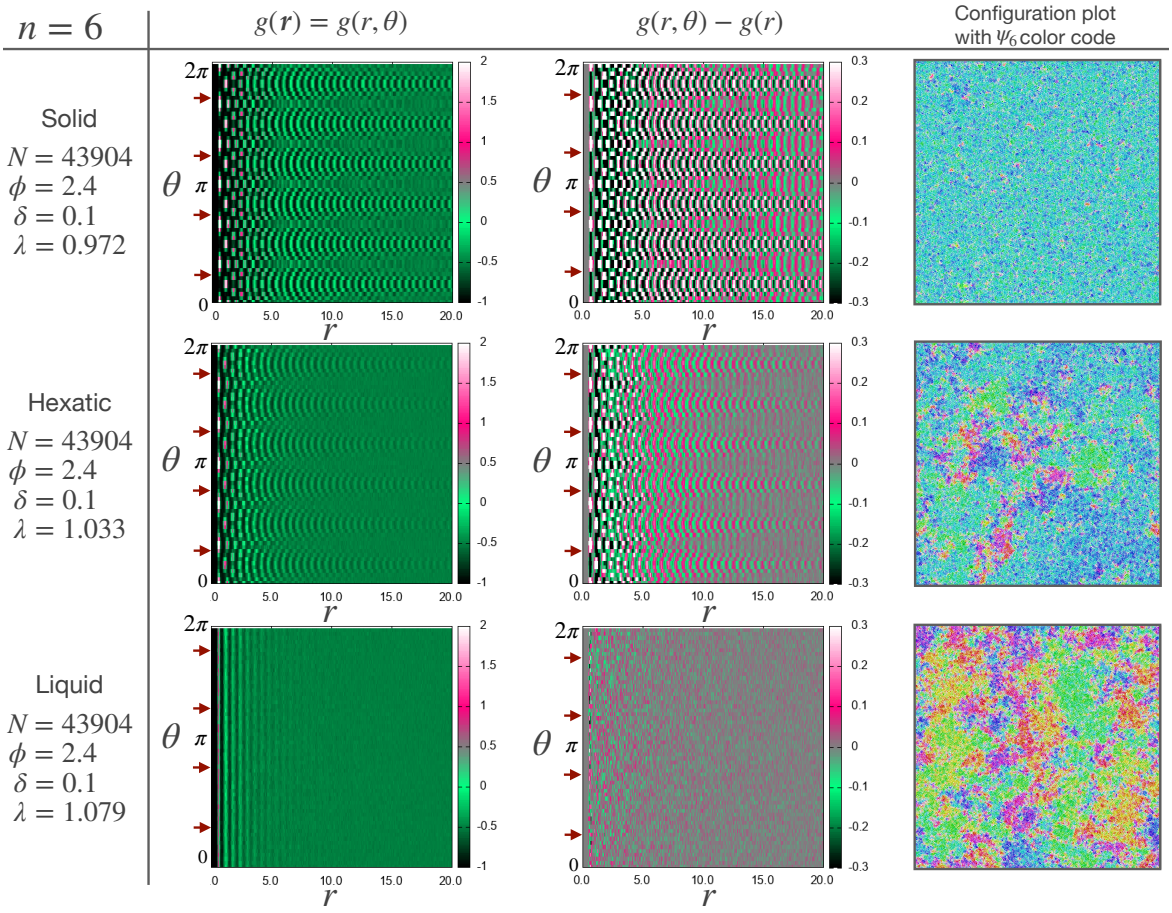


Figure II.36: **Evidence for effective isotropic dynamics around the two-step melting.** Data is for the potential with $n = 6$ at $\phi = 2.4$ for $N = 43904$ and persistence lengths around the melting transitions with $\delta = 0.1$. First column: pair-correlation function $g(r, \theta)$ in polar coordinates averaged over 100 configurations. Second column: difference between $g(r, \theta)$ and its angular average $g(r)$. Third column: configuration snapshots with ψ_6 color code as indicated in *e.g.* Fig. II.23. The red arrows indicate $\pi/4, 3\pi/4, 5\pi/4$ and $7\pi/4$.

Also at high persistence lengths, within the MIPS region, the square-shaped ϵ-space does not introduce anisotropic effects in the pair-correlation function as shown in Fig. II.37, which corresponds to the same parameters as in Fig. II.15. Indeed, $g(r, \theta) - g(r)$ shows a four-fold rotational symmetry at large r for $\phi = 0.6$. However, this is due to the stripe-shape coexistence and only indicates that the density distribution in x-direction is not the same as in y-direction at long distances. Anisotropic effects due to the square-shaped ϵ-space should manifest at small r. At small r anisotropic effects are undetectable within other sources of noise for all parameters.

The appendix contains an additional figure (Fig. A.12) for $n = 16$ and $\delta = 0.1$ with data in the liquid below the MIPS region and in the MIPS region confirming the effective isotropic dynamics.

If ϵ-induced anisotropic effects existed, they should also manifest in the shape of the

phase coexistence. For example, detectable anisotropic effects should compress the clusters more in the diagonal directions. This kind and comparable behavior are not observed.

Remark: Earlier studies [99] on self-propelled particles show that the pair-correlation function is anisotropic if measured with respect to the propulsion direction. Tagging a particle and assigning a polarity to it according to its propulsion direction, it is more likely to find particles in front of it than behind it. This behavior is also to expect for the kinetic Monte Carlo algorithm.

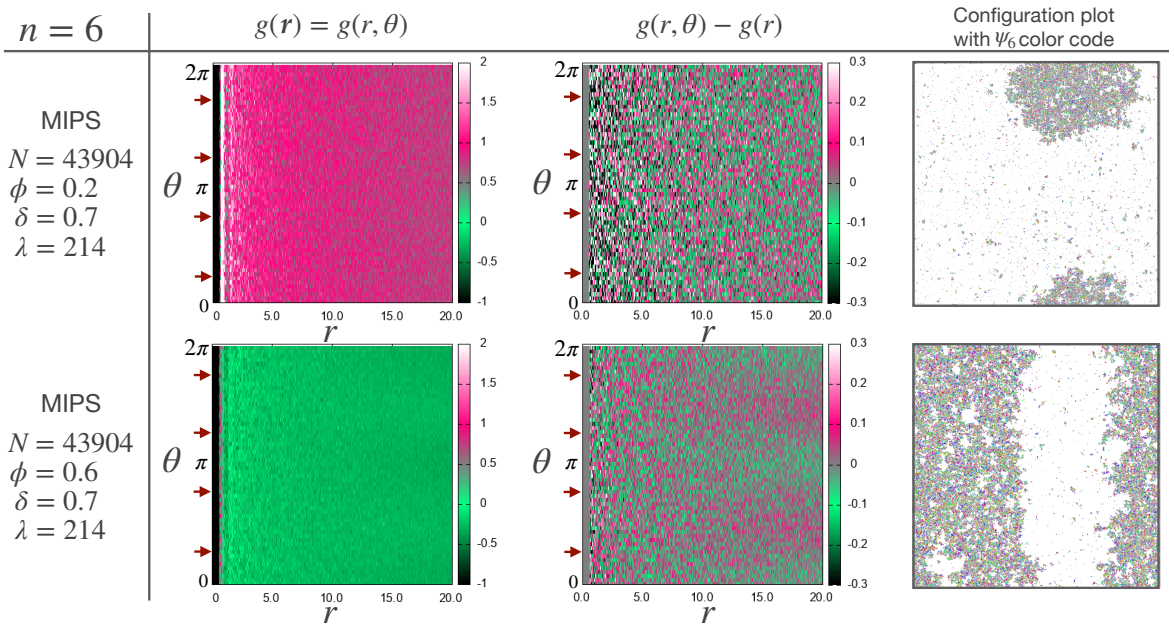


Figure II.37: **Evidence for effective isotropic dynamics in the MIPS region.** Data is for the potential with $n = 6$ at $\phi = 0.2$ and $\phi = 0.6$ for $N = 43904$ and persistence lengths inside the MIPS region with $\delta = 0.7$. First column: pair-correlation function $g(r, \theta)$ in polar coordinates averaged over 100 configurations. Second column: difference between $g(r, \theta)$ and its angular average $g(r)$. Third column: configuration snapshots with ψ_6 color code as indicated in *e.g.* Fig. II.23. The red arrows indicate $\pi/4, 3\pi/4, 5\pi/4$ and $7\pi/4$.

II.4 Dimensional reduction of the kinetic Monte Carlo dynamics

The previous section II.3 presented the full quantitative phase diagram of two-dimensional persistently moving particles. The phase diagram is plotted on a $\lambda - \phi$ plane, that is, on a two-parameter space, keeping the value of δ fixed. Different values of δ shift the phase transition lines, but the qualitative picture of the phase diagram remains unchanged. For example, the phase diagrams presented in subsection II.3.4 corresponds to $\delta = 0.1$, whereas the discussion about MIPS in subsection II.3.2 primary based on data for $\delta = 0.7$. This choice for δ was made in favor of a reduced run-time. Reasonable mixing times in standard equilibrium Monte Carlo are achieved by following the "*time-honored rule of thumb*" [42]: chose a δ, such that the Metropolis filter accepts on average every second displacement

(acceptance rate = rejection rate = $\frac{1}{2}$). This rule comes from two competing mechanisms: 1) if δ is very small, the change in the total energy in the Metropolis filter is small, thus the acceptance rate is high, but the change made in the configuration per Monte Carlo step is small; 2) large δ, on the other hand, lead to large changes in the configuration within one Monte Carlo step, but the acceptance rate decreases drastically.

In order to ensure high efficiency of the algorithm close to the equilibrium melting transitions, $\delta = 0.1$ was chosen to satisfy this "one-half rule" to study the two-dimensional melting. On the other hand, MIPS, as shown in the phase diagram, forms at relatively low densities and high persistence lengths. Following the "one-half rule", the lower density regime already favors larger δ. Furthermore, as particles within the dense liquid are kinetically arrested, changes in a MIPS configuration are mainly due to displacements of the particles in the gas phase and at the liquid-gas interface. Therefore, a computational speed-up can be achieved, if particles in the gas phase can move with big steps, thus additionally favoring larger δ.

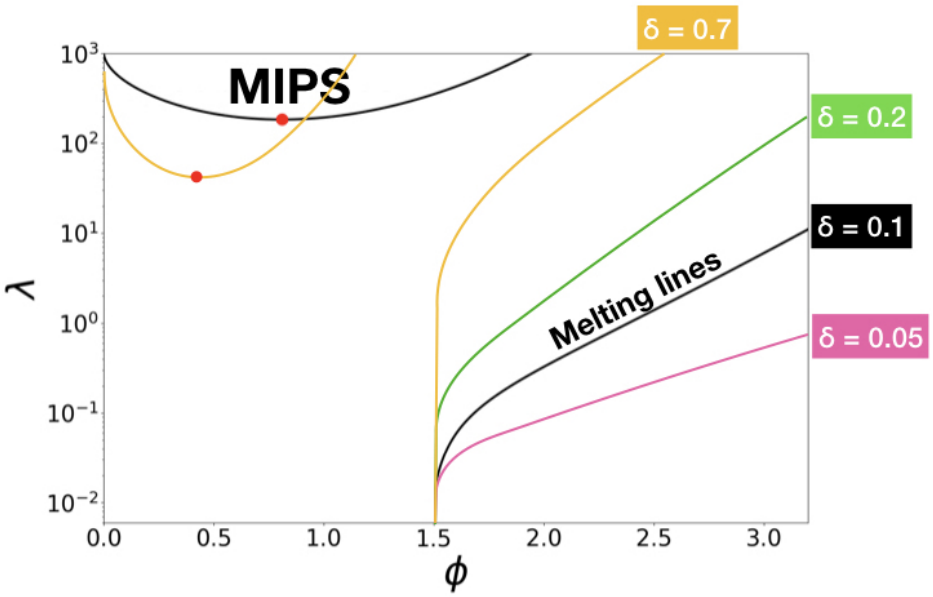


Figure II.38: **δ-dependence of the phase diagram.** Shown is the approximate tendency of the quantitative change of the phase diagram for different δ, indicated by colors.

This different choice of δ raises the question: if and how the phase diagram changes with δ? Fig. II.38 shows that with increasing δ, the MIPS region becomes narrower and the onset moves to smaller densities and smaller persistence lengths[12]. The linear-response regime of the melting transition extends up to larger λ with increasing δ. In the subsequent regime, the slope of the curves increases with δ (note the semi-log scale).

The question is whether it is possible to rescale the phase diagrams for different δ, such that the phase boundaries converge, leading to a unique phase diagram. This is the goal of this section, where primarily three questions are addressed:

1. Can the three independent parameters in the discrete-time Monte Carlo dynamics be

[12]The shift of the onset to smaller persistence lengths with increasing δ leads to an additional computational speed up for the investigation of MIPS for larger δ.

reduced to two relevant parameters?

2. How would this compare with the passive limit, where the system is known to have a single relevant parameter?

3. How do the dimensional reduction and its inherent limitation in the Monte Carlo dynamics extend to other stochastic Models of active Matter?

II.4.1 One-dimensional single particle: approximate dynamics

The dimensional reduction happens, when δ is small. Considering the numerical values of the parameters used in the simulations, this small-δ limit is justified. For an intuitive understanding this is first illustrated in an approximate version of the Monte Carlo dynamics. For a single particle in a one-dimensional confining potential $U(x)$, this dynamics is given by a discrete-time ($n = 0, 1, 2, \dots$) update rule:

$$\begin{aligned} \epsilon_{n+1} &= \epsilon_n + r_n + R\left(\frac{\epsilon_n}{\delta}\right), \qquad \text{with} \qquad \langle r_n\rangle = 0, \qquad \langle r_n r_{n'}\rangle = \sigma^2 \boldsymbol{\delta}_{n,n'}, \\ x_{n+1} &= x_n + \epsilon_n\, f(x_n, \epsilon_n), \qquad \text{with} \qquad f(x,\epsilon) = \min\left\{1, e^{-\frac{U(x+\epsilon)-U(x)}{k_{\mathrm{B}}T}}\right\}. \end{aligned} \tag{II.14}$$

Here R denotes the reflecting boundary at $\epsilon = \pm\delta$ (without specifying if further), $\boldsymbol{\delta}_{n,n'}$ is the Kronecker delta, and $f(x,\epsilon)$ is the mean acceptance due to the Metropolis filter.

For the small δ, a new set of rescaled coordinates is defined as

$$t = n\,\delta, \qquad v(t) = \frac{\epsilon_n}{\delta}, \qquad \xi(t) = \frac{r_n}{\delta^2}, \qquad x(t) = x_n.$$

This leads to the rescaled dynamics

$$\begin{aligned} \frac{v(t+\delta) - v(t)}{\delta} &= \xi(t) + \tilde{R}(v(t)), \qquad \text{with} \qquad \langle\xi(t)\rangle = 0, \qquad \langle\xi(t)\xi(t')\rangle = \frac{\sigma^2}{\delta^4}\,\boldsymbol{\delta}_{\frac{t}{\delta},\frac{t'}{\delta}} \\ \frac{x(t+\delta) - x(t)}{\delta} &= v(t)\, f\big(x(t), v(t)\delta\big). \end{aligned}$$

When δ is small, expanding in powers of δ, leads to

$$\begin{aligned} \dot{v}(t) &= \xi(t) + \tilde{R}(v(t)) + \mathcal{O}(\delta) \qquad \text{with} \qquad \langle\xi(t)\rangle = 0, \qquad \langle\xi(t)\xi(t')\rangle = \frac{1}{\lambda}\boldsymbol{\delta}(t-t') + \mathcal{O}(\frac{\delta}{\lambda}) \\ \dot{x}(t) &= v(t)\, f\big(x(t), v(t)\delta\big) + \mathcal{O}(\delta) \end{aligned}$$

where the definition $\lambda = \frac{\delta^3}{\sigma^2}$ is used and the continuous limit of the Kronecker delta $\boldsymbol{\delta}_{\frac{t}{\delta},\frac{t'}{\delta}} = \delta\,\boldsymbol{\delta}(t-t') + \mathcal{O}(\delta^2)$, with $\boldsymbol{\delta}(x)$ being the Dirac delta. Similarly expanding the Metropolis filter for small δ leads to

$$\begin{aligned} f\big(x(t), v(t)\delta\big) &= \min\left\{1, \exp\left(-\frac{U(x+\delta v) - U(x)}{k_{\mathrm{B}}T}\right)\right\} \\ &= \min\left\{1, \exp\left(-\delta v \frac{U'(x)}{k_{\mathrm{B}}T} - \frac{\delta^2 v^2}{2}\frac{U''(x)}{k_{\mathrm{B}}T} + \cdots\right)\right\}. \end{aligned}$$

Defining $\Gamma_1 = \frac{\delta}{k_B T}$, it follows

$$\begin{aligned} f\big(x(t), v(t)\delta\big) &= \min\left\{1, \exp\left(-\Gamma_1 v U'(x)\big[1 + \frac{\delta v}{2}\frac{U''(x)}{U'(x)} + \cdots\big]\right)\right\} \\ &\approx \min\left\{1, \exp\left(-\Gamma_1 v U'(x)\right)\right\}\,, \quad \text{if } \delta\frac{U''(x)}{U'(x)} \ll 1 \\ &= h(x(t), v(t))\,. \end{aligned} \tag{II.15}$$

This leads to the continuous dynamics in these rescaled coordinates

$$\dot{v}(t) = \xi(t) + \tilde{R}(v(t)) + \mathcal{O}(\delta)\,, \text{ with } \langle\xi(t)\rangle = 0, \langle\xi(t)\xi(t')\rangle = \frac{1}{\lambda}\boldsymbol{\delta}(t-t') + \mathcal{O}(\frac{\delta}{\lambda}) \tag{II.16a}$$

$$\dot{x}(t) = v(t)\, h\big(x(t), v(t)\big) + \mathcal{O}(\delta) + \mathcal{O}\left(\delta\frac{U''(x)}{U'(x)}\right)\,. \tag{II.16b}$$

There are only two relevant parameters in this continuous dynamics, given by

$$\Gamma_1 = \frac{\delta}{k_B T}\,, \text{ and } \lambda = \frac{\delta^3}{\sigma^2}\,.$$

Even though the starting dynamics is an approximation to the kinetic Monte Carlo update, it correctly describes the relevant parameters, which is shown later. However, this dimensional reduction has its range of validity and this can be seen from the subleading order terms, which are ignored in the small-δ limit. This parameter range is given by:

1. $\delta \ll \lambda$ (for $\xi(t)$ correlation term),
2. $\delta \ll \frac{1}{\sqrt{\lambda}}$ (as δ has to be smaller than $\xi(t)$ in the equation for $v(t)$ which is of order $\xi \sim \frac{1}{\sqrt{\lambda}}$), and
3. $\delta \ll 1$ and $\delta \ll \frac{U'(x)}{U''(x)}$.

The last condition is particularly interesting: for a confining one-dimensional power-law potential (II.9) the condition translates to $\delta \ll |L - x|$. This means, near the box wall ($x \sim L - \delta$) the above continuous description breaks down, as the subleading order terms become non-negligible. In the many-particle system, this is equivalent to demanding δ much smaller than the global mean inter-particle distance d.

In summary, this continuous dynamics could break down (1) in the passive limit, (2) at very high persistence lengths, and (3) at high density.

The primary goal of this analysis is to see from (II.16a) and (II.16b) that the four parameters in the dynamics described by (II.14) reduce to only two relevant parameters λ and Γ in the small-δ limit. As long as these two parameters are kept fixed the probability distribution is invariant, thus providing a scaling for a change in δ.

II.4.2 Exact analysis of the kinetic Monte Carlo dynamics

The approximate dynamics in (II.14) illustrates how to reduce the relevant number of parameters. Here the goal is to achieve this starting from the exact discrete-time Master equation of the kinetic Monte Carlo dynamics.

a) Discrete-time Master equation for a single particle

The kinetic Monte Carlo dynamics is Markovian in the (x, ϵ) parameter space, where time is discrete and denoted again by $n = 0, 1, 2, \ldots$. The conditional probability for a transition $(y, \epsilon') \to (x, \epsilon)$ in one time step is given by the Markov matrix

$$M(x, \epsilon | y, \epsilon') = g(\epsilon, \epsilon') W_\epsilon(x, y) \,, \tag{II.17}$$

where, ϵ is sampled with probability $g(\epsilon, \epsilon')$ and $W_\epsilon(x, y)$ is due to the Metropolis filter. In the appendix A.1 it is shown that the conditional probability for ϵ, given the previous displacement ϵ', satisfies

$$g(\epsilon, \epsilon') = \frac{1}{2\delta} + \frac{1}{\delta} \sum_{k=1}^{\infty} \exp\left[-\frac{\pi^2 \sigma^2 k^2}{8\delta^2} \right] \cos\left(\frac{k\pi}{2\delta}(\epsilon + \delta) \right) \cos\left(\frac{k\pi}{2\delta}(\epsilon' + \delta) \right) \,. \tag{II.18}$$

Using the Metropolis filter (II.1), gives

$$W_\epsilon(x, y) = f(y, \epsilon)\, \boldsymbol{\delta}(x - y - \epsilon) + [1 - f(y, \epsilon)]\, \boldsymbol{\delta}(x - y)$$

where $f(x, \epsilon)$ defined earlier in (II.14) can be rewritten as

$$f(y, \epsilon) = 1 - \Theta\left(\frac{U(y + \epsilon) - U(y)}{k_{\rm B} T} \right) \left\{ 1 - \exp\left(-\frac{U(y + \epsilon) - U(y)}{k_{\rm B} T} \right) \right\}, \tag{II.19}$$

with $\Theta(x)$ being the Heaviside step function. This gives the discrete-time Master equation

$$\begin{aligned} P_{n+1}(x, \epsilon) &= \int dy \int_{-\delta}^{\delta} d\epsilon'\, M(x, \epsilon | y, \epsilon') P_n(y, \epsilon') \\ &= \int_{-\delta}^{\delta} d\epsilon' g(\epsilon, \epsilon') \left\{ f(x - \epsilon, \epsilon) P_n(x - \epsilon, \epsilon') + [1 - f(x, \epsilon)] P_n(x, \epsilon') \right\} \,. \end{aligned} \tag{II.20}$$

Remarks:

1. The essential Markov property $\int dx d\epsilon M(x, \epsilon | y, \epsilon') = 1$, which is required to preserve probability, is satisfied, as $\int dx W_\epsilon(x, y) = 1$, and $\int d\epsilon g(\epsilon, \epsilon') = 1$.

2. The approximate dynamics $x_{n+1} = x_n + \epsilon_n f(x, \epsilon)$ in (II.14), with the average acceptance $f(x, \epsilon)$, would have a different Master equation

$$P_{n+1}(x, \epsilon) \simeq \int d\epsilon' g(\epsilon, \epsilon') P_n\left(x - \epsilon' f(x, \epsilon), \epsilon' \right) \,.$$

3. The expression (II.18) is equivalent to

$$g(\epsilon, \epsilon') = \frac{1}{\delta} \sum_{k=-\infty}^{\infty} \left\{ \frac{\exp\left[-\frac{\left(\frac{\epsilon - \epsilon'}{\delta} + 4k \right)^2}{2\frac{\sigma^2}{\delta^2}} \right]}{\sqrt{2\pi \frac{\sigma^2}{\delta^2}}} + \frac{\exp\left[-\frac{\left(-\frac{\epsilon + \epsilon' + 2\delta}{\delta} + 4k \right)^2}{2\frac{\sigma^2}{\delta^2}} \right]}{\sqrt{2\pi \frac{\sigma^2}{\delta^2}}} \right\} \,, \tag{II.21}$$

which can be seen by using
$\vartheta_3(\frac{\pi}{2}z, e^{-\pi^2 t}) = 1 + 2\sum_{k=1}^{\infty} e^{-\pi^2 k^2 t}\cos(k\pi z) = \frac{1}{\sqrt{\pi t}}\sum_{k=-\infty}^{\infty} e^{-\frac{(z+2k)^2}{4t}}$. In this second expression for $g(\epsilon,\epsilon')$, the connection to the well-known mirror charge solution of the diffusion equation for reflecting boundary conditions becomes apparent.

b) Passive limit

It is now verified that detailed balance is recovered in the passive limit $\frac{\sigma^2}{\delta^2} \to \infty$.

Defining $P_n(x) = \int_{-\delta}^{\delta} d\epsilon P_n(x,\epsilon)$, the Master equation (II.20) can be written in an useful alternative form

$$P_{n+1}(x) = P_n(x) + \int_{-\delta}^{\delta} d\epsilon \int_{-\delta}^{\delta} d\epsilon' g(\epsilon,\epsilon') \left\{ f(x-\epsilon,\epsilon) P_n(x-\epsilon,\epsilon') - f(x,\epsilon) P_n(x,\epsilon') \right\} . \quad \text{(II.22)}$$

In the passive limit, it is easy to see from (II.18) that $g(\epsilon,\epsilon') = \frac{1}{2\delta}$, thus

$$P_{n+1}(x) = P_n(x) + \frac{1}{2\delta} \int_{-\delta}^{\delta} d\epsilon \left\{ f(x-\epsilon,\epsilon) P_n(x-\epsilon) - f(x,\epsilon) P_n(x) \right\} . \quad \text{(II.23)}$$

In the steady state $P_{n+1}(x) = P_n(x)$, thus

$$\int d\epsilon f(x-\epsilon,\epsilon) P_n(x-\epsilon) = \int d\epsilon f(x,\epsilon) P_n(x) = \int d\epsilon f(x,-\epsilon) P_n(x) \quad \text{(II.24)}$$

(with $\epsilon \to -\epsilon$ in the last line). Using (II.23) and (II.24), it is now trivial to verify that detailed balance is satisfied with the Gibbs-Boltzmann probability:

$$\frac{P_n(x-\epsilon)}{P_n(x)} = \frac{f(x,-\epsilon)}{f(x-\epsilon,\epsilon)} = \frac{\min\left\{1, \exp\left(-\frac{U(x-\epsilon)-U(x)}{k_B T}\right)\right\}}{\min\left\{1, \exp\left(-\frac{U(x)-U(x-\epsilon)}{k_B T}\right)\right\}} = \exp\left(-\frac{U(x-\epsilon)-U(x)}{k_B T}\right) . \quad \text{(II.25)}$$

c) Dimensional reduction in the small-δ limit

It is shown later that for small δ, the passive and the persistent limit behave differently. Different sets of rescaled coordinates are defined in the two limits. In the persistent limit, a ballistic scaling is chosen

$$t = n\,\delta, \qquad v = \frac{\epsilon}{\delta}, \qquad x = x\,, \quad \text{(II.26)}$$

whereas in the passive limit a diffusive scaling is chosen

$$t = n\,\delta^2, \qquad v = \frac{\epsilon}{\delta}, \qquad x = x\,. \quad \text{(II.27)}$$

The reason for this scaling is to reduce the effective number of parameters in the dynamics.

Persistent limit

The discrete-time Master equation (II.20) can be rewritten as

$$P_{n+1}(x,\epsilon) = \int d\epsilon' g(\epsilon,\epsilon') P_n(x,\epsilon') + \int d\epsilon' g(\epsilon,\epsilon') \left\{ f(x-\epsilon,\epsilon) P_n(x-\epsilon,\epsilon') - f(x,\epsilon) P_n(x,\epsilon') \right\} . \tag{II.28}$$

Under the ballistic scaling (II.26) the rescaled probability satisfies $\frac{1}{\delta}\tilde{P}_t(x,v) = P_n(x,\epsilon)$ and $\frac{1}{\delta}\tilde{g}(v,v') = g(\epsilon,\epsilon')$ (from normalization arguments) thus (II.28) becomes

$$\tilde{P}_{t+\delta}(x,v) = \int dv' \tilde{g}(v,v') \tilde{P}_t(x,v') + \int dv' \tilde{g}(v,v') \left\{ f(x-\delta v,\delta v) \tilde{P}_t(x-\delta v,\delta v') - f(x,\delta v) \tilde{P}_t(x,\delta v') \right\} .$$

Using the definition of $h(x,v) \simeq f(x,\delta v)$ in (II.15) in the small-δ limit, expending the x components in powers of δ and the v components in terms of $(v'-v)$ the equation becomes

$$\tilde{P}_t(x,v) + \delta \frac{\partial}{\partial t}\tilde{P}_t(x,v) + \cdots = \int dv' \tilde{g}(v,v') [\tilde{P}_t(x,v) + (v'-v)\partial_v \tilde{P}_t(x,v) + \frac{(v'-v)^2}{2}\partial_v^2 \tilde{P}_t(x,v) + \cdots] - \delta \int dv' \tilde{g}(v,v') v \frac{\partial}{\partial x} \left\{ h(x,v) \tilde{P}_t(x,v') \right\} + \cdots , \tag{II.29}$$

where orders $\geq \mathcal{O}(\delta^2)$ where neglected. With $\int dv'\, \tilde{g}(v,v') = 1$ it follows

$$\frac{\partial}{\partial t}\tilde{P}_t(x,v) = \frac{a_1(v)}{\delta}\partial_v \tilde{P}_t(x,v) + \frac{a_2(v)}{2\delta}\partial_v^2 \tilde{P}_t(x,v) - \int dv' \tilde{g}(v,v') v \frac{\partial}{\partial x} \left\{ h(x,v) \tilde{P}_t(x,v') \right\} + \cdots ,$$

where

$$a_n(v) = \int dv' (v'-v)^n \tilde{g}(v,v') .$$

At this point, one may continue using the expression (II.21) for $\tilde{g}(v,v')$, where the reflecting boundary is inbuilt in the expression. Alternatively, the expression

$$\tilde{g}(v,v') = \frac{1}{\sqrt{2\pi\frac{\delta}{\lambda}}} \exp\left[-\frac{(v-v')^2}{2\frac{\delta}{\lambda}} \right]$$

can be used (which is the free case) in combination with a zero-current condition on $\tilde{P}_t(x,v)$ for the reflecting boundary. Both choices describe the same result. In this alternative description, however, it is easy to see that $a_1(v) = 0$ due to symmetry, and $a_2(v) = \frac{\delta}{\lambda}$, leading to a Fokker-Planck equation

$$\frac{\partial}{\partial t}\tilde{P}_t(x,v) = \frac{1}{2\lambda}\partial_v^2 \tilde{P}_t(x,v) - \frac{\partial}{\partial x} \left\{ v h(x,v) \tilde{P}_t(x,v) \right\} . \tag{II.30}$$

with the reflecting boundary condition

$$\frac{\partial}{\partial v}\tilde{P}_t(x,v) = 0 \qquad \text{for } v = \pm 1.$$

Here the definitions $\lambda = \frac{\delta^3}{\sigma^2}$ and $\Gamma_1 = \frac{\delta}{k_B T}$ are used. Equation (II.30) shows that the probability depends on this two parameters only.

Remarks:

1. The above Fokker-Planck equation is equivalent to the coupled Langevin equation (II.16).
2. The scaling in (II.26) for small δ means that the Monte Carlo dynamics of x_n for $n \gg 1$ is equivalent to the continuous dynamics of $x(t)$ for $t \gg \delta$, provided they both have the same λ and Γ_1. This also suggests that both dynamics have the same steady-state distribution.
3. This equivalence may break down if the subleading terms in the derivation (II.29) become non-negligible, giving rise to the same criteria discussed earlier in subsection II.4.1 for the approximate dynamics.
4. Until now the potential $U(x)$ is general. The specific power-law potential offers a redefinition of Γ_1.

Passive limit

In the passive limit, it was noted [13] that there is a single relevant parameter when $U(r)$ is a power-law potential. Clearly, this cannot be achieved from the two parameters λ and Γ_1 in the persistent limit. The limitation of the above continuous description was already suggested by the first criteria in subsection II.4.1. This indicates, a different dynamics for the passive case, which can be obtained using the diffusive scaling in (II.27) in the discrete-time Master equation (II.20).

In the passive limit, the conditional probability distribution for ϵ is given by $g(\epsilon, \epsilon') = \frac{1}{2\delta}$, *i.e.*, ϵ is uniformly chosen in the interval $[-\delta, \delta]$. Using this in (II.22) and integrating over ϵ leads to

$$P_{n+1}(x) = P_n(x) + \frac{1}{2\delta}\int_{-\delta}^{\delta} d\epsilon \left\{ f(x-\epsilon,\epsilon)P_n(x-\epsilon) - f(x,\epsilon)P_n(x) \right\} ,$$

giving the evolution of the probability of x only. Using the diffusive scaling in (II.27) it follows

$$\tilde{P}_{t+\delta^2}(x) = \tilde{P}_t(x) + \frac{1}{2}\int_{-1}^{1} dv \left\{ f(x-\delta v,\delta v)\tilde{P}_t(x-\delta v) - f(x,\delta v)\tilde{P}_t(x) \right\} ,$$

with $\tilde{P}_t(x) = P_n(x)$. Expanding in powers of small δ leads to

$$\tilde{P}_{t+\delta^2}(x) = \tilde{P}_t(x) - \frac{\delta}{2}\frac{d}{dx}[A(x)\tilde{P}_t(x)] + \frac{\delta^2}{4}\frac{d^2}{dx^2}[B(x)\tilde{P}_t(x)] + \cdots ,$$

with the definitions

$$A(x) = \int_{-1}^{1} dv\, v\, f(x,\delta v)\,, \text{ and } B(x) = \int_{-1}^{1} dv\, v^2\, f(x,\delta v)\,. \tag{II.31}$$

Using the expression for $f(x,\delta v)$ in (II.19) it follows

$$\begin{aligned} A(x) =& \int_{-1}^{1} dv\, v \; - \int_{-1}^{1} dv\, v\, \Theta\Big(\frac{U(x+\delta v)-U(x)}{k_{\rm B}T}\Big)\Big\{1-e^{-\frac{U(x+\delta v)-U(x)}{k_{\rm B}T}}\Big\} \\ =& -\int_{-1}^{1} dv\, v\, \Theta\Big(-\frac{\delta v\, F(x)}{k_{\rm B}T}\Big)\Big\{1-e^{\frac{\delta v\, F(x)}{k_{\rm B}T}}\Big\}+\cdots \\ =& \frac{\delta\, F(x)}{k_{\rm B}T}\int_{-1}^{1} dv\, v^2\, \Theta\Big(-v\, F(x)\Big)+\cdots\,, \end{aligned}$$

with the force $F(x) = -\frac{\partial}{\partial x}U(x)$ and a Taylor expansion for $\delta \to 0$ of the exponential in the last line. The two cases $F(x) > 0$ and $F(x) < 0$ lead to the same result for the integral ($\frac{1}{3}$), thus giving

$$A(x) = \frac{\delta\, F(x)}{3k_{\rm B}T} + \cdots\,.$$

In a same way it follows for $B(x)$ (the term with $\Theta(..)$ contributes to order δ and is thus neglected)

$$B(x) = \frac{2}{3} + \mathcal{O}(\delta)$$

Together, this leads to

$$\tilde{P}_{t+\delta^2}(x) = \tilde{P}_t(x) - \frac{\delta^2}{6k_{\rm B}T}\frac{d}{dx}[F(x)\tilde{P}_t(x)] + \frac{\delta^2}{6}\frac{d^2}{dx^2}[\tilde{P}_t(x)] + \cdots\,,$$

resulting in the well-known Fokker-Planck equation for a passive particle in a potential

$$\frac{\partial \tilde{P}_t(x)}{\partial t} = -\frac{1}{k_{\rm B}T}\frac{\partial}{\partial x}[F(x)\tilde{P}_t(x)] + \frac{\partial^2}{\partial x^2}[\tilde{P}_t(x)]\,. \tag{II.32}$$

Remarks:

1. This corresponds to the standard Langevin description of a passive particle
$$\dot{x}(t) = \beta F(x) + \eta(t) \qquad \langle \eta(t)\eta(t')\rangle = 2\boldsymbol{\delta}(t-t') \tag{II.33}$$
2. The steady-state probability $P(x) \sim e^{-\frac{U(x)}{k_{\rm B}T}}$, thus the single relevant parameter is composed by the ratio $\frac{U(x)}{k_{\rm B}T}$.
3. If the ballistic scaling (II.26) was used for the passive case, it would have resulted in
$$\frac{\partial P_t(x)}{\partial t} = \frac{\Gamma_1}{6}\frac{\partial}{\partial x}[F(x)P_t(x)]\,, \tag{II.34}$$
which clearly does not capture the correct Physics!

This analysis shows that for small δ the persistent limit has two relevant parameters (Γ_1 and λ) and the passive limit has a single parameter. There is no smooth transition between the two limits when δ is small. Furthermore, it was demonstrated that the order of the limits $\delta \to 0$ and $\lambda \to 0$ is not exchangeable.

d) Multi-particle continuous limit for small δ

It follows the generalization of the above single-particle case to the N-particle case with a inter-particle potential $U[\mathbf{x}]$, where $\mathbf{x} = \{x_1, \cdots, x_N\}$. The goal is to determine the relevant parameters in this case.

Persistent limit

The following continuous-time[13] N-particle Fokker-Planck equation ($\sim$-notation removed for simplicity) corresponds to (II.30)

$$\frac{\partial}{\partial t} P_t[\mathbf{x},\mathbf{v}] = \frac{1}{2\lambda} \sum_i \frac{\partial^2}{\partial v_i^2} P_t[\mathbf{x},\mathbf{v}] - \sum_i \frac{\partial}{\partial x_i} \left\{ v_i h_i(\mathbf{x}, v_i) P_t[\mathbf{x},\mathbf{v}] \right\} , \tag{II.35}$$

with the reflecting boundary condition

$$\frac{\partial}{\partial v_i} P_t[\mathbf{x},\mathbf{v}] = 0 \qquad \text{for } v_i = \pm 1.$$

Here,

$$h_i(\mathbf{x}, v_i) = \min \left\{ 1, e^{\Gamma_1 v_i F_i[\mathbf{x}]} \right\} , \qquad \text{with force on } x_i \qquad F_i[\mathbf{x}] = -\frac{\partial U[\mathbf{x}]}{\partial x_i} .$$

The equivalent Langevin description is

$$\dot{v}_i(t) = \xi_i(t) + R(v_i(t)) \quad \text{with} \quad \langle \xi_i(t) \rangle = 0, \quad \langle \xi_i(t) \xi_j(t') \rangle = \frac{1}{\lambda} \boldsymbol{\delta}_{i,j} \boldsymbol{\delta}(t - t') \tag{II.36a}$$

$$\dot{x}_i(t) = v_i(t)\, h_i\big(\mathbf{x}(t), v_i(t)\big) . \tag{II.36b}$$

Power-law interaction potential

For the specific choice of the inverse power-law inter-particle potential in (II.10) with $n = 6$, the force on particle i is

$$F_i[\mathbf{x}] = 6 u_0 \gamma^6 \sum_{j \neq i} \frac{1}{(x_i - x_j)^7} .$$

With this specific choice, the number of parameters in the continuum description can be further reduced, by scaling the length scales with the global average inter-particle distance

$$d = \frac{L}{N} = \frac{\gamma}{\phi} ,$$

with L being the system size, and the density

$$\phi = \frac{\gamma N}{L} .$$

[13] Here the number of particles N is already incorporated in a rescaled time unit.

With the following new scaled coordinates

$$\tilde{t} = \frac{t}{d}, \qquad \tilde{v}(\tilde{t}) = v(t), \qquad \tilde{x}(\tilde{t}) = \frac{x(t)}{d}, \qquad \tilde{\xi}(\tilde{t}) = d\,\xi(t)\,,$$

it can be checked that the corresponding probability in the scaled coordinate is given by the same form as (II.35)

$$\frac{\partial}{\partial \tilde{t}} \tilde{P}_{\tilde{t}}[\tilde{\mathbf{x}}, \tilde{\mathbf{v}}] = \frac{1}{2\tilde{\lambda}} \sum_i \frac{\partial^2}{\partial \tilde{v}_i^2} \tilde{P}_{\tilde{t}}[\tilde{\mathbf{x}}, \tilde{\mathbf{v}}] - \sum_i \frac{\partial}{\partial \tilde{x}_i} \left\{ \tilde{v}_i h_i(\tilde{\mathbf{x}}, \tilde{\mathbf{v}}_i) \tilde{P}_{\tilde{t}}[\tilde{\mathbf{x}}, \tilde{\mathbf{v}}] \right\}, \tag{II.37}$$

with a new

$$h_i(\tilde{\mathbf{x}}, \tilde{v}_i) = \min \left\{ 1, \exp \left(\Gamma \tilde{v}_i \sum_{j \neq i} \frac{1}{(\tilde{x}_i - \tilde{x}_j)^7} \right) \right\},$$

and

$$\tilde{\lambda} = \frac{\lambda}{d}, \text{ and } \Gamma = \frac{6 u_0 \gamma^6 \delta}{k_B T d^7}.$$

In a similar way, also the scaling parameters in the Langevin equations can be reduced to two. For numerical confirmation, see Fig. II.39a.

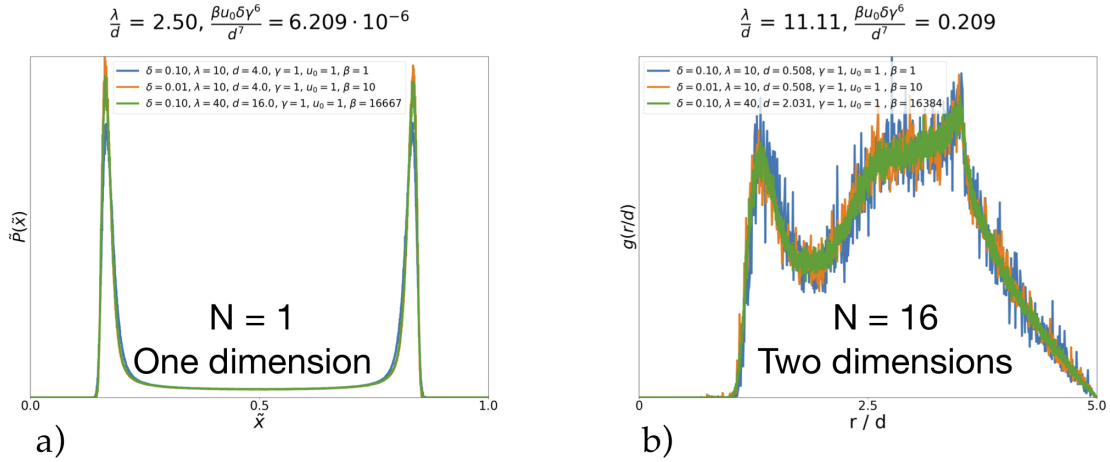


Figure II.39: **Scaling collapse for different δ.** a) One-dimensional case: Histogram of the position of a single particle in a potential (same case as in subsection II.2.1). Shown is data for different δ, λ and β, but constant $\frac{\lambda}{d}$ and $\frac{\beta u_0 \delta \gamma^6}{d^7}$. b) Two-dimensional many-particle case: Pair-correlation function, again for different δ, λ and β, but constant $\frac{\lambda}{d}$ and $\frac{\beta u_0 \delta \gamma^6}{d^7}$.

Remarks:

1. Equation (II.37) implies that the active/persistent (with limitations) phase behavior can be characterized by only two parameters, which can also be expressed in terms of the dimensionless density ϕ

$$\tilde{\lambda} = \frac{\delta^3}{\sigma^2 \gamma} \phi \text{ and } \Gamma = \frac{u_0}{k_B T} \frac{6\delta}{\gamma} \phi^7.$$

2. Equivalently, the scaled steady-state probability $P\left(\frac{x}{\gamma}\sqrt{\pi\phi}\right)$ is determined by $\tilde{\lambda}$ and Γ. There is still a third parameter, which is the spatial range of $\tilde{x}$, which is the rescaled system size. However, when the system size is large as in the case concerning the main results of this thesis, this dependence is only in the subleading order in the system size.

3. It is straightforward to generalize (II.37) to higher dimensions. For example, in two dimensions, where $\phi = \frac{N\gamma^2}{V}$ and $d = \sqrt{\frac{V}{N\pi}} = \frac{\gamma}{\sqrt{\pi\phi}}$, the two relevant parameters are $\tilde{\lambda} = \frac{\delta^3}{\sigma^2\gamma}\sqrt{\pi\phi}$ and $\Gamma = \frac{u_0}{k_\mathrm{B}T}\frac{6\delta}{\gamma}(\pi\phi)^{7/2}$ (see Fig. II.39b).

Passive limit

A straightforward generalization of (II.32) gives

$$\frac{\partial}{\partial t}P_t[\mathbf{x}] = -\frac{1}{6}\left[\frac{6\gamma^6 u_0}{k_\mathrm{B}T}\right]\sum_i \frac{\partial}{\partial x_i}\left\{\sum_{j\neq i}\frac{1}{(x_i-x_j)^7}P_t[\mathbf{x}]\right\} + \frac{1}{6}\sum_i \frac{\partial^2}{\partial x_i^2}P_t[\mathbf{x}]\,.$$

The second re-scaling with the global mean inter-particle distance requires for the passive limit again the diffusive scaling in time, thus

$$\tilde{t} = \frac{t}{d^2}, \qquad \tilde{x}(\tilde{t}) = \frac{x(t)}{d}\,.$$

The Fokker-Planck equation becomes

$$\frac{\partial}{\partial \tilde{t}}\tilde{P}_{\tilde{t}}[\tilde{\mathbf{x}}] = -\frac{1}{6}\Gamma_0\sum_i \frac{\partial}{\partial \tilde{x}_i}\left\{\sum_{j\neq i}\frac{1}{(\tilde{x}_i-\tilde{x}_j)^7}P_{\tilde{t}}[\tilde{\mathbf{x}}]\right\} + \frac{1}{6}\sum_i \frac{\partial^2}{\partial \tilde{x}_i^2}P_{\tilde{t}}[\tilde{\mathbf{x}}]\,, \tag{II.38}$$

with

$$\Gamma_0 = \begin{cases} \frac{6u_0\gamma^6}{k_\mathrm{B}Td^6}\,, & \text{in 1D} \\ \frac{6u_0}{k_\mathrm{B}T}(\pi\phi)^3\,, & \text{in 2D}\,. \end{cases}$$

The probability only depends on Γ_0, as reported earlier [13].

Remark:
The original kinetic Monte Carlo dynamics has three independent relevant parameters, δ, σ and $\frac{U(x)}{k_\mathrm{B}T}$. For the multi-particle case, following a similar analysis as above, these three parameters can be written as

$$\frac{\delta}{d}\,,\ \frac{\lambda}{d}\,,\ \text{and}\ \Gamma_0\,.$$

This three-parameter space covers the entire phase diagram, including the passive limit. The reduction to two parameters can be done when δ is small. However, this leads to a singular behavior, where the passive and the persistent limit are described by different sets of parameters, without a smooth interpolation between the two regimes. This is related to the non-exchangeable order of limits $\delta \to 0$ and $\lambda \to 0$.

II.4.3 Continuous limit following standard steps

The analysis in the previous subsection II.4.2 shows that the same set of reduced scaling parameters cannot be used for the passive and the persistent limit. Is this singular behavior due to the discrete nature of the Monte Carlo dynamics? This is investigated in this subsection II.4.3 by defining the continuous limit of the kinetic Monte Carlo dynamics *without taking δ small* by following standard procedures (*e.g.* [40, 208, 209]).

The discrete-time dynamics is (II.20) with the transition probability (II.17). In the standard approach to the continuous limit, it is considered that one MC step takes the time dt. The continuous limit is then recovered by taking the limit $dt \to 0$. However, in order to follow this standard procedure, the transition probability (II.17) needs to be adjusted such that $dt \to 0$ makes sense. There are two important considerations:

1. in the $dt \to 0$ limit, the system has no time to jump, thus
$$\lim_{dt\to 0} M_{dt}(x,\epsilon|y,\epsilon') = \boldsymbol{\delta}(x-y)\,\boldsymbol{\delta}(\epsilon-\epsilon')\,,$$
with the subscript denoting the transition time dt.
2. if $dt = 1$, the Monte Carlo transition probability in (II.17) should be recovered for all transitions
$$M_{dt=1}(x,\epsilon|y,\epsilon') = M(x,\epsilon|y,\epsilon')\,.$$

These two considerations are met with the choice

$$M_{dt}(x,\epsilon|y,\epsilon') = \frac{\exp\left[-\frac{(\epsilon-\epsilon')^2}{2\sigma^2 dt}\right]}{\sqrt{2\pi\sigma^2 dt}}\left[\boldsymbol{\delta}(x-y)+dt\left\{f(y,\epsilon)\,\boldsymbol{\delta}(x-y-\epsilon)-f(y,\epsilon)\,\boldsymbol{\delta}(x-y)\right\}\right]+\cdots\,.$$

This choice, which is not unique, can be justified self-consistently (see the following paragraph "Self-consistency check"). There is no reflecting boundary in ϵ, which is later treated as a zero-current condition.

Using this in (II.20) leads to the continuous-time Master equation:

$$\begin{aligned} P_{t+dt}(x,\epsilon) &= \int dy \int d\epsilon'\, M_{dt}(x,\epsilon|y,\epsilon')P_t(y,\epsilon') \\ &= \int d\epsilon'\, g_{dt}(\epsilon,\epsilon')P_t(x,\epsilon') \\ &\quad + dt\int d\epsilon'\, g_{dt}(\epsilon,\epsilon')\left\{f(x-\epsilon,\epsilon)\,P_t(x-\epsilon,\epsilon') - f(x,\epsilon)\,P_t(x,\epsilon')\right\}, \end{aligned} \tag{II.39}$$

where

$$g_{dt}(\epsilon,\epsilon') = \frac{\exp\left[-\frac{(\epsilon-\epsilon')^2}{2\sigma^2 dt}\right]}{\sqrt{2\pi\sigma^2 dt}}\,.$$

The Kramers-Moyal expansion (see subsection I.3.2) as Taylor expansion for small dt is used, to go from the Master equation to the Fokker-Planck equation. For example, in the first term $P_t(x,\epsilon') = P_t(x,\epsilon) + (\epsilon'-\epsilon)\frac{d}{dx}P_t(x,\epsilon) + \cdots$, and thus

$$\int d\epsilon'\, g_{dt}(\epsilon,\epsilon')\,P_t(x,\epsilon') = a_0(\epsilon)\,P_t(x,\epsilon) - \frac{\partial}{\partial\epsilon}[a_1(\epsilon)\,P_t(x,\epsilon)] + \frac{1}{2}\frac{\partial^2}{\partial\epsilon^2}[a_2(\epsilon)\,P_t(x,\epsilon)]\,,$$

with

$$a_0(\epsilon) = \int d\epsilon'\, g_{dt}(\epsilon', \epsilon) = 1$$
$$a_1(\epsilon) = \int d\epsilon'\, (\epsilon' - \epsilon)\, g_{dt}(\epsilon', \epsilon) = 0$$
$$a_2(\epsilon) = \int d\epsilon'\, (\epsilon' - \epsilon)^2\, g_{dt}(\epsilon', \epsilon) = dt\, \sigma^2\,.$$

This gives

$$\int d\epsilon'\, g_{dt}(\epsilon, \epsilon')\, P_t(x, \epsilon') = P_t(x, \epsilon) + dt \frac{\sigma^2}{2} \frac{\partial^2}{\partial \epsilon^2} P_t(x, \epsilon)\,. \tag{II.40}$$

In the second term of the above Master equation, the leading contribution comes from $dt \to 0$. Using $g_{dt\to 0}(\epsilon, \epsilon') = \boldsymbol{\delta}(\epsilon - \epsilon')$, it follows

$$\int d\epsilon'\, g_{dt}(\epsilon, \epsilon') \Big\{ f(x-\epsilon, \epsilon)\, P_t(x-\epsilon, \epsilon') - f(x, \epsilon)\, P_t(x, \epsilon') \Big\} = f(x-\epsilon, \epsilon)\, P_t(x-\epsilon, \epsilon) - f(x, \epsilon)\, P_t(x, \epsilon) + \cdots\,. \tag{II.41}$$

Substituting (II.40) and (II.41), in the Master equation (II.39) results in the Fokker-Planck equation

$$\partial_t P_t(x, \epsilon) = \frac{\sigma^2}{2} \frac{\partial^2}{\partial \epsilon^2} P_t(x, \epsilon) + f(x - \epsilon, \epsilon) P_t(x - \epsilon, \epsilon) - f(x, \epsilon) P_t(x, \epsilon)\,, \tag{II.42}$$

with the reflecting boundary added as an additional zero-current condition at $\epsilon = \pm\delta$

$$\left. \frac{\partial P_t(x, \epsilon)}{\partial \epsilon} \right|_{\epsilon = \pm\delta} = 0\,. \tag{II.43}$$

This analysis shows that on a coarse-grained time scale (number of Monte Carlo steps $\gg 1$), the Monte Carlo dynamics is described by the above continuum description (II.42).

Self-consistency check

1. Integrating (II.42) over ϵ, gives

   $$\partial_t P_t(x) = \int_{-\delta}^{\delta} d\epsilon \Big[f(x - \epsilon, \epsilon) P_t(x - \epsilon, \epsilon) - f(x, \epsilon) P_t(x, \epsilon) \Big]\,.$$

   The first term vanished because of (II.43). In the passive case, using that all ϵ are equally probable, and $P_t(x, \epsilon) = \frac{1}{2\delta} P_t(x)$ independent of ϵ, it follows

   $$\partial_t P_t(x) = \frac{1}{2\delta} \int_{-\delta}^{\delta} d\epsilon \Big[f(x - \epsilon, \epsilon) P_t(x - \epsilon) - f(x, \epsilon) P_t(x) \Big]\,. \tag{II.44}$$

   That the Gibbs-Boltzmann distribution gives the steady state and the detailed balance is satisfied, can be seen by first changing in the integration variable $\epsilon \to -\epsilon$ in the last term and then comparing with (II.25).

2. Until now, there was no assumption made on the size of δ. The earlier results for the small-δ limit can be recovered.

   Passive case:
   The passive case in (II.44) changes under the diffusive scaling ($\tilde{t} = t\,\delta^2$, $v(\tilde{t}) = \epsilon/\delta$, $\tilde{P}_{\tilde{t}}(x) = P_t(x)$) to

$$\begin{aligned}\delta^2 \partial_{\tilde{t}} \tilde{P}_{\tilde{t}}(x) =& \frac{1}{2}\int_{-1}^{1} dv \Big[f(x-\delta v, \delta v)\tilde{P}_{\tilde{t}}(x-\delta v) - f(x,\delta v)\tilde{P}_{\tilde{t}}(x)\Big] \\ =& -\frac{\delta}{2}\frac{\partial}{\partial x}[A(x)\tilde{P}_{\tilde{t}}(x)] + \frac{\delta^2}{4}\frac{\partial^2}{\partial x^2}[B(x)\tilde{P}_{\tilde{t}}(x)]\end{aligned}$$

   with the same $A(x)$ and $B(x)$ defined in (II.31). Using their results, it is straightforward to see that (II.32) is recovered.

   Persistent case:
   The persistent limit can be confirmed using (II.42). Under the ballistic scaling ($\tilde{t} = t\,\delta$, $v(\tilde{t}) = \epsilon/\delta$, $\tilde{P}_{\tilde{t}}(x,v) = \frac{1}{\delta}P_t(x,\epsilon)$), it becomes

$$\begin{aligned}\delta \partial_{\tilde{t}} \tilde{P}_{\tilde{t}}(x,v) =& \frac{\sigma^2}{2\delta^2}\frac{\partial^2}{\partial v^2}\tilde{P}_{\tilde{t}}(x,v) + f(x-\delta v,\delta v)\tilde{P}_{\tilde{t}}(x-\delta v, v) - f(x,\delta v)\tilde{P}_{\tilde{t}}(x,v) \\ =& \frac{\sigma^2}{2\delta^2}\frac{\partial^2}{\partial v^2}\tilde{P}_{\tilde{t}}(x,v) - \delta\frac{\partial}{\partial x}[v\, f(x,\delta v)\tilde{P}_{\tilde{t}}(x,v)] + \cdots .\end{aligned} \tag{II.45}$$

   Taking $\delta \to 0$, it follows

$$\partial_{\tilde{t}} \tilde{P}_{\tilde{t}}(x,v) = \frac{\sigma^2}{2\delta^3}\frac{\partial^2}{\partial v^2}\tilde{P}_{\tilde{t}}(x,v) - \frac{\partial}{\partial x}[v\, h(x,v)\tilde{P}_{\tilde{t}}(x,v)]$$

   where $f(x,\delta v) = h(x,v) + \cdots$ is used, as earlier. This result agrees with (II.30).

Remark: Even when starting with the continuous description of the Monte Carlo dynamics, the singular behavior between the passive and persistent limit arises for $\delta \to 0$. This singularity arises only, if a dimensional reduction is attempted. However, in case the phase diagram is described in a three-parameter space, this singularity does not appear. These three parameters can be found from (II.45), and these are λ, δ, and $\frac{u_0\gamma^6}{k_B T}$, which, when further rescaled in terms of d, gives (dropping the $\sim$-notation)

$$\partial_t P_t(x,v) = \frac{\sigma^2 d}{2\delta^3}\frac{\partial^2}{\partial v^2}P_t(x,v) + \frac{d}{\delta}f(x-\frac{\delta}{d}v,\frac{\delta}{d}v)P_t(x-\frac{\delta}{d}v,v) - \frac{d}{\delta}f(x,\frac{\delta}{d}v)P_t(x,v)\,, \tag{II.46}$$

with the three relevant parameters

$$\frac{d}{\lambda}\,,\ \frac{d}{\delta}\,,\ \text{and}\ \Gamma_0\,.$$

In this three-parameter space, the passive limit can be achieved smoothly. This can be seen by using $P_t(x,v) = \frac{1}{2}P_t(x)$, integrating (II.46) over v and using the reflecting boundary condition on v, thus

$$\partial_t P_t(x) = \frac{1}{2}\int_{-\delta/d}^{\delta/d} dy \Big[f(x-y,y)P_t(x-y) - f(x,-y)P_t(x)\Big]\,,$$

where the sign of y in the last term was changed. Even though, the integration range depends on $\frac{\delta}{d}$, one can show following (II.25) that the steady state is given by the Gibbs distribution, which depends only on Γ_0. This recovers the known result for the passive case.

II.4.4 Two other stochastic models of self-propelled dynamics

The analysis in the previous subsections II.4.2 and II.4.3 shows that the singular behavior of the passive limit in the kinetic Monte Carlo dynamics is not due to the discreteness of the dynamics, but is rather a consequence of the demand to reduce the relevant three-dimensional parameter space to two dimensions. Moreover, it was demonstrated that the three-parameter space reduces to a single relevant parameter in the passive limit. Here, the goal is to see if a similar phenomenon appears in other stochastic models of active dynamics. These two dynamics are the active Ornstein-Uhlenbeck process [92] and the active random acceleration process, which are *a priori* continuous. The latter is an active version of the well-known random acceleration process [210]. Both dynamics have in common that the particles move with a velocity of fluctuating amplitude. This is the essential difference from the active Brownian particle, where the velocity amplitude is constant.

The discussion focuses on a single particle in one dimension under the influence of a confining potential. However, the results are straightforward to generalize to many-particle systems, even in higher dimensions.

a) The active random acceleration process

The dynamics for a single particle is described by a fluctuating velocity ϵ_n and the position x_n at a *continuous time* n. The velocities are sampled in the same manner as in the kinetic Monte Carlo dynamics and described by

$$\begin{aligned} \dot{\epsilon}_n &= r_n + \tilde{R}\left(\frac{\epsilon_n}{\delta}\right), \\ \text{with } \langle r_n r_{n'}\rangle &= \sigma^2 \boldsymbol{\delta}(n-n'), \end{aligned} \tag{II.47}$$

with $\tilde{R}$ being a force taking care of the reflecting boundary condition at $\pm\delta$. The position of the particle involves following

$$\begin{aligned} \dot{x}_n &= v_0\epsilon_n + \beta\, F(x_n) + s_n, \\ \text{with } \langle s_n s_{n'}\rangle &= 2D\boldsymbol{\delta}(n-n'), \end{aligned} \tag{II.48}$$

with the self-propulsion force $v_0\epsilon_n$. The specific choice, of putting β in the force term of (II.48) is motivated by the aim to compare with the kinetic Monte Carlo results. The validity of this choice is justified later in the text below equation (II.53).

At this point, it is important to see a crucial difference between the active random acceleration process with the kinetic Monte Carlo dynamics. In the latter dynamics, it was possible to keep the maximum jump length δ fixed and to tune the self-propulsion force by changing the standard deviation σ of the random walk in the reflecting box. This is illustrated in subsection II.2.1 and subsection II.2.2. For example, Fig. II.6 shows that the particle penetrates the wall potential further (the peak positions shift closer to the walls), if solely σ is decreased and all other parameters are kept constant. In the kinetic Monte Carlo algorithm, a larger persistence times means more attempts in the Metropolis filter to accept a move in a certain direction and, in consequence, increases the probability for configurations with higher total energies (again, see Fig. II.6). Hence, the self-propulsion force in the kinetic Monte Carlo dynamics can be changed by changing σ only. This is clearly

not the case in the active random acceleration process described by (II.47) and (II.48). The self-propulsion force is $v_0\epsilon_n$, thus decreasing only σ would not increase the self-propulsion force but only the time particles stay *e.g.* in a fighting configuration (see Fig. II.40a). In the active random acceleration process, the self-propulsion force could in principle be tuned by either changing the maximum jump length δ or by changing the parameter v_0. Later, it will be clear that the "right" tuning parameter for the self-propulsion force is v_0. Fig. II.40b shows that tuning v_0 leads to the same behavior as tuning σ in the kinetic Monte Carlo dynamics (compare with Fig. II.6).

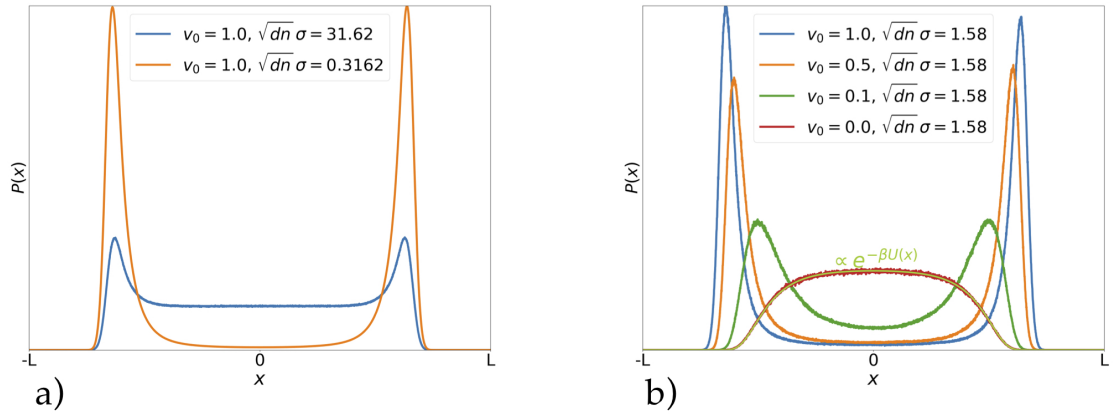


Figure II.40: **Tuning the self-propulsion force in the active random acceleration process.** Shown are probability distributions of the position of a single particle confined in a potential as in (II.9) with $n = 6$. a) confirms that a decrease in σ, while keeping all other parameters constant, does not lead to an increase of the self-propulsion force. The positions of the peaks are identical for the two curves with wildly different σ. b) shows that the self-propulsion force can be tuned by v_0. The particle penetrates the wall potential further with increasing v_0. $v_0 = 0$ leads to the equilibrium behavior. Other simulation parameter, not indicated in the legend, are $\delta = 100$, $L = 2$, $\gamma = 1.0$, $k_\mathrm{B}T = 1.0$, and $D = 1.0$. The time step for the simulation was chosen as $dn = 0.001$.

The corresponding Fokker-Planck equation of (II.47) and (II.48) is

$$\frac{\partial}{\partial n}P_n(x,\epsilon) = \frac{\sigma^2}{2}\frac{\partial^2}{\partial \epsilon^2}P_n(x,\epsilon) + D\frac{\partial^2}{\partial x^2}P_n(x,\epsilon) - \beta\frac{\partial}{\partial x}[F(x)P_n(x,\epsilon)] - v_0\frac{\partial}{\partial x}[\epsilon P_n(x,\epsilon)]\,,$$

with the reflecting boundary condition for the displacement

$$\frac{\partial}{\partial \epsilon}P_n(x,\epsilon) = 0\,, \text{for } \epsilon = \pm\delta\,.$$

Using the ballistic scaling $t = n\delta$, $v(t) = \frac{\epsilon_n}{\delta}$, $x(t) = x_n$, $\xi(t) = \frac{r_n}{\delta^2}$, and $\eta(t) = \frac{s_n}{\delta}$, it follows first $P_n(x,\epsilon) = \frac{1}{\delta}\tilde{P}_t(x,v)$, thus the rescaled Fokker-Planck equation becomes (dropping the $\sim$-convention for P_t)

$$\frac{\partial}{\partial t}P_t(x,v) = \frac{\sigma^2}{2\delta^3}\frac{\partial^2}{\partial v^2}P_t(x,v) + \frac{D}{\delta}\frac{\partial^2}{\partial x^2}P_t(x,v) - \frac{\beta}{\delta}\frac{\partial}{\partial x}[F(x)P_t(x,v)] - v_0\frac{\partial}{\partial x}[vP_t(x,v)]\,, \quad \text{(II.49)}$$

with the new reflecting boundary condition

$$\frac{\partial}{\partial v}P_t(x,v) = 0 \text{ for } v = \pm 1\,. \quad \text{(II.50)}$$

In this case, δ does not have to be small and no subleading terms are neglected, unlike in obtaining the continuous limit in the kinetic Monte Carlo dynamics. The steady-state properties depend on three parameters $\frac{1}{\lambda}$, $\frac{D}{\delta}$ and $\frac{\beta}{\delta}$ (again with $\lambda = \frac{\delta^3}{\sigma^2}$). Keeping these three parameters fixed leads to the same steady-state distribution independent of the microscopic parameters, *e.g.* δ.

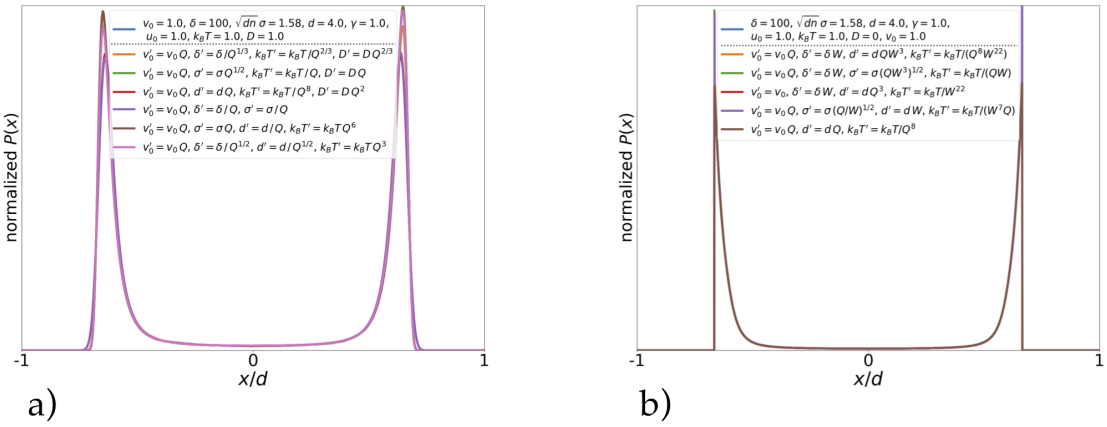


Figure II.41: **Scaling of the active random acceleration process.** Shown are the rescaled probability distributions of the rescaled position of a single particle confined in a potential as in (II.9) with $n = 6$. In both figures the blue line corresponds to the reference parameter set. All other graphs have different parameter sets, obtained from the reference set under the condition to keep the scaling parameters constant. a) parameter variations for $D \neq 0$, $Q = 0.1$, $\Gamma^* = 6.1 \cdot 10^{-5}$, $v_0 \frac{\lambda}{d} = 100$ and $\frac{D}{\delta d} \frac{\lambda}{d} = 0.25$. b) parameter variations for $D = 0$, $Q = 0.1$, $W = 2.0$, $\Gamma^* = 6.1 \cdot 10^{-5}$, $v_0 \frac{\lambda}{d} = 100$. The time step for the simulation was chosen as $dn = 0.001$.

These parameters can be made dimensionless by proceeding with the scaling of the length scale by some characteristic length d of the system. This could be the size of the confining box in the one-particle case, and might be replaced by the mean average inter-particle distance in the many-particle case. Following the scaling $\tilde{t} = \frac{t}{d}$, $\tilde{v}(\tilde{t}) = v(t)$, $\tilde{x}(\tilde{t}) = \frac{x(t)}{d}$, $\tilde{\xi}(\tilde{t}) = \xi(t)d$, $\tilde{\eta}(\tilde{t}) = \eta(t)$, with $P_t(x, v) = \frac{1}{d}\tilde{P}_{\tilde{t}}(\tilde{x}, \tilde{v})$, the Fokker-Planck equation for a particle in a potential as in (II.9)[14] with $n = 6$ becomes (dropping again the $\sim$-notation)

$$\begin{aligned}\frac{\partial}{\partial t}P_t(x,v) =& \frac{d}{2\lambda}\frac{\partial^2}{\partial v^2}P_t(x,v) + \frac{D}{\delta d}\frac{\partial^2}{\partial x^2}P_t(x,v) \\ &- \frac{6u_0\gamma^6}{k_\mathrm{B}T\delta d^7}\frac{\partial}{\partial x}\left[f(x)P_t(x,v)\right] - v_0\frac{\partial}{\partial x}\left[vP_t(x,v)\right],\end{aligned} \tag{II.51}$$

with $f(x) = -(1-x)^{-7} + (1+x)^{-7}$. In this form, the steady-state distribution depends on three dimensionless[15] scaling parameters:

$$\frac{D}{\delta d}\frac{\lambda}{d} = \frac{D\delta^2}{\sigma^2 d^2}, \quad v_0\frac{\lambda}{d} = v_0\frac{\delta^3}{\sigma^2 d}, \text{ and finally, } \Gamma^* = \frac{6u_0\gamma^6}{k_\mathrm{B}T\delta d^7}\frac{\lambda}{d} = \frac{6u_0\gamma^6\delta^2}{k_\mathrm{B}T\sigma^2 d^8}.$$

[14] The parameter L is renamed as d.

[15] All three parameter are dimensionless. $[\epsilon_n] = \frac{L}{T}$, $[\delta] = \frac{L}{T}$, $[r_n] = \frac{L}{T^2}$, $[\sigma^2] = \frac{L^2}{T^3}$; $[x_n] = L$, $[\beta F] = \frac{L}{T}$, $[s_n] = \frac{L}{T}$, $[D] = \frac{L^2}{T}$; The ballistic scaling leads to $[v] = 1$. The d scaling leads directly to $[x] = 1$, $[\frac{\lambda}{d} = \frac{\delta^3}{\sigma^2 d}] = 1$ and $[\frac{D}{\delta d}] = 1$. As $[f(x)] = 1$, $[\beta F = \frac{\beta u_0 \gamma^6}{d^7}] = \frac{L}{T}$, and thus $[\frac{\beta u_0 \gamma^6}{\delta d^7}] = 1$.

This is confirmed by numerical simulations of the Langevin equations in Fig. II.41a for $D \neq 0$ and in Fig. II.41b for a reduced parameter set with $D = 0$, with the main focus on different combination on how to rescale a change in the self-propulsion force.

The effect of a finite D is to increase the width of the peaks. A comparison with the result of the kinetic Monte Carlo dynamics shows a similarity with the distribution for $D \neq 0$.

Remarks:

1. In the self-propelled limit, the choice $D = 0$ leads to a reduction of the three-dimensional parameter space to two dimensions. However, this choice is strictly restricted to the self-propelled limit, which can be seen by studying the passive limit.

   The passive limit is recovered under a vanishing self-propulsion force for $v_0 = 0$, thus also $P_t(x, v)$ factorizes as $P_t(x)P_t(v)$ (see (II.48)). Using this property and integrating (II.51) on both sides over v leads directly to the passive limit Fokker Planck equation

   $$\frac{\partial}{\partial t}P_t(x) = \frac{D}{\delta d}\frac{\partial^2}{\partial x^2}P_t(x) - \frac{6u_0\gamma^6}{k_\mathrm{B}T\delta d^7}\frac{\partial}{\partial x}\left[f(x)P_t(x)\right] , \tag{II.52}$$

   as

   $$\int_{-1}^{1} dv\, P_t(x, v) = P_t(x) , \text{ and}$$
   $$\int_{-1}^{1} dv\, \frac{\partial^2}{\partial v^2}P_t(x, v) = \left[\frac{\partial}{\partial v}P_t(x, v)\right]_{v=-1}^{1} = 0 \text{ (due to (II.50))} .$$

   The equilibrium steady state depends only on one parameter, which can be shown by using the steady-state property $\frac{\partial}{\partial t}P_t(x) = 0$, thus

   $$0 = \frac{D}{\delta d}\frac{\partial^2}{\partial x^2}P_t(x) - \frac{6u_0\gamma^6}{k_\mathrm{B}T\delta d^7}\frac{\partial}{\partial x}\left[f(x)P_t(x)\right] ,$$

   which has the steady-state distribution

   $$P_s(x) \propto \exp\left(\frac{\Gamma_0}{D}\int^x dy\, f(y)\right) \propto \exp\left(-\frac{\Gamma_0}{D}u(x)\right) , \tag{II.53}$$

   with $u(x) = (1 - x)^{-6} + (1 + x)^{-6}$. Equation (II.53) shows that the specific choice of putting β in the force term of (II.48) is legitimate in equilibrium, as it leads to the correct result for $D = 1$ with the correct equilibrium scaling parameter Γ_0 (also see Fig. II.40b for $v_0 = 0$).

   In consequence, $D = 1$ is an additional condition on the system, in order to recover the equilibrium scaling parameter.

2. With this choice of $D = 1$, the steady-state Fokker-Planck equation can be rewritten as

   $$\begin{aligned} 0 = &\frac{\delta d^2}{2\lambda}\frac{\partial^2}{\partial v^2}P_t(x, v) + \frac{\partial^2}{\partial x^2}P_t(x, v) \\ &- \Gamma_0\frac{\partial}{\partial x}\left[f(x)P_t(x, v)\right] - v_0\delta d\frac{\partial}{\partial x}\left[vP_t(x, v)\right] . \end{aligned} \tag{II.54}$$

Here there are three relevant parameters

$$\Gamma_0\,,\, v_0\delta d\,,\text{ and }\frac{\delta d^2}{\lambda}\,,$$

with one of them being the equilibrium scaling parameter Γ_0.

3. In the passive limit, Γ_0 is the only relevant parameter and the other two become redundant. This can be seen by using $v_0 = 0$, which makes the coupling term between x and v in (II.54) disappear, thus $P_t(x,v) = P_t(x)\,P_t(v)$ and the steady-state Fokker-Planck equation decouples in two parts,

$$\begin{aligned}0 =&\frac{\delta\, d^2}{2\lambda}\frac{\partial^2}{\partial v^2}P_t(v)\,,\text{ and}\\ 0 =&\frac{\partial^2}{\partial x^2}P_t(x) - \Gamma_0\frac{\partial}{\partial x}\left[f(x)P_t(x)\right]\,,\end{aligned}$$

where the distribution for the position depends only on Γ_0.

b) The active Ornstein-Uhlenbeck process

In the active Ornstein-Uhlenbeck process the displacement ϵ is not strictly confined, but performs a random walk in a harmonic potential $\frac{\alpha}{2}\epsilon^2$. The coupled Langevin equations of the active Ornstein-Uhlenbeck process are

$$\begin{aligned}\dot\epsilon_n &= -\alpha\,\epsilon_n + r_n &&\text{with }\langle r_n\rangle = 0\,,\quad \langle r_n r_{n'}\rangle = 2D_a\boldsymbol{\delta}(n-n')\,,\text{ and}\\ \dot x_n &= v_0\epsilon_n + \beta F(x_n) + s_n &&\text{with }\langle s_n\rangle = 0\,,\quad \langle s_n s_{n'}\rangle = 2D\boldsymbol{\delta}(n-n')\,.\end{aligned}$$

One motivation to study this model is to see if the dimensional reduction is possible, when the reflecting boundary on the velocity ϵ is removed.

It can be shown[16] that the auto-correlation function of the displacements is

$$\langle\epsilon_n\epsilon_{n'}\rangle = \frac{D_a}{\alpha}\exp\left(-\frac{n-n'}{\alpha^{-1}}\right)\,,$$

thus the auto-correlation time is $\tau = \alpha^{-1}$ and a typical scale for the displacement is $\sqrt{\langle\epsilon_n^2\rangle} = \sqrt{\frac{D_a}{\alpha}}$. By choosing

$$\alpha = \tfrac{\sigma^2}{\delta^2}\text{ and }D_a = \sigma^2\,,$$

it is possible to relate to the kinetic Monte Carlo dynamics, as in this case $\tau = \frac{\delta^2}{\sigma^2}$ and the typical scale of the displacements becomes $\sqrt{\langle\epsilon_n^2\rangle} = \delta$.

There is no hard boundary condition for the displacement ϵ in the active Ornstein-Uhlenbeck process, thus $\epsilon \in (-\infty,\infty)$. Uncorrelated movements could, in principle, be achieved by $\alpha\to\infty$, thus $\tau\to 0$. However, this corresponds to sampling ϵ from a random walk on an infinite line, which would lead to a non-local dynamics. Therefore, in the active Ornstein-Uhlenbeck process, the tuning parameter for the self-propulsion must be v_0.

[16] The general solution for displacements is $\epsilon_n = \int_{-\infty}^{n} dt\, e^{-\alpha(n-t)}r_t$, thus $\langle\epsilon_n\epsilon_{n'}\rangle = \int_{-\infty}^{n}dt\int_{-\infty}^{n'}dt'\,e^{-\alpha(n-t)-\alpha(n'-t')}\langle r_t r_{t'}\rangle = \frac{D_a}{\alpha}e^{-\alpha(n-n')}$

Choosing again the ballistic scaling $t = n\delta$, $v(t) = \frac{\epsilon_n}{\delta}$ and $\xi(t) = \frac{r_n}{\delta^2}$ for ϵ, and $x(t) = x_n$, and $\eta(t) = \frac{s_n}{\delta}$ for the space gives

$$\dot{v}(t) = -\frac{\sigma^2}{\delta^3}v(t) + \xi(t) \text{ with } \langle \xi(t)\xi'(t)\rangle = 2\frac{\sigma^2}{\delta^3}\boldsymbol{\delta}(t-t')$$
$$\dot{x}(t) = v_0\, v(t) + \frac{\beta}{\delta}F(x(t)) + \eta(t) \text{ with } \langle \eta(r)\eta(t')\rangle = 2\frac{D}{\delta}\boldsymbol{\delta}(t-t')\,,$$

thus the steady state is characterized by four parameters $\frac{1}{\lambda} = \frac{\sigma^2}{\delta^3}$, $\frac{\beta}{\delta}$, $\frac{D}{\delta}$ and v_0, which are just like in the active random acceleration process. The corresponding Fokker-Planck equation is

$$\frac{\partial}{\partial t}P_t(x,v) = \frac{1}{\lambda}\frac{\partial^2}{\partial v^2}P_t(x,v) + \frac{1}{\lambda}\frac{\partial}{\partial v}[vP_t(x,v)] + \frac{D}{\delta}\frac{\partial^2}{\partial x^2}P_t(x,v) - \frac{\beta}{\delta}\frac{\partial}{\partial x}[F(x)P_t(x,v)] - v_0\frac{\partial}{\partial x}[vP_t(x,v)]\,. \tag{II.55}$$

In comparison with the Fokker-Planck equation (II.49) of the active random acceleration process, (II.55) has an additional term, as there is no reflecting boundary condition for the velocity. However, the steady state ($\frac{\partial}{\partial t}P_t(x,v) = 0$) depends on three parameter only, which are $\frac{D\lambda}{\delta}$, $v_0\lambda$, and the third one from $\frac{\beta\lambda}{\delta}F(x)$.

Specifying the potential the particle is trapped in by the potential in (II.9) with $n = 6$ and then proceeding with the scaling by the spatial length scale d ($\tilde{t} = \frac{t}{d}$, $\tilde{v}(\tilde{t}) = v(t)$, $\tilde{x}(\tilde{t}) = \frac{x(t)}{d}$, $\tilde{\xi}(\tilde{t}) = \xi(t)d$, $\tilde{\eta}(\tilde{t}) = \eta(t)$) the equations of motion become (dropping the $\sim$-notation)

$$\dot{v}(t) = -\frac{d}{\lambda}v(t) + \xi(t) \text{ with } \langle \xi(t)\xi'(t)\rangle = 2\frac{d}{\lambda}\boldsymbol{\delta}(t-t')$$
$$\dot{x}(t) = v_0\, v(t) + \hat{\Gamma}f(x) + \eta(t) \text{ with } \langle \eta(r)\eta(t')\rangle = \frac{2D}{\delta d}\boldsymbol{\delta}(t-t')\,,$$

with $f(x) = -(1-x)^{-7} + (1+x)^{-7}$ and $\hat{\Gamma} = \frac{6\beta u_0\gamma^6}{\delta d^7}$. Rescaling the Fokker-Planck equation in (II.55) leads to

$$\frac{\partial}{\partial t}P_t(x,v) = \frac{d}{\lambda}\frac{\partial^2}{\partial v^2}P_t(x,v) + \frac{d}{\lambda}\frac{\partial}{\partial v}[vP_t(x,v)] + \frac{D}{\delta d}\frac{\partial^2}{\partial x^2}P_t(x,v) - \frac{6u_0\gamma^6}{k_{\mathrm{B}}T\delta d^7}\frac{\partial}{\partial x}[f(x)P_t(x,v)] - v_0\frac{\partial}{\partial x}[vP_t(x,v)]\,. \tag{II.56}$$

Thus finally, it turns out that the active Ornstein-Uhlenbeck process has the same three dimensionless[17] scaling parameters as in the active random acceleration process, namely

$$\frac{D}{\delta d}\frac{\lambda}{d} = \frac{D\delta^2}{\sigma^2 d^2}\,,\; v_0\frac{\lambda}{d} = v_0\frac{\delta^3}{\sigma^2 d} \text{ and } \Gamma^* = \frac{6u_0\gamma^6}{k_{\mathrm{B}}T\delta d^7}\frac{\lambda}{d} = \frac{6u_0\gamma^6\delta^2}{k_{\mathrm{B}}T\sigma^2 d^8}\,.$$

Remarks:

[17] All scaling parameters are dimensionless just in the same manner as for the active random acceleration process.

1. The passive limit Fokker-Planck equation is recovered for $v_0 = 0$, thus $P_t(x,v) = P_t(x)P_t(v)$. With this condition, integrating (II.56) over $v \in (-\infty, \infty)$ leads to

$$\frac{\partial}{\partial t}P_t(x) = \frac{D}{\delta d}\frac{\partial^2}{\partial x^2}P_t(x) - \frac{6u_0\gamma^6}{k_{\rm B}T\delta d^7}\frac{\partial}{\partial x}[f(x)P_t(x)]\,,$$

as

$$\begin{aligned}
&\int_{-\infty}^{\infty} dv\, P_t(x,v) = P_t(x)\,,\\
&\int_{-\infty}^{\infty} dv\, \frac{\partial^2}{\partial v^2}P_t(x,v) = 0\,,\ \text{as}\ ,P_t(x,v) \to 0\ \text{for}\ v \to \pm\infty\\
&\int_{-\infty}^{\infty} dv\, \frac{\partial}{\partial v}[v\,P_t(x,v)] = 0\,,\ \text{as}\ ,P_t(x,v) \to 0\ \text{for}\ v \to \pm\infty\,.
\end{aligned}$$

This Fokker-Planck equation is exactly the same as in the active random acceleration process (II.52) and thus has the same steady state solution (II.53), which depends on a single parameter that is $\frac{\Gamma_0}{D}$.

2. Again, considering the additional condition $D = 1$ (in order to be able to access the correct passive limit) the steady-state Fokker-Planck equation where $\frac{\partial}{\partial t}P_t(x,v) = 0$, can be rewritten as

$$\begin{aligned}
0 =& \frac{\delta d^2}{\lambda}\frac{\partial^2}{\partial v^2}P_t(x,v) + \frac{\delta d^2}{\lambda}\frac{\partial}{\partial v}[vP_t(x,v)]\\
&+ \frac{\partial^2}{\partial x^2}P_t(x,v) - \Gamma_0\partial x\,[f(x)P_t(x,v)] - v_0\delta d\frac{\partial}{\partial x}[vP_t(x,v)]\,,
\end{aligned}$$

thus the characteristic scaling parameters are just the same as in the active random acceleration process

$$\Gamma_0\,, v_0\delta d\,,\ \text{and}\ \frac{\delta d^2}{\lambda}\,.$$

It is straightforward to check that the passive case $v_0 = 0$ decouples the probability $P_t(x,v) = P_t(x)P_t(v)$, thus the passive steady state depends on Γ_0 only.

II.4.5 Summary

Even though the analysis for the active random acceleration process and the active Ornstein-Uhlenbeck process is presented only for a single particle in a confining one-dimensional potential, it is straightforward to extend the analysis to many particles and to higher dimensions. The same set of scaling parameters is valid for a pair potential of the form[18] $U(r) = u_0(\frac{\gamma}{r})^n$ with $n = 6$ and the dimension enters only through the characteristic length scale d, when it is expressed in terms of ϕ (see paragraph d) in subsection II.4.2).

The following table summarizes the scaling results of the different dynamics considered in this section II.4.

[18] A different n changes the exponents in the Γ-scaling parameters.

	relevant scaling parameters	passive limit scaling parameters	dimensional reduction in active limit
kinetic Monte Carlo	Γ_0, $\frac{\lambda}{d}$, $\frac{\delta}{d}$	$\Gamma_0 = \frac{6u_0\gamma^6}{k_\mathrm{B}Td^6}$	$\Gamma = \frac{6u_0\gamma^6\delta}{k_\mathrm{B}Td^7}$, $\frac{\lambda}{d}$, (δ small)
active random acceleration process	Γ_0, $v_0\delta d$, $\frac{\delta d^2}{\lambda}$, ($D=1$)	Γ_0 ($D=1$)	$\Gamma^* = \frac{6u_0\gamma^6\delta^2}{k_\mathrm{B}T\sigma^2d^8}$, $v_0\frac{\lambda}{d}$, ($D=0$)
active Ornstein-Uhlenbeck process	Γ_0, $v_0\delta d$, $\frac{\delta d^2}{\lambda}$, ($D=1$)	Γ_0 ($D=1$)	Γ^*, $v_0\frac{\lambda}{d}$ ($D=0$)

Table II.3: Summary of the dimensionless scaling parameter for the three dynamics considered in this section II.4 in the active/self-propelled and passive limit.

This section II.4 started with the aim to find the minimum set of relevant parameters to describe the phase behavior in the kinetic Monte Carlo dynamics. In general, the many-particle phase diagram can be described on a three-parameter space (Γ_0, $\frac{\lambda}{d}$, $\frac{\delta}{d}$), which includes both, the passive and the self-propelled limit. When δ is small, in the active region (with limits of validity), the parameter space can be reduced to two dimensions. However, this makes the passive region disjoint from the rest of the phase diagram, where the relevant parameter is different. This is a feature common with the two other continuous stochastic models of self-propelled dynamics. The important observations are the following:

1. For a full characterization of the phase diagram, three parameters are necessary.

2. In restrictive regions of the persistent limit, it is possible to effectively reduce to two parameters. However, from this limit, taking the persistence to zero only connects to the zero temperature passive dynamics. For example, in the Monte Carlo dynamics, see equation (II.34) which corresponds to zero temperature. In the other two stochastic models, as shown in the table, the two-parameter regime is obtained by setting $D = 0$, which equivalently corresponds to zero temperature in the passive limit.

3. This singular behavior near the passive limit is not due to the discrete nature of the Monte Carlo dynamics, nor is it due to the Metropolis filter. This is confirmed by the analysis of the two continuous stochastic models of persistent dynamics.

4. The small-δ limit is not a necessary criterion for a continuous limit of the discrete-time Monte Carlo dynamics. However, the small-δ limit is one way of reducing the relevant number of parameters. The continuous limit of the Monte Carlo dynamics is given in (II.42) without δ being small.

5. Even though the small-δ limit could reduce the number of relevant parameters, it introduces different continuous dynamics in the passive and in the persistent case, which have different characteristic scaling parameters. This difference is related to the non-commuting order of limits $\delta \to 0$ and $\lambda \to 0$. More precisely, taking the

$\lambda \to 0$ limit before the $\delta \to 0$ limit leads to the passive Langevin equation (II.33), with Γ_0 as the characteristic parameter. On the other hand, taking the limit $\delta \to 0$, while keeping λ finite, leads to the active/persistent coupled Langevin equations (II.36a) and (II.36b), where the characteristic parameter is Γ. Proceeding here with $\lambda \to 0$ does not make Γ equal to Γ_0. Such a singular behavior of different continuous limits is well-known in driven diffusive models of non-equilibrium systems. For example, in exclusion processes, the exchange of the order of limits of vanishing bias and the thermodynamic limit lead to different hydrodynamic descriptions[211].

II.5 Pressure in the kinetic Monte Carlo

The nature of melting transitions in two-dimensional equilibrium particle systems has been long debated [128, 142, 144–146, 153, 154, 177, 184, 185, 212–216]. The contentious point concerned the question whether the transitions are of first order, or of continuous nature and on the very existence of the hexatic phase. First-order transitions are characterized by finite correlation lengths. However, the distinction from a pure power-law correlation associated with a continuous transition can be hard in numerical simulations of finite systems. The investigation of the equation of state (pressure over volume) in a (N, V, T) ensemble offers an alternative approach to unambiguously identify a first-order transition.

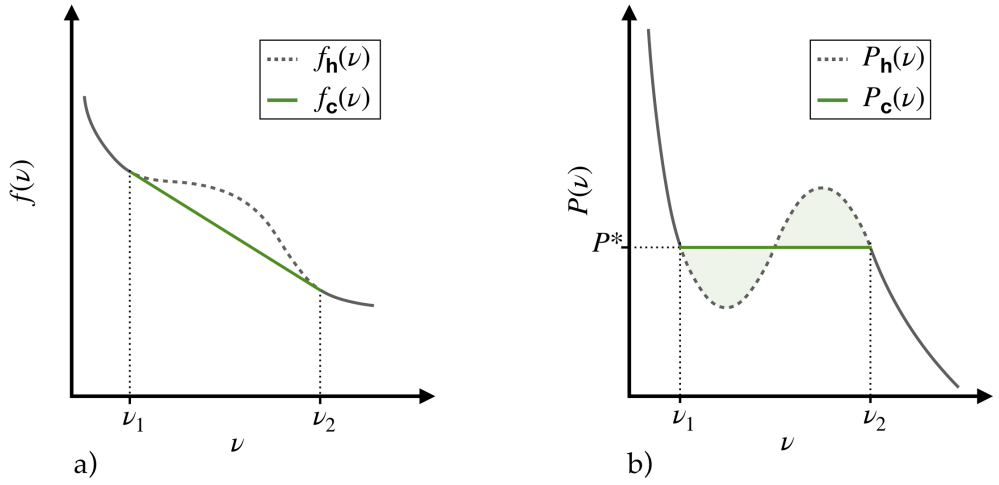


Figure II.42: **First-order phase transition.** a) Schematic of the theoretical free energy per particle f_h for a homogeneous particle system around a first-order phase transition as a function of the specific volume ν. The concave shape induces a phase coexistence in the real particle system that follows f_c. b) Schematic of the corresponding pressure as a function of ν. The real system shows a phase coexistence in the interval $\nu_1 < \nu < \nu_2$ and follows P_c, as the dashed loop for P_h is thermodynamically unstable.

Assuming a homogeneous density distribution, the resulting theoretical free energy of a system undergoing a first-order phase transition is concave, see Fig. II.42. The schematic shows the free energy per particle $f(v) = \frac{F}{N}$ as a function of the specific volume $v = \frac{V}{N}$ for a system around a first-order transition. For a homogeneous system, the free energy f_h

is concave within the interval $v_1 < v < v_2$, which corresponds to an increase of the free energy. However the real system has an alternative to following this increase. It minimizes f by phase separating in a dilute phase with the proportion $n_2 = \frac{N_2}{N}$ and a dense phase with $n_1 = \frac{N_1}{N} = 1 - n_2$, thus

$$f_c(v) = f_h(v_1) + n_2[f_h(v_2) - f_h(v_1)] < f_h(v)\,, \quad n_2 = \frac{v - v_1}{v_2 - v_1} \in [0, 1]\,.$$

This behavior is reflected in the pressure $P = -\frac{\partial f}{\partial v}$. The theoretical curve resulting from $f_h(v)$ shows a pressure loop, known as Van-der-Waals loop. The pressure of the real system does not follow this theoretical prediction, but stays constant within the interval of the first-order transition. The constant value P^* can be determined using the "Maxwell construction" which equalizes the two shaded areas enclosed by the loop and P^*.

The analysis of a similar pressure loop[19] played a key role in closing the debate about the nature of the equilibrium melting transitions in two dimensions. However, the existence of a thermodynamic pressure in non-equilibrium active systems is a substantial question and has been intensely discussed in the recent literature [47, 48, 51, 102, 105, 206]. Even though [48] shows that pressure is not a state function for generic active fluids (*e.g.* particles of arbitrary shape, arbitrary alignment-interactions, *etc.*), the work of Solon *et. al* [51] gives an explicit proof that pressure is, after all, well-defined in a specific class of active particle systems. This class consists of self-propelled (persistently moving), symmetric particles, without alignment interactions and torque-free pairwise inter-particle forces, as well as torque-free wall interactions. The kinetic Monte Carlo dynamics discussed in this thesis belongs to this narrow class of models, where it may be possible to define a mechanical pressure that can be interpreted as the thermodynamic pressure, in the sense that the expression for pressure does not depend explicitly on the wall interaction.

The definition of pressure within the dynamics discussed in this thesis would offer an approach to identify first-order transitions within the two-step melting scenario outside equilibrium reported here. It would also provide a tool to quantify the effect of persistent motion further. Does persistent motion has a similar role as the softness of the potential, thus the first-order transitions observed in the equilibrium melting scenario disappear with increasing persistence as suggested in [108]? In addition, it would allow for a detailed study of the observed motility-induced liquid-gas coexistence [51, 105].

To follow the derivation of an expression for pressure in [51] a Langevin description of the dynamics is required, thus this section II.5 approaches an expression for pressure for the small-δ limit of the kinetic Monte Carlo dynamics. It was shown in section II.4 that the kinetic Monte Carlo dynamics has a Langevin description in this limit, whereas the general continuous description by the Fokker-Planck equation in (II.42) cannot be easily mapped to a Langevin description.

II.5.1 Pressure in the passive limit of kinetic Monte Carlo

The goal of this subsection II.5.1 is to transmit the principle idea of the derivation of pressure by studying the passive limit of the kinetic Monte Carlo dynamics. In this limit, the final

[19] In contrast to the Van-der-Waals loop, the Mayer-Woods loop observed in [12, 192] is an artifact of the finite system size [202].

expression must correspond to the equilibrium virial expression for pressure and thus offers a consistency check of the approach.

To derive an expression for the mechanical pressure, an additional external force $F^{(e)}(x_i)$ on each particle is introduced, which plays the role of a confining wall. It is well-known that the equilibrium expression for pressure is independent of the wall potential and solely depends on correlations in the bulk. The Fokker-Planck equation in (II.38) changes to (dropping for simplicity the $\sim$-notation for the scaled coordinates)

$$\frac{\partial}{\partial t}P_t[\mathbf{x}] = -\beta\sum_i \frac{\partial}{\partial x_i}F_i(\mathbf{x})P_t[\mathbf{x}] - \beta\sum_i \frac{\partial}{\partial x_i}F^{(e)}(x_i)P_t[\mathbf{x}] + \sum_i \frac{\partial^2}{\partial x_i^2}P_t[\mathbf{x}]\,,$$

with $\beta F_i(\mathbf{x}) = \Gamma_0 \sum_{j\neq i} \frac{1}{(x_i-x_j)^7}$ and $\Gamma_0 = \frac{6u_0\gamma^6}{k_{\mathrm{B}}Td^6}$. The temperature ($k_{\mathrm{B}}T = \beta^{-1}$) is included as a prefactor in the force term. This choice still satisfies the fluctuation-dissipation relation.

The corresponding multi-particle Langevin equation is

$$\dot{x}_i(t) = \beta F_i(\mathbf{x}) + \beta F^{(e)}(x_i) + \eta_i(t) \qquad \left\langle \eta_i(t)\,\eta_j(t')\right\rangle = 2\boldsymbol{\delta}_{i,j}\boldsymbol{\delta}(t-t')\,. \tag{II.57}$$

In the following the inter-particle force is written as

$$\beta F_i(\mathbf{x}) = \Gamma_0 \sum_j \frac{\mathrm{sign}(x_i-x_j)}{|x_i-x_j|^7} = \beta\sum_j \Phi(x_i-x_j)\,, \tag{II.58}$$

with the sum over all particles, including the ith one, as the force on a particle by itself is zero, which is taken care of by the sign function ($\mathrm{sign}(0) = 0$). The Langevin equation is written in coordinates scaled by d.

The starting point consists of the definition of a microscopic density function (often called fluctuating distribution function)

$$\widehat{\psi}_t(x) = \sum_i \boldsymbol{\delta}(x - x_i(t)).$$

$\widehat{\psi}_t(x)dx$ gives the number of particles in the interval $[x, x+dx]$ at time t, during one time evolution (it is not a probability).

The time evolution of $\widehat{\psi}_t(x)$ is given by (see A.7 for details)

$$\frac{d}{dt}\widehat{\psi}_t(x) = -\frac{\partial}{\partial x}\left\{\eta(x,t) + \beta\widehat{\psi}_t(x)\sum_j \Phi(x-x_j) + \beta F^{(e)}(x)\widehat{\psi}_t(x) - \frac{\partial^2\widehat{\psi}_t(x)}{\partial x^2}\right\} \tag{II.59a}$$

where $\Phi(x)$ is given in (II.58) and

$$\langle\eta(x,t)\rangle = 0\,, \qquad \langle\eta(x,t)\,\eta(x',t')\rangle = 2\,\widehat{\psi}_t(x)\boldsymbol{\delta}(t-t')\boldsymbol{\delta}(x-x')\,. \tag{II.59b}$$

Equation (II.59a) gives the time evolution of the density in one realization (history) of a Monte Carlo simulation. The average over the ensemble (over noise $\eta(x,t)$) leads to the average density $\rho_t(x) = \langle\widehat{\psi}_t(x)\rangle$ and its time evolution as a continuity equation

$$\begin{aligned}\frac{d}{dt}\rho_t(x) =& -\frac{\partial}{\partial x}J_t(x)\\ J_t(x) =& \beta\left\langle\widehat{\psi}_t(x)\sum_j\Phi(x-x_j)\right\rangle + \beta F^{(e)}(x)\,\rho_t(x) - \frac{\partial\rho_t(x)}{\partial x}\,.\end{aligned}$$

The first term in the current can be rewritten as

$$\left\langle \widehat{\psi}_t(x) \sum_j \Phi(x - x_j) \right\rangle = \left\langle \widehat{\psi}_t(x) \int dy \sum_j \boldsymbol{\delta}(y - x_j)\Phi(x - y) \right\rangle = \int dy\, \Phi(x-y) \left\langle \widehat{\psi}_t(x)\, \widehat{\psi}_t(y) \right\rangle .$$

This leads to the ensemble-averaged particle current

$$J_t(x) = \beta \int dy\, \Phi(x - y) \left\langle \widehat{\psi}_t(x)\, \widehat{\psi}_t(y) \right\rangle + \beta\, F^{(e)}(x)\rho_t(x) - \frac{\partial \rho_t(x)}{\partial x} ,$$

with the last term being a Fick's-law term.

As the particles are confined in some external wall potential, the particle current must vanish in the steady state, and therefore,

$$-F^{(e)}(x)\rho(x) = \int dy\, \Phi(x - y) \left\langle \widehat{\psi}(x)\, \widehat{\psi}(y) \right\rangle - k_{\mathrm{B}}T \frac{d\rho(x)}{dx} . \tag{II.60}$$

Pressure

The mechanical pressure is the average force exerted by all particles on the external wall. Here, $F^{(e)}(x)$ is defined as force exerted by the wall on a particle at position x. Using Newtons third law, the pressure on the right wall is thus given by

$$p = -\int_{\Lambda}^{\infty} dx\, F^{(e)}(x)\rho(x) ,$$

where the lower integration limit Λ could be any point inside the bulk, with the assumption that the external force vanishes at this point. The upper limit could be any point where the wall potential becomes infinite. Using (II.60), it follows

$$p = k_{\mathrm{B}}T\, \bar{\rho} + \int_{\Lambda}^{\infty} dx \int_{-\infty}^{\infty} dy\, \Phi(x - y) \left\langle \widehat{\psi}(x)\, \widehat{\psi}(y) \right\rangle ,$$

where $\rho(\infty) = 0$ and $\rho(\Lambda) = \bar{\rho}$ was used, with $\bar{\rho}$ being the bulk density. The expression can be further simplified

$$p = k_{\mathrm{B}}T\, \bar{\rho} + \int_{\Lambda}^{\infty} dx \int_{-\infty}^{\Lambda} dy\, \Phi(x - y) \left\langle \widehat{\psi}(x)\, \widehat{\psi}(y) \right\rangle , \tag{II.61}$$

where the contribution from the y-integral over range $[\Lambda, \infty]$ vanishes because $\Phi(x - y) = -\Phi(y - x)$. This is the expression for the mechanical pressure [51].

Remarks:

1. The expression for pressure (II.61) does not depend on the wall potential. In fact, the same expression holds for periodic boundary conditions. In this sense, it is a thermodynamic pressure.
2. The first term $\bar{\rho}k_{\mathrm{B}}T$ is the ideal gas term.
3. The second term involves the pair-correlation $g(r) = \left\langle \widehat{\psi}(0)\widehat{\psi}(r) \right\rangle$, and corresponds to the standard interaction part in the virial expression.

II.5.2 Pressure in the persistent limit of kinetic Monte Carlo

The calculation in the previous subsection II.5.1 can be generalized for the persistent limit. The corresponding Langevin description of the rescaled Fokker-Planck equation in (II.37) for the persistent regime in the small-δ limit is

$$\dot{v}_i(t) = \xi_i(t) + \tilde{R}(v_i(t)) \text{ with } \langle \xi_i(t) \rangle = 0, \quad \langle \xi_i(t)\, \xi_j(t') \rangle = 2D_a \boldsymbol{\delta}_{i,j} \boldsymbol{\delta}(t-t') \tag{II.62}$$

$$\dot{x}_i(t) = v_i(t)\, h_i\big(\mathbf{x}(t), v_i(t)\big)\,, \tag{II.63}$$

with $D_a = \frac{d\sigma^2}{2\delta^3} = \frac{d}{2\lambda}$ and

$$h_i(\mathbf{x}, v_i) = \min\left\{1, e^{\Gamma v_i F_i[\mathbf{x}]}\right\} \qquad \text{and} \qquad \Gamma = \frac{6u_0\gamma^6\delta}{k_{\mathrm{B}}Td^7}\,.$$

To derive the expression for the mechanical pressure, an external force term $F^{(e)}(x_i)$ acting on a particle at x_i must be added in (II.63), representing the confining wall. Moreover, it is possible to add an additional noise term η, which can be dropped at any point by simply choosing $D = 0$, thus the Langevin equation for x becomes

$$\begin{aligned} \dot{x}_i(t) &= v_i(t)\, h_i\big(\mathbf{x}(t), v_i(t)\big) + F^{(e)}(x_i) + \eta_i(t)\,, \text{ with} \\ \langle \eta_i(t) \rangle &= 0, \quad \langle \eta_i(t)\, \eta_j(t') \rangle = 2D\, \boldsymbol{\delta}_{i,j} \boldsymbol{\delta}(t-t')\,. \end{aligned} \tag{II.64}$$

Remark: In case the term $v_i(t)\, h_i\big(\mathbf{x}(t), v_i(t)\big)$ can be written as a derivative of some inter-particle potential, this system equilibrates at a temperature determined by D. In this sense, the additional noise term η provides a source for thermal fluctuations, different from the "temperature" T incorporated in Γ. However, this term cannot be written as a gradient force, which is usually the case for systems outside equilibrium. This means that T, in this persistent limit, does not have an interpretation as temperature.

The corresponding Fokker-Planck equation has the form

$$\begin{aligned} \frac{\partial}{\partial t} P_t[\mathbf{x}, \mathbf{v}] =& D \sum_i \frac{\partial^2}{\partial x_i^2} P_t[\mathbf{x}, \mathbf{v}] + D_a \sum_i \frac{\partial^2}{\partial v_i^2} P_t[\mathbf{x}, \mathbf{v}] \\ & - \sum_i \frac{\partial}{\partial x_i} \big\{ v_i h_i(\mathbf{x}, v_i) P_t[\mathbf{x}, \mathbf{v}] \big\} - \sum_i \frac{\partial}{\partial x_i} \Big\{ F^{(e)}(x_i) P_t[\mathbf{x}, \mathbf{v}] \Big\} \end{aligned}$$

with the zero-current condition

$$\frac{\partial}{\partial v_i} P_t[\mathbf{x}, \mathbf{v}] = 0\,, \text{ at } v_i = \pm 1\,,$$

which takes care of the reflecting boundary condition on $v_i(t)$.

In the following, the inter-particle force is again redefined as

$$F_i(\mathbf{x}) = \sum_j \frac{\mathrm{sign}(x_i - x_j)}{|x_i - x_j|^7} = \sum_j \Phi(x_i - x_j)\,.$$

The corresponding fluctuating distribution function is now a function of both x and v

$$\widehat{\psi}_t(x,v) = \sum_i \boldsymbol{\delta}(x - x_i(t))\boldsymbol{\delta}(v - v_i(t)) \tag{II.65}$$

and its time evolution is given by (see A.8)

$$\begin{aligned}\frac{d}{dt}\widehat{\psi}_t(x,v) = &- \frac{\partial}{\partial v}\left\{\xi_t(x,v) - D_a\frac{\partial}{\partial v}\widehat{\psi}_t(x,v)\right\} \\ &- \frac{\partial}{\partial x}\left\{\eta_t(x,v) + \widehat{\psi}_t(x,v)\, v\, \chi\left[\Gamma v \int dx'dv'\, \Phi(x-x')\, \widehat{\psi}_t(x',v')\right]\right. \\ &\left. + F^{(e)}(x)\widehat{\psi}_t(x,v) - D\frac{\partial}{\partial x}\widehat{\psi}_t(x,v)\right\}\,,\end{aligned} \tag{II.66}$$

where the function $\chi[s]$ is defined as

$$\chi[s] = \min\{1, e^s\}\,,$$

and

$$\begin{aligned}\langle \xi_t(x,v)\rangle &= 0 \qquad \left\langle \xi_t(x,v)\, \xi_{t'}(x',v')\right\rangle = 2D_a\, \widehat{\psi}_t(x,v)\boldsymbol{\delta}(t-t')\boldsymbol{\delta}(x-x')\boldsymbol{\delta}(v-v') \\ \langle \eta_t(x,v)\rangle &= 0 \qquad \left\langle \eta_t(x,v)\, \eta_{t'}(x',v')\right\rangle = 2D\, \widehat{\psi}_t(x,v)\boldsymbol{\delta}(t-t')\boldsymbol{\delta}(x-x')\boldsymbol{\delta}(v-v')\,.\end{aligned}$$

The time evolution does not contain a term with $\tilde{R}$ for the reflecting boundaries anymore. This condition is taken care of by

$$\xi_t(x,v) - D_a\frac{\partial}{\partial v}\widehat{\psi}_t(x,v) = 0 \qquad \text{at } v = \pm 1\,, \tag{II.67}$$

which imposes that there is no outgoing current at the v-space boundary.

Hierarchy of moments and an expression for pressure

To gain an formula for the mechanical pressure, expressions for the average density and other moments are needed. The particle density, and the local velocity, in one realization is defined as

$$\begin{aligned}\widehat{\rho}_t(x) &= \int_{-1}^{1} dv\, \widehat{\psi}_t(x,v)\,, \\ \widehat{m}_t(x) &= \int_{-1}^{1} dv\, v\widehat{\psi}_t(x,v)\,.\end{aligned}$$

The ensemble-averaged density $\rho_t(x) = \langle\widehat{\rho}_t(x)\rangle$ follows a continuity equation (see A.9 for details)

$$\frac{d}{dt}\rho_t(x) = -\frac{d}{dx}J_\rho(x,t)\,, \tag{II.68}$$

with the particle current

$$J_\rho(x,t) = \int_{-1}^{1} dv \left\langle \widehat{\psi}_t(x,v)\, v\, \chi\left[\Gamma v \int dx'dv'\Phi(x-x')\widehat{\psi}_t(x',v')\right]\right\rangle + F^{(e)}(x)\rho_t(x) - D\frac{d}{dx}\rho_t(x)\,.$$

Due to the confining wall, the average particle current must vanish in the steady state, thus

$$-F^{(e)}(x)\rho(x) = \int_{-1}^{1} dv \left\langle \widehat{\psi}(x,v)\, v\, \chi\left[\Gamma v \int dx' dv' \Phi(x-x')\widehat{\psi}(x',v')\right]\right\rangle - D\frac{d}{dx}\rho(x)\,.$$

The expression simplifies further, if $\chi[s] = 1 - \Theta[-s](1-e^s)$ is used, leading to

$$\begin{aligned} &-F^{(e)}(x)\rho(x) = -D\frac{d}{dx}\rho(x) + m(x) \\ &-\int_{-1}^{1} dv \left\langle \widehat{\psi}(x,v)\, v\, \Theta\left[-\Gamma v \int dx' \Phi(x-x')\widehat{\rho}(x')\right]\left(1 - e^{\Gamma v \int dx' \Phi(x-x')\widehat{\rho}(x')}\right)\right\rangle\,, \end{aligned}$$

where $m(x) = \langle \widehat{m}(x)\rangle$ is the ensemble average of the mean velocity vector $\widehat{m}(x)$. Thus, finally the mechanical pressure on the right wall is given by

$$\begin{aligned} p = &-\int_{\Lambda}^{\infty} dx\, F^{(e)}(x)\rho(x) = D\bar{\rho} + \int_{\Lambda}^{\infty} dx\, m(x) \\ &-\int_{\Lambda}^{\infty} dx \int_{-1}^{1} dv \left\langle \widehat{\psi}(x,v)\, v\, \Theta\left[-\Gamma v \int_{-\infty}^{\infty} dx' \Phi(x-x')\widehat{\rho}(x')\right]\left(1 - e^{\Gamma v \int_{-\infty}^{\infty} dx' \Phi(x-x')\widehat{\rho}(x')}\right)\right\rangle\,, \end{aligned} \tag{II.69}$$

where the upper integration boundary can be again any point where the wall potential becomes infinite, thus $\rho(\infty) = 0$ and Λ can be any point deep inside the bulk, where the wall potential vanishes, thus $\rho(\Lambda) = \bar{\rho}$ is the bulk density.

Remarks:

1. Clearly the expression for pressure depends on the bulk density $\bar{\rho}$, the velocity field $m(x)$, and higher moments like $\widehat{G}(x) = \int dv\, v^3 \widehat{\psi}(x,v)$, and their correlations (*e.g.* $\langle \widehat{m}(x)\widehat{G}(x')\rangle$). There is a hierarchy of these moments, thus they need to be calculated order by order. In some cases this hierarchy can be closed, as for example in the active Ornstein-Uhlenbeck process (see next section II.6) or for Active Brownian spheres [51].

2. Although there is a linear dependence on the bulk density, it is not the same as the ideal gas term in equilibrium. It follows for non-interacting ($\Phi = 0$) persistently moving particles

$$\int_{-1}^{1} dv\, v \left\langle \widehat{\psi}_t(x,v)\right\rangle = \int_{-1}^{1} dv\, vP(v|x)\underbrace{P(x)}_{\bar{\rho}} = \bar{\rho}\underbrace{\int_{-1}^{1} dv\, vP(v|x)}_{\langle v(x)\rangle}\,,$$

   where $\langle v(x)\rangle$ is the single particle velocity distribution. In this case(II.69) becomes

$$p = \left[D + \int_{\Lambda}^{\infty} dx \langle v(x)\rangle\right]\bar{\rho}\,,$$

   where the prefactor plays the role of an effective temperature.

Mean velocity field, and higher moments

The expression for pressure involves $m(x)$ and higher moments. Multiplying (II.66) with v and integrating over v and then taking the ensemble average leads, in the steady state ($\frac{dm(x)}{dt} = 0$), to

$$0 = D_a\,[\psi(x,-1) - \psi(x,1)] - \frac{d}{dx}\left\{\int_{-1}^{1} dv \left\langle \widehat{\psi}(x,v)\, v^2\, \chi\left[\Gamma v \int dx' \Phi(x-x')\widehat{\rho}(x')\right]\right\rangle \right.$$
$$\left. + F^{(e)}(x) m(x) - D\frac{d}{dx} m(x)\right\}\,.$$

The calculation of the pressure for this problem gets difficult, especially because of the non-smooth properties of the Metropolis filter. Although the calculation may be possible to carry out with reasonable approximations, it is left for a future project. Instead, the next section II.6 analysis the pressure in the active Ornstein-Uhlenbeck process, where a similar calculation can be carried out by closing the hierarchy under certain reasonable assumptions.

II.6 Pressure in the active Ornstein-Uhlenbeck process

This section II.6 is dedicated to the calculation of the mechanical pressure in the active Ornstein-Uhlenbeck process, first analyzed in [217], and then further investigated in [104]. The aim is to demonstrate that the hierarchy of moments can be closed in this case under certain reasonable assumptions, leading to a closed-form formula for the pressure.

The active Ornstein-Uhlenbeck process in a many-particle system with $i = 1, 2 \ldots, N$ is described by

$$\begin{aligned} \dot{v}_i(t) &= -\alpha v_i(t) + \eta_i(t)\,, \ \text{with} \\ \langle \eta_i(t)\rangle &= 0\,,\ \langle \eta_i(t)\,\eta_j(t')\rangle = 2D_a\boldsymbol{\delta}(t-t')\boldsymbol{\delta}_{ij} \end{aligned} \tag{II.70}$$

and

$$\begin{aligned} \dot{x}_i(t) &= v_0 v_i(t) + F_i(\mathbf{x}) + \xi_i(t)\,, \ \text{with} \\ \langle \xi_i(t)\rangle &= 0\,,\ \langle \xi_i(t)\,\xi_j(t')\rangle = 2D_t\boldsymbol{\delta}(t-t')\boldsymbol{\delta}_{ij}\,, \end{aligned} \tag{II.71}$$

with $\mathbf{x} = \{x_1, \cdots, x_N\}$ and $F_i(\mathbf{x})$ is the total force on particle i, including inter-particle forces, as well as forces exerted by an external potential.

The time evolution of the fluctuating distribution function, which has the same form as in (II.65), is given by (see A.10 for details)

$$\begin{aligned} \frac{d}{dt}\widehat{\psi}_t(x,v) = &-\frac{\partial}{\partial v}\left\{\sqrt{2D_a\widehat{\psi}_t(x,v)}\widehat{\eta}(x,v,t) - \alpha v\widehat{\psi}_t(x,v) - D_a\frac{\partial}{\partial v}\widehat{\psi}_t(x,v)\right\} \\ &-\frac{\partial}{\partial x}\left\{\sqrt{2D_t\widehat{\psi}_t(x,v)}\widehat{\xi}(x,v,t) + v_0 v\widehat{\psi}_t(x,v)\right. \\ &\left. + \sum_i \widehat{\rho}_i(x,v,t)F_i(\mathbf{x}'(t)) - D_t\frac{\partial}{\partial x}\widehat{\psi}_t(x,v)\right\}, \end{aligned} \tag{II.72}$$

with $\widehat{\rho}_i(x,v,t) = \boldsymbol{\delta}(x - x_i(t))\boldsymbol{\delta}(v - v_i(t))$ and

$$\begin{aligned} \left\langle \widehat{\xi}(x,v,t) \right\rangle &= 0 \qquad \left\langle \widehat{\xi}(x,v,t)\, \widehat{\xi}(x',v',t') \right\rangle = \boldsymbol{\delta}(t-t')\boldsymbol{\delta}(x-x')\boldsymbol{\delta}(v-v')\,, \\ \langle \widehat{\eta}(x,v,t) \rangle &= 0 \qquad \left\langle \widehat{\eta}(x,v,t)\, \widehat{\eta}(x',v',t') \right\rangle = \boldsymbol{\delta}(t-t')\boldsymbol{\delta}(x-x')\boldsymbol{\delta}(v-v')\,. \end{aligned} \tag{II.73}$$

Assuming that the particles interact via pair-wise forces, with $F(x_i, x_j)$ being the force the j^{th} particle exerts on the i^{th} one, and that the particles are under the influence of some external potential, which exerts the force $F^{(e)}(x_i)$ on the i^{th} particle, the total force $F_i(\mathbf{x})$ on particle i can be specified as

$$F_i(\mathbf{x}) = F^{(e)}(x_i) + \sum_{j \neq i} F(x_i, x_j)\,.$$

With this assumption, the force term in (II.72) can be written as

$$\begin{aligned} \sum_i \widehat{\rho}_i(x,v,t) F_i(\mathbf{x}'(t)) &= \sum_i \widehat{\rho}_i(x,v,t) F^{(e)}(x) + \sum_i \widehat{\rho}_i(x,v,t) \sum_{j \neq i} F(x, x_j) \\ &= \widehat{\psi}_t(x,v) F^{(e)}(x) + \sum_i \sum_{j \neq i} F(x, x_j) \widehat{\rho}_i(x,v,t)\,, \end{aligned}$$

as $\widehat{\psi}_t(x,v) = \sum_i \widehat{\rho}_i(x,v,t)$. By further specifying the pairwise inter-particle forces as

$$\begin{aligned} &F(x_i, x_j) = F(x_i - x_j) = \text{sign}(x_i - x_j) |F(|x_i - x_j|)|\,, \text{ with} \\ &F(x_i, x_j) = 0 \text{ if } i = j\,, \end{aligned}$$

it follows

$$\begin{aligned} &\sum_i \sum_{j \neq i} F(x, x_j) \boldsymbol{\delta}(x - x_i(t)) \boldsymbol{\delta}(v - v_i(t)) = \sum_j F(x - x_j) \widehat{\psi}_t(x,v) \\ &= \widehat{\psi}_t(x,v) \int dx' dv' \sum_j \boldsymbol{\delta}(x' - x_j(t)) \boldsymbol{\delta}(v' - v_j(t)) F(x - x') \\ &= \widehat{\psi}_t(x,v) \int dx' dv' F(x - x') \widehat{\psi}_t(x',v') = \widehat{\psi}_t(x,v) \int dx' F(x - x') \widehat{\rho}_t(x')\,, \end{aligned}$$

where the definition

$$\widehat{\rho}_t(x) = \int dv\, \widehat{\psi}_t(x,v) \tag{II.74}$$

is used. Therefore (II.72) becomes

$$\begin{aligned} \frac{d}{dt}\widehat{\psi}_t(x,v) = &- \frac{\partial}{\partial v}\Big\{ \sqrt{2D_a \widehat{\psi}_t(x,v)}\, \widehat{\eta}(x,v,t) - \alpha v \widehat{\psi}_t(x,v) - D_a \frac{\partial}{\partial v} \widehat{\psi}_t(x,v) \Big\} \\ &- \frac{\partial}{\partial x}\Big\{ \sqrt{2D_t \widehat{\psi}_t(x,v)}\, \widehat{\xi}(x,v,t) + v_0 v \widehat{\psi}_t(x,v) \\ &+ F^{(e)}(x) \widehat{\psi}_t(x,v) + \widehat{\psi}_t(x,v) \int dx' F(x - x') \widehat{\rho}_t(x') - D_t \frac{\partial}{\partial x} \widehat{\psi}_t(x,v) \Big\}\,. \end{aligned} \tag{II.75}$$

Moments and pressure

As in the case of the kinetic Monte Carlo dynamics, the calculation of pressure requires the calculation of the moments for the distribution $\widehat{\psi}_t(x,v)$. The 0^{th} moment $\widehat{\rho}_t(x)$ is defined in (II.74). Integrating (II.75) over v on both sides leads to[20]

$$\frac{d}{dt}\widehat{\rho}_t(x) = -\frac{\partial}{\partial x}\Big\{v_0\widehat{m}_t(x) + F^{(e)}(x)\widehat{\rho}_t(x) + \int dx' F(x-x')\widehat{\rho}_t(x)\widehat{\rho}_t(x')\Big\}$$
$$+ D_t\frac{\partial^2}{\partial x^2}\widehat{\rho}_t(x) - \int dv\frac{\partial}{\partial x}\left[\sqrt{2D_t\widehat{\psi}_t(x,v)}\widehat{\xi}(x,v,t)\right] - \int dv\frac{\partial}{\partial v}\left[\sqrt{2D_a\widehat{\psi}_t(x,v)}\widehat{\eta}(x,v,t)\right],$$

with the 1^{st} moment defined as

$$\widehat{m}_t(x) = \int dv\, v\,\widehat{\psi}_t(x,v)\,. \tag{II.76}$$

Following the Itō convention, the time evolution of the ensemble-averaged density $\rho_t(x) = \langle\widehat{\rho}_t(x)\rangle$ follows a continuity equation of the form (as the mean of the noise is zero, see (II.73))

$$\frac{d}{dt}\rho_t(x) = -\frac{\partial}{\partial x}J_t(x)\,,$$

with

$$J_t(x) = v_0 m_t(x) + F^{(e)}(x)\rho_t(x) + \int dx' F(x-x')\big\langle\hat{\rho}_t(x)\hat{\rho}_t(x')\big\rangle - D_t\frac{\partial}{\partial x}\rho_t(x)\,. \tag{II.77}$$

In the steady state $\frac{d}{dt}\rho_t(x) = 0$, thus the current $J_t(x)$ must be constant. Having chosen a confining potential as boundary condition for the particle system, the current must be zero. With (II.77), it thus follows

$$0 = v_0 m(x) + F^{(e)}(x)\rho(x) - D_t\frac{\partial}{\partial x}\rho(x) + I_1(x)\,,\ \text{with} \tag{II.78}$$
$$I_1(x) = \int dx' F(x-x')\big\langle\hat{\rho}(x)\hat{\rho}(x')\big\rangle\,.$$

An expression for the average steady-state velocity $m(x)$ of a particle at position x can be gained from its time evolution (see A.11)

$$\frac{d}{dt}m_t(x) = -\frac{\partial}{\partial x}\Big\{v_0 Q_t(x) + F^{(e)}(x)m_t(x) + I_2(x)\Big\} + D_t\frac{\partial^2}{\partial x^2}m_t(x) - \alpha m_t(x)\,,\ \text{with} \tag{II.79}$$
$$I_2(x) = \int dx'\, F(x-x')\,\big\langle\widehat{\rho}_t(x')\widehat{m}_t(x)\big\rangle\,,$$

which includes the ensemble average of the 2^{nd} moment

$$\widehat{Q}_t(x) = \int dv\, v^2\widehat{\psi}_t(x,v)\,.$$

[20] $\int_{-\infty}^{\infty} dv\frac{\partial^2}{\partial v^2}\widehat{\psi}_t(x,v) = \Big[\frac{\partial}{\partial v}\widehat{\psi}_t(x,v)\Big]_{v=-\infty}^{\infty} = 0$, because of the confinement of v in the harmonic potential and $\int_{-\infty}^{\infty} dv\frac{\partial}{\partial v}\Big[\alpha v\widehat{\psi}_t(x,v)\Big] = \Big[\alpha v\widehat{\psi}_t(x,v)\Big]_{v=-\infty}^{\infty} = 0$, for the same reasoning.

In the steady state $\frac{d}{dt}m_t(x) = 0$, thus

$$\alpha m(x) = -\frac{\partial}{\partial x}\left\{ v_0 Q(x) + F^{(e)}(x)m(x) - D_t \frac{\partial}{\partial x} m(x) + I_2(x) \right\} . \tag{II.80}$$

As in the previous subsection II.5.1, the mechanical pressure on the right wall of the potential, which exerts $F^{(e)}$ on the particles, is given by

$$P = -\int_\Lambda^\infty dx\, F^{(e)}(x)\rho(x)\,, \tag{II.81}$$

where the lower integration boundary Λ can be any point inside the bulk, where the wall force vanishes, and the upper boundary can be any point at which the wall potential becomes infinite. With (II.78) it follows that (see A.12 for details)

$$P = \frac{v_0}{\alpha}[v_0\, Q(\Lambda) + I_2(\Lambda)] + D_t\, \rho(\Lambda) + \int_\Lambda^\infty dx\, I_1(x)\,, \tag{II.82}$$

where the two assumptions

$$m(\Lambda) = 0 \quad \text{and} \quad \frac{\partial}{\partial x} m(x)\Big|_{x=\Lambda} = 0$$

were made for the steady-state bulk mean velocity[21].

It can be shown (see A.13) that for large system sizes

$$Q(\Lambda) \simeq \frac{D_a}{\alpha}\rho(\Lambda)\,. \tag{II.83}$$

The assumption leading to the closure of the hierarchy of moments is that the probability to find a particle with a certain velocity is independent of the exact position inside the bulk, thus

$$P(x = \Lambda, v) \simeq \rho(\Lambda)P(v)\,.$$

Furthermore, the last term in (II.82) can be recast as

$$\int_\Lambda^\infty dx\, I_1(x) = \underbrace{\int_\Lambda^\infty dx \int_{-\infty}^\Lambda dx'\, F(x-x')\langle\widehat{\rho}_t(x')\widehat{\rho}_t(x)\rangle}_{:=P_D} + \underbrace{\int_\Lambda^\infty dx \int_\Lambda^\infty dx'\, F(x-x')\langle\widehat{\rho}_t(x')\widehat{\rho}_t(x)\rangle}_{=0\,,\text{ as } F(x-x')=-F(x'-x)}\,,$$

[21] These assumptions on the bulk mean velocity allow for a check of (II.78). The wall force was assumed to vanish inside the bulk, thus $F^{(e)}(\Lambda) = 0$. Furthermore, it follows in the steady state that $m(\Lambda) = 0$ and $\frac{\partial}{\partial x}\rho(x)\big|_{x=\Lambda} = 0$, thus the integral

$$I_1(\Lambda) = \int_{-\infty}^\infty dx' F(\Lambda - x')\langle\widehat{\rho}(\Lambda)\widehat{\rho}(x')\rangle = 0$$

must vanish inside the bulk. This is a consistent consequence, as the net force in the bulk must be zero.

where P_D is the standard interaction part in the pressure of equilibrium systems. The pressure in the bulk of the particle system can be thus expressed as

$$P = \underbrace{\rho_t(\Lambda)\left[D_t + \frac{v_0^2}{\alpha^2}D_a\right]}_{:=P_0} + \underbrace{\frac{v_0}{\alpha}I_2(\Lambda)}_{:=P_I} + P_D\,,$$

where P_0 corresponds to the ideal gas contribution in the virial equation if $v_0 = 0$, P_D is the second virial term and P_I is the indirect contribution incorporating the correlation between density and velocity (see (II.79)).

It is straightforward to check that the passive limit $v_0 = 0$ recovers the passive virial expression for pressure.

II.7 Discussion

The numerical simulation results presented in this thesis demonstrate for the concerned model (see section II.1) of self-propelled particles that the two-step melting from a solid to a hexatic to a liquid phase is preserved far from equilibrium (where the scenario is well established) even up to quite high persistence lengths (see subsections II.3.3 and II.3.4). Under the persistent kinetic Monte Carlo dynamics, the effect of self-propulsion is to shift the melting transitions to higher densities. There is reason to believe that in the limit of small activities, active particle systems can retain an effective equilibrium description at a coarse-grained level [92, 93, 107, 206, 218]. The results presented here considerably extend this finding, as it positively identifies the continuation of the equilibrium phases at large persistence lengths. The stability of the hexatic phase (which is explicitly identified through the orientational and positional correlation functions) is particularly noteworthy. Its presence illustrates that the dissociation of the ordering between the orientational and positional degrees of freedom is preserved even at large activities. The results give rise to the conjecture that for all activities, the hexatic phase is stable in a finite density interval and that, in the limit of infinite persistence lengths, the liquid–hexatic phase transition shifts to infinite densities.

Most importantly, the analysis utilized here conclusively identifies the hexatic phase through the defining exponential decay of its positional correlation functions and algebraic decay of orientational correlation functions (see subsections II.3.3 and II.3.4). Even though the existence of the hexatic phase far from equilibrium was suggested earlier in driven-granulate experiments [219], the correlation functions could not be evaluated precisely in these experiments, because the system sizes were very small. First experimental indications of order-disorder transitions in a system of self-propelled particles at high packing fractions are found in [220].

Furthermore, unambiguous evidence is presented, supporting that in this two-dimensional self-propelled particle system, MIPS manifests itself as a liquid–gas coexistence (see subsections II.3.2 and II.3.5). Similar to equilibrium both of these phases (liquid and gas) feature short-range order. Therefore, this excludes other possibilities like crystals, polycrystals, and gel phases. Furthermore, the presented full phase diagram on the density-persistence plane shows the (non-equilibrium) two-step melting scenario as a phenomenon which is separated from MIPS by a liquid phase (see subsection II.3.4). However, the extension of

this separation, as well as the extension of the hexatic phase to the limit of infinite densities and activities cannot be assured by simulations and requires new theoretical approaches. As observed in other active models (see subsection I.4.1), the MIPS region begins at relatively low densities and high persistence lengths. Drawing analogy with the equilibrium liquid-gas coexistence, this suggests a critical point at the onset of MIPS. This scenario was first confirmed [221] in a system of active Brownian particles.

The reason behind the choice of the soft r^{-6} potential in this thesis is the very small positional correlation length in the equilibrium hexatic phase, which makes it possible to unambiguously distinguish the hexatic phase from the solid even for moderate system sizes. However, real-world experiments usually deal with much stiffer potentials [18, 19, 75, 76]. This makes it important to characterize the influence of such stiffer potentials on the phase diagram. It turns out, as shown in subsection II.3.4, that even for a stiff potential (r^{-16}) the phase diagram is qualitatively equivalent to that of the r^{-6} potential: the two-step melting scenario (including the hexatic phase) survives high persistence lengths and MIPS remains (as liquid-gas coexistence) separated from the melting transitions. The investigation of the melting for even stiffer potentials requires the simulation of larger systems as the positional correlation length of the hexatic phase grows [13]. Therefore, an improved algorithmic approach is required to study the activity-induced melting for stiff potentials, especially for the hard-disk limit r^{-n} with $n \to \infty$. However, the kinetic Monte Carlo approach studied here reaches the steady state even in the hard-disk limit for small densities and high persistence lengths. This is already within the parameter space where MIPS appears and it manifests as liquid-gas coexistence (see subsection II.3.5) just like for the soft potential. Thus, even though the hard-disk melting is not studied here, there is sufficient evidence to conjecture that the qualitative phase diagram does not change drastically while approaching the hard-disk limit.

As described in subsection I.4.1, there is no consensus on the precise nature of the coexisting phases observed for monodisperse self-propelled particles. For example, in [97] MIPS is described as coexistence between a "*solid-like and gas state*", in [18] as coexistence between a "*dense large cluster and a dilute gas phase*", or in [98] as a coexistence between a "*dense and dilute phase*", where the dense phase "*exhibits structural properties consistent with a two-dimensional colloidal crystal near the crystal-hexatic transition point*". As mentioned in subsection II.3.2, the positional and the orientational correlation functions are not defined inside the coexistence region. Therefore, reliable statements about the nature of the coexisting phases are difficult to make without steady-state data of the homogeneous phases at the boundary of the MIPS region. This approach is also followed in [108] which presents a full phase diagram of symmetric active Brownian particles. It is stated in [108] that the dense phase of the MIPS "*can be either disordered (liquid) or ordered (hexatic or solid)*". For this to happen, the MIPS boundary must interact with the melting transitions. The work in [108] reports that the activity-induced two-step melting scenario[22] with the intermediate hexatic phase extends up to high activities and moreover, the melting transitions merge with the MIPS boundary. This result suggests that the high-density phase of MIPS in active Brownian particles could be either liquid, hexatic or solid.

First results for the full phase diagram of particles following the active Ornstein-Uhlenbeck

[22] First hints for melting transitions at high densities for the active Brownian model were given in [107, 199] together with the qualitative picture that self-propulsion shifts the melting transitions to higher densities, but without evidence for the hexatic phase.

process were presented in [222]. The results for the kinetic Monte Carlo dynamics presented here, the active Brownian dynamics results in [108] and the active Ornstein-Uhlenbeck results in [222] agree in the observation that the two-step melting scenario (including the hexatic phase) is robust under finite persistence. Differences may be found in the precise interaction of the melting transitions with the boundary of the MIPS region. Furthermore, [108] reports deviations from the equilibrium limiting exponents (0.33 and 0.25) for the positional and orientational correlations predicted in equilibrium by the BKTHNY theory (see subsection II.3.3 and section I.7). In contrast, the data presented in this thesis suggests that the equilibrium limiting exponents are robust even at high activity (see subsection II.3.3). This points towards the possibility that a coarse-grained free-energy functional exists[51, 93, 107, 223], such that both MIPS and the two-step melting are covered under one effective equilibrium theory.

Such an effective equilibrium description may allow for well-defined state variables, such as pressure. Although pressure is not a state variable in generic active systems, the model studied in this thesis belongs to the narrow class with torque-free dynamics where pressure could be defined [48, 51]. However, the computation of an expression for pressure in the kinetic Monte Carlo model is not straightforward and the calculation in section II.5 is left with an expression that still needs to be explored further. The effect of persistence could be reflected as a change in the effective pressure. For example, in the phase diagram in subsection II.3.4, at sufficiently high persistence lengths (say at $\lambda_1 = const.$), an increase in density induces a gas–liquid coexistence, in striking analogy with the van-der-Waals physics found in equilibrium fluids of attractive particles (e.g. the Lennard-Jones system). Comparing the full equilibrium phase diagram of attractive particles with the here obtained phase diagram of self-propelled particles would suggest that the effective pressure decreases with increasing persistence. An even further density increase at the same λ_1 finally induces the ordering transitions in the phase diagram presented here, which again resembles the behavior of an equilibrium Lennard-Jones system. This only strengthens the analogy with an equilibrium scenario which is still to be explored.

The above discussion shows, that an expression for the pressure is highly desirable. It would offer a tool to specify the precise kind of transitions in the non-equilibrium two-step melting scenario, which remains an unanswered question in this thesis. An expression for the pressure would furthermore allow for a more detailed study of MIPS.

As shown in section II.6, an expression for a thermodynamic pressure can be derived for the active Ornstein-Uhlenbeck process. The same [51] applies for the active Brownian dynamics. The pressure was used in both models to characterize MIPS [51, 104, 105, 224, 225] and also exploited recently in [108] to determine the phase transitions in the two-step melting scenario under the influence of self propulsion. The study in [108] uses a potential stiff enough to exhibit a first-order liquid-hexatic transition at equilibrium. The authors state that at sufficiently high self propulsion the first-order transitions becomes a continuous transition, thus self propulsion would play a similar role as the softness of the inter-particle potential (see sections I.7, I.8 and subsection II.3.4).

As mentioned above, the results in [108], [222] and the results presented in this thesis suggest that the qualitative picture of the interplay of MIPS with the two-step melting transitions does depend on how persistence is introduced in the microscopic dynamics. Studies on an active dumbbell system [106, 205] furthermore suggest that the shape of the particles affects the phase diagram even stronger. Firstly, it is shown in [106, 205] that also the equi-

librium dumbbell system undergoes a two-step melting scenario with a first-order liquid-hexatic transition. Secondly, it is stated that the MIPS region continuously extends from the equilibrium liquid-hexatic coexistence and persists as such throughout the whole studied parameter range. However, the common result in all these studies (the here presented results and [106, 108, 205, 222]) is that the two-step melting scenario holds outside equilibrium and that the hexatic phase is robust under self-propulsion. In fact, the statement in [106, 205] goes even further as the dumbbell system has effective alignment interactions which lead to collective motion in the form of rotating clusters within the coexistence [205]. First experimental studies [226] suggest that additional alignment interactions may not destroy spatial order but lead to the phenomenon of "flowing crystals". As the studied system sizes are small, conclusive statements (relying on the robust criteria of the decay of spatial and orientational correlation functions) are still to be obtained. Theoretical and numerical studies come to contradicting conclusions regarding the questions of the possibility of spatial order under the influence of additional alignment interactions. In [227, 228] it is stated that spatial order is indeed possible, whereas [228] states that alignment interactions destroy spatial order.

Other studies focus on the question of phase transitions in self-propelled polydispersed particle systems [103, 229]. The investigations in [229] build on the same kinetic Monte Carlo approach exploited in this thesis, whereas [103] relies on the active Brownian dynamics. Both studies report that the freezing transition is shifted to higher densities with increasing self-propulsion. Furthermore [103] presents evidence for a MIPS region that is separated from the freezing transition by a liquid phase in analogy to the phase diagram presented here.

The comparison of these recent studies with the findings of this thesis strengthens a notion of universality in the system of active matter. It clearly shows that not only the equilibrium phases survive in presence of self-propulsion, but also new collective behavior emerges. In real systems, the presence of additional interactions, conservation laws, and symmetries may lead to more intricate behavior. Nevertheless, it is likely that even for such general cases thermodynamic phases could be clearly defined, in spite of the lack of state variables similar to equilibrium. Whether the notion of orders of phase transitions, criticality, universal scaling laws can be extended to these phase behaviors remains to be explored. The future of active matter, and more generally of the non-equilibrium physics is full of such challenging questions waiting to be answered.

III – Phase transitions in one dimension

Abstract: *There is a misconception, widely shared amongst physicists, that the equilibrium free energy of a one-dimensional classical model with finite-ranged interactions, and at non-zero temperatures, cannot show any singularities as a function of the coupling constants. This chapter presents an instructive counter-example. This is a model of thin rigid linear rods of equal length 2ℓ whose centers lie on a one-dimensional lattice, of lattice spacing a. The interaction between rods is a soft-core interaction, having a finite energy U per overlap of rods. Here, it is shown that the equilibrium free energy per rod $\mathcal{F}(\frac{\ell}{a}, \beta)$, at inverse temperature β, has an infinite number of singularities, as a function of $\frac{\ell}{a}$.*

III.1 Introduction

One-dimensional systems have their benefits, as they are often easier to treat analytically than their higher-dimensional counterparts and still they can be of physical relevance. Many natural phenomena have an effective representation in one dimension, *e.g.*, fluctuating interfaces [230, 231], binding of polymers [232, 233], wetting transitions [234], transport in molecular motors [235], *etc.*. In one of the well-known examples, the scaling laws of the Kondo problem (related to the anomalous behavior of resistivity in metals due to the scattering of conduction electrons with magnetic impurities) is understood by its equivalence to a one-dimensional Ising model with $\frac{1}{r^2}$ interactions [20]. Indeed, such exact solutions lead sometimes to advances in a much broader context. A large number of fundamental results in non-equilibrium physics in recent times arose out of one-dimensional models. However, most studies in equilibrium physics are in higher dimensions, and one-dimensional systems are often deemed as uninteresting. This could be primarily due to a common belief that one-dimensional systems do not show phase transitions, or more precisely: in any one-dimensional classical system, in thermal equilibrium, having finite-ranged pairwise interactions, the thermodynamic potential cannot show a singular dependence on the control parameters [236]. Clearly, typical models in graduate textbooks, namely, the Ising model, the Potts model, the rotor model, do not show phase transitions in one dimension, except (perhaps) at zero or infinite temperature, and this strengthens this belief. It is well-known that Ising himself came to the incorrect conclusion in his thesis (1925) that his model lacks phase transitions even in higher dimensions. *"Es wird gezeigt, dass ein solches Modell noch keine ferromagnetische Eigenschaften besitzt, und dieser Aussage auch auf das dreidimensionale*

Modell ausgedehnt."[1]

There is no general proof for the absence of one-dimensional phase transitions [10]. The origin of the folk wisdom about their absence is perhaps an unsubstantiated generalization of a rigorous result due to van Hove [9] on the absence of phase transitions in a one-dimensional system of particles with a non-vanishing hard-core length and finite-ranged inter-particle interactions. This result was later extended to lattice models [237] and long-ranged interactions of a power-law decay with distance [22, 23, 238]. The belief further grew out of essentially two arguments: **one**, about the absence of phase transitions as a function of temperature in one-dimensional models having a finite-dimensional irreducible transfer matrix [10] and **second**, the Landau-Peierls argument about the absence of long-range-order in one-dimensional systems, when creating a domain-wall has a finite energy cost [115]. However, their arguments do not cover all possible scenarios, and several counter-examples of equilibrium phase transitions in one-dimensional models have been known for a long time: DNA unzipping [232, 233], interface depinning [230], hidden-state models [239], and condensation in zero-range models [240]. Nevertheless, the incorrect belief persists. This is probably because all these models are defined in higher dimensions and they have an effective one-dimensional representation. In examples of truly one-dimensional models [239], the phase transitions appear in unrealistic complex parameter values.

In this chapter, the goal is to clarify this aspect of one-dimensional phase transitions. For this, first, the issue is discussed with a brief summary of existing models, where the attempts were mostly to circumvent the Landau-Peierls argument or the Perron-Frobenius theorem. This part of the discussion is influenced by the paper of Cuesta *et al.* [10]. Afterwards, a new model is presented which is truly one-dimensional and undergoes an *infinite* number of phase transitions, equivalently, it has an *infinite* number of singularities in the free energy. Importantly, these phase transitions are due to a different mechanism than the models studied earlier. The singularities in the free energy are robust, geometrical in origin, and come from the changes in the structure of the two-body allowed phase space as the coupling constant is changed. The chapter is concluded with a discussion on the generality of this mechanism and its extension to higher dimensions or even outside equilibrium.

III.2 Arguments for absence of phase transition

Landau-Peierls argument

One of the most well-known arguments for the absence of phase transitions in one dimension is due to Landau [115] and Peierls [37]. The argument is best described for the Ising model, although it is straightforward to generalize. The one-dimensional Ising model is a two-state model defined on a linear chain of L sites (*periodic* boundary for simplicity) with a spin variable S_i assigned to each site i which can take the value $S_i = \pm 1$. Each spin interacts with its nearest neighbors only such that the energy of a spin configuration is given by the Hamiltonian

$$H = -J \sum_{i=1}^{L} S_i S_{i+1} \tag{III.1}$$

[1] Later, it is shown that such a model does not yet own ferromagnetic properties and this statement can be extended to the three-dimensional model. Source: D. Thouless, "Three lectures on low-dimensional phase transitions", Trier, August 17-19, (2012).

where J is the ferromagnetic interaction strength.

The spins in a fully ordered state are either all $+1$ or all -1. Both states have the least amount of energy and at zero temperature the system is stuck in one of these configurations. At a non-zero temperature, the spins fluctuate which results in the creation of domains with positive and negative spins. Because of the nearest neighbor interaction, the energy cost for the domain creation originates solely from the domain boundaries. The energy for N such domain walls is $E = 2NJ$ and the entropy from distributing the walls in the system is $S = k_{\mathrm{B}} \log \frac{L!}{N!(L-N)!}$. Clearly, the entropy gain grows higher than the energy costs as N is increased. The free energy at temperature T is

$$F = E - TS = 2NJ - k_{\mathrm{B}}T \log \frac{L!}{N!(L-N)!} \, .$$

For large N and L, minimizing the free energy and taking Sterling's approximation gives the most probable value for the number of domain walls

$$\overline{N} \simeq L \, \frac{e^{-\frac{2J}{k_{\mathrm{B}}T}}}{1 + e^{-\frac{2J}{k_{\mathrm{B}}T}}} \, .$$

Hence, there is a thermodynamically large number of domains at any finite temperature, and thus long-range order is not possible.

This problem can also be treated from a dynamical perspective. If a disordered state with many domain walls has to become ordered at finite temperature, the domain walls must annihilate each other. However, due to the short-ranged interaction, there is no effective force between the domain walls which can move them closer to each other for the annihilation. As a result, the system remains disordered. Clearly, the short-ranged interaction is crucial for this argument. In a system with long-range interactions, the energy cost for the domain creation may grow faster than the entropy and the system may show a phase transition. The minimum range for such long-range interactions is given by Ruelle [22] and Dyson [238]. They proved that the pair-interaction decaying as $\frac{1}{r^2}$ (r is the distance between variables) sets this boundary between the presence and the absence of long-range order in one dimension [2].

Degenerate spectrum of the transfer matrix

The above Landau-Peierls argument is not rigorous. In the literature, a rigorous analysis is often presented using the fact that the free energy is non-analytic at a phase transition. The associated question is: could such non-analyticity arise in one dimension and what could prevent it? This can be easily answered in the context of the Ising model (III.1) with the transfer matrix. The canonical partition function for this model is

$$\mathcal{Z} = \sum_{\{S_i = \pm 1\}} e^{\beta J \sum_{i=1}^{L} S_i S_{i+1}} = Trace(\mathcal{T}^L) \tag{III.2}$$

[2] In this transition the domain walls are like the topological defects in Kosterlitz-Thouless transition or 2D melting. In fact, this problem of the Ising model with inverse square interaction was the very beginning of the work on defect mediated transitions by Kosterlitz and Thouless [6].

with the transfer matrix

$$\mathcal{T} = \begin{pmatrix} e^{\beta J} & e^{-\beta J} \\ e^{-\beta J} & e^{\beta J} \end{pmatrix} .$$

The two eigenvalues of the transfer matrix are

$$\lambda_1 = 2\cosh\beta J \qquad \text{and} \qquad \lambda_2 = 2\sinh\beta J\,,$$

thus the partition function is

$$\mathcal{Z} = \lambda_1^L + \lambda_2^L\,.$$

Therefore, the free energy density in the thermodynamic limit is given by

$$f = -\lim_{L\to\infty}\frac{1}{\beta L}\log\mathcal{Z} = -\frac{1}{\beta}\log\max\{\lambda_1,\lambda_2\}\,.$$

The eigenvalue λ_1 is the largest for any non-zero temperature and it is an analytic function of the coupling strength βJ. Hence, the free energy is also analytic and therefore, phase transitions in the one-dimensional Ising model are absent at non-zero temperature. However, in the zero temperature limit, the two eigenvalues converge and the largest eigenvalue becomes doubly degenerate. This introduces a non-analyticity in the zero temperature limit.

This picture easily generalizes for other models and provides a mechanism for the appearance of singularities in the free energy (more examples are given later). The general understanding is that singularities in the free energy originate from the degeneracy of the largest eigenvalue of the transfer matrix. Conditions for this degeneracy are set by the well-known Perron-Frobenius theorem [40]. The precise statement is the following.

The Perron-Frobenius theorem: *If $\mathcal{T}$ is a square, finite, irreducible*[3] *matrix with all elements being non-negative, then its maximum eigenvalue is real, positive and non-degenerate.*

The transfer matrix for a n-state model in one dimension is $n \times n$-dimensional. All entries in the transfer matrix are by construction due to Boltzmann factor and therefore positive (unless, for infinite energy or at zero temperature). In this case, the Perron-Frobenius theorem [40] ensures that the largest eigenvalue is non-degenerate and hence the appearance of a phase transition is not possible in such one-dimensional models.

III.3 Examples of phase transitions

In this scenario for the transfer matrix, the only way a phase transition can take place is if the conditions required for the Perron-Frobenius theorem to hold are not met. The most famous example of this is the two-dimensional Ising model which undergoes a phase transition at a finite non-zero temperature. How does this happen? In the two-dimensional Ising model on a periodic $L \times M$ square lattice, each column can be interpreted as one site on a one-dimensional lattice of length L, where each site takes 2^M configurations (due to the M spins). The transfer matrix [27, 241] is therefore $2^M \times 2^M$-dimensional. In the thermodynamic limit, when L and M become infinite, the transfer matrix also becomes infinite,

[3] A matrix is irreducible if the matrix cannot be put in a block upper triangular form by row-column permutation [10]. If all matrix elements are non-zero, then the matrix is irreducible. This is mostly considered in this thesis.

thus the Perron-Frobenius theorem does not apply any longer. The largest eigenstate could become degenerate even at a finite non-zero temperature as shown by Onsager [242] (for a simpler analysis see [241, 243]).

This could also happen in models which are effectively one-dimensional. A few of such examples are discussed below with the focus on how the conditions for the Perron-Frobenius theorem are bypassed.

Kittel's model

Another way of circumventing the Perron-Frobenius theorem is by hard-core interactions which make certain entries in the transfer matrix zero. This is shown in a model by Kittel [232] and Nagle [244]. They proposed a simple model for KH_2PO_4, which is also a single-ended zipper model of DNA. It consists of a zipper of L links which is fixed at one end (say right) and can be opened only from the other end (say left) (see illustration in Fig. III.1). The links are ordered from left to right as $i = 1, 2, \cdots, L$. The L^{th} link is always intact. The required energy to open the i^{th} link is J if all previous links $1, \cdots, i-1$ are already open. Otherwise, the energy needed is infinite, thus the i^{th} link cannot be opened. In addition, each open link can take Ω number of conformations. The question is if there is a phase transition between a state where the zipper is fully open until the $(L-1)^{\text{th}}$ link to a state where it is partly open (by a non-zero fraction of sites in the thermodynamic limit).

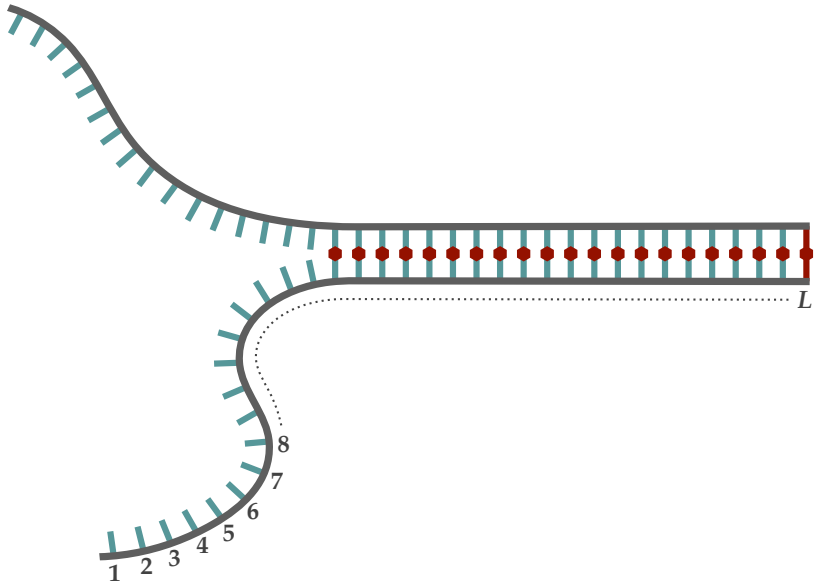


Figure III.1: **The Kittel's model of DNA unzipping.** The two strands can be unzipped only from the left and an amount of energy J needed for breaking each link. The rightmost link cannot be broken.

To write the Hamiltonian for the model, a variable S_i is assigned to the i^{th} link such that $S_i = 0$ if the link is closed, $S_i = 1, 2, \ldots, \Omega$ when the link is open and it is in one of its Ω-fold

degenerate states. The Hamiltonian for the allowed configurations is

$$H = J \sum_{i=1}^{L-1} (1 - \delta_{S_i,0}) \ ,$$

with the additional condition $S_L = 0$ (as the rightmost zipper can not be opened). The partition function is

$$\mathcal{Z} = \sum_{S_1} \cdots \sum_{S_{L-1}} e^{-\beta J \sum_{i=1}^{L-1} \left(1-\delta_{S_i,0}\right)} \prod_{i=1}^{L-1} \left[1 - \delta_{S_i,0} \left(1 - \delta_{S_{i+1},0}\right)\right] \ ,$$

where the last product terms are to ensure the condition that the zipper can only be opened from the left side. It is easy to see that the partition function can be written as a product of transfer matrices

$$\mathcal{Z} = \sum_{S_1} e^{-\beta J \left(1-\delta_{S_1,0}\right)} \sum_{S_2} \mathcal{T}(S_1, S_2) \sum_{S_3} \mathcal{T}(S_2, S_3) \cdots \sum_{S_{L-1}} \mathcal{T}(S_{L-2}, S_{L-1}) \, , \tag{III.3}$$

with the transfer matrix

$$\mathcal{T}(S, S') = e^{-\beta J \left(1-\delta_{S',0}\right)} \left[1 - \delta_{S,0} \left(1 - \delta_{S',0}\right)\right] \ .$$

It follows in a bra-ket notation

$$\mathcal{Z} = \langle A | \mathcal{T}^{L-2} | 1 \rangle \, , \tag{III.4}$$

where the vector

$$\langle A | = \begin{pmatrix} 1 & a & \cdots & a \end{pmatrix} \ ,$$

with $a = e^{-\beta J}$ and $|1\rangle$ is a unit vector of dimension $1+\Omega$. The transfer matrix is of dimension $(1 + \Omega) \times (1 + \Omega)$ and given by

$$\mathcal{T} = \begin{pmatrix} 1 & 0 & \cdots & 0 \\ 1 & a & \cdots & a \\ . & . & \cdots & . \\ . & . & \cdots & . \\ . & . & \cdots & . \\ 1 & a & \cdots & a \end{pmatrix} \ . \tag{III.5}$$

The transfer matrix has three eigenvalues $\lambda_1 = a\Omega$, $\lambda_2 = 1$, and $\lambda_3 = 0$. The last eigenvalue is of degeneracy $\Omega - 1$. The eigenvectors for the first two eigenvalues are

$$|v_1\rangle = \begin{pmatrix} 0 \\ 1 \\ . \\ . \\ . \\ 1 \end{pmatrix} \qquad \text{and} \qquad |v_2\rangle = \begin{pmatrix} 1 - a\Omega \\ 1 \\ . \\ . \\ . \\ 1 \end{pmatrix} \ .$$

Note, that the eigenvectors are not orthogonal. To solve the partition function (III.4), $|A\rangle$ and $|1\rangle$ are expressed as

$$|A\rangle = \frac{1}{1-a\Omega}\left\{[a(1-a\Omega)-1]\,|v_1\rangle + |v_2\rangle\right\}\,,$$
$$|1\rangle = \frac{1}{1-a\Omega}\left\{-a\Omega|v_1\rangle + |v_2\rangle\right\}\,,$$

which (when explicitly written) gives

$$\mathcal{Z} = \frac{1-\left(\Omega e^{-\beta J}\right)^N}{1-\Omega e^{-\beta J}}\,.$$

A straightforward algebra gives the thermodynamic free energy density

$$f = -\lim_{L\to\infty}\frac{1}{\beta L}\log\mathcal{Z} = -\frac{1}{\beta}\log\max(\lambda_1,\lambda_2)\,,$$

with $\lambda_1 = e^{-\beta J}$ and $\lambda_2 = 1$.

This precisely indicates when a non-analyticity in f is possible: it appears when λ_1 and λ_2 cross each other. This happens at the transition temperature $T_c = \frac{J}{k_B \log\Omega}$. Clearly, Ω needs to be more than one for the transition to be at finite temperature. The phase transition appears between a fully open state ($|v_1\rangle$ when $\lambda_1 < \lambda_2$) and a partially (macroscopically) closed state ($|v_2\rangle$ when $\lambda_2 < \lambda_1$).

How is this result consistent with the Perron-Frobenius theorem? For the theorem to apply, all elements of the transfer matrix have to be non-zero and positive, which is not the case for (III.5). It is also important to note that simply breaking this condition does not ensure degeneracy (a phase transition), which is clear from the case with $\Omega = 1$. This case has null entries in the transfer matrix but the phase transition is only at infinite temperature.

Chui-Weeks's model

As mentioned earlier, the phase transition in the two-dimensional Ising model is an example where the Perron-Frobenius theorem is bypassed by the infinite size of the transfer matrix. A similar scenario is realized in an interface model proposed by Chui and Weeks [230]. This is defined by the Hamiltonian

$$H = J\sum_{i=1}^{L}|h_i - h_{i+1}| - K\sum_{i=1}^{L}\delta_{h_i,0}\,,$$

where h_i is the height variable of site i on a one-dimensional lattice with *periodic* boundary conditions. This belongs to the family of models known as the solid-on-solid (SOS) model which describes surfaces without overhangs [245]. The height variable takes only non-negative *integer* values, *i.e.* $h_i \geq 0$. This condition represents the impenetrable substrate the surface is on. The first term in the Hamiltonian is the contribution from the surface tension and the second one is the binding energy to the substrate (Fig. III.2). The question is: does the interface undergoes a phase transition between a bound state, where it is attached to the substrate, to an unbound state?

Following a similar construction as in the Kittel's model it can be shown that the partition function

$$\mathcal{Z} = \text{Trace } \left(\mathcal{T}^L\right)$$

with the transfer matrix

$$\mathcal{T}(h,h') = e^{-\beta J|h-h'|}\left[1+\left(e^{-\beta K}-1\right)\delta_{h,0}\right] .$$

Note that none of the matrix elements of the transfer matrix is zero, therefore, the matrix is irreducible. However, the conditions for the Perron-Frobenius theorem are not met as the matrix is infinite-dimensional, unlike in the Kittel's model. This allows the possibility of a degenerate largest eigenstate. This is seen from the eigenvalues [10]. If $\kappa < (1-\omega)^{-1}$ where $\kappa = e^{-\beta K}$ and $\omega = e^{-\beta J}$, then there is a continuous spectrum of eigenvalues given by

$$\lambda_1(\beta) = \frac{1+\omega}{1-\omega}, \qquad \text{and} \qquad \lambda_2(\beta) = \frac{1-\omega}{1+\omega}.$$

Clearly, in this case, the largest eigenvalue is $\lambda_1(\beta)$. However, if $\kappa > (1-\omega)^{-1}$, then there is an additional eigenvalue

$$\lambda_0(\beta) = \frac{\kappa(1-\omega^2)(\kappa-1)}{\kappa(1-\omega^2)-1}$$

and clearly this becomes the largest eigenvalue.

This shows that there is a crossing of the largest eigenvalue at temperature T_c where $\kappa = (1-\omega)^{-1}$ and this leads to a non-analytic change in the free energy. This corresponds to a transition between a phase below T_c, where the interface is macroscopically bound to the substrate, and an unbound phase above T_c, where the interface is free [10]. This is an example of the so-called roughening or wetting transition.

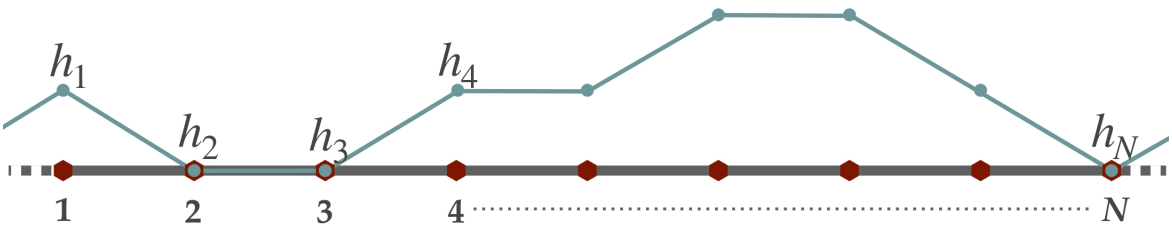


Figure III.2: **Chui-Weeks's model of interfaces.** The height of the interface h_i at site i can fluctuate only above the lattice and it takes integer values. When the interface is attached to the lattice, the binding energy is K per lattice site.

Continuous state model

A similar phase transition is found in a generalization of the Chui-Weeks's model where the height variable is continuous [231]. Another example with a continuous state space is a model of DNA denaturation by Dauxois and Peyards [233]. The transfer matrix becomes an **integral transfer operator** in both examples, which are generally defined by how the

operator acts on a continuous function. For example, the eigenvalue equation of such an integral transfer operator $\mathcal{T}(x, y)$ is defined by

$$\int dy\, \mathcal{T}(x, y)v(y) = \lambda v(x)\,,$$

with λ being the eigenvalue and $v(x)$ is the associated eigenvector. One such example is explicitly analyzed later in section III.4. The important point is that the Perron-Frobenius theorem does not immediately apply for such an integral operator. It is difficult to analytically find the eigenvalues for these two continuous models [231, 233]. However, using analytical approximations and numerical computation there is compelling evidence [233] that there is a crossing of the largest eigenvalue, which gives rise to a non-analytic free energy and therefore to a phase transition.

At the same time, having a continuous state space does not necessarily mean that there is a phase transition. In fact, the work of van Hove, which is often incorrectly cited as the proof for the impossibility of a one-dimensional phase transition, deals with interacting particles on a continuous space. Indeed, statements like "*1D systems with short-ranged interactions can not have a phase transition*" are often quoted as the "van Hove's theorem" [10]. However, van Hove did not make such a general statement in the original paper (written in French) [9]. The precise model that van Hove studied is a system of N identical particles, lying in a segment of length L at the positions $x_i \in [0, L]$, for $i = 1, \ldots, N$. There is a pairwise interaction between the particles with an interaction potential $U(|x_i - x_j|)$, such that the total energy of the system

$$E = \sum_{i<j} U(|x_i - x_j|)\,.$$

In the original work [9], the interaction was

$$U(x) = \begin{cases} \infty & \text{for } 0 \le x \le d_0, \\ V(x) & \text{for } d_0 < x < d_1, \\ 0 & \text{for } x > d_1\,. \end{cases}$$

This means, the particles have a hard-core diameter d_0 which interacts only at distances smaller than d_1 by an interaction potential $V(x)$ which is continuous and it is assumed to be bounded from below (*i.e.* does not go to $-\infty$).

Using the integral transfer operator approach, van Hove rigorously showed [9] that the largest eigenvalue remains non-degenerate at all non-zero temperatures, and it, therefore, leaves the free energy without a singularity. This was interpreted as an evidence for the absence of phase transition. Clearly, van Hove's result was for this very precise example and does not exclude phase transitions in general one-dimensional systems. Later, Ruelle [22] extended the results of van Hove to a lattice version under the same basic hypothesis. As for the range of interactions, the work of Ruelle [22], Dyson [238], and later Fröhlich and Spencer [23] showed that pair interactions decaying faster than $\frac{1}{r^2}$ do not show phase transitions in one dimension.

Even to date, a necessary and sufficient condition for the existence of phase transitions in one-dimensional systems is hard to formulate. This question was discussed in some details recently by Cuesta and Sánchez [10], who provided a sharper criterion for the absence of

phase transitions based on a generalization of the Perron-Frobenius theorem for integral operators. The precise criterion [10] is too technical to explain in this thesis. The simple understanding is that phase transitions in one dimension are **not** possible for a finite ranged inter-particle interaction under the following conditions [10].

- The system has to be perfectly homogeneous, *e.g.*, made of identical particles. This clearly excludes any aperiodic or disordered medium. In fact, there is no known theorem excluding phase transitions for an inhomogeneous one-dimensional system [10].
- There should be no external fields and the potential energy should only depend on the inter-particle separation.

The aim of the above discussion was to point out that the existence of phase transitions in effective one-dimensional systems with short-ranged interactions is not a new result. In spite of these examples, the belief about the non-existence of phase transitions persisted. This is perhaps because, most of these known examples are two-dimensional (interfaces, unzipping of DNA) and have an effective one-dimensional representation. *The original contribution from this part of the thesis, presented in what follows, is to show that singularities in the free energy can arise in a clearly one-dimensional model with short-ranged interactions even at a finite temperature. The mechanism is different from the ones studied in earlier examples, i.e. the degeneracy of the largest eigenstate of a transfer matrix.* This is discussed in the rest of this chapter.

III.4 New example: a model of interacting rods

In its simplest version, the model consists of linear rigid rods of equal length 2ℓ, whose midpoints are fixed at the lattice sites of a one-dimensional lattice of lattice spacing a with a periodic boundary condition. The rods are free to rotate in the plane, as illustrated in Fig. III.3. A configuration of N rods is specified by a set of N angles θ_i, with $0 \leq \theta_i \leq \pi$, for $i = 1$ to N. It is assumed that there is an interaction between the rods, which depends on their overlap. Each overlap between a pair of nearest neighbor rods costs a constant energy U_1. Between a pair of next nearest neighbors the overlap energy is U_2 and between a pair of r^{th} nearest neighbors the overlap energy is U_r respectively. The total number of overlaps between the r^{th} neighbors is n_r (see Fig. III.3). Clearly, n_r is zero, if $r > 2\kappa$ where $\kappa = \frac{\ell}{a}$. The total energy of the system is

$$\mathcal{H} = \sum_i n_i U_i \,.$$

This is similar to the hard-rod model that has been studied extensively in the literature, starting with Onsager [246–249]. The proposed model differs in two significant ways: the centers of the rods are fixed on a lattice, and the overlap energy U_i can be of any sign (attractive or repulsive soft-cores). A somewhat similar model of non-spherical molecules whose centers are fixed at equispaced points along a line, but orientations can change, was studied earlier in [247], but no phase transition was reported. It is important to note that the interaction is not necessarily hard-core in the here proposed model. This is in contrast to Kittel's model, where the hard-core interaction was the primary reason behind the phase transition as it turned certain elements of the transfer matrix to zero. Hence, Kittel's model did not fulfill the condition for the Perron-Frobenius theorem.

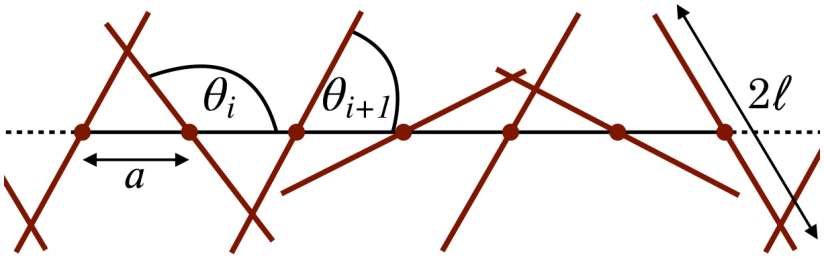


Figure III.3: **A configuration of 7 rods on a line with periodic boundary conditions.** The spacing between rods is a. In the displayed configuration, the number of nearest neighbor overlaps $n_1 = 4$ (overlap at the periodic boundary counts once) and the number of next nearest neighbor overlaps is $n_2 = 1$.

In equilibrium, the free energy per rod of this system is denoted by $\mathcal{F}(\frac{\ell}{a} = \kappa, \beta)$, where β is the inverse temperature. Here, it is shown that $\mathcal{F}(\kappa, \beta)$ is an analytic function of β, as expected, but has a non-analytic dependence on κ. In fact, there are infinitely many transitions: as κ is varied, $\mathcal{F}(\kappa, \beta)$ is singular at every positive integer value of κ, for all β. The singularities remain unchanged irrespective of the sign of U_i, whether the interaction is repulsive or attractive. Later, it is shown that there are also other singularities at some non-integer values of κ. For example, the probability distribution of orientations changes qualitatively when κ is changed across $\frac{1}{\sqrt{2}}$.

III.4.1 Simple case: nearest neighbor interaction

First, the simplest case is considered to explain the basic idea and the singularities: hard-core interactions between the rods, *i.e.* $U_1 = \infty$. Clearly, this case does not allow for overlaps, thus $n_i = 0$ for all $i \geq 1$. Therefore, without loss of generality, it can be assumed that $U_i = 0$ for all $i \geq 2$. For this case, $\mathcal{F}_1(\kappa)$ denotes the free energy per site in the thermodynamic limit (due to hard-core interactions β is irrelevant and hence omitted).

a) Singular free energy

First, the dependence of the free energy on the coupling constant κ is discussed. For $\kappa \leq \frac{1}{2}$ the rods do not interact and the free energy does not change with κ until $\kappa = \frac{1}{2}$ where the length of the rods becomes equal to the distance between the lattice sites.

Beyond $\kappa = \frac{1}{2}$, the free energy increases monotonically as a function of κ as shown in Fig. III.4a. However, this change is non-analytic at certain points. (How this graph is obtained is explained shortly.) There are three types of singularities: (i) the second derivative $\mathcal{F}_1''(\kappa)$ is discontinuous at $\kappa = \frac{1}{2}$, (ii) for κ near 1, say $\kappa = 1 + \epsilon$, with $|\epsilon| \ll 1$, the first derivative $\mathcal{F}_1'(\kappa)$ diverges as $\log(|\epsilon|)$, and (iii) for $\frac{1}{\sqrt{2}} < \kappa < 1$, there is an additional singularity which can be seen in the probability distribution of the orientations $P_\kappa(\theta)$ of the rods (see Fig. III.5). The distribution has square-root singularities as a function of θ, which are not present for lower values of κ.

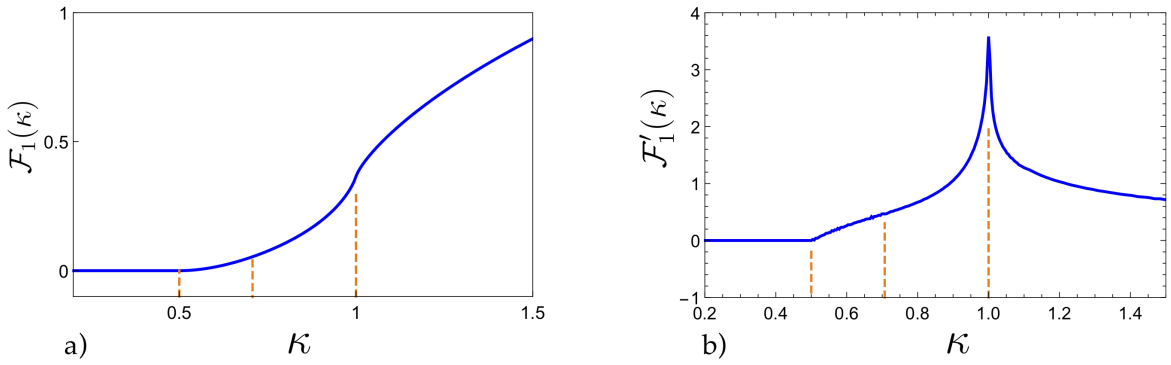


Figure III.4: **Free energy for hard rods ($U_1 = \infty$).** a) Monotonic increase of $\mathcal{F}_1(\kappa)$ as a function of κ. b) Singularity in the first derivative of the free energy $\mathcal{F}'_1(\kappa)$. The points of the singularities are denoted by the orange dashed lines. There is a logarithmic divergence at $\kappa = 1$, a non-analytic change at $\kappa = \frac{1}{2}$ and an additional non-analyticity at $\kappa = \frac{1}{\sqrt{2}}$ which it is not visible in the plot (discussed in the text).

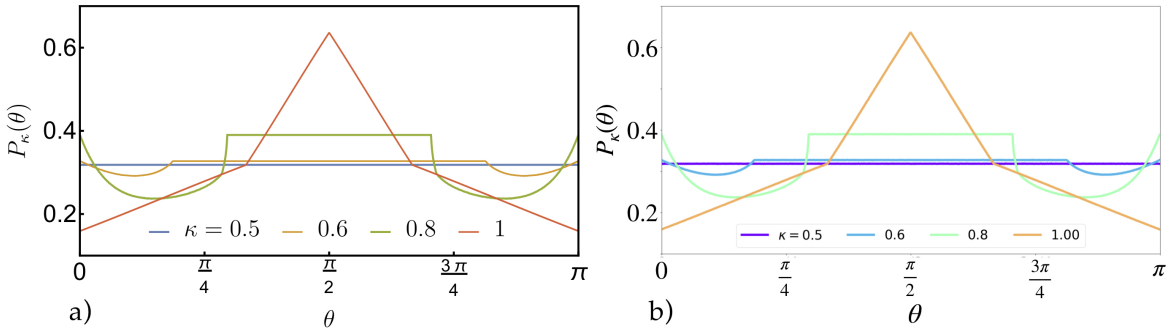


Figure III.5: **Probability distribution of the orientation of the hard rods.** a) Generated from (III.10) using the eigenvector $\psi_\kappa(\theta)$ associated to the largest eigenvalue of the transfer matrix. b) Generated using Monte Carlo simulations. Due to the geometry (see Fig. III.3) the angular range $\theta \in [0, \pi]$ is sufficient to uniquely specify the orientation of a rod.

The first two singularities are shown in Fig. III.4b, where the first derivative $\mathcal{F}'_1(\kappa)$ is plotted against κ. The derivative $\mathcal{F}'_1(\kappa)$ is exactly zero for $\kappa < \frac{1}{2}$, and nonzero for $\kappa > \frac{1}{2}$, initially increasing linearly. It has a sharp peak near $\kappa = 1$. This peak has a logarithmic divergence which is shown in Fig. III.6, where $\mathcal{F}'_1(\kappa)$ is plotted on a semi-log scale as a function of the distance from $\kappa = 1$. The nearly linear dependence on $\log|\kappa - 1|$ shows the logarithmic divergence.

The third type of singularity manifests in the probability distribution of the orientations $P_\kappa(\theta)$ and is plotted in Fig. III.5. For $\kappa < \frac{1}{2}$, all angles are equally likely and $P_\kappa(\theta)$ takes a constant value π^{-1}. For $\frac{1}{2} < \kappa < \frac{1}{\sqrt{2}}$, $P_\kappa(\theta)$ has a non-trivial dependence on θ when $|\cos\theta| > \frac{1}{2\kappa}$, but the derivative $P'_\kappa(\theta)$ remains finite. In the range $\frac{1}{\sqrt{2}} < \kappa < 1$, $P_\kappa(\theta)$ has a square-root cusp singularity at $\sin\theta = \kappa$ where the first derivative $P'_\kappa(\theta)$ is infinite. There is no visible signature of this singularity in the functional dependence of $\mathcal{F}_1(\kappa)$ on κ in Fig. III.4. It is possible that the singularity may appear in higher order derivatives.

These singularities indicate phase transitions which have a geometrical origin and are much different from the other known examples discussed in the previous section III.3.

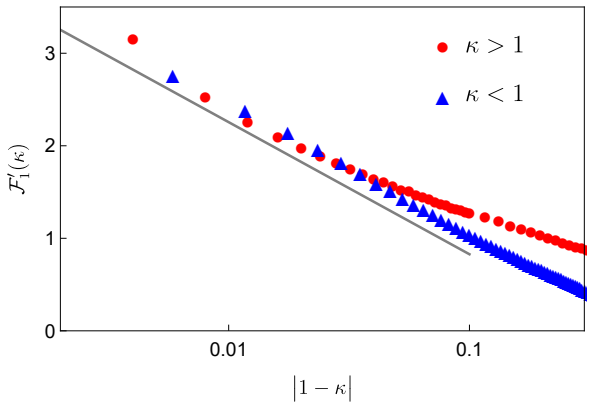


Figure III.6: **Logarithmic divergence** of the first derivative of the free energy $\mathcal{F}_1'(\kappa)$ near $\kappa = 1$, for $U_1 = \infty$. The x-axis is in log-scale. The deviations at small values from a straight line are due to finite size effects.

b) Integral transfer operator

Here, it is clarified how these plots of the free energy are obtained and the origin of the singularities is discussed. To present the results in slight generality, it is considered that U_1 is arbitrary and $U_i = 0$ for all $i \geq 2$. This means that there is a certain energy U_1 for the nearest neighbor overlap, but for other neighbor overlaps there is no energy cost. It is simple to see that the case $U_1 = \infty$ (discusses before) is included in this example.

The thermodynamic free energy per rod is given in terms of the partition function as

$$\mathcal{F}_1(\kappa) = -\lim_{N\to\infty} \frac{1}{\beta\, N} \log \mathcal{Z}_N(\kappa)\,,$$

where the partition function for this example is

$$\mathcal{Z}_N(\kappa) = \prod_{i=1}^{N} \int_0^{\pi} d\theta_i\, e^{-\beta U_1\, \tau(\theta_i,\theta_{i+1})}$$

with the periodic boundary condition $N+1 \equiv 1$ and $\tau(\theta',\theta)$ is 1 or 0 depending on whether the two neighboring rods with the orientations θ' and θ overlap or not.

Following a similar approach to that in the Ising model (see (III.2)) or in the Kittel's model (see (III.3)), the partition function can be expressed in terms of an integral transfer operator $\mathcal{T}_\kappa(\theta,\theta')$ which is defined for a pair of nearest neighbor rods with angles (θ',θ) such that

$$\mathcal{T}_\kappa(\theta',\theta) = \begin{cases} e^{-\beta U_1} & \text{when the rods overlap,} \\ 1 & \text{when no overlap.} \end{cases} \tag{III.6}$$

The partition function for the periodic boundary condition is

$$\begin{aligned} \mathcal{Z}_N(\kappa) &= \left[\prod_{i=1}^{N} \int_0^{\pi} d\theta_i\right]\, \mathcal{T}_\kappa(\theta_1,\theta_2)\cdots\mathcal{T}_\kappa(\theta_{N-1},\theta_N)\mathcal{T}_\kappa(\theta_N,\theta_1) \\ &= \text{Trace}(\mathcal{T}_\kappa^N)\,. \end{aligned}$$

Unlike in the Ising model or in the Kittel's model, where $\mathcal{T}_\kappa$ is a transfer matrix, it is an integral transfer operator in the case discussed here, just as in the Dauxois and Peyards model [233]. The Perron-Frobenius theorem does not directly apply here. However, there

is a generalization known as the Perron-Frobenius-Jentzsch theorem [10] which applies for integral operators. The precise statement requires technical details like Banach spaces, compactness of integral operators, and is avoided here. This theorem suggests that the integral operator in (III.6) has a non-degenerate largest eigenvalue which is positive and this is essentially due to the compact range of possible values of the orientation of the rods[4]. The validity of this result can be simply assured by discretizing the angular variables such that $\mathcal{T}_\kappa$ becomes a transfer matrix. In this case, the Perron-Frobenius theorem holds and the largest eigenvalue is non-degenerate. Making the discretization finer and extrapolating the eigenvalue spectrum to the continuous limit, it can be seen that the largest eigenvalue remains non-degenerate. This is precisely how the eigenvalues are determined in this work which leads to the plots of the free energy in Fig. III.4.

The largest eigenvalue $\Lambda(\kappa)$ and its eigenvector $\psi_\kappa(\theta)$ are the solution of the integral equation

$$\Lambda(\kappa)\psi_\kappa(\theta) = \int_0^\pi d\theta' \;\; \mathcal{T}_\kappa(\theta,\theta')\psi_\kappa(\theta')\,, \tag{III.7}$$

and similarly for the second largest eigenvalue $\Lambda^{(1)}(\kappa)$ and its eigenvector $\psi_\kappa^{(1)}(\theta)$, and so on.

The first observation is that the integral transfer operator $\mathcal{T}_\kappa(\theta,\theta')$ has the obvious symmetries

$$\mathcal{T}_\kappa(\theta,\theta') = \mathcal{T}_\kappa(\pi-\theta,\pi-\theta')\,, \tag{III.8a}$$
$$\mathcal{T}_\kappa(\theta,\theta') = \mathcal{T}_\kappa(\pi-\theta',\pi-\theta)\,. \tag{III.8b}$$

In addition $\mathcal{T}_\kappa(\theta,\theta')$ is real. This means all its eigenvalues are real and the partition function is

$$\mathcal{Z}_N(\kappa) = \text{Trace}(\mathcal{T}_\kappa^N) = \Lambda(\kappa)^N + \left(\Lambda^{(1)}(\kappa)\right)^N + \cdots\,.$$

In the thermodynamic limit $N\to\infty$ the free energy density

$$\mathcal{F}_1(\kappa) = -\lim_{N\to\infty}\frac{1}{\beta\,N}\log\left[\Lambda(\kappa)^N + \left(\Lambda^{(1)}(\kappa)\right)^N + \cdots\right] = -\frac{1}{\beta}\log\Lambda(\kappa)\,.$$

The κ dependence of the free energy density is shown in Fig. III.4, which is determined for $U_1=\infty$ by numerically diagonalizing the transfer matrix, using 1000 grid points for the integration range of $\theta=[0,\pi]$ and then determining the largest eigenvalue.

The probability distribution of the orientation $P_\kappa(\theta)$ of a rod can also be expressed in terms of the transfer operator. Due to the periodic boundary condition all rods are equivalent. The following formula is written considering the first rod. The probability of its orientation

$$P_\kappa(\theta_1) = \frac{\left[\prod_{i>1}\int_0^\pi d\theta_i\right]\;\mathcal{T}_\kappa(\theta_1,\theta_2)\cdots\mathcal{T}_\kappa(\theta_{N-1},\theta_N)\mathcal{T}_\kappa(\theta_N,\theta_1)}{\text{Trace}(\mathcal{T}_\kappa^N)}\,.$$

[4] For $\kappa<\frac{1}{2}$, $\mathcal{T}_\kappa(\theta',\theta)=1$ for all θ' and θ. In this case, the largest eigenvalue $\Lambda=1$ is non-degenerate and its eigenvector $\psi_\kappa(\theta)=\frac{1}{\sqrt{\pi}}$. All other eigenvalues are zero with an infinite degeneracy of eigenvectors following $\int_0^\pi d\theta\,\widehat{\psi}_\kappa(\theta)=0$. This can also be seen in Fig. III.7.

The matrix $\mathcal{T}_\kappa$ is symmetric (see (III.8b)), thus there is an orthonormal set of eigenvectors, which leads to the representation [250]

$$\mathcal{T}_\kappa(\theta,\theta') = \Lambda(\kappa)\psi_\kappa(\theta)\psi_\kappa(\theta') + \Lambda^{(1)}(\kappa)\psi_\kappa^{(1)}(\theta)\psi_\kappa^{(1)}(\theta') + \cdots . \tag{III.9}$$

Using the orthonormality condition

$$\int_0^\pi d\theta\, \psi_\kappa^{(n)}(\theta)\psi_\kappa^{(m)}(\theta) = \delta_{n,m}$$

(with $\psi_\kappa^{(0}(\theta) \equiv \psi_\kappa(\theta)$) leads in the large N limit to

$$P_\kappa(\theta_1) \simeq \psi_\kappa(\theta_1)^2 . \tag{III.10}$$

The distribution for hard rods (for $U_1 = \infty$) in Fig. III.5a is determined from the eigenvector $\psi_\kappa(\theta)$ by discretizing the angular variable with 1000 grid points for the integration range of $\theta = [0, \pi]$.

The spatial correlation of the orientation can be determined in a very similar way. Starting with

$$P_\kappa(\theta_1,\theta_r) = \frac{\left[\prod_{i=2}^{r-1}\int_0^\pi d\theta_i\right]\mathcal{T}_\kappa(\theta_1,\theta_2)\cdots\mathcal{T}_\kappa(\theta_{r-1},\theta_r)\left[\prod_{j=r+1}^{N}\int_0^\pi d\theta_j\right]\mathcal{T}_\kappa(\theta_r,\theta_{r+1})\cdots\mathcal{T}_\kappa(\theta_N,\theta_1)}{\mathrm{Trace}(\mathcal{T}_\kappa^N)}$$

and (III.9), it is simple to show that

$$P_\kappa(\theta_1,\theta_r) = \frac{\Lambda(\kappa)^N\psi_\kappa(\theta_1)^2\psi_\kappa(\theta_r)^2 + \Lambda^{(1)}(\kappa)^{r-1}\Lambda(\kappa)^{N-r+1}\psi_\kappa(\theta_1)\psi_\kappa(\theta_r)\psi_\kappa^{(1)}(\theta_1)\psi_\kappa^{(1)}(\theta_r) + \cdots}{\Lambda(\kappa)^N + \Lambda^{(1)}(\kappa)^N + \cdots} .$$

For large N and assuming $1 \ll r \ll N - r$ (without a loss of generality) it follows

$$P_\kappa(\theta_1,\theta_r) = \psi_\kappa(\theta_1)^2\psi_\kappa(\theta_r)^2 + \left(\frac{\Lambda^{(1)}(\kappa)}{\Lambda(\kappa)}\right)^{r-1}\psi_\kappa(\theta_1)\psi_\kappa(\theta_r)\psi_\kappa^{(1)}(\theta_1)\psi_\kappa^{(1)}(\theta_r) + \cdots .$$

Along with (III.10), the connected correlation is

$$\langle\theta_1\theta_r\rangle - \langle\theta_1\rangle\langle\theta_r\rangle \simeq e^{-\frac{r}{\xi}}$$

with the correlation length (up to a numerical prefactor)

$$\xi \sim \frac{1}{\log\left(\frac{\Lambda(\kappa)}{\Lambda^{(1)}(\kappa)}\right)} . \tag{III.11}$$

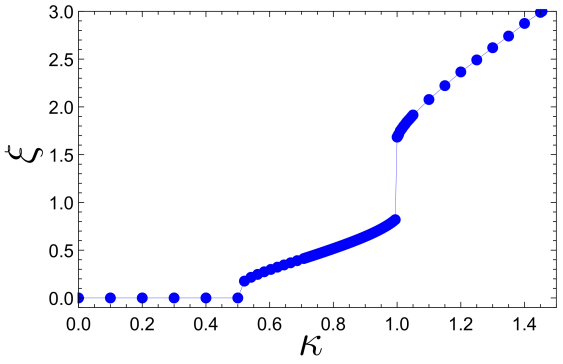


Figure III.7: **Correlation length.** The correlation length ξ in (III.11) is plotted with increasing κ where the eigenvalues are numerically determined by discretizing the angular variable and then diagonalizing the associated transfer matrix. The actual correlation length is up to a multiplicative constant. The plot shows that the correlation length remains finite.

This clearly shows that the correlation length is finite as long as the largest eigenvalue is non-degenerate, *i.e.*, $\Lambda(\kappa) \neq \Lambda^{(1)}(\kappa)$. This is the case for the here discussed example of interacting rods and shown in Fig. III.7.

c) Origin of singularities

The singularities in the Free energy are due to the non-analytic dependence of the largest eigenvalue $\Lambda(\kappa)$ on κ, thus the source of these singularities is geometric in nature. This can be most simply seen in the structure of the transfer matrix, which is illustrated in Fig. III.8. The shaded regions in the θ-θ' plane correspond to values of (θ, θ') where the rods intersect and the matrix element is $e^{-\beta U_1}$. The plain regions correspond to non-intersecting rods and the matrix element is 1. As κ is increased, the shaded regions grow in size and the eigenvalue of the transfer matrix decreases. For $\frac{1}{\sqrt{2}} < \kappa < 1$, the slope of the boundary of the shaded region becomes infinite or zero at some points. When $\kappa = 1$, the boundary becomes a set of straight lines. For $\kappa > 1$, the two shaded patches, which are disjoint when $\kappa < 1$, merge into a single connected shaded region. Precisely these topological changes in the structure of the available phase space lead to the singularities in the free energy function $\mathcal{F}_1(\kappa)$ which is shown later.

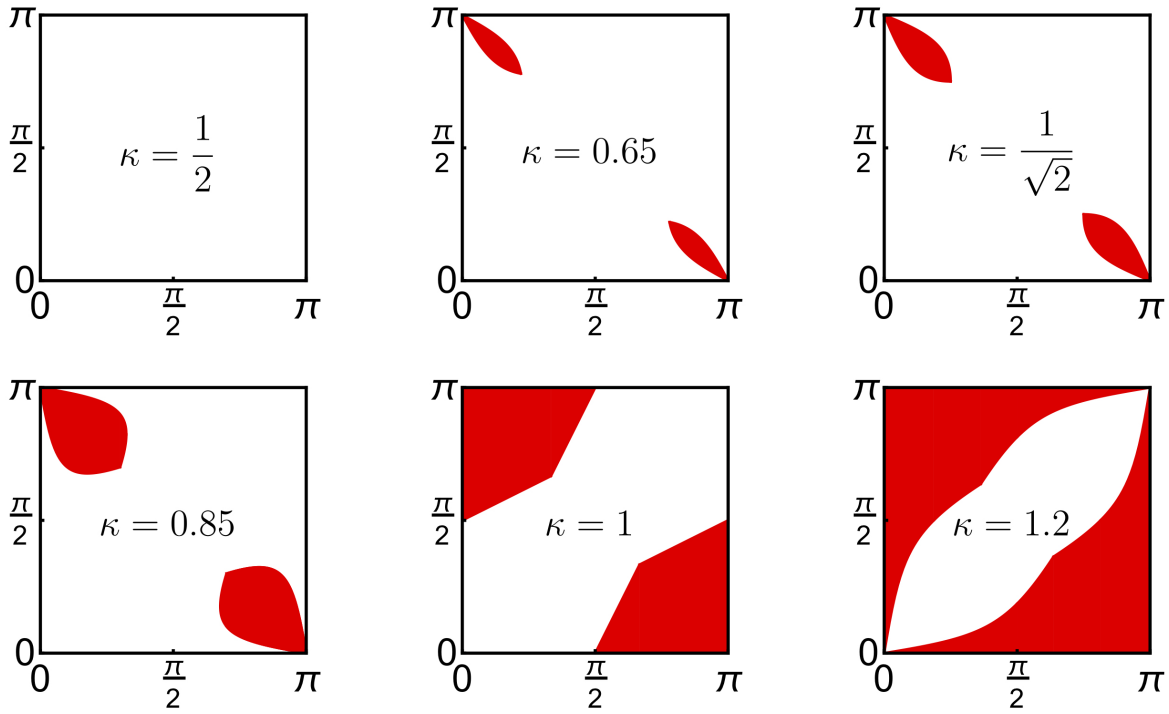


Figure III.8: **The transfer matrix**. $\mathcal{T}_\kappa(\theta', \theta)$ is shown on the θ-θ' plane for different values of κ (indicated in the figure). The red-shaded regions denote (θ, θ') values where the rods overlap and $\mathcal{T}_\kappa = e^{-\beta U_1}$. In the plain regions, rods do not overlap and $\mathcal{T}_\kappa = 1$.

d) Structure of the transfer matrix

The equation for the boundary of the shaded region in Fig. III.8 can be easily written down from simple geometry. Using the symmetry (III.8b), it is sufficient to specify the matrix elements of $\mathcal{T}_\kappa$ only for the range $\theta \in [0, \frac{\pi}{2}]$.

For $\kappa < \frac{1}{2}$, there are no overlaps and $\mathcal{T}_\kappa = 1$ as shown in Fig. III.8.

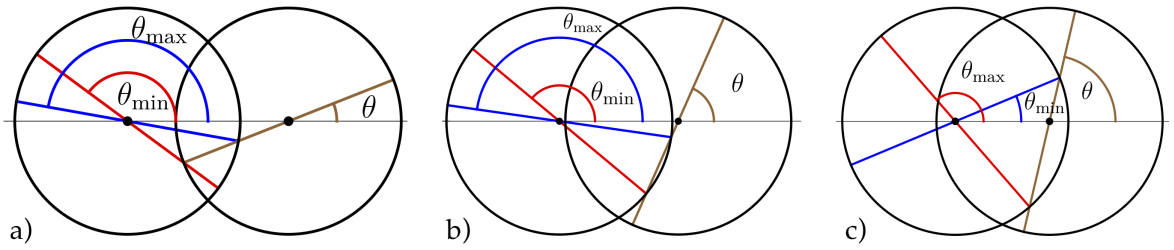


Figure III.9: **Overlap criteria for a pair of nearest neighbor rods.** The left rod has the orientation θ' and the right rod is described by θ. The values for κ are in the range a) $\frac{1}{2} \leq \kappa < \frac{1}{\sqrt{2}}$, b) $\frac{1}{\sqrt{2}} < \kappa < 1$, and c) $\kappa > 1$. Overlaps occur for $\theta' \in [\theta_{\min}, \theta_{\max}]$, except in the last case where overlaps occur for $\theta' \in [0, \theta_{\min}]$ or $\theta' \in [\theta_{\max}, \pi]$. At $\kappa = \frac{1}{2}$ the circles touch for the first time. At $\kappa = \frac{1}{\sqrt{2}}$ the circles cross each other at an angle $\frac{\pi}{2}$. At $\kappa = 1$ the perimeter of the circles touches each others center.

If $\frac{1}{2} < \kappa \leq \frac{1}{\sqrt{2}}$, an overlap of the nearest neighbor rods is possible only if $\cos\theta < \frac{1}{2\kappa}$ and $\theta' \in [\theta_{\min}, \theta_{\max}]$ (see Fig. III.9a) where

$$\theta_{\min}(\theta) = \pi - \arctan\left(\frac{\sin\theta}{\kappa^{-1} - \cos\theta}\right),$$
$$\theta_{\max}(\theta) = \pi + \theta - \arcsin\left(\frac{\sin\theta}{\kappa}\right).$$

For $\frac{1}{\sqrt{2}} \leq \kappa \leq 1$, an overlap is possible if $\sin(\theta) \leq \kappa$ and $\theta' \in [\theta_{\min}, \theta_{\max}]$, where $\theta_{\min}$ has different expressions for different ranges of the orientation θ of the right rod (see Fig. III.9b). It can be found that, for any $\theta \in [0, \pi]$,

$$\theta_{\max} = \pi + \theta - \arcsin\left(\frac{\sin\theta}{\kappa}\right). \tag{III.12}$$

On the other hand, for $\theta_{\min}$, if $\theta \in [0, \arccos\left(\frac{1}{2\kappa}\right)]$, then

$$\theta_{\min} = \pi - \arctan\left(\frac{\sin\theta}{\kappa^{-1} - \cos\theta}\right), \tag{III.13}$$

whereas, if $\theta \in [\arccos\left(\frac{1}{2\kappa}\right), \arcsin\left(\kappa\right)]$, then

$$\theta_{\min} = \arcsin\left(\frac{\sin\theta}{\kappa}\right) + \theta\,.$$

For $\kappa > 1$, the elements $\mathcal{T}_\kappa(\theta', \theta) \neq 1$ if $\theta' < \theta_{\min}$ or $\theta' > \theta_{\max}$, where $\theta_{\max}$ has different expressions for different ranges of θ (see Fig. III.9c). It can be shown that for any $\theta \in [0, \pi]$,

$$\theta_{\min} = \theta - \arcsin\left(\frac{\sin\theta}{\kappa}\right).$$

On the other hand, if $\theta \in [0, \arccos\frac{1}{\kappa}]$, then

$$\theta_{\max} = \arctan\left(\frac{\sin\theta}{\cos\theta - \kappa^{-1}}\right),$$

if $\theta \in [\arccos \frac{1}{\kappa}, \arccos \frac{1}{2\kappa}]$, then

$$\theta_{\max} = \pi + \arctan\left(\frac{\sin\theta}{\cos\theta - \kappa^{-1}}\right) ,$$

and if $\theta \in [\arccos \frac{1}{2\kappa}, \frac{\pi}{2}]$, then

$$\theta_{\max} = \theta + \arcsin\left(\frac{\sin\theta}{\kappa}\right) .$$

The shape of the boundary of the overlap regions $\theta_{\max}$ and $\theta_{\min}$ is given in Fig. III.10 for different ranges of κ.

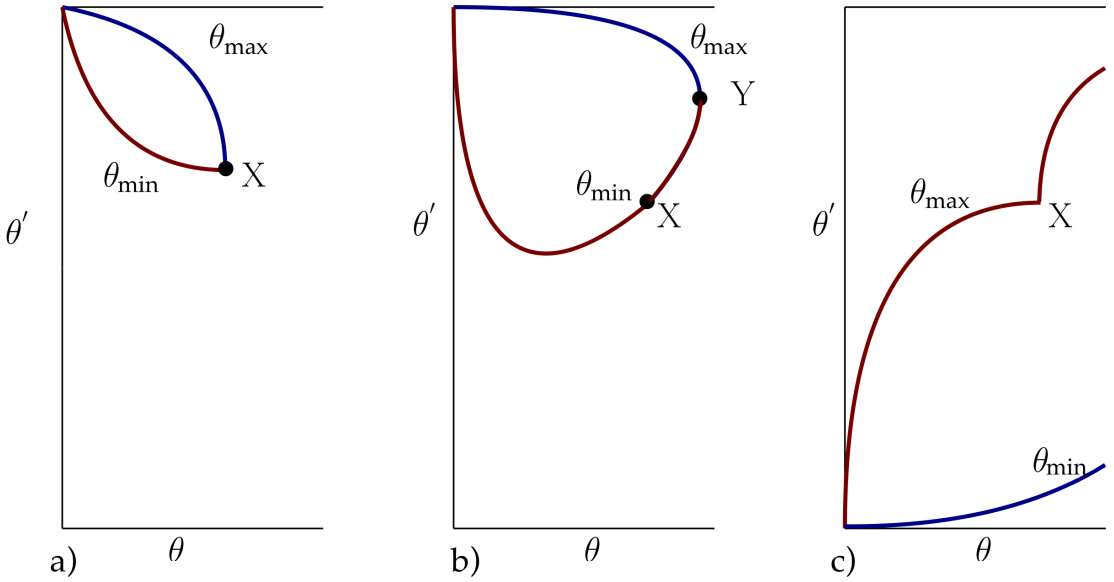


Figure III.10: **Boundary shape of the overlap region in the transfer matrix.** The plots are for different ranges of κ. a) $\frac{1}{2} \leq \kappa < \frac{1}{\sqrt{2}}$, b) $\frac{1}{\sqrt{2}} < \kappa < 1$, and c) $\kappa > 1$. Only the range $\theta < \frac{\pi}{2}$ is shown, as the rest of the region can be constructed using the symmetry (III.8b). The point X denotes $\theta = \arccos \frac{1}{2\kappa}$ and Y denotes $\theta = \arcsin \kappa$.

e) Precise nature of the singularities

1) At $\kappa = \frac{1}{2}$: For $\kappa < \frac{1}{2}$, no overlap is possible and the rods can rotate freely without any energy cost. The associated transfer operator $\mathcal{T}_\kappa(\theta', \theta) = 1$ for all angles and there are no shaded regions as shown in Fig. III.8. The largest eigenvalue is $\Lambda(\kappa) = 1$ and the corresponding eigenvector is $\psi_\kappa(\theta) = \frac{1}{\sqrt{\pi}}$. All other eigenvalues are zero. As κ is increased beyond $\frac{1}{2}$ the nearest neighbor interaction sets in.

From a first-order perturbation theory, where κ is varied around $\kappa = \frac{1}{2}$, the correspond-

ing change in the largest eigenvalue is given by[5]

$$\begin{aligned}\Delta\Lambda \simeq & \int_0^\pi d\theta \int_0^\pi d\theta' \psi_{\frac{1}{2}}(\theta)\Delta T_\kappa(\theta,\theta')\psi_{\frac{1}{2}}(\theta') \\ = & \langle\psi_{\frac{1}{2}}|\Delta T|\psi_{\frac{1}{2}}\rangle\,,\end{aligned}$$

where $\Delta T_\kappa = \mathcal{T}_\kappa - \mathcal{T}_{\frac{1}{2}}$ denotes the corresponding change in the transfer operator. If $\kappa = \frac{1}{2} - \epsilon$ (with positive and small ϵ), the transfer matrix remains the same, *i.e.* $\Delta T_\kappa = 0$ and therefore $\Delta\Lambda = 0$. However, if $\kappa = \frac{1}{2} + \epsilon$ (with positive and small ϵ), using $\psi_{\frac{1}{2}}(\theta) = \frac{1}{\sqrt{\pi}}$ leads to the corresponding change in the eigenvalue

$$\Delta\Lambda \simeq \left(e^{-\beta U_1} - 1\right)\frac{A}{\pi}\,, \tag{III.14}$$

where A is the area of the overlap region (twice the area of the enclosed region in Fig. III.10a), which is given by

$$A = 2\int_0^{\arccos\frac{1}{2\kappa}} d\theta \int_{\theta_{\min}(\theta)}^{\theta_{\max}(\theta)} d\theta'\,. \tag{III.15}$$

To evaluate this area for $\kappa = \frac{1}{2} + \epsilon$ with small ϵ

$$\arccos\frac{1}{1+2\epsilon} \simeq 2\sqrt{\epsilon}\,,$$

can be used and consequently

$$\begin{aligned}\theta_{\min} \simeq & \pi - \theta(1+4\epsilon) + \theta^3\,, \\ \theta_{\max} \simeq & \pi - \theta(1-4\epsilon) - \theta^3\,.\end{aligned}$$

Using these in the equations (III.14) and (III.15) gives

$$\Delta\Lambda \simeq \frac{32\epsilon^2}{\pi}\left(e^{-\beta U_1} - 1\right)\,.$$

Thus the free energy per site is given by

$$\mathcal{F}_1(\kappa) = -\frac{1}{\beta}\log(1+\Delta\Lambda) \simeq \begin{cases} 0 & \text{for } \kappa = \frac{1}{2} - \epsilon\,, \\ \frac{32\epsilon^2}{\pi\beta}\left(1 - e^{-\beta U_1}\right) & \text{for } \kappa = \frac{1}{2} + \epsilon\,. \end{cases}$$

The second derivative of the free energy $\mathcal{F}_1''(\kappa)$ with respect to κ is therefore discontinuous at $\kappa = \frac{1}{2}$.

2) At κ= 1: For this value, the boundary of the overlap region in the θ-θ' plane becomes a set of straight lines (see Fig. III.8 and Fig. III.11). The transfer matrix $\mathcal{T}_\kappa(\theta',\theta)$ can be exactly diagonalized by converting the integral eigenvalue equation (III.7) into a second-order differential equation. The details are given in the next paragraph f) of this subsection III.4.1 where it is shown that the largest eigenvalue of the transfer matrix for $\kappa = 1$ is non vanishing and the eigenvector $\psi_1(\theta)$ is positive everywhere with a finite ratio of its maximum and minimum values.

[5] The term $\langle\psi_{\frac{1}{2}}|\Delta\psi\rangle + \langle\Delta\psi|\psi_{\frac{1}{2}}\rangle$, where $\Delta\psi = \psi_\kappa - \psi_{\frac{1}{2}}$, vanish due to normalization $\langle\psi_\kappa|\psi_\kappa\rangle = 1$ just like in the standard perturbation theory in Quantum mechanics.

To analyze how the eigenvalue $\Lambda(\kappa)$ varies near $\kappa = 1$, $\kappa = 1 - \epsilon$ is considered, with $\epsilon > 0$. In addition, the corresponding change in the transfer matrix is defined as $\Delta T_\epsilon = \mathcal{T}_{1-\epsilon} - \mathcal{T}_1$. To the first-order in ϵ, the change in the eigenvalue is given by

$$\Lambda(1-\epsilon) = \Lambda(1) + \langle\psi_1|\Delta T_\epsilon|\psi_1\rangle \cdots ,$$

where $\psi_1(\theta)$ is the eigenvector of the transfer matrix corresponding to the largest eigenvalue at $\kappa = 1$. As $\mathcal{T} = e^{-\beta U_1}$ in the overlap region and $\mathcal{T} = 1$ when there is no overlap, this change $\langle\psi_1|\Delta T_\epsilon|\psi_1\rangle \propto (1 - e^{-\beta U_1})\Delta A$ where ΔA is the change in the overlap area shown in Fig. III.12a. Here it is used that $\psi_1(\theta)$ is positive everywhere and the ratio between its maximum and minimum values remains finite. It can be shown that ΔA varies as $\epsilon \log \frac{1}{\epsilon}$. To see this, the symmetries (III.8a) and (III.8b) of the transfer matrix can be used and it shows that the change in the area ΔA is four times the area of the shaded region in Fig. III.12b. One of the boundaries of this shaded region is a straight line $\theta' = \frac{1}{2}\theta + \frac{\pi}{2}$. The asymptotic shape of the other boundary near $(0, \frac{\pi}{2})$ is a hyperbola. This can be seen by introducing the rescaled coordinates (ξ, η), where

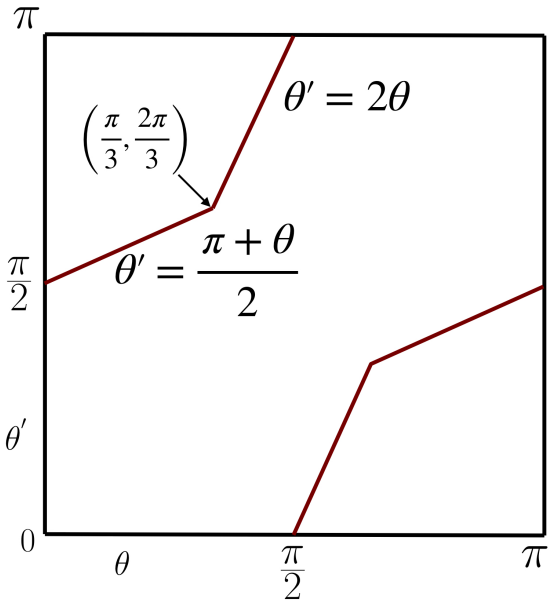


Figure III.11: **Overlap boundary for $\kappa = 1$.** The straight line boundaries of the overlap region in the transfer matrix for $\kappa = 1$.

$$\xi = \frac{\theta}{\sqrt{\epsilon}}, \qquad \text{and} \qquad \eta = \frac{\theta_{\min} - \left(\frac{\pi}{2} + \frac{\theta}{2}\right)}{\sqrt{\epsilon}} .$$

Writing the equation (III.13) in terms of this scaled coordinates and solving in the small ϵ limit gives a scaled hyperbolic curve $\eta\,\xi = 1$. This implies that to the leading order in small ϵ, the curved boundary of the shaded region in Fig. III.12b follows $\eta = \frac{1}{\xi}$, *i.e.* a hyperbola. Therefore, the area of this shaded region is $\epsilon \int \eta\, d\xi$, where the upper limit of the integral varies as $\frac{1}{\sqrt{\epsilon}}$. The area thus varies as $\epsilon \log \frac{1}{\epsilon}$. Keeping the exact prefactors in the calculation gives

$$\Delta A \simeq 4\left(\epsilon \ln \frac{\pi^2}{6} - \epsilon \ln \epsilon + \epsilon\right)$$

for small ϵ.

On the other hand, the eigenvector $\psi_1(\theta)$ is positive everywhere and the ratio between its maximum and minimum values remains finite. This implies that the change in the matrix element has the same qualitative dependence on ϵ as the area of the shaded regions and therefore

$$\Lambda(1-\epsilon) - \Lambda(1) = K_1 \epsilon \log \frac{1}{\epsilon} + K_2 \epsilon + \cdots , \tag{III.16}$$

where K_1 and K_2 are positive constants. A similar argument holds for negative ϵ.

This shows that the first derivative of the largest eigenvalue $\Lambda(\kappa)$ has a logarithmic divergence near $\kappa = 1$ and therefore also $\mathcal{F}'(\kappa)$ has a logarithmic divergence as seen in Fig. III.6.

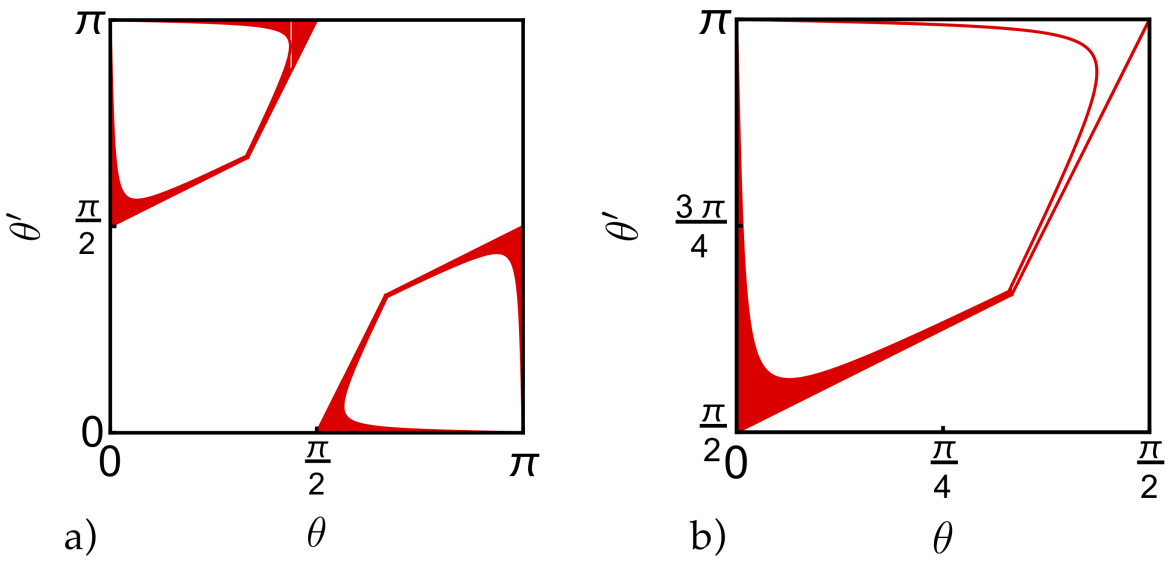


Figure III.12: **Change in the transfer matrix near** $\kappa = 1$**:** a) The plot shows the difference in overlap area ΔA between the transfer matrix $\mathcal{T}_{1-\epsilon}$ and $\mathcal{T}_1$ for $\epsilon = 0.02$ on the θ-θ' plane. b) The plot indicates the symmetry where the shaded area is $\frac{1}{4}$ of the shaded area in a).
The area of the shaded region varies as $\epsilon \log \frac{1}{\epsilon}$, for small ϵ.

At $\kappa = \frac{1}{\sqrt{2}}$: There is a cusp singularity in the distribution of the orientation of the rods which starts at $\kappa = \frac{1}{\sqrt{2}}$ and stays in the range $\frac{1}{\sqrt{2}} < \kappa < 1$. For its analysis $\theta_0 = \sin^{-1}\kappa$ is defined. It can be easily seen that there is no overlap with neighbors (for any angle θ' of the latter) if the angle of a rod satisfies $\theta \in [\theta_0, \pi - \theta_0]$. On the other hand, if θ is outside this interval, the rods can intersect if θ' lies in the intervals $[\theta_{\text{min}}, \theta_{\text{max}}]$ or $[\pi - \theta_{\text{max}}, \pi - \theta_{\text{min}}]$, with the expression for θ_{min} and θ_{max} given in (III.12) to (III.13). The important point is that the length of the intervals $|\theta_{\text{max}} - \theta_{\text{min}}|$ varies as $\sqrt{\theta_0 - \theta}$ for $\theta \to \theta_0$. In this case, it can be seen from the eigenvalue equation (III.7) that

$$\psi_\kappa(\theta) = K_3 - K_4 \int_{\theta_{\text{min}}(\theta)}^{\theta_{\text{max}}(\theta)} \psi_\kappa(\theta')d\theta',$$

where K_3 and K_4 are functions of κ only. Using the fact that $\psi_\kappa(\theta')$ is bounded by non-zero constants (from above and from below), it follows for θ approaching θ_0 from below that

$$\psi_\kappa(\theta) \approx K_3 - K_5\sqrt{\theta_0 - \theta},$$

where K_5 depends only on κ. This shows that $\psi_\kappa(\theta)$ has a cusp singularity at $\theta = \theta_0$. Because the probability density $P_\kappa(\theta)$ is equal to $\psi_\kappa(\theta)^2$, it has equivalently a cusp singularity for $\theta = \arcsin\kappa$.

f) Exact diagonalization for $\kappa = 1$

When $\kappa = 1$, the boundary of the overlap region is a set of straight lines and the associated transfer matrix $\mathcal{T}_\kappa(\theta, \theta')$ is sketched in Fig. III.11. This makes the calculation of the

eigenvalue and the associated eigenvector simple. The eigenequation is

$$\int_0^\pi d\theta'\, \psi_\kappa(\theta')\, T_\kappa(\theta', \theta) = \Lambda\, \psi_\kappa(\theta).$$

In (III.8b) the eigenvector has the symmetry $\psi_\kappa(\theta) = \psi_\kappa(\pi - \theta)$. Considering this and the shape of the transfer matrix (see Fig. III.11) the eigenvector is

$$\psi_\kappa(\theta) = \begin{cases} \psi_\kappa^{(1)}(\theta) & \text{for } 0 < \theta \leq \frac{\pi}{3}\,, \\ \psi_\kappa^{(2)}(\theta) & \text{for } \frac{\pi}{3} < \theta \leq \frac{\pi}{2}\,. \end{cases}$$

If $\psi_\kappa^{(1)}(\theta = \frac{\pi x}{3}) = P(x)$, and $\psi_\kappa^{(2)}(\theta = \frac{\pi}{2} - \frac{x\pi}{6}) = Q(x)$ for $0 \leq x \leq 1$, then with the definition

$$\mathcal{N} = \int_0^{\frac{\pi}{2}} d\theta'\, \psi_\kappa(\theta')\,,$$

the eigenvalue equation becomes

$$\frac{\mathcal{N}}{\pi} + \frac{1}{6}\int_0^x dy Q(y) + e^{-\beta U_1}\frac{1}{6}\int_x^1 dy Q(y) + e^{-\beta U_1}\frac{1}{3}\int_0^1 dy P(y) = \frac{\Lambda}{\pi}\, P(x)\,,$$

and

$$\frac{\mathcal{N}}{\pi} + \frac{1}{6}\int_0^1 dy Q(y) + \frac{1}{3}\int_x^1 dy P(y) + e^{-\beta U_1}\frac{1}{3}\int_0^x dy P(y) = \frac{\Lambda}{\pi}\, Q(x)\,,$$

with

$$\frac{\mathcal{N}}{\pi} = \frac{1}{3}\int_0^1 dx P(x) + \frac{1}{6}\int_0^1 dx Q(x)\,.$$

These integral equations can be converted into the following coupled differential equations

$$\frac{\Lambda}{\pi}\frac{dP}{dx} = \left(1 - e^{-\beta U_1}\right)\frac{Q(x)}{6}\,, \tag{III.17}$$

$$\frac{\Lambda}{\pi}\frac{dQ}{dx} = -\left(1 - e^{-\beta U_1}\right)\frac{P(x)}{3}\,. \tag{III.18}$$

Solutions of these equations are given by

$$P(x) = \frac{N}{\Lambda}\left[(1 + e^{-\beta U_1})\cos kx + \sqrt{2}\sin kx\right]\,,$$
$$Q(x) = \frac{N}{\Lambda}\left[2\cos kx - \sqrt{2}(1 + e^{-\beta U_1})\sin kx\right]\,,$$

where

$$\Lambda \equiv \Lambda(1) = \left(1 - e^{-\beta U_1}\right)\frac{\pi}{3\sqrt{2}k} \qquad \text{with} \qquad k = \arctan\left(\frac{1 - e^{-\beta U_1}}{\sqrt{2}(2 + e^{-\beta U_1})}\right)\,.$$

Note that there is an infinite spectrum of eigenvalues Λ. Here, only the largest one is determined. Other eigenfunctions, and eigenvalues (including the anti-symmetric ones) can also be determined similarly. They come from the higher harmonic solution of (III.17) and (III.18).

III.4.2 Soft-core interaction

The above analysis of singularities strongly depends on the fact that the partition function can be written in terms of the integral transfer operator. This is straightforward for the case of the hard-core interactions between rods (which forbids overlaps). The same holds also when there are nearest neighbor interactions only, *i.e.* U_1 is non-zero, but $U_i = 0$ for all $i > 1$. However, in the general case of soft pairwise interactions, overlaps beyond the nearest neighbors are allowed (see Fig. III.13) and such overlaps cost a non-zero amount of energy, *i.e* $U_i \neq 0$ for i. For such interactions, a formulation in terms of integral transfer operators could be possible by increasing the number of variables in the operator. However, it makes the analysis difficult and it is avoided for this discussion.

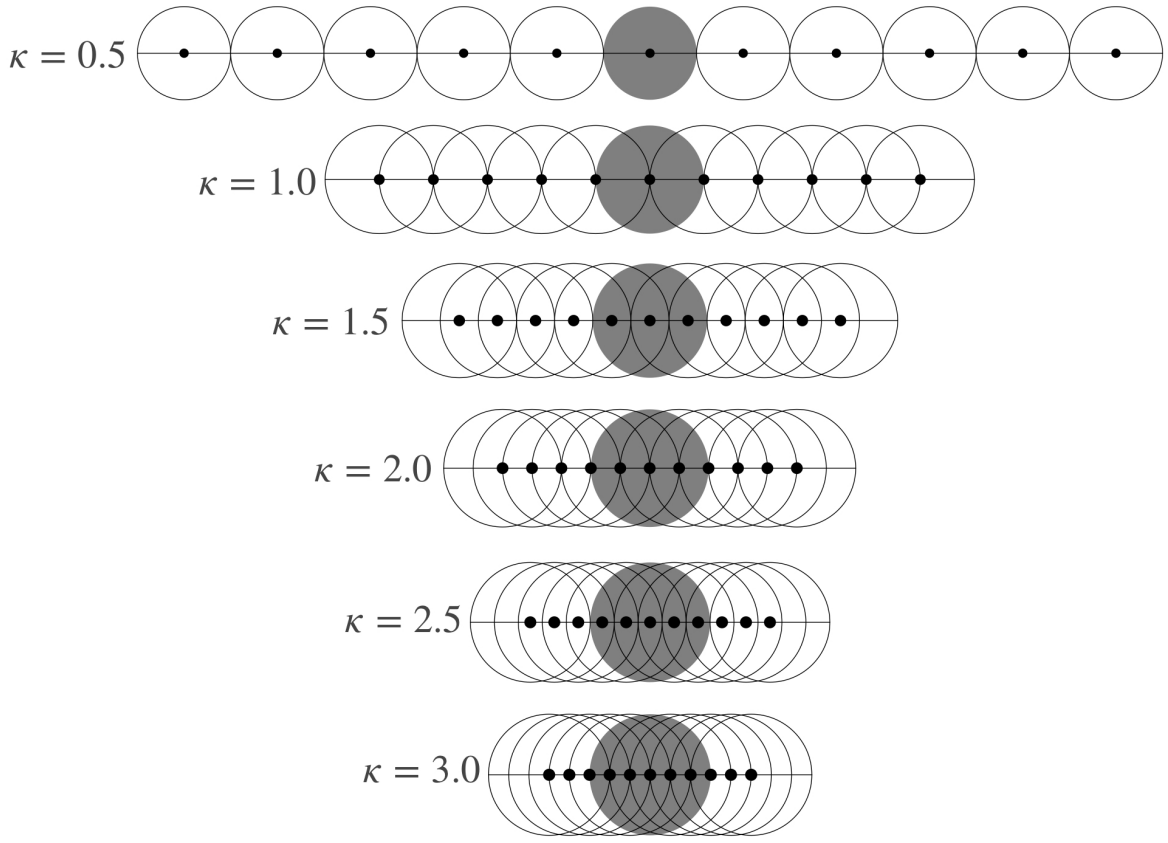


Figure III.13: **Overlap of accessible area of rods.** Each circle denotes the accessible area of a rod. In the chosen definition, κ is the ratio between the radius of the circles and the distance between the neighboring centers. As κ is increased the accessible areas start to overlap. The i^{th} neighbors start to overlap at $\kappa = \frac{i}{2}$ and the figures are shown for these values. The central circle is colored gray to make the overlap visible. The logarithmic singularities appear at integer values of κ when the perimeter of a circle crosses the center of another circle.

Nevertheless, the basic picture is still simple to convey. The next neighbor pair-interactions U_i can be treated as perturbations to the problem with only non-zero U_1. For example, switching on the next-neighbor interaction (U_2 non-zero) gives rise to a logarithmic singularity at $\kappa = 2$. Similarly, making U_3 non-zero leads to a logarithmic singularity at $\kappa = 3$.

It was shown in Fig. III.9 that the logarithmic singularity at $\kappa = 1$ arises when the circular accessible area for a rod touches the center of its nearest neighbor, which leads to a non-analytic change in the overlap region between the two nearest neighbor rods. The same is demonstrated in Fig. III.13. In addition, the figure shows that at every integer value of $\kappa = i$, the circular accessible area of a rod touches the center of its i^{th} neighbor rod. Denoting the rod orientations as θ_0 and θ_i, this suggest that the overlap region in the (θ_0, θ_i)-plane, for $i > 1$, again has a similar hyperbolic shape as for the nearest neighbor case discussed earlier (see Fig. III.12). Following similar steps as in (III.16), it can be seen that the largest eigenvalue $\Lambda(\kappa)$ at $\kappa = i$ has a singularity of the form $(i - \kappa) \log |\frac{1}{\kappa - i}|$. This means that at every positive integer value of κ the free energy has a logarithmic singularity and the system therefore owns an infinite number of phase transitions.

It is important to distinguish the points $\kappa = \frac{i}{2}$ where the i^{th} neighbors start to interact (Fig. III.13). It was discussed earlier that the nearest neighbor interaction for $i = 1$ starts at $\kappa = \frac{1}{2}$ and this leads to a discontinuity in the second derivative of the free energy. Following a similar perturbation argument as before, it is to expect that there is such a discontinuity at $\kappa = \frac{i}{2}$ for all integer i. However, they are difficult to see, especially at integer values of κ where the discontinuity is overshadowed by the logarithmic singularity.

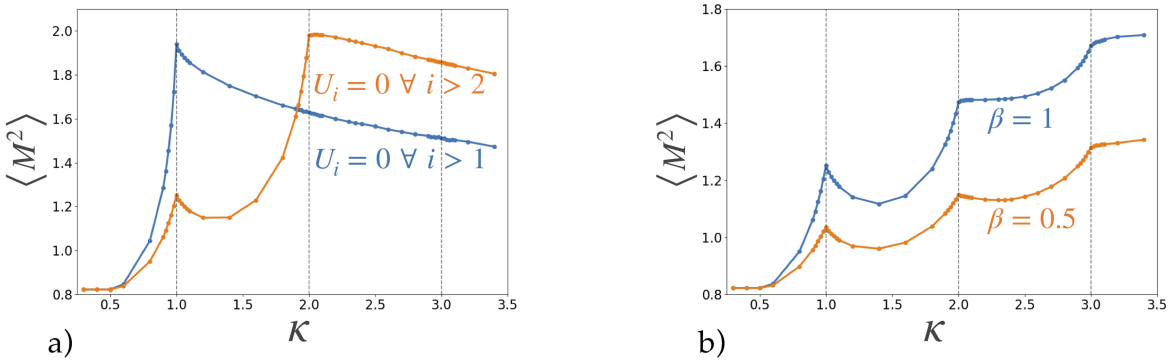


Figure III.14: **Variance of the angular distribution.** (a) For a system of rods with only nearest neighbor interactions and another system with up to next nearest neighbor interaction. (b) For a system where all neighbor interactions have a non-zero overlap energy. The results are generated from a Monte Carlo simulation of a system of 100 rods and averaged over 10^6 sample configurations. The results in (b) are for two different temperatures, indicating that the singularities are located at the same values of κ and they are robust.

It is difficult to calculate the free energy for this case, but still, the presence of these singularities can be seen in measurable quantities. For example, Fig. III.14 provides evidence of these additional transitions from Monte Carlo simulations. Details concerning the algorithm are presented in the next subsection III.4.3. Due to symmetry, it is clear that $\langle \theta \rangle = \frac{\pi}{2}$ for all values of κ and there is no spatial long-range correlations in the system. However, at the integer values of κ the variance of the angle defined by

$$\langle M^2 \rangle = \frac{1}{N} \left\langle \left[\sum_{i=1}^{N} (\theta_i - \tfrac{\pi}{2}) \right]^2 \right\rangle$$

shows singularities. Fig. III.14a shows how the singularities appear as the interaction between nearest neighbor (only U_1 non-zero) and then the next nearest neighbors (only U_1 and U_2 non-zero) are successively turned on. In the first case, the singularity appears only at $\kappa = 1$, while the second case shows an additional singularity at $\kappa = 2$, but no detectable singularity at $\kappa = 3$. Fig. III.14b shows the singularities in the case $U_i = 1$ for all i, *i.e.* all overlaps are allowed and they cost energy. It also shows that the positions of these singularities do not depend on the value of the inverse temperature β (as long as it remains nonzero). Note that there is no detectable singularity in the variance at $\kappa = \frac{1}{2}$ and $\kappa = \frac{3}{2}$. This is possibly because the discontinuity in the second derivative in the free energy is too week to detect.

As discussed before, there are other types of singularities which are difficult to see in the free energy. However, they can be seen in the angular distribution of the orientation of the rods (see Fig. III.15). Additional singularities appear as the interactions between neighbors are added, which shows a complex dependence of the probability $P_\kappa(\theta, \beta)$ on the angle θ and the parameter κ. This is shown in Fig. III.15. The data originates from a Monte Carlo simulation on a system with $\beta U_i = 1$ for all $i \geq 1$.

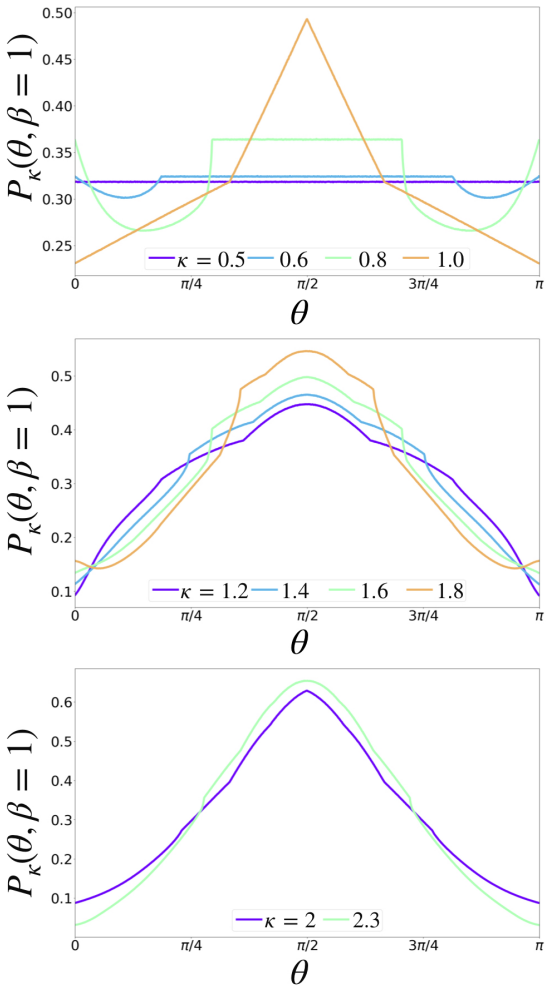


Figure III.15: **Probability distribution of the rods' orientation.** The data results from Monte Carlo simulations of $N = 100$ rods with $\beta U_i = 1$ for all $i \geq 1$ and $\beta = 1$. The curves correspond to different values of κ indicated in the legend.

For $\kappa \leq \frac{1}{2}$, where the rods do not interact, the distribution is uniform. As κ is increased above $\frac{1}{2}$, the distribution function shows a discontinuous first derivative when $\cos\theta = \frac{1}{2\kappa}$. This derivative discontinuity becomes a *cusp* singularity for $\kappa > \frac{1}{\sqrt{2}}$. The two symmetrically located cusps move in position with increasing values of κ and merge at $\kappa = 1$. At this value, a new pair of singularities develops. There are in total four singularities in the distribution function for the entire range $1 < \kappa < 2$. At $\kappa = 2$, two of these singularities merge, but an additional pair of singularities emerges. It can be seen from the figures that whenever κ crosses an integer multiple of $\frac{1}{\sqrt{2}}$, a new pair of *cusp* singularities develops. These singularities move towards each other with increasing κ. This is expected to continue when new neighbor interactions set in as κ is increased.

III.4.3 Monte Carlo simulation of interacting rods

A Monte Carlo algorithm with Metropolis filter is used to sample the equilibrium distribution of configurations of rods. As described before, the system consists of N rods, each of length 2ℓ, whose centers are fixed on the lattice points of a periodic lattice with the lattice spacing a (see Fig. III.3). A configuration is specified by a set of N angles θ_i, with $0 \leq \theta_i \leq \pi$, for $i = 1 \dots N$.

In each Monte Carlo step, a random rod i with θ_i is chosen and a random number $\Delta\theta$ is sampled from a uniform distribution $P(\Delta\theta) = \frac{1}{2\delta}$ for $\Delta\theta \in [-\delta, \delta]$ and $P(\Delta\theta) = 0$ otherwise. The change $\theta_i \to \widetilde{\theta}_i$, with $\widetilde{\theta}_i = \theta_i + \Delta\theta$ is accepted with the Metropolis probability $P_{\mathrm{M}} = \min[1, e^{-\beta\Delta E}]$, where ΔE is the total energy change due to the move $\theta_i \to \widetilde{\theta}_i$.

The energy change ΔE depends on the chosen interaction. In this thesis it is assumed that an overlap between rods cost a constant energy U_r, with r specifying the order of the neighbor (*e.g.* $r = 1$ corresponds to the nearest neighbors and $r = 2$ to the next nearest neighbors, *etc.*). Therefore, the calculation of ΔE requires the total number of overlaps with the r^{th} neighbors.

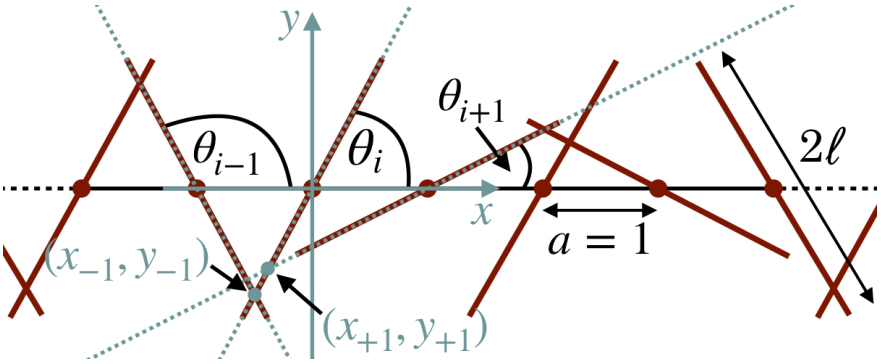


Figure III.16: **How to computationally detect overlaps.** Shown is a configuration of 7 rods of total length 2ℓ. The lattice spacing $a = 1$ and κ is varied by changing ℓ. The origin of the blue coordinate system is located at the center of rod i. Therefore, the center of rod $i + 1$ is at the point $x = 1$, the center of rod $i - 1$ is at $x = -1$, *etc.*.

The overlaps of rod i are determined with the aid of a relative coordinate system. The origin is placed at the lattice point associated to the rod i, as depicted in Fig. III.16. Here, the lattice spacing a is constant ($a = 1$) and κ is varied by changing ℓ. This ensures that in this coordinate system the center of each rod lies on the $x-$axis at integer values j (*e.g.* the center of rod i is at $j = 0$, for rod $i + 1$ it is at $j = 1$, for rod $i - 1$ at $j = -1$, *etc.*). In this coordinate system, a linear equation (*i.e.* $y = mx + n$) can be associated to each rod (see dashed blue lines in Fig. III.16). Then, the slope $m_{i+j} = \tan(\theta_{i+j})$ and the intercept $n_{i+j} = -jm_{i+j}$. Overlaps are detected by the determination of the point of interception (x_j, y_j) between the linear equation representing rod i

$$y = m_i x$$

and the linear equations representing the neighbors

$$y = m_{i+j}x + n_{i+j}\,, \quad \text{with} \quad j \neq 0\,.$$

The interception point is given by

$$x_j = \frac{n_{i+j}}{m_i - m_{i+j}} \quad \text{and} \quad y_j = m_i x_j \,.$$

The rod i overlaps with its neighbor $i+j$ if both conditions

$$\underbrace{x_j^2 + y_j^2 \le \ell^2}_{\text{for rod } i} \quad \text{and} \quad \underbrace{(j - x_j)^2 + y_j^2 \le \ell^2}_{\text{for rod } i+j}$$

are satisfied, which ensures that the point (x_j, y_j) is not further away than ℓ form the center of the respective rods. For example, in Fig. III.16, only (x_{-1}, y_{-1}) associated to the left neighbor satisfies this condition but not (x_{+1}, y_{+1}) associated to the right neighbor. Note that this scheme can be easily generalized to a two-dimensional grid.

As described before, the ratio $\kappa = \frac{\ell}{a}$ defines the range of potential overlaps. If $\kappa < \frac{1}{2}$ overlaps are not possible, thus $\Delta E = 0$ and hence $P_{\mathrm{M}} = 1$ for all possible moves $\theta_i \to \widetilde{\theta}_i$. For $\kappa < 1$, overlaps are possible only with the nearest neighbors, thus $j = \pm 1$. Equivalently, for $\kappa < \frac{3}{2}$ the range $j = \pm 1, \pm 2$ must be considered and so on. The total energy change is then given by

$$\Delta E = \sum_r (\widetilde{n}_r - n_r) U_r \,,$$

where r runs over the range $(j_{\mathrm{min}}, j_{\mathrm{min}} + 1, \ldots, -1, 1, \ldots, j_{\mathrm{max}} - 1, j_{\mathrm{max}})$ set by κ,

$$n_r = \begin{cases} 1\,, & \text{if rod } i \text{ with } \theta_i \text{ overlaps with rod } i + r\,, \\ 0\,, & \text{otherwise}\,, \end{cases}$$

and

$$\widetilde{n}_r = \begin{cases} 1\,, & \text{if rod } i \text{ with } \widetilde{\theta}_i \text{ overlaps with rod } i + r\,, \\ 0\,, & \text{otherwise}\,. \end{cases}$$

III.5 Discussions

There is clear evidence for an infinite number of robust singularities in the free energy of the interacting rods as a function of the coupling constant κ at any finite temperature. The origin of these singularities is the non-analytic change in the geometry of the phase space that (in the simple cases) leads to a change in the shape of the transfer matrix. This is different from other standard mechanisms of phase transitions usually studied in the literature [10]. The model presented here differs from the well-studied models of hard rods [246–249] only in the aspect that the centers of the rods are placed on a regular lattice and the distance between them cannot fluctuate. Some important aspects of the phase transition and its generality are discussed below.

As discussed earlier, there are essentially two existing lines of reasoning for the absence of phase transitions in one-dimensional systems: (a) the non-degeneracy of the largest eigenvalue of the transfer matrix due to the Perron-Frobenius theorem, and (b) the Landau-Peierls free energy argument. All the proposed models of one-dimensional phase transitions are based on attempts to circumvent these two arguments (see [10]). In the here presented example, the Perron-Frobenius theorem indeed applies and the largest eigenvalue

remains non-degenerate even at the transition point. However, the singularity arises because the matrix elements are non-analytic functions of the control parameter κ and could even be discontinuous functions. Note that there is no long-range order, thus the Landau-Peierls argument is not contradicted.

It is important to note that the free energy $F(\kappa, \beta)$ is a non-convex function of κ (see Fig. III.4(a)), thus the question of thermodynamic stability naturally arises. Here, κ is a parameter related to the density and convexity of the free energy as a function of the density is a fundamental property which is essential for thermodynamic stability. However, in the discussed model, the spacing between particles is fixed and cannot be changed. Therefore, this question of stability does not arise. The question would have arisen if the spacing between the rods is allowed to fluctuate. However, in that case, the free energy is convex, but there are no singularities, which is in agreement with all the previous studies of this model [247–249].

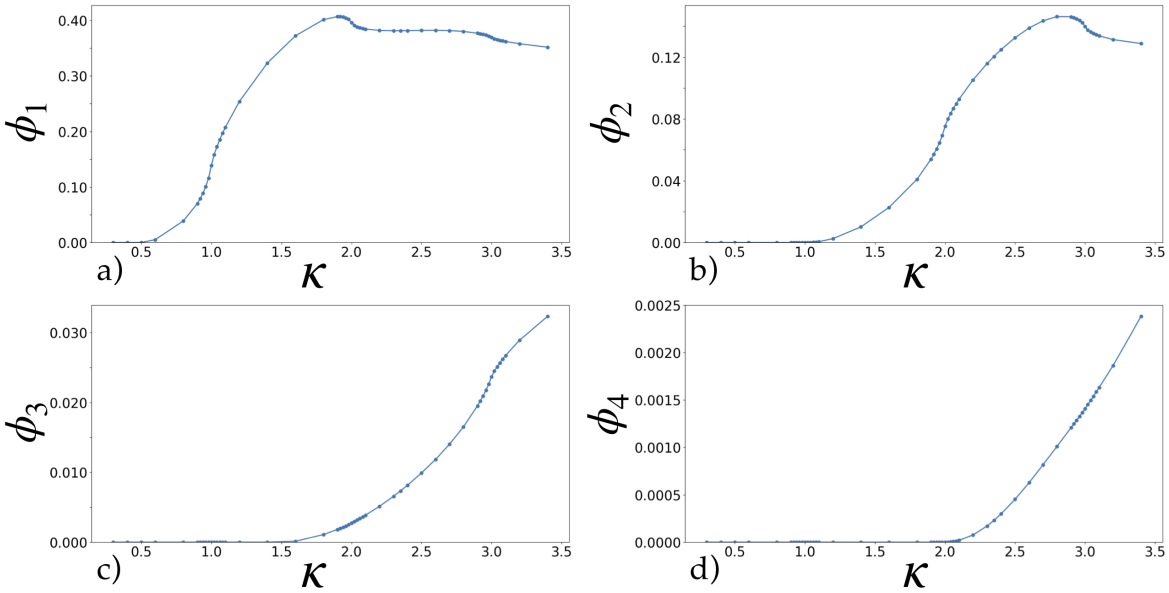


Figure III.17: **Observable.** Numerical result of the observable ϕ_i (for $i = 1$ in a), $i = 2$ in b), $i = 3$ in c), and $i = 4$ in d)) as κ is varied. It can be seen that ϕ_i continuously changes from zero to non-zero value at $\kappa = \frac{i}{2}$, indicating a phase transition.

A pressing question is: are the points of non-analyticity of the free energy in this system also *phase transition points* between distinct phases, or are they similar to the fluid-fluid transition (*e.g.* the liquid-gas transition), where a non-analyticity in the free energy occurs along a line within the same fluid phase? This could be addressed by considering the fraction ϕ_i as the order parameter, which is defined by

$$\phi_i = \frac{\langle n_i \rangle}{N} \tag{III.19}$$

where n_i is the number of i^{th} neighbor rods that overlap and the angular brackets denote the thermal average. Clearly, $\phi_1 = 0$ for $\kappa < \frac{1}{2}$ and non-zero otherwise. Similarly, ϕ_2 is zero for $\kappa < 1$ and non-zero otherwise. More generally, the order parameter ϕ_i is exactly zero

for $\kappa < \frac{i}{2}$, and non-zero otherwise. This is shown in Fig. III.17 obtained from the Monte Carlo simulations. This shows that distinct values of $\lfloor 2\kappa \rfloor$ (where $\lfloor \cdot \rfloor$ denotes floor function) correspond to thermodynamically distinct phases of the system which are distinguished by the values of the order parameter ϕ_i. Of course, these phases could be further split using additional criteria, for example, by using the number of cusps in the orientation distribution. In this case, additional phase transitions appear whenever κ is an integer multiple of $\frac{1}{2}$ or $\frac{1}{\sqrt{2}}$. A schematic of such a phase diagram is drawn in Fig. III.18.

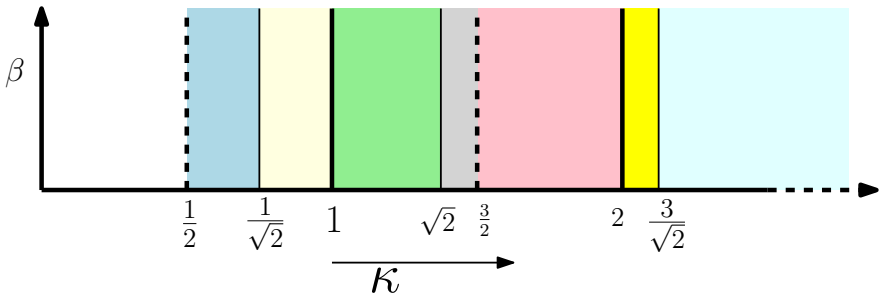


Figure III.18: **Phase diagram.** A schematic phase diagram showing the different phase transition lines in the β-κ plane, when all U_i are non-zero and finite. All lines are parallel to the β-axis. The phases can be distinguished by the possible order parameter ϕ_i in (III.19) and the number of cusps in the distribution of the orientation of rods.

Do these phase transitions come under the classification of a first-order and a continuous transition? Unlike to a continuous transition, the correlation length for the fluctuations of the orientation remains finite even at the transition points. In the simple case of only nearest neighbor interactions, this can be seen from the non-vanishing spectral gap of the transfer matrix (see (III.11)). On the other hand, in the most prominent transitions at the integer values of κ, the first derivative of the free energy is *divergent*, unlike a jump discontinuity in a conventional first-order transition. Therefore, the transitions seen in this example, are neither a continuous transition nor a conventional first-order transition.

The singularities observed in this model are robust and appear for objects of different shapes, like crosses, or T- or Y-shapes. These are generic to all hard-core or soft-core models.

a) Two dimensions

The singularities also occur in higher dimensions, however, the behavior is rather complex. This is seen in Monte Carlo simulations of interacting rods on a square lattice with periodic boundary conditions. The rods are pinned at their centers at the lattice sites and they are free to rotate in the lattice-plane. Similarly to one dimension, the singularities can be seen in the variance of the orientation of the rods. For a $N \times N$ square lattice, a quantity related to the variance of orientation is

$$\chi(\kappa) = \frac{\langle M^2 \rangle - \langle M \rangle^2}{N^2}, \qquad \text{with} \qquad M = \sum_{i=1}^{N} \sin 2\theta_i \,. \tag{III.20}$$

The Monte Carlo simulation result of $\chi(\kappa)$ is presented in Fig. III.19 and shows a diverging peak near $\kappa = 1$. Extending the one-dimensional argument, the peak is expected to be at

$\kappa = 1$. The shift of the peak position from this value indicates a more complex behavior where a KT-type transition may preempt the logarithmic singularity. A similar behavior is observed on a triangular lattice. This is an ongoing project that is not covered in this thesis.

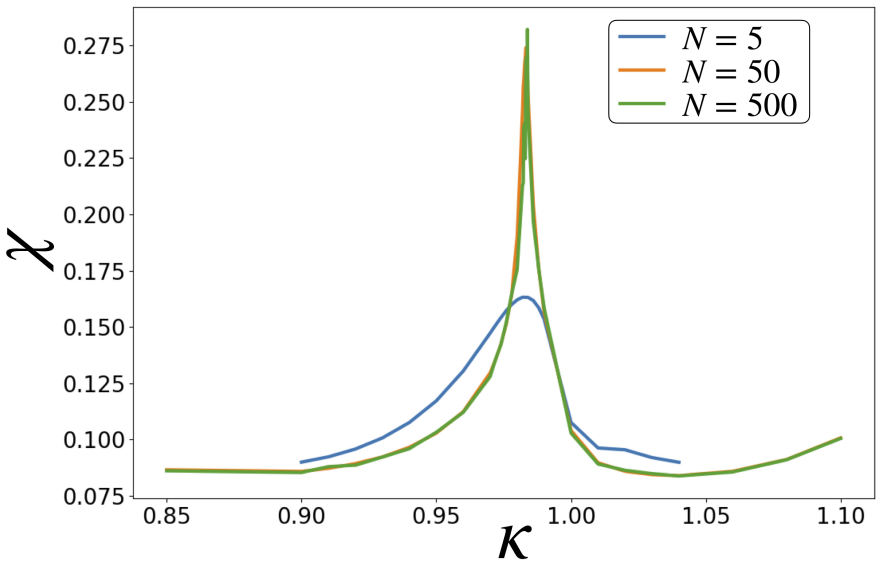


Figure III.19: **Singularity in 2D.** The observable $\chi(\kappa)$ defined in (III.20) for an $N \times N$ square lattice with three different system sizes $N = 5$, $N = 50$, and $N = 500$. The plot shows a diverging peak near $\kappa = 1$.

b) Non-equilibrium steady state

The mechanism of singularity also extends outside equilibrium. This can be seen in the well-known context of energy transport when the system is coupled with two different heat baths at two different temperatures. The system reaches a non-equilibrium steady state where a non-zero energy current flows on average from the high-temperature bath to the low-temperature bath. Such non-equilibrium steady state has remained the prime example in recent developments of non-equilibrium statistical physics [251]. A quantity that is of primary interest is the conductivity defined by

$$D = \frac{Q_t}{tN\Delta T},$$

where Q_t is the net flow of energy in time t passing through the system of length N from the bath at temperature $T + \Delta T$ to the bath at temperature T, when t and N are large. The properties of the conductivity D in the limit of large system lengths have been studied a lot over the last few decades. One of the main questions is whether the diffusivity is finite, *i.e.*, whether the Fourier's law is valid in one dimension.

The coupling to the heat bath and the transport of heat is straightforward to define in the system of hard rods. Inside the bulk, the orientations of rods are updated following an energy preserving update rule (only transitions are allowed for which the energy change is zero), whereas at the boundary, the orientation of rods is updated with a Metropolis filter with the temperature of the reservoir. In the simplest version of the model (where only the

nearest neighbor overlaps costs the energy U), it can be shown that the conductivity in the large N limit is

$$D \propto A(\kappa)\,,$$

where $A(\kappa)$ is the overlap area in the integral transfer operator $\mathcal{T}_\kappa$ defined in (III.6) (area of the shaded regions in Fig. III.8). Then, in this problem the conductivity D is finite and Fourier's law is valid. More interestingly, the conductivity shows a similar singularity as in the equilibrium case when the overlap area $A(\kappa)$ undergoes non-analytic changes with κ. This indicates a phase transition in the non-equilibrium steady state.

A – Appendix

A.1 Discrete-time probability distribution of the displacements

The probability distribution of a Gaussian distributed variable ϵ depends on its standard deviation σ and mean μ

$$P_{\mu,\sigma}(\epsilon) = \frac{1}{\sqrt{2\pi\sigma^2}} e^{-\frac{(\epsilon-\mu)^2}{2\sigma^2}} .$$

Consider a coordinate transformation such that each $\epsilon \in (-\infty, \infty)$ is folded within the interval $\epsilon' \in (-\delta, \delta)$

$$\epsilon' = C(\epsilon, \delta) = \begin{cases} q - \delta & \text{if } q < 2\delta \\ 3\delta - q & \text{if } q \geq 2\delta \,, \end{cases} \tag{A.1}$$

with $q = (\epsilon+\delta) \bmod 4\delta$, with $a \bmod b = a - b \left\lfloor \frac{a}{b} \right\rfloor$, i. e., $0 \leq q < 4\delta$, where $\lfloor a \rfloor$ is the floor function. This is the one-dimensional version of the folding scheme (II.2) of the displacement random walk of the persistent kinetic Monte Carlo algorithm (first introduced in section II.1). Fig. A.1 illustrates this scheme[1].

The inverse function of the folding corresponds to the reflection of the interval $(-\delta, \delta)$ on the entire space $(-\infty, \infty)$

$$\begin{aligned} \epsilon_n^+ &= C_+^{-1}(\epsilon', \delta) = (4n-1)\delta + (\epsilon' + \delta) \,, \\ \epsilon_n^- &= C_-^{-1}(\epsilon', \delta) = (4n-1)\delta - (\epsilon' + \delta) \,. \end{aligned} \tag{A.2}$$

With $n \in \mathbb{Z}$, C_+^{-1} generates all possible $\epsilon_n^+ \in (\{4n-1\}\delta, [\{4n-1\}+2]\delta)$ and C_-^{-1} generates all possible $\epsilon_n^- \in ([\{4n-1\}-2]\delta, \{4n-1\}\delta)$.

With (A.2) it is possible to calculate the probability distribution of ϵ'

$$\begin{aligned} P_{\mu,\sigma,\delta}(\epsilon') &= \int_{-\infty}^{\infty} P_{\mu,\sigma}(\epsilon) \left(\delta \left[\epsilon - C_-^{-1}(\epsilon', \delta) \right] + \delta \left[\epsilon - C_+^{-1}(\epsilon', \delta) \right] \right) d\epsilon \\ &= \sum_{n=-\infty}^{\infty} \left(\frac{1}{\sqrt{2\pi\sigma^2}} e^{-\frac{(\epsilon_n^- - \mu)^2}{2\sigma^2}} + \frac{1}{\sqrt{2\pi\sigma^2}} e^{-\frac{(\epsilon_n^+ - \mu)^2}{2\sigma^2}} \right) \\ &= \frac{\vartheta_3\left(\frac{\pi(\epsilon'-\mu)}{4\delta}, e^{-\frac{\pi^2\sigma^2}{8\delta^2}}\right) + \vartheta_3\left(-\frac{\pi(2\delta+\mu+\epsilon')}{4\delta}, e^{-\frac{\pi^2\sigma^2}{8\delta^2}}\right)}{4\delta} \,, \end{aligned} \tag{A.3}$$

[1] It is possible to reproduce this folding scheme with a accordion folded sheet of paper. The ϵ-axis is perpendicular to the folded edges. Choosing a range from $-M\delta$ to $+M\delta$ with $M \in \mathbb{N}$, then the edges are at all multiples of $(2m+1)\delta$ with $m \in \mathbb{Z}$ and $-M \leq m \leq M$. Piercing a needle through the accordion folded paper stack leaves a hole indicating $\epsilon' \in [-\delta, \delta]$ and all $\epsilon \in [-M\delta, M\delta]$ associated to this ϵ'.

with

$$\vartheta_3(u,q) = 1 + 2\sum_{n=1}^{\infty} q^{n^2}\cos(2nu)\,.$$

As the rest of the discussion in this section A.1 deals only with ϵ' confined in the interval $(-\delta,\delta)$, the prime-notation is dropped for simplicity. With $\kappa = \delta/\sigma$, the last equation leads to

$$P_{\mu,\kappa,\delta}(\epsilon) = \frac{\vartheta_3(\frac{\pi(\epsilon-\mu)}{4\delta}, e^{-\frac{\pi^2\kappa^{-2}}{8}}) + \vartheta_3(-\frac{\pi(2\delta+\mu+\epsilon)}{4\delta}, e^{-\frac{\pi^2\kappa^{-2}}{8}})}{4\delta} \tag{A.4}$$

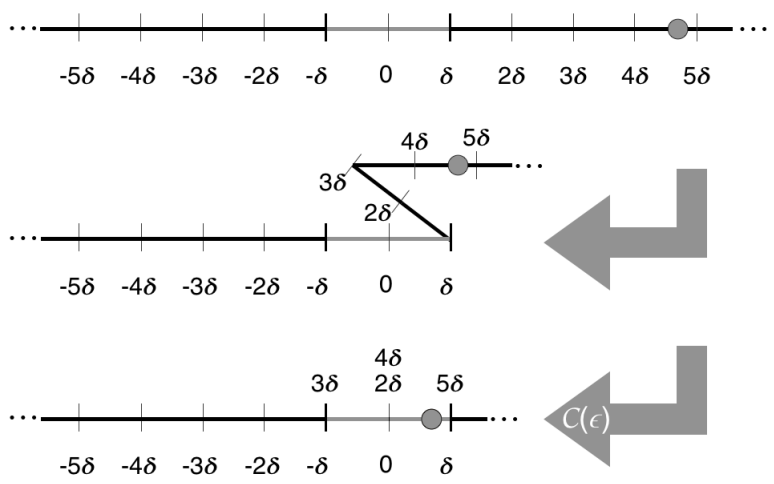


Figure A.1: **Illustration of the displacement's folding scheme in** (A.1). The upper row shows a sampled ϵ (gray dot) which is then folded into the interval $-\delta < \epsilon' < \delta$.

From $P_{\mu,\kappa,\delta}(\epsilon_0)$, a random number $\epsilon_0 \in (-\delta,\delta)$ can be directly sampled. Choosing now $\mu = \epsilon_0$, a second random number depending on ϵ_0 can be sampled from $P_{\epsilon_0,\kappa,\delta}(\epsilon_1)$. $\epsilon_0 \to \epsilon_1$ corresponds now to a single-step random walk from the distribution (A.4). With (A.4), the auto-correlation function $\langle\epsilon_0\epsilon_1\rangle$ can be calculated

$$\langle\epsilon_0\epsilon_1\rangle_{\mu,\kappa,\delta} = \int_{-\delta}^{\delta}\int_{-\delta}^{\delta} d\epsilon_0 d\epsilon_1 P(\epsilon_0,\mu,\kappa,\delta)P(\epsilon_1,\epsilon_0,\kappa,\delta)\epsilon_0\epsilon_1\,. \tag{A.5}$$

Fig. A.2 shows a numerical integration result of the auto-correlation function for a fixed $\delta = 0.1$ and a) different κ as a function of μ and b) different μ as a function of κ. Fig. A.2a demonstrates clearly that the auto-correlation vanishes in the $\kappa \to 0$ limit for all values of μ. Furthermore, it shows that the auto-correlation depends on μ. The auto-correlation for $\mu = 0$ in Fig. A.2b has a maximum around $\kappa^{-1} \sim 0.6$. The auto-correlation vanishes at small κ. However, at fixed δ, a large κ means a small standard deviation σ leading to small values for ϵ_0 and ϵ_1, which explains the decay to zero for $\kappa^{-1} \to 0$ and $\mu = 0$.

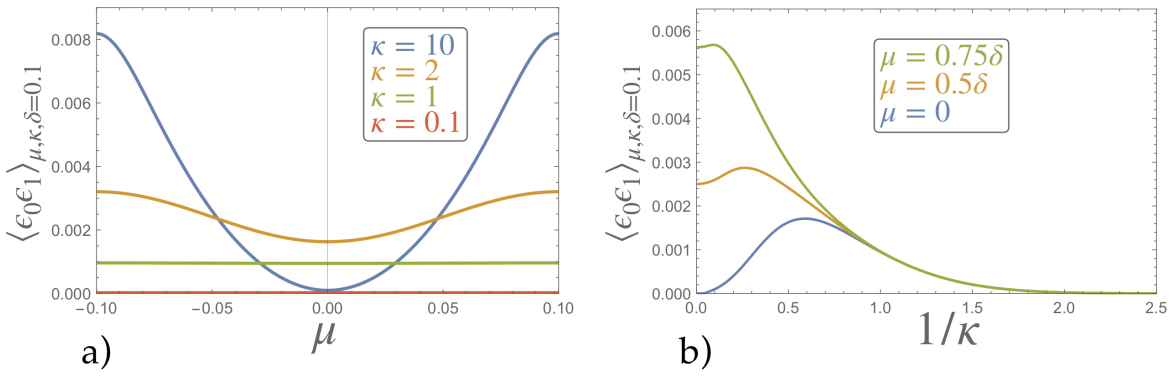


Figure A.2: Numerical integration of $\langle \epsilon_0 \epsilon_1 \rangle_{\mu,\sigma,\delta}$ (A.5) for a fixed $\delta = 0.1$ and a) three different σ as a function of μ and b) three different μ as a function of σ.

Following the description of the kinetic Monte Carlo approach in section II.1, the discrete-time i random walk of ϵ_i involves by choosing ϵ_{i-1} as the mean for the sampling of ϵ_i. Over a long run, each possible mean value $\mu \in (-\delta, \delta)$ contributes equally to $\langle \epsilon_{i-1} \epsilon_i \rangle_{\mu,\kappa,\delta}$. The arithmetic mean over μ is

$$\overline{\langle \epsilon_{i-1} \epsilon_i \rangle}_{\kappa,\delta} = \frac{1}{\int_{-\delta}^{\delta} d\mu} \int_{-\delta}^{\delta} \langle \epsilon_{i-1} \epsilon_i \rangle_{\mu,\kappa,\delta} d\mu \,. \tag{A.6}$$

The result of a numerical integration in comparison with simulation data of the ϵ random walk are shown in Fig. A.3. The agreement is excellent. It should be noted that the connected auto-correlation function $\overline{\langle \epsilon'_0 \epsilon'_1 \rangle}_{\kappa,\delta} - \overline{\langle \epsilon'_0 \rangle}_{\kappa,\delta} \overline{\langle \epsilon'_1 \rangle}_{\kappa,\delta}$ leads to the same result.

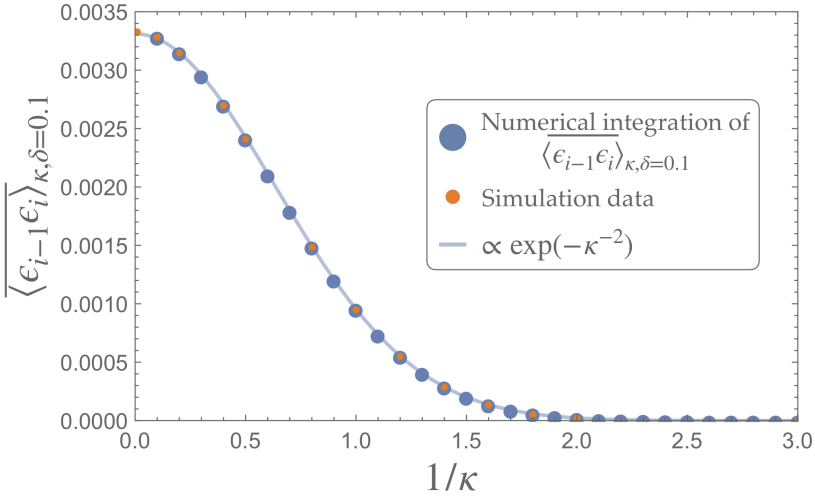


Figure A.3: Numerical integration of $\overline{\langle \epsilon_{i-1} \epsilon_i \rangle}_{\kappa,\delta}$ in (A.6) for a fixed $\delta = 0.1$ as a function of κ and the simulation result for comparison. The blue curve is a fit of the numerical integration.

A.2 Grid/cell scheme

The Metropolis filter in the kinetic Monte Carlo approach requires the calculation of the total energy change $\Delta E = E - E'$ caused by a trial move $\boldsymbol{r}_i \to \boldsymbol{r}_i + \boldsymbol{\epsilon}_i$, for details see section II.1. The calculation of the total energy $E = \sum_{i=1}^{N} \sum_{j=i+1}^{N} U(r_{ij})$ in principle requires the knowledge of all inter-particle distances r_{ij}. However, if the total energy change is caused by the displacement of a single particle i, then ΔE is given by

$$\Delta E = \sum_{j=1, j\neq i}^{N} \left[U(|\boldsymbol{r}_i + \boldsymbol{\epsilon}_i - \boldsymbol{r}_j|) - U(|\boldsymbol{r}_i - \boldsymbol{r}_j|) \right],$$

hence the algorithm scales as $\mathcal{O}(N)$.

As mentioned in subsection II.3.1, the system size dependent scaling is avoided by choosing a suitable cut-off radius r_c [13] for the here studied inter-particle pair potential

$$U(r_{ij}) = u_0 (\gamma / r_{ij})^n , \tag{A.7}$$

with $n = 6, 16$ (first defined in (II.10)), thus the pair potential is given by [13]

$$\tilde{U}(r_{ij}) = U(\min[r_{ij}, r_\mathrm{c} = 1.8]) .$$

Then, given that the absolute total displacement satisfies $|\boldsymbol{\epsilon}| < r_\mathrm{c}$, the total energy change caused by the displacement of particle i is given by

$$\Delta E = \sum_{j} [U(|\boldsymbol{r}_i + \boldsymbol{\epsilon}_i - \boldsymbol{r}_j|) - U(|\boldsymbol{r}_i - \boldsymbol{r}_j|)] , \tag{A.8}$$

where the sum $\sum_j$ includes all particles j, which satisfy the conditions

$$j \neq i \quad \wedge \quad (|\boldsymbol{r}_i + \boldsymbol{\epsilon}_i - \boldsymbol{r}_j| < r_\mathrm{c} \quad \vee \quad |\boldsymbol{r}_i - \boldsymbol{r}_j| < r_\mathrm{c}) . \tag{A.9}$$

Considering a particle displacement as shown in Fig. A.4, this condition means that only the particles whose centers are located within the red circle, or within the dashed red circle need to be considered for the calculation of the total energy change. This condition leads thus to the smallest number of necessary operations to compute the total energy change and leads to a scaling which is independent of the total number of particles N. On the other hand, the knowledge of all particles satisfying the condition (A.9) again requires a prior knowledge about all $|\boldsymbol{r}_i + \boldsymbol{\epsilon}_i - \boldsymbol{r}_j|$ and $|\boldsymbol{r}_i - \boldsymbol{r}_j|$. However, when using a standard tool [42] of particle simulations this does not need to be calculated in every step.

If the particle positions are confined on a two-dimensional box, with L_x and L_y being the edge lengths which do not have to be equal, than the concept of the grid/cell scheme [42] is to divide this box into sub-boxes of size $\ell_\mathrm{x} \times \ell_\mathrm{y}$ as illustrated in Fig. A.4. The sub-box size is given by

$$\ell_\mathrm{z} = \frac{L_\mathrm{z}}{n_\mathrm{z}} ,$$

where

$$n_\mathrm{z} = \lfloor L_\mathrm{z} / r_\mathrm{c} \rfloor$$

is the number of sub-boxes in z-direction, with z = x, y, and $\lfloor a \rfloor$ is the floor function. With this definition $r_c < \ell_z < 2r_c$.

The particle positions associate each particle to one particular sub-box. If the displacement of particle i leads to a position $\boldsymbol{r}_i + \boldsymbol{\epsilon}_i$ which is located in the same sub-box (for simplicity say b) as the original position $\boldsymbol{r}_i$ of the particle (see Fig. A.4a), then it follows from (A.8) with (A.9) that the total energy can be calculated from

$$\Delta E = \sum_B \sum_{j_B} [U(|\boldsymbol{r}_i + \boldsymbol{\epsilon}_i - \boldsymbol{r}_{j_B}|) - U(|\boldsymbol{r}_i - \boldsymbol{r}_{j_B}|)] \,. \tag{A.10}$$

Here, B runs over all neighboring sub-boxes of b and also includes b (indicated by the green square in Fig. A.4a and j_B are the particles located within the sub-boxes (excluding i).

As $r_c < \ell_z < 2r_c$, it is clear from Fig. A.4a that the green square always contains the particles located within the red circles which are relevant to calculate the total energy change. The other particles located outside the red circles do not contribute to the energy change, thus this grid/cell scheme does a bit more work than required by (A.8) with (A.9) but nevertheless fulfills the main purpose of reducing the scaling of the algorithm from $\mathcal{O}(N)$ to a constant number independent of the system size N. Fig. A.4b) shows the least efficient situation of this grid/cell scheme. Here the trial position is located in an edge-connected neighboring cell. The illustration shows clearly that this case requires that B in (A.10) runs over all neighboring cells of $\boldsymbol{r}_i + \boldsymbol{\epsilon}_i$ and the neighboring cells of $\boldsymbol{r}_i$.

The efficiency of the grid/cell scheme increases for large volumes, where $L_z \gg r_c$ as this results in sub-boxes with $r_c \lesssim \ell_z$.

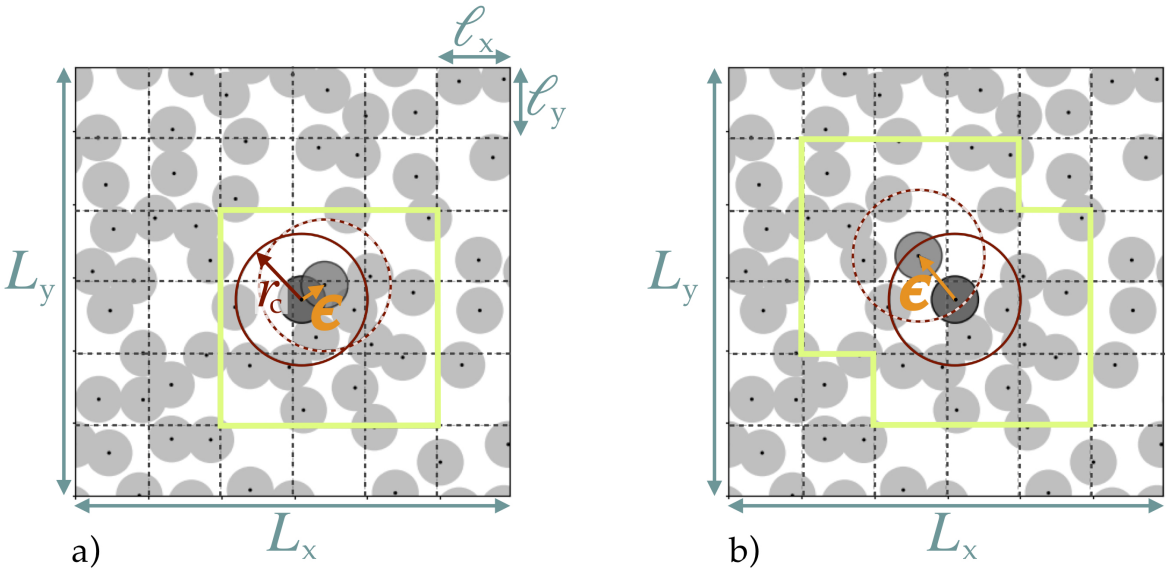


Figure A.4: **Grid/cell scheme.** The particle positions (black dots) are confined in a $L_x \times L_y$ box with periodic boundary conditions. The parameter γ of the inter-particle potential (A.7) is indicated by the gray disks. Shown is the trial displacement $\boldsymbol{r}_i + \boldsymbol{\epsilon}_i$ of a particle i. The red circle around the original position of the particle indicates the cut-off radius r_c of the potential. The dashed red circle indicates the cut-off radius around the new test position $\boldsymbol{r}_i + \boldsymbol{\epsilon}_i$. The space is divided into sub-boxes of size $\ell_x \times \ell_y$, with $2r_c > (\ell_x, \ell_y) > r_c$.

This implementation requires to keep track of the particle positions in the grid cells. One possible implementation is described in chapter 2.4.1 of [42] for hard disks, which can be easily extended to soft spheres. In the hard-disk case, it is sufficient to check for overlaps created by the displacement. In addition, $r_c = \gamma$, which is the hard-disk diameter for $n \to \infty$. If the volume is big enough thus $r_c \lesssim \ell_z$, each cell can contain at most four hard-disk centers.

A.3 Orientational correlation function at the outer boundary of MIPS

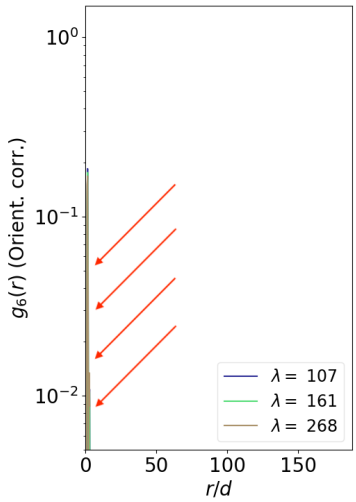


Figure A.5: **Orientational correlation function at the outer boundary of MIPS.** The data is for $\phi = 1.0$, $\delta = 0.7$, $N = 10976$ for different λ indicated in the legend. The correlation function is clearly short-ranged and thus confirms the liquid character of the cluster phase within MIPS.

A.4 Convergence data for the activity-induced two-step melting

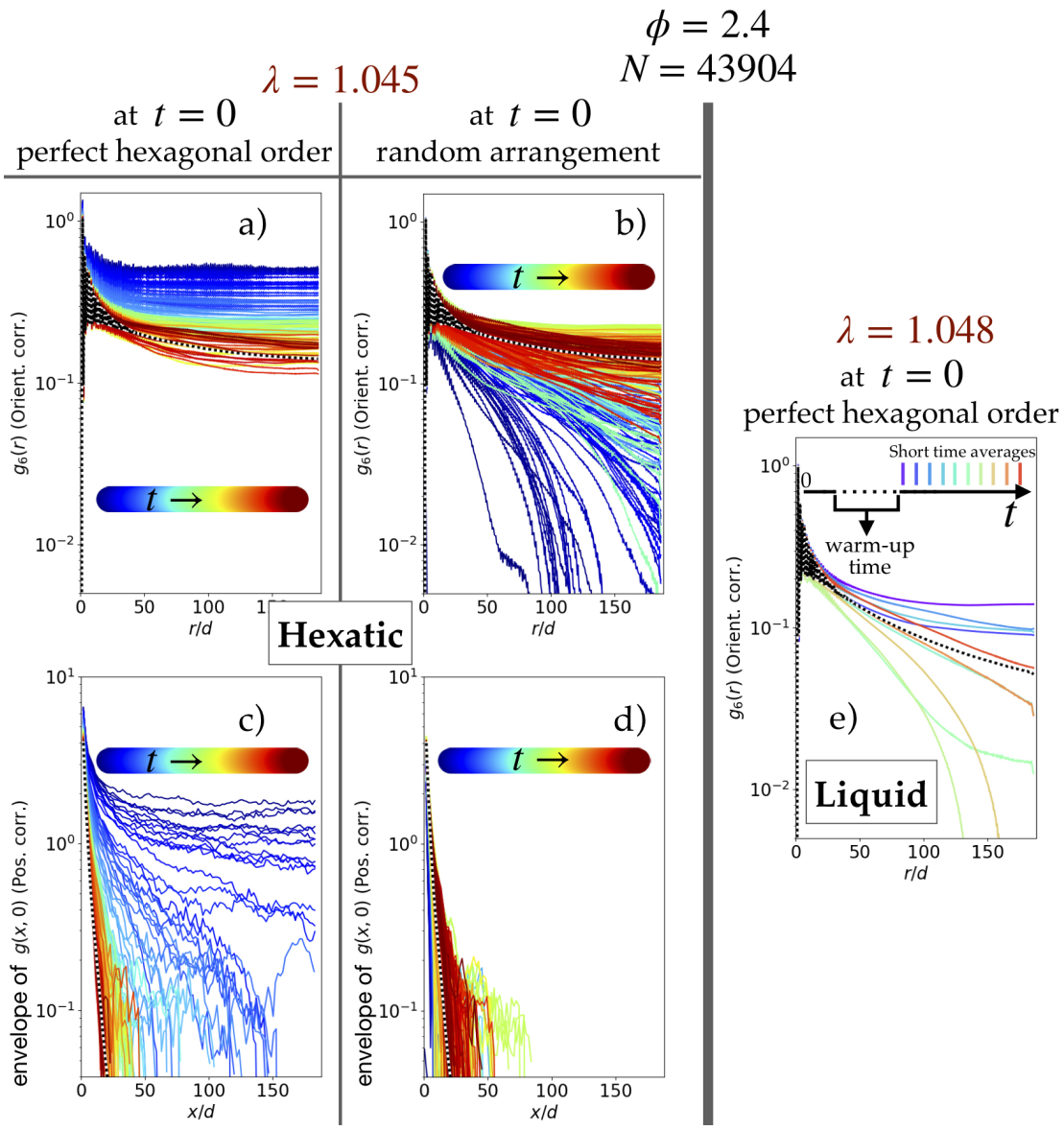


Figure A.6: **Convergence to the hexatic phase.** Data for $\phi = 2.4$, $N = 43904$, $\delta = 0.1$ and the potential $n = 6$. Compare with Fig. II.23 and Fig. II.25. a) to d) show the time evolution (indicated color code in linear scale) of single configurations for $\lambda = 1.045$. At $t = 0$ the particles in a) and c) are arranged on a perfect hexagonal lattice. In contrast, in b) and d) the configuration at $t = 0$ is random. a) and b) show the time evolution of the orientational correlation function. c) and d) show the time evolution of the positional correlation function. Both initial arrangements converge to the same steady state represented by the black-and-white dashed line. $\lambda = 1.045$ is very close to the liquid-hexatic transition. Figure e) shows data for a slightly larger persistence length $\lambda = 1.048$. Shown are short-time averages for the orientational correlation function, each containing 20 configurations after the warm-up time. Even after a long warm-up time, the system does not show a clear convergence towards a steady state and jumps between an exponential decay and a power-law decay. This behavior appears close to the transition and is due to the finite system size. Previous simulations show that it is to expect that this persistence can be associated with a liquid state point for larger systems.

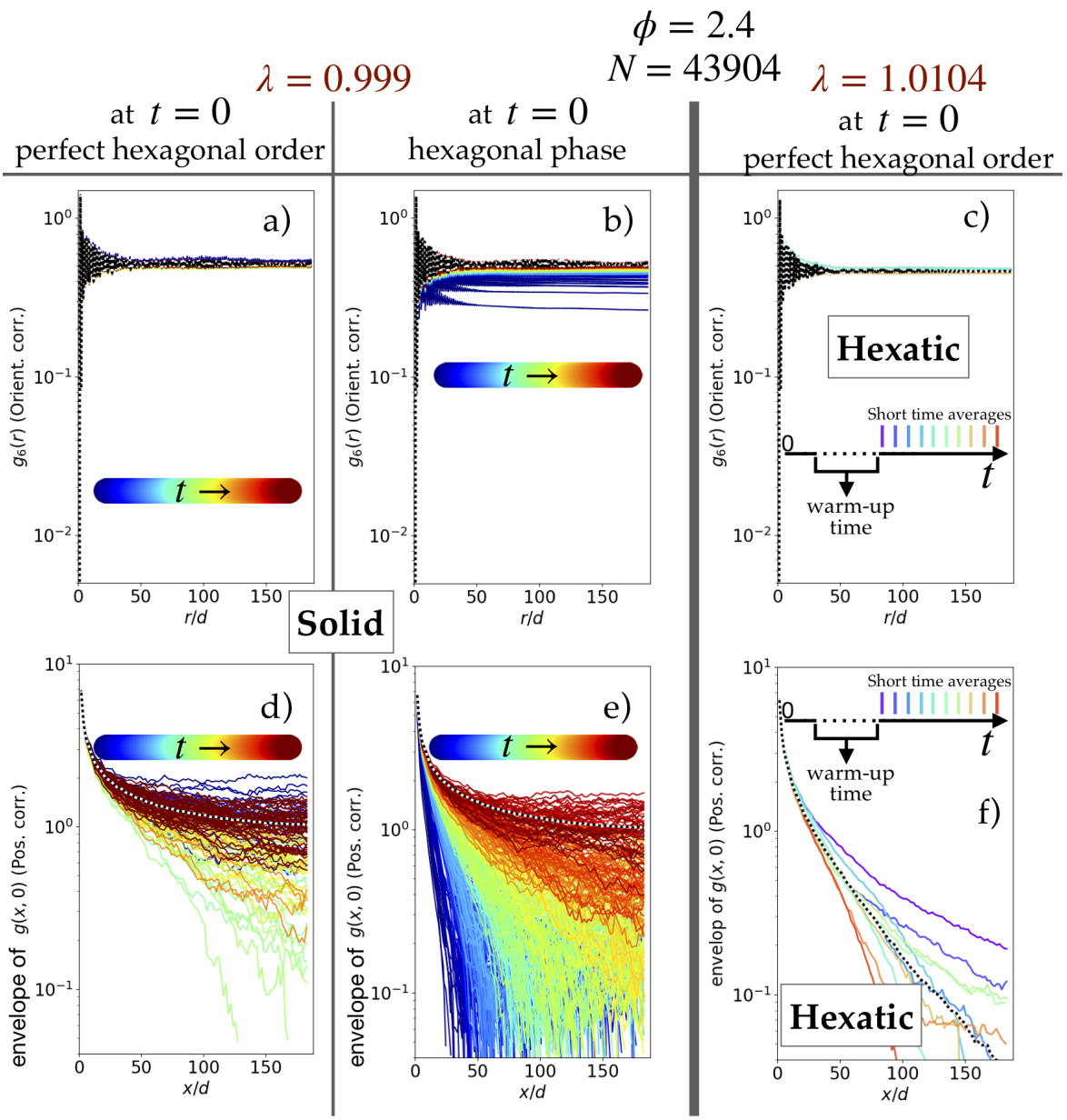


Figure A.7: **Convergence to the solid phase.** Data for $\phi = 2.4$, $N = 43904$, $\delta = 0.1$ and the potential $n = 6$. Compare with Fig. II.23 and Fig. II.25. a) to d) show the time evolution (indicated color code in linear scale) of single configurations for $\lambda = 0.999$. At $t = 0$ the particles in a) and d) are arranged on a perfect hexagonal lattice. In contrast, in b) and e) the configuration at $t = 0$ is a state point in the hexatic phase. a) and b) show the time evolution of the orientational correlation function. c) and d) show the time evolution of the positional correlation function. Both initial arrangements converge to the same steady state represented by the black-and-white dashed line. Note the overshoot (green curves) in d) while approaching the steady state. This behavior is observed regularly in the data during the warm-up and appears "oscillation-like". However, once the steady state is reached, correlation functions of individual configurations show only small deviations from the mean, thus the behavior of approaching the steady state resembles a damped oscillation but was not further investigated. $\lambda = 0.999$ is very close to the hexatic-solid transition. c) and f) show data for a slightly larger persistence length $\lambda = 1.0104$. Shown are short-time averages for the orientational correlation function c) and positional correlation function f) together with the total time average (black-white dashed line) clearly indicating the hexatic phase.

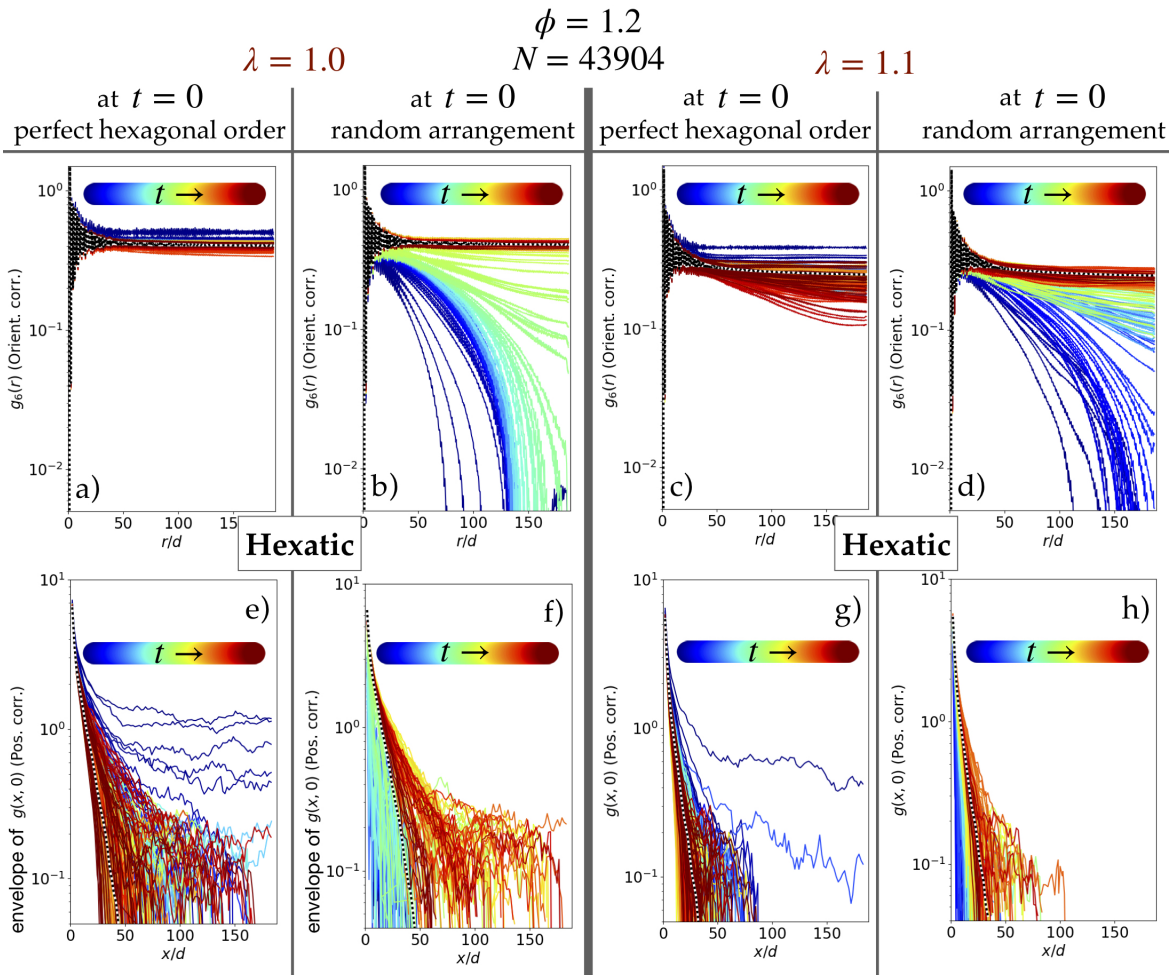


Figure A.8: **Convergence to the hexatic phase for** $n = 16$**.** Data for $\phi = 2.4$, $N = 43904$, $\delta = 0.1$ and the potential $n = 16$. Compare with Fig. II.26 and Fig. II.27. Time evolution (indicated color code in linear scale) of single configurations for $\lambda = 1.0$ (left) and $\lambda = 1.1$ (right). At $t = 0$ the particles in a), e), c) and g) are arranged on a perfect hexagonal lattice. In contrast, in b), d), f) and h) the configuration at $t = 0$ is random. a) to d) show the time evolution of the orientational correlation function. e) to h) show the time evolution of the positional correlation function. Both initial arrangements converge to the same steady state represented by the black-and-white dashed line.

A.5 MIPS under the influence of the potential stiffness

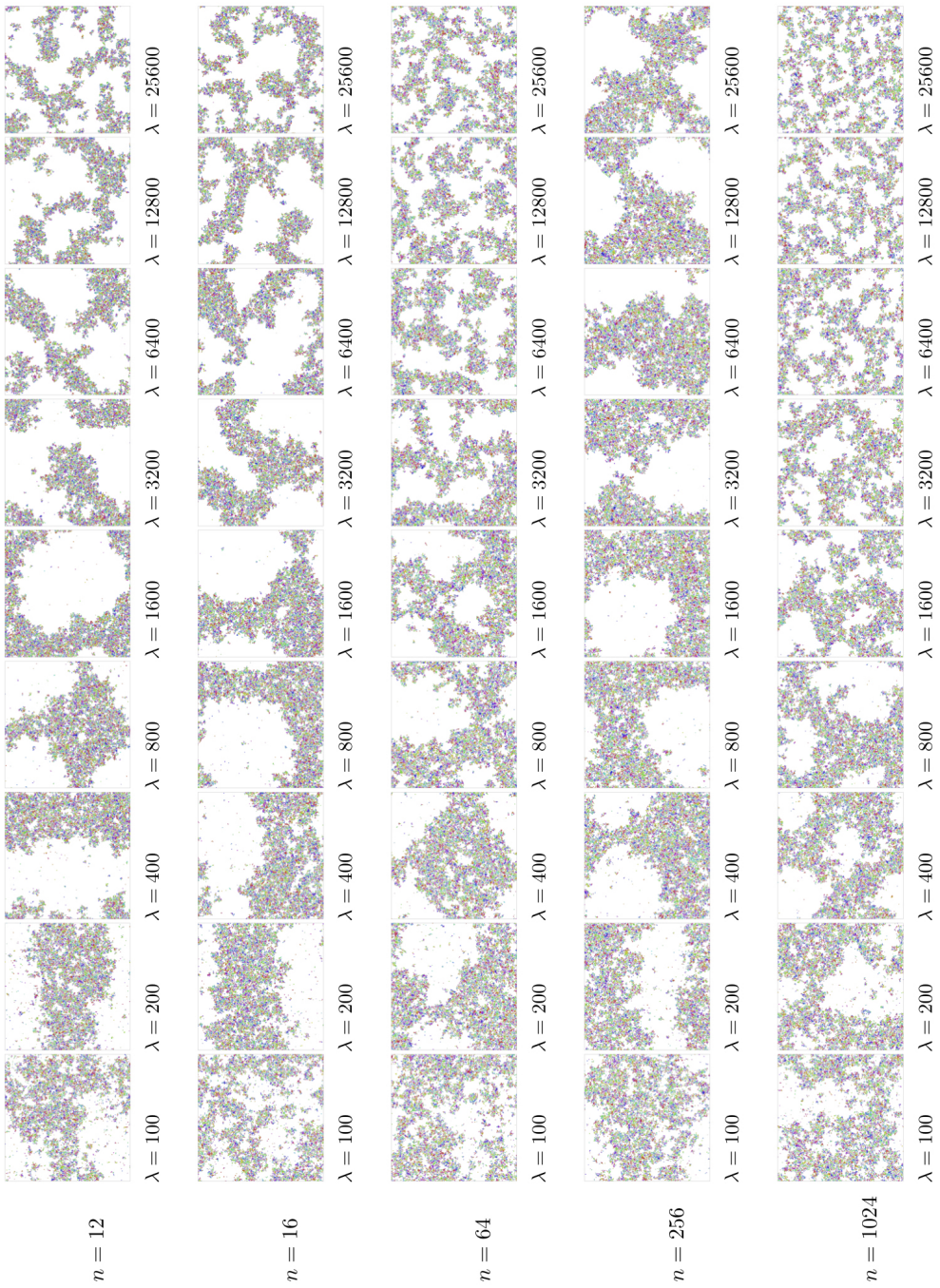


Figure A.9: MIPS in ψ_6 color code for different power-law potentials $U \propto r^{-n}$ and persistence lengths λ. $N = 10976$, $\phi = 0.4$, $\delta = 0.7$. A macroscopic phase separation is clear for all potentials at $\lambda = 200$. The coarsening process slows down for higher λ, leaving some configurations in the state where microscopic density inhomogeneities are formed but have not merged yet. No orientational order visible. (Color code indicated, *e.g.*, in Fig. II.23c).

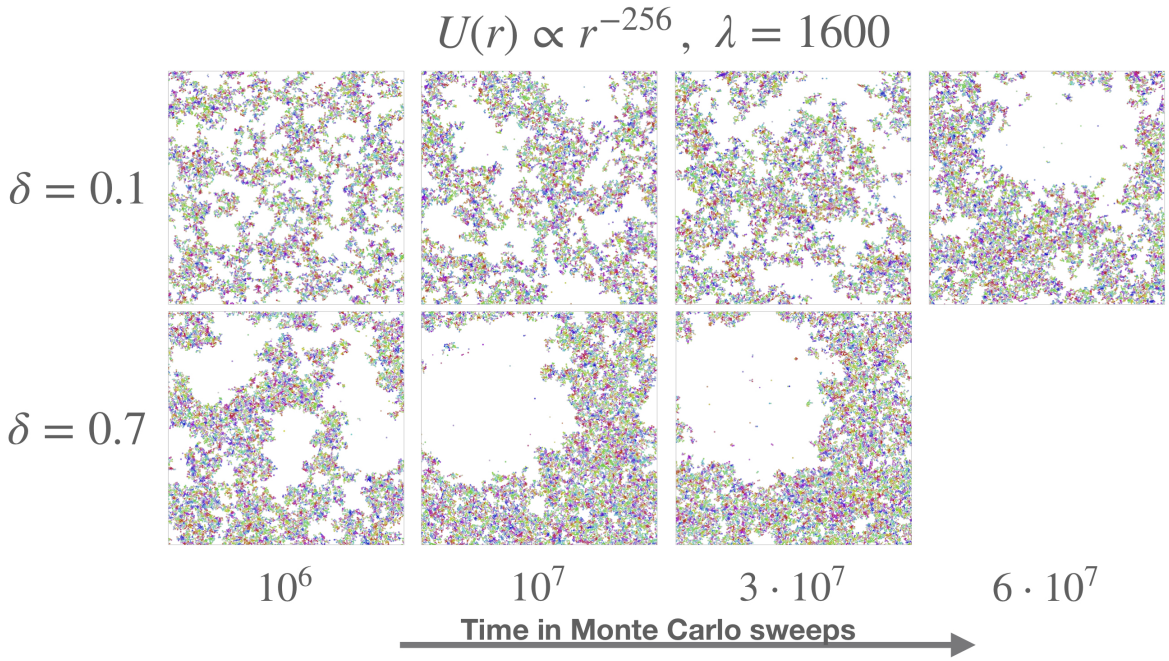


Figure A.10: **Coarsening process for MIPS under the influence of δ.** Configuration snapshots, with ψ_6 color-coded particles (indicated, *e.g.*, in Fig. II.23c) for $N = 10976$.

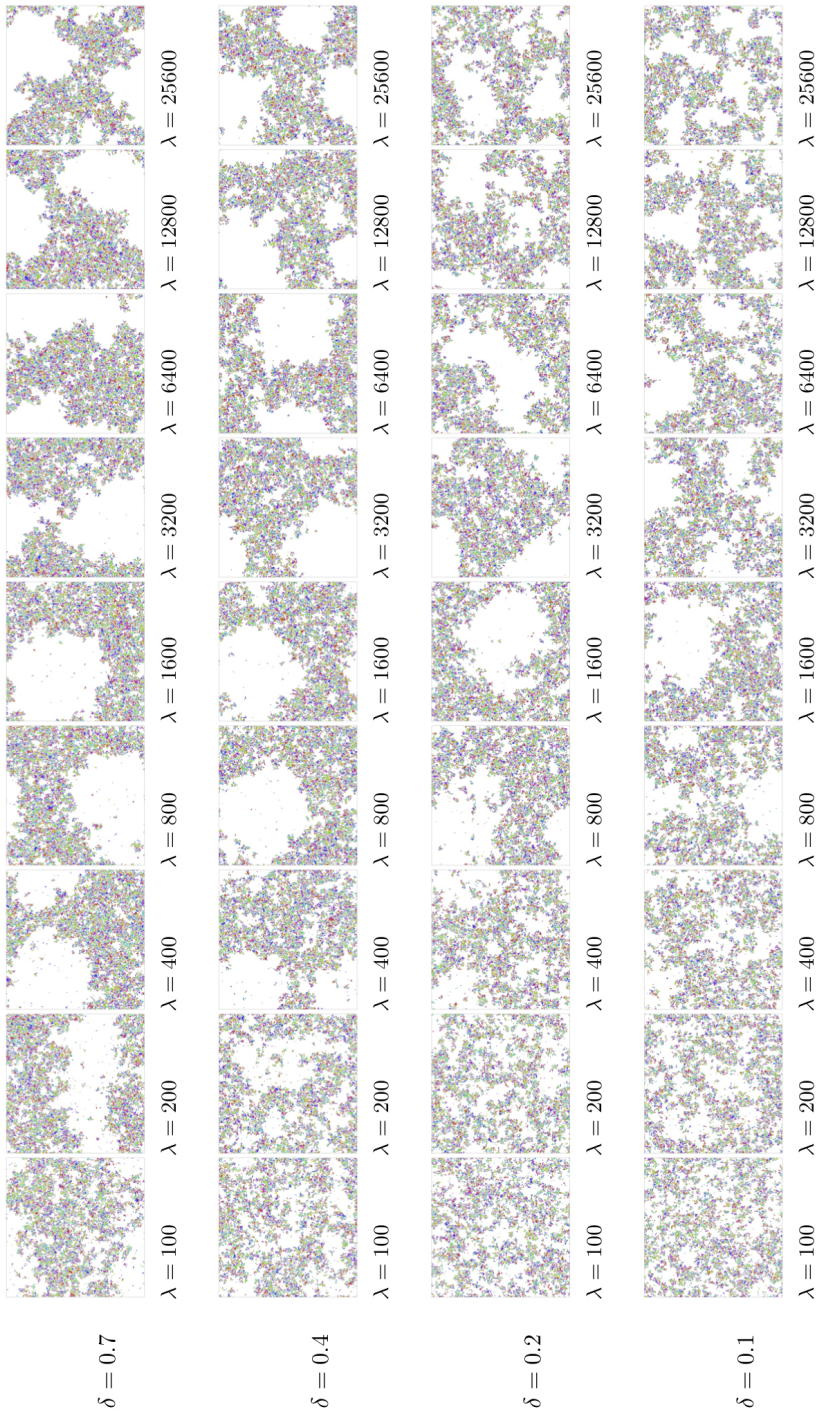


Figure A.11: MIPS in ψ_6 color-coded configuration snapshots for $U \propto r^{-256}$, a range of different δ and persistence lengths λ. $N = 10976$, $\phi = 0.4$. The runtimes for individual δ are comparable, whereas runtimes between different δ may vary strongly (smaller δ have larger runtimes, for details see A.14). (Color code indicated, *e.g.*, in Fig. II.23c.)

A.6 Further evidence for negligible anisotropic effects in 2D

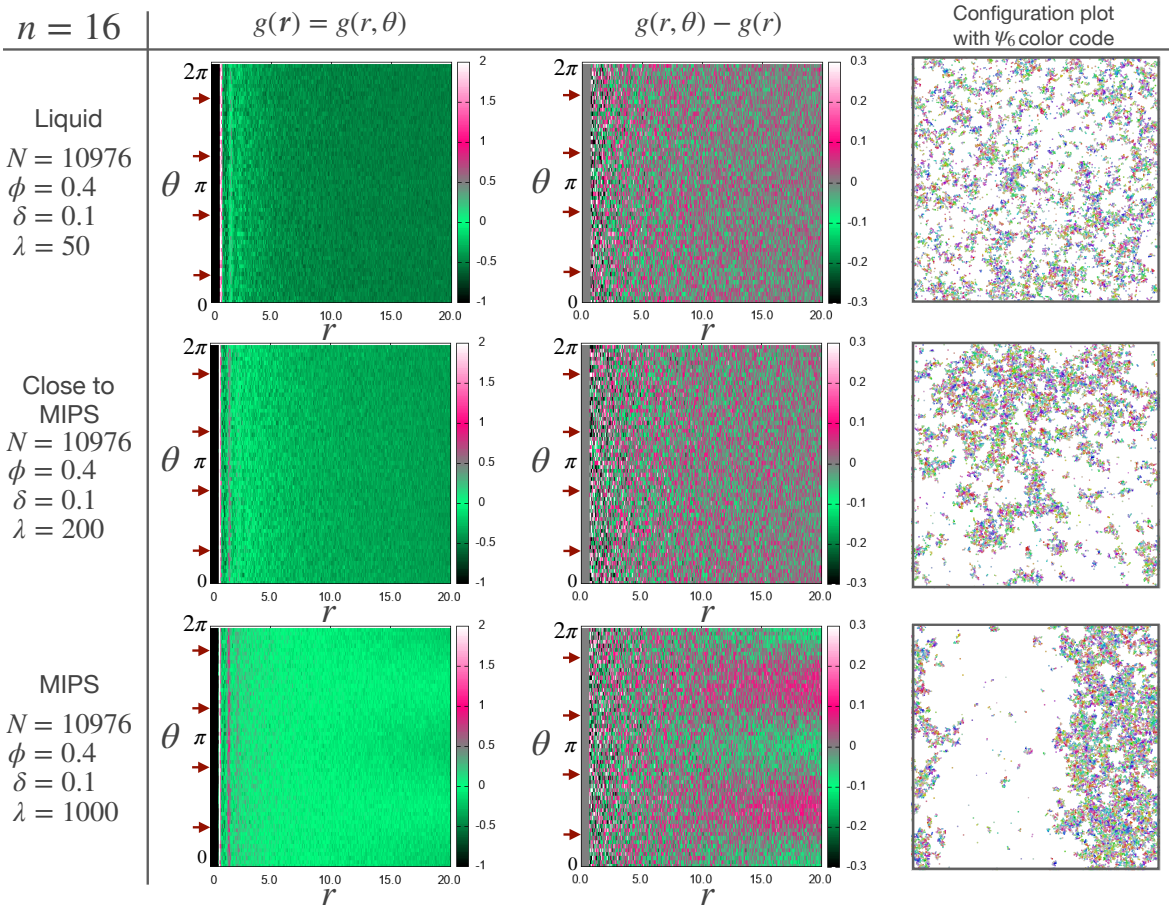


Figure A.12: **Evidence for effective isotropic dynamics below and in the MIPS region.** Data is for the potential with $n = 16$ at $\phi = 0.4$ for $N = 10976$ and for persistence lengths inside the MIPS region with $\delta = 0.1$. First column: pair-correlation function $g(r,\theta)$ in polar coordinates averaged over 100 configurations. Second column: difference between $g(r,\theta)$ and its angular average $g(r)$. Third column: configuration snapshots with ψ_6 color code as indicated in, *e.g.*, Fig. II.23. The red arrows indicate $\pi/4, 3\pi/4, 5\pi/4$ and $7\pi/4$.

A.7 Time evolution of fluctuating distribution function, passive case

To derive the time evolution of the fluctuating distribution function in (II.59a) an arbitrary test function $R(x)$ is defined, such that $R(x_i(t)) = \int dx\, \boldsymbol{\delta}(x - x_i(t))R(x)$. The time evolution can be written as

$$\frac{d}{dt}R(x_i(t)) = \int dx\, R(x)\, \frac{d}{dt}\boldsymbol{\delta}(x - x_i(t))\,. \tag{A.11}$$

By writing (II.57) as

$$x_i(t+dt) = x_i(t) + dt\,\beta F_i(\mathbf{x}) + dt\,\beta F^{(e)}(x_i) + d\omega(t)\,,$$
$$\text{with}$$
$$\langle d\omega(t)\rangle = 0\,, \text{and } \langle d\omega(t)^2\rangle = 2\,dt\,,$$

it follows,

$$\begin{aligned} R(x_i(t+dt)) =& R\left(x_i(t) + d\omega(t) + dt\beta F_i(\mathbf{x}(t)) + dt\beta F^{(e)}(x_i(t))\right) \\ =& R(x_i(t)) + [d\omega(t) + dt\beta F_i(\mathbf{x}(t)) + dt\beta F^{(e)}(x_i(t))]\frac{\partial R(x_i(t))}{\partial x_i} + \frac{1}{2}d\omega(t)^2\frac{\partial^2 R(x_i(t))}{\partial x_i^2} + \cdots\,. \end{aligned}$$

The $dt \to 0$ limit, leads to

$$\frac{d}{dt}R(x_i(t)) = [\eta_i(t) + \beta F_i(\mathbf{x}(t)) + \beta F^{(e)}(x_i(t))]\frac{\partial R(x_i(t))}{\partial x_i} + \frac{\partial^2 R(x_i(t))}{\partial x_i^2},$$

where $\frac{d\omega(t)}{dt} = \eta_i(t)$ and $\lim_{t\to 0}\frac{d\omega(t)^2}{dt} = 2$ were used (following Itō convention). Using the Dirac delta function, the above equation can be recast as

$$\frac{d}{dt}R(x_i(t)) = \int dx\,\boldsymbol{\delta}(x - x_i(t))\left\{\left[\eta_i(t) + \beta F_i(\mathbf{x}'(t)) + \beta F^{(e)}(x)\right]\frac{\partial R(x)}{\partial x} + \frac{\partial^2 R(x)}{\partial x^2}\right\},$$

where $\mathbf{x}'(t)$ denotes the set of particle positions x_j with the i^{th} position $x_i = x$. Integrating by parts leads to

$$\begin{aligned} \int_{-\infty}^{\infty} dx\,\boldsymbol{\delta}(x - x_i(t))F_i(\mathbf{x}'(t))\frac{\partial R(x)}{\partial x} =& \underbrace{\left[\boldsymbol{\delta}(x - x_i(t))F_i(\mathbf{x}'(t))R(x)\right]_{x=\pm\infty}}_{\substack{=0 \text{ as the particles are confined,} \\ \text{thus } |x_i(t)|<\infty\,\forall\,t}} \\ & - \int_{-\infty}^{\infty} dx\,R(x)\frac{\partial}{\partial x}\left[\boldsymbol{\delta}(x - x_i(t))F_i(\mathbf{x}'(t))\right]\,. \end{aligned}$$

and similarly

$$\begin{aligned} \int_{-\infty}^{\infty} dx\,\boldsymbol{\delta}(x - x_i(t))\,F^{(e)}(x)\,\frac{\partial R(x)}{\partial x} =& -\int_{-\infty}^{\infty} dx\,R(x)\frac{\partial}{\partial x}\left[\boldsymbol{\delta}(x - x_i(t))F^{(e)}(x)\right] \\ \int_{-\infty}^{\infty} dx\,\boldsymbol{\delta}(x - x_i(t))\,\eta_i(t)\,\frac{\partial R(x)}{\partial x} =& -\int_{-\infty}^{\infty} dx\,R(x)\frac{\partial}{\partial x}\left[\boldsymbol{\delta}(x - x_i(t))\eta_i(t)\right] \end{aligned}$$

Furthermore

$$\begin{aligned} &\int_{-\infty}^{\infty} dx\,\boldsymbol{\delta}(x - x_i(t))\,D\,\frac{\partial^2 R(x)}{\partial x^2} = \\ &\underbrace{\left[\boldsymbol{\delta}(x - x_i(t))\,D\,\frac{\partial R(x)}{\partial x}\right]_{x=\pm\infty}}_{=0} - \int_{-\infty}^{\infty} dx\,\frac{\partial R(x)}{\partial x}\frac{\partial}{\partial x}\left[D\boldsymbol{\delta}(x - x_i(t))\right] = \\ &-\underbrace{\left[D\,R(x)\frac{\partial}{\partial x}\boldsymbol{\delta}(x - x_i(t))\right]_{x=\pm\infty}}_{=0} + \int_{-\infty}^{\infty} dx\,R(x)\frac{\partial^2}{\partial x^2}\left[D\boldsymbol{\delta}(x - x_i(t))\right]\,, \end{aligned}$$

thus finally

$$\frac{d}{dt}R(x_i(t)) = \int dx R(x) \left\{ -\frac{\partial}{\partial x}\boldsymbol{\delta}(x - x_i(t)) \Big[\eta_i(t) + \beta F_i(\mathbf{x}'(t)) + \beta F^{(e)}(x) \Big] + \frac{\partial^2 \boldsymbol{\delta}(x - x_i(t))}{\partial x^2} \right\} .$$

Comparing this expression with (A.11), it must follow that

$$\frac{d}{dt}\boldsymbol{\delta}(x - x_i(t)) = -\frac{\partial}{\partial x}\boldsymbol{\delta}(x - x_i(t)) \Big[\eta_i(t) + \beta F_i(\mathbf{x}'(t)) + \beta F^{(e)}(x) \Big] + \frac{\partial^2 \boldsymbol{\delta}(x - x_i(t))}{\partial x^2} .$$

As $\widehat{\psi}_t(x) = \sum_i \boldsymbol{\delta}(x - x_i(t))$, summing over all i in the above equation leads to the time evolution of the fluctuating distribution function

$$\frac{d}{dt}\widehat{\psi}_t(x) = -\frac{\partial}{\partial x}\eta(x,t) - \beta\frac{\partial}{\partial x}\sum_i \boldsymbol{\delta}(x - x_i(t)) F_i(\mathbf{x}'(t)) - \beta\frac{\partial}{\partial x}\Big[F^{(e)}(x)\widehat{\psi}_t(x) \Big] + \frac{\partial^2 \widehat{\psi}_t(x)}{\partial x^2} ,$$

where

$$\eta(x,t) = \sum_i \boldsymbol{\delta}(x - x_i(t))\eta_i(t) .$$

Using (II.57) one can easily show (II.59b).

The term with F_i can be rewritten using (II.58)

$$\sum_i \boldsymbol{\delta}(x - x_i(t)) F_i(\mathbf{x}'(t)) = \sum_i \boldsymbol{\delta}(x - x_i(t)) \sum_j \Phi(x - x_j) = \widehat{\psi}_t(x) \sum_j \Phi(x - x_j) ,$$

thus leading to the time evolution in (II.59a).

A.8 Time evolution of fluctuating distribution function, persistent case

Here the time evolution of the fluctuating distribution function in (II.66) is derived following the same procedure as in A.7. The test function becomes $R(x, v)$ and is defined, such that $R(x_i(t), v_i(t)) = \int dx \int dv\, \boldsymbol{\delta}(x - x_i(t))\boldsymbol{\delta}(v - v_i(t))R(x, v)$. This gives

$$\frac{d}{dt}R(x_i(t), v_i(t)) = \int dx\, dv\, R(x, v)\, \frac{d}{dt}[\boldsymbol{\delta}(x - x_i(t))\boldsymbol{\delta}(v - v_i(t))] . \tag{A.12}$$

By writing (II.62) as

$$\begin{aligned} v_i(t + dt) = v_i(t) + dt\, \tilde{R}(v_i(t)) + d\widehat{\omega}_i(t) \,, \text{with} \\ \langle d\widehat{\omega}_i(t) \rangle = 0 \,\text{and}\, \langle d\widehat{\omega}_i(t)^2 \rangle = 2D_a\, dt \,, \end{aligned}$$

and (II.64) as

$$\begin{aligned} x_i(t + dt) = x_i(t) + dt\, v_i(t)\, h_i\big(\mathbf{x}(t), v_i(t)\big) + dt\, F^{(e)}(x_i) + d\omega_i(t) \,, \text{with} \\ \langle d\omega_i(t) \rangle = 0 \,\text{and}\, \langle d\omega_i(t)^2 \rangle = 2D\, dt \,, \end{aligned}$$

it follows (after the Taylor expansion and after taking the $dt \to 0$ limit),

$$\frac{d}{dt}R(x_i(t),v_i(t)) = \Big[\eta_i(t) + v_i(t)\, h_i\big(\mathbf{x}(t),v_i(t)\big) + F^{(e)}(x_i(t))\Big]\,\frac{\partial R(x_i(t),v_i(t))}{\partial x_i} + \Big[\xi_i(t) + \tilde{R}(v_i(t))\Big]\,\frac{\partial R(x_i(t),v_i(t))}{\partial v_i} + D\frac{\partial^2 R(x_i(t),v_i(t))}{\partial x_i^2} + D_a\frac{\partial^2 R(x_i(t),v_i(t))}{\partial v_i^2},$$

where $\frac{d\omega(t)}{dt} = \eta_i(t)$, $\frac{d\hat{\omega}_i(t)}{dt} = \xi_i(t)$ and $\lim_{t\to 0}\frac{d\omega(t)^2}{dt} = 2D$, $\lim_{t\to 0}\frac{d\hat{\omega}_i(t)^2}{dt} = 2D_a$ were used, following the Itō convention. The equation can be recast as

$$\frac{d}{dt}R(x_i(t),v_i(t)) = \int dx\,dv\,\boldsymbol{\delta}(x-x_i(t))\boldsymbol{\delta}(v-v_i(t))\Big\{\Big[\eta_i(t) + v\, h_i\big(\mathbf{x}'(t),v\big) + F^{(e)}(x)\Big]\,\frac{\partial R(x,v)}{\partial x} + \Big[\xi_i(t) + \tilde{R}(v)\Big]\,\frac{\partial R(x,v)}{\partial v} + D\frac{\partial^2 R(x,v)}{\partial x^2} + D_a\frac{\partial^2 R(x,v)}{\partial v^2}\Big\},$$

where $\mathbf{x}'(t)$ denotes the set of particle positions x_j with the i^{th} position $x_i = x$. Integrating by parts leads to

$$\frac{d}{dt}R(x_i(t),v_i(t)) = \int dx\,dv\,R(x,v)\Big\{-\frac{\partial}{\partial x}\Big[\boldsymbol{\delta}(x-x_i(t))\boldsymbol{\delta}(v-v_i(t))\Big\{\eta_i(t) + v\, h_i\left(\mathbf{x}'(t),v\right) + F^{(e)}(x)\Big\}\Big] - \frac{\partial}{\partial v}\Big[\boldsymbol{\delta}(x-x_i(t))\boldsymbol{\delta}(v-v_i(t))\Big\{\xi_i(t) + \tilde{R}(v)\Big\}\Big] + D\frac{\partial^2}{\partial x^2}\big[\boldsymbol{\delta}(x-x_i(t))\boldsymbol{\delta}(v-v_i(t))\big] + D_a\frac{\partial^2}{\partial v^2}\big[\boldsymbol{\delta}(x-x_i(t))\boldsymbol{\delta}(v-v_i(t))\big]\Big\}.$$

Comparing the above expression with (A.12) and using the definition $\widehat{\rho}_i(x,v,t) = \boldsymbol{\delta}(x - x_i(t))\boldsymbol{\delta}(v - v_i(t))$ it must follow that

$$\frac{d}{dt}\widehat{\rho}_i(x,v,t) = -\frac{\partial}{\partial x}\Big\{\widehat{\rho}_i(x,v,t)\Big[\eta_i(t) + v\, h_i\big(\mathbf{x}'(t),v\big) + F^{(e)}(x)\Big]\Big\} - \frac{\partial}{\partial v}\Big\{\widehat{\rho}_i(x,v,t)\Big[\xi_i(t) + \tilde{R}(v)\Big]\Big\} + D\frac{\partial^2}{\partial x^2}\widehat{\rho}_i(x,v,t) + D_a\frac{\partial^2}{\partial v^2}\widehat{\rho}_i(x,v,t)\,.$$

Because $\widehat{\psi}_t(x,v) = \sum_i \widehat{\rho}_i(x,v,t)$, summing over all i in the above equation leads to the time evolution of the fluctuating distribution function in (II.66), as

$$\sum_i \widehat{\rho}_i(x,v,t) h_i(\mathbf{x}'(t),v) = \sum_i \widehat{\rho}_i(x,v,t)\min\Big[1,\exp\Big(\Gamma v\sum_j \Phi(x-x_j)\Big)\Big]$$

and

$$\sum_j \Phi(x - x_j) = \sum_j \int dx'\, dv'\, \boldsymbol{\delta}(x' - x_j(t))\, \boldsymbol{\delta}(v' - v_j(t))\, \Phi(x - x') \\ = \int dx'\, dv'\, \widehat{\psi}_t(x', v')\, \Phi(x - x')\,,$$

thus

$$\sum_i \widehat{\rho}_i(x, v, t) h_i(\mathbf{x}'(t), v) = \widehat{\psi}_t(x, v)\, \chi \left[\Gamma v \int dx'\, dv'\, \Phi(x - x')\, \widehat{\psi}_t(x', v') \right],$$

where the function $\chi[s]$ is defined as

$$\chi[s] = \min\{1, e^s\}\,.$$

A.9 Continuity equation of the particle density

The equation in (II.66) can be recast as

$$\frac{d}{dt}\widehat{\psi}_t(x, v) = -\frac{\partial}{\partial v}\widehat{J}_v(x, v, t) - \frac{\partial}{\partial x}\widehat{J}_\rho(x, v, t)\,,$$

with

$$\widehat{J}_v(x, v, t) = \xi_t(x, v) - D_a \frac{\partial}{\partial v}\widehat{\psi}_t(x, v)\,,$$

and

$$\widehat{J}_\rho(x, v, t) = \eta_t(x, v) + \widehat{\psi}_t(x, v)\, v\, \chi \left[\Gamma v \int dx' dv'\, \Phi(x - x')\, \widehat{\psi}_t(x', v') \right] \\ + F^{(e)}(x) \widehat{\psi}_t(x, v) - D \frac{\partial}{\partial x}\widehat{\psi}_t(x, v)\,.$$

Integrating $\widehat{J}_\rho(x, v, t)$ over v leads to

$$\widehat{J}_\rho(x, t) = \int dv\, \widehat{J}_\rho(x, v, t) \\ = \int dv\, \eta_t(x, v) + \int dv\, \widehat{\psi}_t(x, v)\, v\, \chi \left[\Gamma v \int dx' dv'\, \Phi(x - x')\, \widehat{\psi}_t(x', v') \right] \\ + \underbrace{\int dv\, F^{(e)}(x) \widehat{\psi}_t(x, v)}_{= F^{(e)}(x) \widehat{\rho}_t(x)} - \underbrace{\int dv\, D \frac{\partial}{\partial x}\widehat{\psi}_t(x, v)}_{= D \frac{\partial}{\partial x}\widehat{\rho}_t(x)}\,,$$

thus the ensemble average gives

$$J_\rho(x, t) = \left\langle \widehat{J}_\rho(x, t) \right\rangle \\ = \int dv\, \underbrace{\langle \eta_t(x, v) \rangle}_{=0} + \left\langle \int dv\, \widehat{\psi}_t(x, v)\, v\, \chi \left[\Gamma v \int dx' dv'\, \Phi(x - x')\, \widehat{\psi}_t(x', v') \right] \right\rangle \\ + F^{(e)}(x) \underbrace{\langle \widehat{\rho}_t(x) \rangle}_{= \rho_t(x)} - D \frac{\partial}{\partial x} \underbrace{\langle \widehat{\rho}_t(x) \rangle}_{= \rho_t(x)}\,.$$

With

$$\begin{aligned}\frac{d}{dt}\rho_t(x) &= \int_{-1}^{1} dv\, \frac{d}{dt}\left\langle \widehat{\psi}_t(x,v)\right\rangle \\ &= -\underbrace{\left\langle \int_{-1}^{1} dv\, \frac{\partial}{\partial v}\widehat{J}_v(x,v,t)\right\rangle}_{=0\text{ , because of (II.67)}} - \frac{\partial}{\partial x}J_\rho(x,t)\end{aligned}$$

equation (II.68) is recovered.

A.10 Active Ornstein-Uhlenbeck process: Time evolution of the fluctuating distribution function

The derivation of the time evolution of the fluctuating distribution function in (II.65) follows the same procedure as in A.7 and A.8. The test function $R(x,v)$ is defined, such that $R(x_i(t),v_i(t)) = \int dx \int dv\, \boldsymbol{\delta}(x-x_i(t))\boldsymbol{\delta}(v-v_i(t))R(x,v)$. This gives

$$\frac{d}{dt}R(x_i(t),v_i(t)) = \int dx\, dv\, R(x,v)\, \frac{d}{dt}\left[\boldsymbol{\delta}(x-x_i(t))\boldsymbol{\delta}(v-v_i(t))\right]\,. \tag{A.13}$$

By writing (II.70) as

$$\begin{aligned} v_i(t+dt) &= v_i(t) - dt\,\alpha v_i(t) + d\widehat{\omega}_i(t)\,, \text{ with} \\ \langle d\widehat{\omega}_i(t)\rangle &= 0\,,\ \langle d\widehat{\omega}_i(t)^2\rangle = 2D_a dt\,,\end{aligned}$$

and (II.71) as

$$\begin{aligned} x_i(t+dt) &= x_i(t) + dt\, v_0 v_i(t) + dt\, F_i(\mathbf{x}(t)) + d\omega_i(t)\,, \text{ with} \\ \langle d\omega_i(t)\rangle &= 0\,,\ \langle d\omega_i(t)^2\rangle = 2D_t dt\,,\end{aligned}$$

it follows after Taylor expanding and taking the $dt\to 0$ limit,

$$\begin{aligned}\frac{d}{dt}R(x_i(t),v_i(t)) =& \left[\xi_i(t) + v_0 v_i(t) + F_i(\mathbf{x}(t))\right]\frac{\partial R(x_i(t),v_i(t))}{\partial x_i} \\ &+ \left[\eta_i(t) - \alpha v_i(t)\right]\frac{\partial R(x_i(t),v_i(t))}{\partial v_i} \\ &+ D_t\frac{\partial^2 R(x_i(t),v_i(t))}{\partial x_i^2} + D_a\frac{\partial^2 R(x_i(t),v_i(t))}{\partial v_i^2},\end{aligned}$$

where $\frac{d\omega(t)}{dt} = \xi_i(t)$, $\frac{d\widehat{\omega}_i(t)}{dt} = \eta_i(t)$ and $\lim_{t\to 0}\frac{d\omega(t)^2}{dt} = 2D_t$, $\lim_{t\to 0}\frac{d\widehat{\omega}_i(t)^2}{dt} = 2D_a$ were used, following the Itō convention. The equation can be recast as

$$\begin{aligned}&\frac{d}{dt}R(x_i(t),v_i(t)) = \int dx\, dv\, \boldsymbol{\delta}(x-x_i(t))\boldsymbol{\delta}(v-v_i(t)) \\ &\Big\{\left[\xi_i(t) + v_0 v + F_i(\mathbf{x}'(t))\right]\frac{\partial R(x,v)}{\partial x} + \left[\eta_i(t) - \alpha v\right]\frac{\partial R(x,v)}{\partial v} \\ &+ D_t\frac{\partial^2 R(x,v)}{\partial x^2} + D_a\frac{\partial^2 R(x,v)}{\partial v^2}\Big\},\end{aligned}$$

where $\mathbf{x}'(t)$ denotes the set of particle positions x_j with the i^{th} position $x_i = x$. Integrating by parts leads to

$$\begin{aligned}
&\frac{d}{dt}R(x_i(t),v_i(t)) = \int dx\,dv\,R(x,v)\\
&\Big\{ -\frac{\partial}{\partial x}\Big[\boldsymbol{\delta}(x-x_i(t))\boldsymbol{\delta}(v-v_i(t))\Big(\xi_i(t)+v_0 v+F_i(\mathbf{x}'(t))\Big)\Big]\\
&-\frac{\partial}{\partial v}\Big[\boldsymbol{\delta}(x-x_i(t))\boldsymbol{\delta}(v-v_i(t))\Big(\eta_i(t)-\alpha v\Big)\Big]\\
&+D_t\frac{\partial^2}{\partial x^2}\Big[\boldsymbol{\delta}(x-x_i(t))\boldsymbol{\delta}(v-v_i(t))\Big]+D_a\frac{\partial^2}{\partial v^2}\Big[\boldsymbol{\delta}(x-x_i(t))\boldsymbol{\delta}(v-v_i(t))\Big]\Big\}\,.
\end{aligned}$$

Comparing this with (A.13) and using the definition $\widehat{\rho}_i(x,v,t) = \boldsymbol{\delta}(x-x_i(t))\boldsymbol{\delta}(v-v_i(t))$, it must follow that

$$\begin{aligned}
\frac{d}{dt}\widehat{\rho}_i(x,v,t) = &-\frac{\partial}{\partial x}\left\{\widehat{\rho}_i(x,v,t)\left[\xi_i(t)+v_0 v+F_i(\mathbf{x}'(t))\right]\right\}-\frac{\partial}{\partial v}\left\{\widehat{\rho}_i(x,v,t)\big[\eta_i(t)-\alpha v\big]\right\}\\
&+D_t\frac{\partial^2}{\partial x^2}\widehat{\rho}_i(x,v,t)+D_a\frac{\partial^2}{\partial v^2}\widehat{\rho}_i(x,v,t)\,.
\end{aligned}$$

As $\widehat{\psi}_t(x,v) = \sum_i \widehat{\rho}_i(x,v,t)$, summing over all i in the above equation leads to the time evolution of the fluctuating distribution function in (II.72).

A.11 Active Ornstein-Uhlenbeck process: Time evolution of the average velocity $m_t(x)$

From the definition of $m_t(x)$ in (II.76) it follows for the ensemble averaged time evolution

$$\frac{d}{dt}m_t(x) = \int dv\,v\frac{d}{dt}\left\langle\hat{\psi}_t(x,v)\right\rangle\,.$$

With (II.75) it follows (Itō convention used)

$$\begin{aligned}\frac{d}{dt}m_t(x) =& -\int dv\, v\frac{\partial}{\partial v}\left[\sqrt{2D_a\left\langle\widehat{\psi}_t(x,v)\right\rangle}\underbrace{\langle\widehat{\eta}(x,v,t)\rangle}_{=0}\right] + \alpha\int dv\, v\frac{\partial}{\partial v}\left[\, v\,\left\langle\widehat{\psi}_t(x,v)\right\rangle\right]\\ &+ D_a\int dv\, v\frac{\partial^2}{\partial v^2}\left\langle\widehat{\psi}_t(x,v)\right\rangle - \int dv\, v\frac{\partial}{\partial x}\left[\sqrt{2D_t\left\langle\widehat{\psi}_t(x,v)\right\rangle}\underbrace{\langle\widehat{\xi}(x,v,t)\rangle}_{=0}\right]\\ &- v_0\frac{\partial}{\partial x}\Big[\underbrace{\int dv\, v^2\langle\widehat{\psi}_t(x,v)\rangle}_{=Q_t(x)}\Big] - \frac{\partial}{\partial x}\Big[F^{(e)}(x)\underbrace{\int dv\, v\,\langle\widehat{\psi}_t(x,v)\rangle}_{=m_t(x)}\Big]\\ &- \frac{\partial}{\partial x}\Big[\int dx' F(x-x')\Big\langle\widehat{\rho}_t(x')\underbrace{\int dv\, v\,\widehat{\psi}_t(x,v)}_{=\widehat{m}_t(x)}\Big\rangle\Big] + D_t\frac{\partial^2}{\partial x^2}\Big[\underbrace{\int dv\, v\langle\widehat{\psi}_t(x,v)\rangle}_{=m_t(x)}\Big]\\ =&\alpha\int dv\, v\frac{\partial}{\partial v}\Big[v\,\langle\widehat{\psi}_t(x,v)\rangle\Big] + D_a\int dv\, v\frac{\partial^2}{\partial v^2}\langle\widehat{\psi}_t(x,v)\rangle - v_0\frac{\partial}{\partial x}Q_t(x)\\ &- \frac{\partial}{\partial x}\Big[F^{(e)}(x)\,m_t(x)\Big] - \frac{\partial}{\partial x}\Big[\int dx' F(x-x')\langle\widehat{\rho}_t(x')\widehat{m}_t(x)\rangle\Big] + D_t\frac{\partial^2}{\partial x^2}m_t(x)\,.\end{aligned}$$

Integration by parts leads to

$$\int_{-\infty}^{\infty} dv\, v\frac{\partial}{\partial v}\, v\,\langle\widehat{\psi}_t(x,v)\rangle = \underbrace{\int_{-\infty}^{\infty} dv\frac{\partial}{\partial v}\, v^2\,\langle\widehat{\psi}_t(x,v)\rangle}_{=0\,,\text{ as } v \text{ is confined}} - \int_{-\infty}^{\infty} dv\, v\,\langle\widehat{\psi}_t(x,v)\rangle = -m_t(x)$$

and

$$\int dv\, v\frac{\partial^2}{\partial v^2}\langle\widehat{\psi}_t(x,v)\rangle = \underbrace{\int dv\frac{\partial}{\partial v}\Big[v\frac{\partial}{\partial v}\langle\widehat{\psi}_t(x,v)\rangle\Big]}_{=0} - \underbrace{\int dv\frac{\partial}{\partial v}\langle\widehat{\psi}_t(x,v)\rangle}_{=0} = 0\,.$$

This leads to the expression in (II.79).

A.12 Active Ornstein-Uhlenbeck process: recasting pressure

Solving (II.78) after $F^{(e)}(x)\rho(x)$ and substituting this in (II.81) leads to

$$\begin{aligned}P &= \int_\Lambda^\infty dx\Big\{v_0 m(x) - D_t\frac{\partial}{\partial x}\rho(x) + I_1(x)\Big\}\\ &= v_0\int_\Lambda^\infty dx\, m(x) + D_t\bar{\rho} + \int_\Lambda^\infty dx\, I_1(x)\,,\end{aligned}$$

with $\bar{\rho} = \rho(\Lambda)$ being the bulk density. The first term can be recast by using the expression for $m(x)$ in (II.80)

$$\begin{aligned}\int_\Lambda^\infty dx\, m(x) =& -\frac{v_0}{\alpha}\int_\Lambda^\infty dx \frac{\partial}{\partial x} Q(x) - \frac{1}{\alpha}\int_\Lambda^\infty dx \frac{\partial}{\partial x}\left[F^{(e)}(x) m(x)\right] \\ &+ \frac{1}{\alpha} D_t \int_\Lambda^\infty dx \frac{\partial^2}{\partial x^2} m(x) - \frac{1}{\alpha}\int_\Lambda^\infty dx \frac{\partial}{\partial x} I_2(x) \\ =& \frac{v_0}{\alpha} Q_t(\Lambda) + \frac{1}{\alpha} F^{(e)}(\Lambda) m(\Lambda) - \frac{1}{\alpha} D_t \frac{\partial}{\partial x} m(x)\Big|_{x=\Lambda} + \frac{1}{\alpha} I_2(\Lambda)\,,\end{aligned}$$

thus

$$\begin{aligned}P =& \frac{v_0}{\alpha}[v_0\, Q(\Lambda) + I_2(\Lambda)] + D_t\, \rho(\Lambda) + \int_\Lambda^\infty dx\, I_1(x) \\ &+ \frac{v_0}{\alpha} F^{(e)}(\Lambda)\, m(\Lambda) - \frac{v_0}{\alpha} D_t \frac{\partial}{\partial x} m(x)\Big|_{x=\Lambda}\,.\end{aligned}$$

The quantity $m(x)$ is the average velocity of particles at position x. This can be seen by writing the expression explicitly

$$\begin{aligned}m(x) &= \left\langle \int dv\, v \sum_{i=1}^N \boldsymbol{\delta}(x - x_i(t))\boldsymbol{\delta}(v - v_i(t)) \right\rangle \\ &= \int dv\, v P(x, v)\,,\end{aligned}$$

where $P(x, v)$ is the probability of finding a particle at position x with velocity v. Assuming that in the steady state $m(\Lambda) = 0$ and $\frac{\partial}{\partial x} m(x)\Big|_{x=\Lambda} = 0$ leads to the expression (II.82).

Starting with the steady-state expression (II.80), the assumption $m(\Lambda) = 0$ requires

$$0 = \frac{\partial}{\partial x} v_0 Q(x)\big|_{x=\Lambda} + \frac{\partial}{\partial x} I_2(x)\big|_{x=\Lambda}\,,$$

which is valid, if

$$v_0 Q(x) + I_2(x) = \text{constant}\,, \quad \forall\, x \text{ in the bulk}\,.$$

A.13 Active Ornstein-Uhlenbeck process: $Q(\Lambda)$

The expression for pressure in (II.82) contains the second moment $Q(\Lambda)$, which is defined as

$$Q(\Lambda) = \int_{-\infty}^\infty dv\, v^2 \underbrace{\left\langle \sum_{i=1}^N \boldsymbol{\delta}(\Lambda - x_i(t))\boldsymbol{\delta}(v - v_i(t)) \right\rangle}_{P(\Lambda, v)}\,.$$

With the assumption $P(\Lambda, v) \simeq \rho(\Lambda) P(v)$ for any point in the bulk Λ, it follows

$$\begin{aligned}Q(\Lambda) &\simeq \rho(\Lambda) \int_{-\infty}^\infty dv\, v^2 P(v) \\ &= \rho(\Lambda) \left\langle v^2 \right\rangle\,.\end{aligned}$$

With the solution of the Langevin equation (II.70) for v

$$v(t) = \int_{-\infty}^{t} ds\, e^{-\alpha(t-s)}\, \eta(s)\,,$$

it follows

$$\begin{aligned}\langle v(t)^2 \rangle &= \int_{-\infty}^{t} ds_1\, ds_2\, e^{-\alpha(t-s_1)} e^{-\alpha(t-s_2)} \underbrace{\langle \eta(s_1)\eta(s_2)\rangle}_{2D_a\boldsymbol{\delta}(s_1-s_2)} \\ &= \int_{-\infty}^{t} ds_1\, e^{-2\alpha(t-s_1)} \int_{-\infty}^{t} ds_2\, 2D_a\boldsymbol{\delta}(s_1-s_2) \\ &= \frac{D_a}{\alpha}\,,\end{aligned}$$

which then leads directly to the expression in (II.83).

A.14 Runtime information

Fig. II.12 MIPS in two dimensions.	$N = 10976$, $\delta = 0.7$, $n = 6$, Snapshots after $1.1 \cdot 10^7$ Monte Carlo sweeps
Fig. II.13 MIPS as result of kinetic arrest.	$N = 43904$, $\delta = 0.7$, $n = 6$, $\lambda = 214$, Snapshots after $1.2 \cdot 10^7$ Monte Carlo sweeps
Fig. II.14 Local-density histogram for MIPS.	$N = 10976$, $\delta = 0.7$, $n = 6$, warm-up time: 10^7 Monte Carlo sweeps, average over 100 configuration recorded in time intervals of $3 \cdot 10^4$ Monte Carlo sweeps
Fig. II.15 Finite-size scaling of local-density histograms.	$N = 43904, 10976, 2744$, $\delta = 0.7$, $n = 6$, warm-up time: $1.2 \cdot 10^7$, $2.2 \cdot 10^7$, $1.4 \cdot 10^7$ Monte Carlo Sweeps average over 400, 500, 500 configurations recorded in time intervals of $1.09 \cdot 10^4$, $8.4 \cdot 10^3$, $1.4 \cdot 10^4$ Monte Carlo Sweeps
Fig. II.16 U-shaped boundary of MIPS.	$N = 10976$, $\delta = 0.7$, $n = 6$, warm-up time: 10^7 Monte Carlo sweeps, average over 100 configuration recorded in time intervals of $3 \cdot 10^4$ Monte Carlo sweeps
Fig. II.18 MIPS as liquid-gas coexistence.	$N = 10976$, $\delta = 0.7$, $n = 6$, Snapshots after $1.1 \cdot 10^7$ Monte Carlo sweeps
Fig. II.19 Two-step melting at small persistence lengths.	$N = 43904$, $\delta = 0.1$, $n = 6$, warm-up time: at least 5.5×10^6 Monte Carlo sweeps, average over 200 configurations recorded in time intervals of 2.7×10^4 Monte Carlo sweeps
Fig. II.21 Activity-induced two-step melting.	$N = 43904$, $\delta = 0.1$, $n = 6$, warm-up time: 1.1×10^7 Monte Carlo sweeps, average over 200 configurations recorded in time intervals of 2.7×10^4 Monte Carlo sweeps
Fig. II.22 Short-time averages.	$N = 43904$, $\delta = 0.1$, $n = 6$, warm-up time: 1.1×10^7 Monte Carlo sweeps, each average contains 20 configurations recorded in time intervals of 2.7×10^4 Monte Carlo sweeps
Fig. II.23 Activity-induced two-step melting far from equilibrium.	$N = 43904$, $\delta = 0.1$, $n = 6$, warm-up time: 8.2×10^6 Monte Carlo sweeps, average over 200 configurations recorded in time intervals of 2.7×10^4 Monte Carlo sweeps

Table A.1: **Runtime information.**

A.15 Publication 1: Thermodynamic phases in two-dimensional active matter

Published in Nature Communications: Juliane U. Klamser, Sebastian C. Kapfer, and Werner Krauth, *Thermodynamic phases in two-dimensional active matter*, Nature Communications **9**, 5045 (2018).

arXiv:1802.10021v1 [cond-mat.stat-mech] 27 Feb 2018

Thermodynamic phases in two-dimensional active matter

Juliane U. Klamser[1,4], Sebastian C. Kapfer[2] & Werner Krauth[1,3,4]

[1]*Laboratoire de Physique Statistique, Département de physique de l'ENS, Ecole Normale Supérieure, PSL Research University, Université Paris Diderot, Sorbonne Paris Cité, Sorbonne Universités, UPMC Univ. Paris 06, CNRS, 75005 Paris, France*

[2]*Theoretische Physik 1, FAU Erlangen-Nürnberg, Staudtstr. 7, 91058 Erlangen, Germany*

[3]*Department of Physics, Graduate School of Science, The University of Tokyo, 7-3-1 Hongo, Bunkyo, Tokyo, Japan*

[4]*Max-Planck-Institut für Physik komplexer Systeme, Nöthnitzer Str. 38, 01187 Dresden, Germany*

Active matter has been intensely studied for its wealth of intriguing properties such as collective motion[1], motility-induced phase separation (MIPS)[2], and giant fluctuations away from criticality[3]. However, the precise connection of active materials with their equilibrium counterparts has remained unclear. For two-dimensional (2D) systems, this is also because the experimental[4–6] and theoretical[7–10] understanding of the liquid, hexatic, and solid equilibrium phases and their phase transitions is very recent. Here, we use self-propelled particles with inverse-power-law repulsions (but without alignment interactions) as a minimal model for 2D active materials. A kinetic Monte Carlo (MC) algorithm allows us to map out the complete quantitative phase diagram. We demonstrate that the active system preserves all equilibrium phases, and that phase transitions are shifted to higher densities as a function of activity. The two-step melting scenario is maintained. At high activity, a critical point

Version of Friday 1st March, 2019, 11:50

opens up a gas–liquid MIPS region. We expect that the independent appearance of two-step melting and of MIPS is generic for a large class of two-dimensional active systems.

The kinetic discrete-step MC dynamics for active matter progresses through individual particle displacements which are accepted or rejected with the standard Metropolis criterion. The proposed displacements of a single particle are correlated in time, leading to ballistic local motion characterised by a persistence length λ that measures the degree of activity (see Fig. 1). Correlations decay exponentially, so that the long-time dynamics remains diffusive. Detailed balance is satisfied only for vanishing activities, that is, in the limit $\lambda \to 0$. Cooperative effects are introduced through a repulsive inverse-power-law pair potential (a $1/r^6$ potential is used). The Metropolis rejections are without incidence on the sequence of proposed moves, which are also uncorrelated between particles so that the active many-particle system is without alignment interactions.

We observe at all densities and activities a nonequilibrium steady state in which spatial correlation functions are well-defined. At vanishing activity λ, we recover the equilibrium phase diagram (see Fig. 2). In particular we observe the exponential decay of positional and orientational correlation functions in the liquid, the power-law decay of orientational correlations yet exponential decay of positional correlations in the hexatic phase, and long-range orientational correlations together with positional power-law decay in the solid. The $1/r^6$ system is particularly amenable to simulation because of its "soft" hexatic phase, characterised by small positional correlation lengths[10]. Soft hexatics have much shorter MC correlation times and reach the thermodynamic limit for smaller system sizes than the hard-disk-like hexatics[9] (that correspond to a $1/r^n$ interac-

tion with $n \to \infty$).

In 2D equilibrium systems, a true crystal with Bragg peaks and long-range positional order exists only in the $\phi \to \infty$ limit, as a consequence of the Mermin–Wagner theorem[12]. We find that the solid phase of the active system also exhibits algebraic positional order, just as in equilibrium. Decreasing the density or, remarkably, increasing the activity weakens positional correlations and eventually melts the solid (see Fig. 2a). Close to the melting transition, the algebraic decay of the positional correlations can be clearly observed in our simulation data (points A and B in Fig. 2b). Together with the long-range orientational order, this explicitly identifies the solid phase (Fig. 2c).

The hexatic phase in equilibrium is characterised through a lower degree of order than the solid, namely through short-range positional correlations (no order) and algebraic orientational correlations (quasi-long-range order). We find precisely such a phase in the active system, in a narrow strip of densities below and activities above the solid phase (see Fig. 2a). Starting from the solid, we indeed observe positional correlations that change qualitatively upon a minute increase in activity while leaving the orientational correlations almost unchanged, leading to hexatic order (from point B to point C in Fig. 2b). Positional correlations in the hexatic decay exponentially beyond the correlation length but the orientational correlations remain quasi-long-ranged (points C through E in Fig. 2c and d). On moving towards the liquid at any point within the hexatic phase, the positional correlation lengths decrease, resulting in a strikingly soft hexatic close to the liquid–hexatic transition (point E in Fig. 2b-d). This soft hexatic maintains orientational quasi-order with extremely short-ranged positional correlations, even at densities for which the equilibrium

system is already deep inside the solid phase. Increasing the activity thus shifts the equilibrium phase boundaries towards higher densities. The stability of the partially ordered hexatic phase is remarkable especially as it takes place for persistence lengths λ significantly larger than the interparticle distance $d = (\pi N/V)^{-1/2}$. Our massive computations give no indications of a direct transition from the solid into the liquid state, even at the highest accessed densities.

MIPS[2] has been frequently reported in 2D active systems but agreement on its interpretation was not reached. Recent work in an active dumbbell system proposes that MIPS continuously extends from the equilibrium liquid–hexatic transition region and that one of the separated phases preserves some degree of order[13]. This is not the case in our system: We observe MIPS as a U-shaped region of liquid–gas coexistence (see Fig. 3a) with an onset at high activity and at relatively low density. Both competing phases in the phase separated state feature exponential decay of orientational and positional correlation functions (see the color-coded configuration snapshots in Fig. 3a). MIPS is thus clearly separated from melting (see Fig. 2a). In a MC simulation, a coarsening process generally precedes macroscopic phase separation in the time evolution towards the steady state. In the active $1/r^6$ system, the transient coarsening leading up to MIPS can be expected to be overcome at earlier times than for hard disks. This makes it easier to distinguish it from the formation of a steady-state gel[11], although we do not expect the nature of the coexisting phases participating in MIPS to depend on the softness of the potential.

The analogy with the liquid–gas coexistence in equilibrium simple fluids suggests the interpretation of the onset of MIPS as a critical point. Indeed, below the onset, the system remains

homogeneous at large length scales with a single-peaked local density distribution (see point H in Fig. 3b). Above the onset of MIPS, the local densities develop a bimodal distribution. The peak positions separate further as λ increases, quantifying the above-mentioned U-shape. Moreover, at a given λ, the peak local densities in the coexistence region are independent of the global density ϕ (see Fig. 3c). This is further substantiated by a finite-size scaling analysis at constant λ (see Fig. 4). The phenomenology thus agrees with that of an equilibrium phase coexistence where the relative proportions of the liquid and gas adapt to the global density, but where the degree of order of each of the phases and their densities remain unchanged. Inside the coexistence region, at small densities, we observe an approximately circular bubble of liquid inside the gas, followed by a stripe-shaped form that winds around the periodic simulation box, and then followed by a bubble of gas inside the liquid. In finite (N, V, T) equilibrium systems, this complex behaviour is brought about by the interface free energy[14,15] which vanishes at the critical point. A detailed analysis of the homogeneous phases, but also of the phase-separated systems, reveals the origin of the phase separation in the kinetic MC model. In the bulk of the coexisting liquid and gas phases, the directions of motion of the individual particles are uncorrelated beyond a very small length scale (see Fig. 4b). At the liquid–gas interface, however, a majority of the increment vectors point inwards towards the liquid phase. Even though a theoretical framework as reliable as statistical mechanics is currently lacking, the effective cohesion in nonequilibrium is often attributed to the so-called swim pressure due to active motion[16–18].

We thus find that two-step melting and MIPS are kept separated by the homogeneous liquid phase, which is both the high-density end of MIPS and the low-density end of the order–disorder

transitions. Intriguingly, the subtle hexatic phase survives at considerable activities. Our massive computations allow us to reach the steady state even for strong activities and for high densities, but only theory will be able to ascertain the stability of the separating liquid phase and of the hexatic state in the $\lambda, \phi \to \infty$ limit. Another open question is how the KTHNY theory of 2D melting[7,19,20], built for equilibrium systems, can be extended to active systems. At the phase transitions, we find the exponents $\simeq 0.33$ and $\simeq 0.25$ predicted by the KTHNY theory for the positional and orientational correlations respectively (e. g. see Fig. 2b and c). This suggests the existence of a coarse-grained functional that plays the role of an equilibrium free energy. More specifically, increased activity appears to reduce a state variable in our system that corresponds to the pressure at equilibrium. This interpretation reconciles both the fact that increased activity induces melting through reduction of the effective pressure, but also that liquid–gas phase coexistence is possible only at high activities, i. e., at low effective pressure, in striking analogy to the behavior of simple fluids in equilibrium. Further work is required to test this hypothesis.

In equilibrium, the nature of the two-step melting phase transitions depends on the softness of the particles, which can be tuned via the exponent n of the inverse-power-law pair potential $U(r) \propto 1/r^n$. The two-step melting scenario for very soft particles ($n \lesssim 6$) comprises two continuous transitions, whereas for harder particles with $n \gtrsim 6$ the liquid–hexatic transition becomes first order[10]. One may speculate that the activity plays a similar role as the hardness of the particles and that at high activities the liquid–hexatic transition becomes first order.

The liquid–gas coexistence phase we observe in kinetic MC is an example of MIPS seen

earlier in active-matter models using Brownian and molecular dynamics simulations[21–25]. As we show, MIPS can be reproduced within kinetic MC dynamics, without added equilibrium-like mixing steps[11]. Indeed, the direction of the individual persistent particle motion suffices to produce the effect: Particles may be kinetically arrested for persistence lengths larger than the mean free path, leading to density inhomogeneities, where particles in dense regions are walled in by particles coming from less dense regions. However, this does not unhinge the coarsening mechanism: The size of the inhomogeneous regions increases with time, and the infinite-time steady state in a finite system is characterized by only two coexisting regions so that, for the studied $1/r^6$ potential, a gel phase is clearly absent. MIPS appears naturally in kinetic MC, and we suggests that it is a generic feature of active matter in 2D and in higher dimensions. Our inverse-power-law interactions provide a tunable set of active-matter models to study phase transitions and phase coexistence.

Methods

Kinetic MC Dynamics for active particles. We use a modified Metropolis algorithm that breaks detailed balance. In each MC step, a displacement by an amount $\boldsymbol{\epsilon}_i$ is proposed for a single randomly chosen particle i. If the displacement were implemented, it would cause a change in the total energy of the system $E \to E'$. The move is accepted with the Metropolis probability $P = \min\left[1, e^{-(E'-E)}\right]$. The total energy is given by $E = \sum_{i<j} U(\boldsymbol{r}_i - \boldsymbol{r}_j)$, where the power–law potential $U(r) = (\gamma/r)^6$ does not introduce an energy scale separate from density. Thus, in equilibrium, the only relevant scale is the dimensionless density $\phi = \gamma^2 N/V$, with the effective temperature in the Metropolis probability scaling as ϕ^3. In nonequilibrium, activity introduces a

new control parameter, expressed in terms of the persistence length λ. Simulations are performed in a $(7 : 4\sqrt{3})$ simulation box with periodic boundary conditions and the soft-sphere potential is truncated as follows: $\tilde{U}(r) = U(\min(r, 1.8\gamma))$.

We introduce activity into the dynamics by choosing the proposed displacement $\boldsymbol{\epsilon}_i'$ of particle i based on the previously proposed displacement $\boldsymbol{\epsilon}_i$ of the same particle. The correlation is introduced in two stages. First, a random vector $\boldsymbol{\eta}$ is sampled from a bivariate normal distribution $\propto \exp[-(\boldsymbol{\eta} - \boldsymbol{\epsilon}_i)^2/2\sigma^2]$, where σ is the standard deviation. In the second stage, $\boldsymbol{\epsilon}_i'$ is generated from $\boldsymbol{\eta}$ using the folding scheme

$$\epsilon_{i,z}' \to \begin{cases} q_{i,z} - \delta & \text{if } q_{i,z} < 2\delta \\ 3\delta - q_{i,z} & \text{if } q_{i,z} \geq 2\delta\,, \end{cases}$$

with $z \in \{\mathrm{x}, \mathrm{y}\}$ and $q_{i,z} = (\eta_z + \delta) \bmod 4\delta$, with $a \bmod b = a - b\left\lfloor \frac{a}{b} \right\rfloor$, i. e., $0 \leq q_{i,z} < 4\delta$, where $\lfloor a \rfloor$ is the floor function. The folding scheme limits the size of the proposed displacements and keeps the dynamics local. The folding scheme is equivalent to a random walk of the displacement variables $\boldsymbol{\epsilon}_i$ in a $[-\delta, \delta]^2$ box with reflecting boundary conditions, see Fig. 1b. Note that the random walk of the displacements is independent of the positions of the particles, as the new increment persists whether the displacement was accepted or not.

The square-shaped displacement box introduces a small degree of anisotropy into the dynamics for $\lambda > 0$. However, we explicitly verify that the resulting steady state is unaffected with respect to the properties concerning this letter. At small densities in the gaseous state, where λ is much smaller than the mean free path, the kinetic MC dynamics effectively reverts to detailed-

balance dynamics as interactions between particles are rare. At higher densities, all large proposed displacements have vanishing Metropolis probabilities, thus leading to effectively isotropic dynamics. In our numerical observation anisotropic effects are undetectable within other sources of noise.

Probability distribution of increments and persistence length. In continuous time, the increment variable $\boldsymbol{\epsilon}$ evolves according to a diffusion equation $\partial_t P(\boldsymbol{\epsilon}, t) = \frac{\sigma^2}{2} \Delta_{\boldsymbol{\epsilon}} P(\boldsymbol{\epsilon}, t)$, with vanishing probability flux through the boundary of the displacement box. The steady-state distribution in the infinite-time limit is the uniform distribution $P = (2\delta)^{-2}$. By a Fourier ansatz, one readily finds that the autocorrelation time τ of increments is dominated by the first harmonic of the displacement box, an that for large t, the autocorrelation function decays as

$$C(t) \equiv \langle \boldsymbol{\epsilon}(t_0 + t) \cdot \boldsymbol{\epsilon}(t_0) \rangle \propto \mathrm{e}^{-t/\tau} \,, \text{ where } \tau = \frac{8\delta^2}{\pi^2 \sigma^2} \,. \tag{1}$$

The position of a free particle evolves as $\boldsymbol{r}(t) \equiv \boldsymbol{r}(t_0) + \int_{t_0}^{t} \mathrm{d}s \, \boldsymbol{\epsilon}(s)$. For times shorter than the autocorrelation time, $t \lesssim \tau$, its mean displacement is essentially given by the increment at time t_0,

$$\langle |\boldsymbol{r}(t) - \boldsymbol{r}(t_0)| \rangle = v \, t + \mathcal{O}(\sqrt{t}), \tag{2}$$

where the drift velocity $v \equiv |\boldsymbol{\epsilon}(t_0)|$ is given by the initial condition of the increment, and the subleading term contains contributions by diffusion of $\boldsymbol{\epsilon}$, including reflections, in the displacement box. Averaging over all initial conditions $\boldsymbol{\epsilon}(t_0)$ with the steady-state uniform distribution, we obtain the mean drift velocity

$$\overline{v} = \frac{\delta}{3} \left[\sqrt{2} + \sinh^{-1}(1) \right] \,.$$

Considering Eqs. (1) and (2), we may identify the persistence length $\lambda \equiv \tau\, \overline{v} \simeq 0.62\delta^3\sigma^{-2}$. The persistence length λ offers a length scale which separates ballistic from diffusive motion. The persistence length defined in this way allows to collapse data for the increment autocorrelations $C(\langle r\rangle = \lambda x) \propto \mathrm{e}^{-(x+c_1x^2+c_2x^3)}$ at widely different activities (see Fig. 1a). The prefactors of the superexponential terms $c_1,\ c_2$ are obtained from a numerical fit.

Measurements. The orientational order is quantified by the correlation function $g_6(r) \propto \langle \sum_{i,j}^{N} \psi_6(\boldsymbol{r}_i)\psi_6(\boldsymbol{r}_j)\delta(r-r_{ij})\rangle$ of the bond-orientational order parameter $\psi_6(\boldsymbol{r}_i)$ calculated with Voronoi weights[26]. $g_6(r)$ is a measure of the correlation of the local sixfold orientational order at distance r. Positional order is studied with the direction-dependent pair correlation function $g(x,y)$. Before averaging this two-dimensional histogram over configurations, each configuration is realigned[9] such that the Δx axis points in the direction of the global orientation parameter $\Psi_6 = \sum_i^N \psi_6(\boldsymbol{r}_i)$. Correlation functions in Fig. 2 are ensemble-averaged over 100 configurations of $\sim 4.4\times10^4$ particles, recorded after a warm-up time of 5×10^6 MC sweeps , with each sweep containing N MC steps. Configurations were recorded in time intervals of 2.7×10^4 MC sweeps.

MIPS is quantified by histograms of local densities. We compute local densities by covering the system with randomly placed test circles of radius 7.5γ. The local dimensionless density of each test circle is $\phi_{\mathrm{loc}} = \gamma^2 N_{\mathrm{loc}}/V_{\mathrm{loc}}$, where N_{loc} are the number of particle centres located within a circle of area V_{loc}. The detailed analysis (see Figs. 3, 4) of MIPS uses $\delta = 0.7\gamma$. The larger δ shifts the liquid–gas coexistence phase boundaries, in particular the critical point, to smaller densities and persistence lengths, which drastically shortens the time to reach the steady state. Configuration snapshots in Fig. 3a were taken after 1.1×10^7 MC sweeps. Data in Fig. 3b consists

of ensemble averages over 100 configurations recorded in time intervals of 3×10^4 sweeps. The $N \sim 4.4 \times 10^4$ ($N \sim 1.1 \times 10^4$, $N \sim 2.7 \times 10^3$) data in Figs. 4 was recorded after 5.5×10^6 (2.2×10^7, 1.4×10^7) sweeps. The average consists of 500 configurations recorded in time intervals of 2.2×10^3 (8.7×10^3, 1.7×10^4) sweeps.

References

1. T. Vicsek, A. Czirók, E. Ben-Jacob, I. Cohen, O. Shochet, Novel Type of Phase Transition in a System of Self-Driven Particles, *Phys. Rev. Lett* **75** 6 (1995).

2. M. E. Cates, J. Tailleur, Motility-Induced Phase Separation, *Annu. Rev. Condens. Matter Phys.* **6**, 219-244 (2015).

3. S. Dey, D. Das, R. Rajesh, Spatial Structures and Giant Number Fluctuations in Models of Active Matter, *Phys. Rev. Lett* **108**, 238001 (2012).

4. K. Zahn, R. Lenke, and G. Maret, Two-Stage Melting of Paramagnetic Colloidal Crystals in Two Dimensions, *Phys. Rev. Lett.* **82**, 2721 (1999).

5. U. Gasser, C. Eisenmann, G. Maret, and P. Keim, Melting of Crystals in Two Dimensions, *Chem. Phys. Chem.* **11**, 963 (2010).

6. A. L. Thorneywork, J. L. Abbott, D. G. A. L. Aarts, and R. P. A. Dullens, Two-Dimensional Melting of Colloidal Hard Spheres, *Phys. Rev. Lett.* **118**, 158001 (2017).

7. B. I. Halperin and D. R. Nelson, Theory of Two-Dimensional Melting, *Phys. Rev. Lett.* **41**, 121 (1978).

8. S. Z. Lin, B. Zheng, and S. Trimper, Computer simulations of two-dimensional melting with dipole-dipole interactions, *Phys. Rev. E* **73**, 066106 (2006).

9. E. P. Bernard and W. Krauth, Two-Step Melting in Two Dimensions: First-Order Liquid-Hexatic Transition, *Phys. Rev. Lett* **107**, 155704 (2011).

10. S. C. Kapfer and W. Krauth, Two-Dimensional Melting: From Liquid-Hexatic Coexistence to Continuous Transitions, *Phys. Rev. Lett* **114**, 035702 (2015).

11. D. Levis and L. Berthier, Clustering and heterogeneous dynamics in a kinetic Monte Carlo model of self-propelled hard disks, *Phys. Rev. E* **89**, 062301 (2014).

12. N. D. Mermin and H. Wagner, Absence of Ferromagnetism or Antiferromagnetism in One- or Two-Dimensional Isotropic Heisenberg Models, *Phys. Rev. Lett.* **17**, 1133 (1966).

13. L. F. Cugliandolo, P. Digregorio, G. Gonnella, and A. Suma, Phase Coexistence in Two-Dimensional Passive and Active Dumbbell Systems, *Phys. Rev. Lett.* **119**, 268002 (2017).

14. J. E. Mayer, and Wm. W. Wood, Interfacial Tension Effects in Finite, Periodic, Two-Dimensional Systems, *J. Chem. Phys.* **42**, 4268 (1965).

15. M. Schrader, P. Virnau, and K. Binder, Simulation of vapor-liquid coexistence in finite volumes: A method to compute the surface free energy of droplets, *Phys. Rev. E* **79**, 061104 (2009).

16. S. C. Takatori, W. Yan, and J. F. Brady, Swim Pressure: Stress Generation in Active Matter, *Phys. Rev. Lett* **113**, 028103 (2014).

17. A. P. Solon, J. Stenhammar, R. Wittkowski, M. Kardar, Y. Kafri, M. E. Cates, and J. Tailleur, Pressure and Phase Equilibria in Interacting Active Brownian Spheres, *Phys. Rev. Lett* **114**, 198301 (2015).

18. A. P. Solon, Y. Fily, A. Baskaran, M. E. Cates, Y. Kafri, M. Kardar and J. Tailleur, Pressure is not a state function for generic active fluids, *Nat. Phys.* **11**, 673 (2015).

19. D. R. Nelson and B. I. Halperin, Dislocation-mediated melting in two dimensions, *Phys. Rev. B* **19**, 2457 (1979).

20. A. P. Young, Melting and the vector Coulomb gas in two dimensions, *Phys. Rev. B* **19**, 1855 (1979).

21. M. E. Cates, Diffusive transport without detailed balance in motile bacteria: does microbiology need statistical physics?, *Rep. Prog. Phys.* **75** 042601 (2012).

22. G. S. Redner, M. F. Hagan, A. Baskaran, Structure and Dynamics of a Phase-Separating Active Colloidal Fluid, *Phys. Rev. Lett* **110**, 055701 (2013).

23. Y. Fily, M. C. Marchetti, Athermal Phase Separation of Self-Propelled Particles with No Alignment, *Phys. Rev. Lett* **108**, 235702 (2012).

24. T. Speck, J. Bialké, A. M. Menzel, H. Löwen, Effective Cahn-Hilliard Equation for the Phase Separation of Active Brownian Particles, *Phys. Rev. Lett* **112**, 218304 (2014).

25. J. Bialké, T. Speck, H. Löwen, Crystallization in a Dense Suspension of Self-Propelled Particles, *Phys. Rev. Lett* **108**, 168301 (2012).

26. W. Mickel, S. C. Kapfer, G. E. Schröder-Turk, and K. Mecke, Shortcomings of the bond orientational order parameters for the analysis of disordered particulate matter, *J. Chem. Phys.* **138**, 044501 (2013).

Acknowledgements We thank Hughes Chaté and Hartmut Löwen for helpful discussions. W.K. acknowledges support from the Alexander von Humboldt Foundation.

Email addresses: juliane_klamser@yahoo.de, sebastian.kapfer@fau.de, werner.krauth@ens.fr.

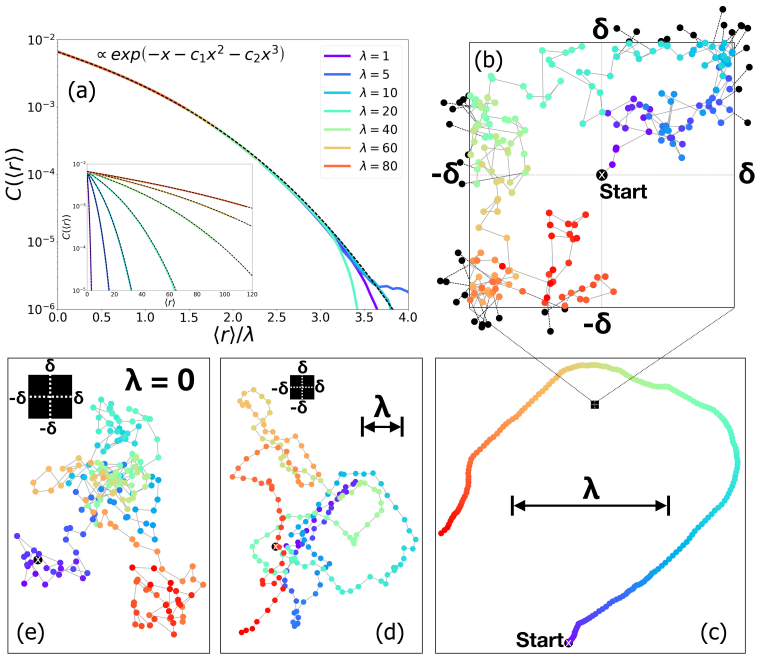


Figure 1: **Kinetic MC algorithm. (a):** Autocorrelation of proposed displacements as a function of the covered distance for a single 2D active particle. The data collapse for widely different activities allows the definition of a persistence length λ (see Methods) (See inset for raw data without rescaling). **(b):** Time evolution of proposed displacements in a box of size $[-\delta, \delta]^2$. The displacement $\boldsymbol{\epsilon}(t)$ is sampled from a bivariate normal distribution with standard deviation σ (here $\sigma \ll \delta$), centred at the previous displacement $\boldsymbol{\epsilon}(t-1)$. Positions sampled outside the box (black points) are folded back, implementing the reflecting boundary condition (see Methods). **(c):** Trajectory for a single particle $\boldsymbol{r}(t) = \sum_{k=1}^{t} \boldsymbol{\epsilon}(k)$, with the corresponding history of displacements from (b). The color gradient changing with time allows to connect (b) and (c), e. g. the last displacements in (b) are in the third quadrant thus the particle in (c) moves to the lower left etc. **(c), (d) and (e):** Sampled trajectories, illustrating the transition from a passive random walk ($\sigma \gg \delta$ in (e)) to a persistent random walk ($\sigma \ll \delta$ in (c)).

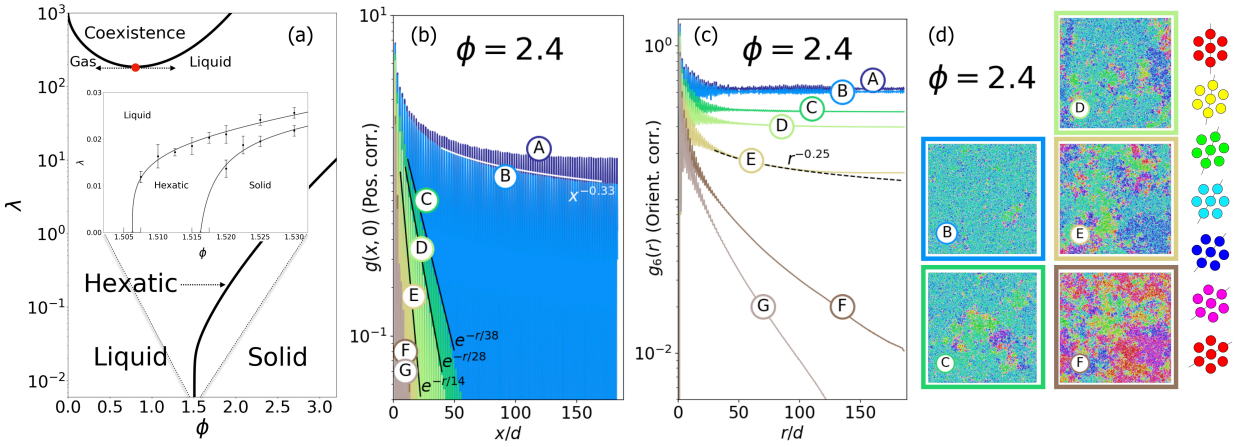


Figure 2: **Complete phase diagram and two-step melting**. Depicted results are for $N \sim 4.4 \times 10^4$ particles and $\delta = 0.1\gamma$, with γ the particle diameter (see Methods). **(a):** Activity λ vs. density ϕ phase diagram. MIPS between a liquid and a gas, at high λ, is situated far above the solid–hexatic-melting lines. The red dot indicates a possible critical point. Inset in (a): Two-step melting for small λ with shift of transition densities to higher values with increasing λ, preserving the equilibrium phases. Two-step melting from the solid is induced by density reduction (as in equilibrium) but also by an increase in λ. **(b), (c), and (d):** Activity-induced two-step melting high above the equilibrium melting densities ($\phi = 2.4$, A: $\lambda = 0.991\gamma$; B: $\lambda = 1.006\gamma$; C: $\lambda = 1.022\gamma$; D: $\lambda = 1.033\gamma$; E: $\lambda = 1.049\gamma$; F: $\lambda = 1.064\gamma$; G: $\lambda = 1.079\gamma$). **(b):** Positional correlation function $g(x, y)$ along the x axis, in units of the interparticle distance d. **(c):** Orientational correlation function $g_6(r)$ along the x axis. **(d):** Snapshots of configurations, particles colour-coded with their local orientation parameter ψ_6. A and B are quasi-long-ranged in $g(x, 0)$ and long-ranged in g_6, thus corresponding to the solid phase. C, D, and E are short-ranged in $g(x, 0)$ and quasi-long-ranged in g_6, thus corresponding to the hexatic phase. F and G decay exponentially in both correlation functions and thus correspond to a liquid.

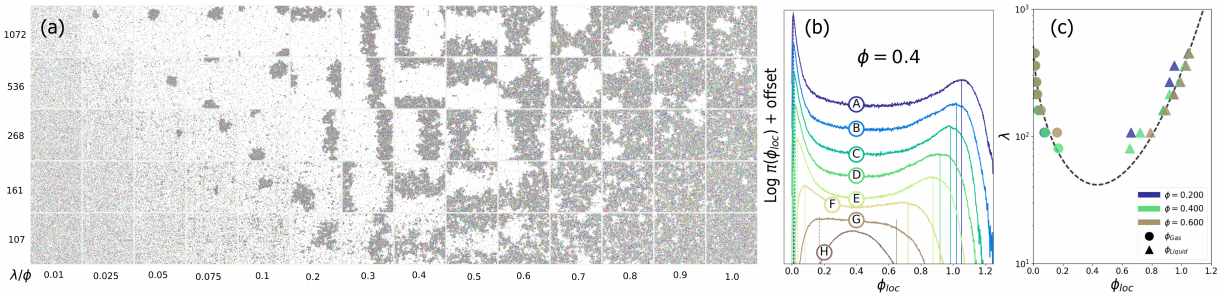


Figure 3: **Characterisation of MIPS**. Data for $N \approx 1.1 \times 10^4$, $\delta = 0.7\gamma$. **(a):** Snapshots of configurations close to the onset of liquid–gas coexistence. (Particles represented in arbitrary size and colour-coded, as in Fig. 2d, according to their local orientation parameter.) U-shaped phase boundary is apparent. Orientational order is short-ranged in both liquid and gas phase. At constant activity λ, the liquid volume fraction grows with increasing density until the liquid entirely fills the system. The location of the critical point depends on δ and it appears at a smaller density and λ than in Fig. 2. **(b):** Histograms of local densities (see Methods for definition) for a variation of activities at constant $\phi = 0.4$ (A: $\lambda = 450\gamma$; B: $\lambda = 359\gamma$; C: $\lambda = 268\gamma$; D: $\lambda = 214\gamma$; E: $\lambda = 161\gamma$; F:$\lambda = 107\gamma$; G: $\lambda = 80\gamma$; H: $\lambda = 54\gamma$; For better presentation, histograms are shifted along the y-axis with increasing λ). Transition from a single-peaked to a double-peaked distribution and increasing separation of peaks with increasing λ. **(c):** Densities of liquid and gas (identified through peak position as in (b)) in an activity λ *vs.* local density $\phi_{\rm loc}$ diagram. This demonstrates independence of phase densities on global density for fixed λ and validates the phase-separation picture.

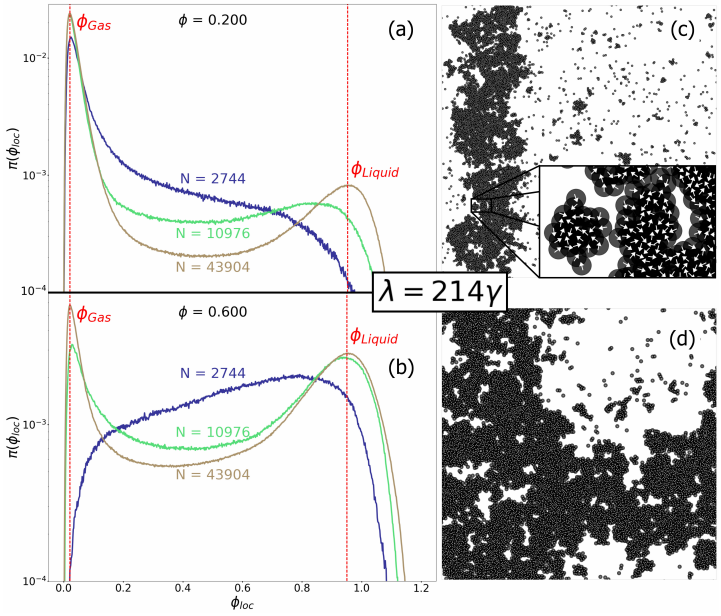


Figure 4: **Finite-size scaling of local density histograms** Data with $\lambda = 214\gamma$ and $\delta = 0.7\gamma$. **(a) and (b):** Local density histograms (see Methods for definitions) for global densities $\phi = 0.2$ and $\phi = 0.6$ (identical x-axis used). Local density peaks sharpen with increasing system size N, and are located at the same value of ϕ_{loc}, demonstrating that in the MIPS region gas and liquid densities are independent of the global density. **(c) and (d):** Snapshots of configurations at global densities corresponding to (a), where the liquid is the minority phase, and (b), where the liquid is the majority phase by volume fraction (cf. height of the peaks in (a) and (b)). **Inset in (c):** Direction of motion of the individual particles indicated by arrows, illustrating the origin of MIPS. The directions of motion are uncorrelated inside the homogeneous liquid and gas. Only particles at the interface move towards the interior of the liquid patch, enclosing particles of the high density region.

A.16 Publication 2: Multiple singularities of the equilibrium free energy in a one-dimensional model of soft rods

Published in Physical Review Letters: Sushant Saryal, Juliane U. Klamser, Tridib Sadhu, and Deepak Dhar, *Multiple Singularities of the Equilibrium Free Energy in a One-Dimensional Model of Soft Rods*, Phys. Rev. Lett. **121**, 240601 (2018).

arXiv:1806.09841v1 [cond-mat.stat-mech] 26 Jun 2018

Multiple singularities of the equilibrium free energy in a one-dimensional model of soft rods

Sushant Saryal,[1] Juliane U. Klamser,[2] Tridib Sadhu,[3,4] and Deepak Dhar[1]

[1] *Indian Institute of Science Research and Education, Pashan, Pune, India.*
[2] *Laboratoire de Physique Statistique, Département de physique de l'ENS, Ecole Normale Supérieure, PSL Research University, Université Paris Diderot, Sorbonne Paris Cité, Sorbonne Universités, UPMC Univ. Paris 06, CNRS, 75005 Paris, France.*
[3] *Tata Institute of Fundamental Research, Mumbai 400005, India.*
[4] *Collège de France, 11 place Marcelin Berthelot, 75231 Paris Cedex 05, France.*

There is a misconception, widely shared amongst physicists, that the equilibrium free energy of a one-dimensional classical model with strictly finite-ranged interactions, and at non-zero temperatures, can not show any singularities as a function of the coupling constants. In this Letter, we discuss an instructive counter-example. We consider thin rigid linear rods of equal length 2ℓ whose centers lie on a one-dimensional lattice, of lattice spacing a. The interaction between rods is a soft-core interaction, having a finite energy U per overlap of rods. We show that the equilibrium free energy per rod $\mathcal{F}(\frac{\ell}{a}, \beta)$, at inverse temperature β, has an infinite number of singularities, as a function of $\frac{\ell}{a}$.

PACS numbers: 05.40.Jc, 02.50.Cw, 87.10.Mn

There is a common belief amongst physicists that in any one-dimensional (1-d) classical system, in thermal equilibrium, having strictly finite-ranged pairwise interactions, the thermodynamic potential cannot show a singular dependence on the control parameters [1]. The origin of this folk wisdom is perhaps an unsubstantiated generalization of a rigorous result due to van Hove [2] on the absence of phase transitions in a one-dimensional system of particles with a non-vanishing hard-core length and finite-ranged inter-particle interaction. This result was later extended to lattice models [3] and long-ranged interactions having a power-law decay with distance [4–6]. The belief further grew out of essentially two (correct) arguments: one, about the absence of phase transitions as a function of temperature in 1-d models having a finite-dimensional irreducible transfer matrix and second, the Landau argument about the absence of symmetry-breaking in 1-d systems, when creating a domain-wall has a finite energy cost [7]. Several counter-examples of equilibrium phase transitions in 1-d models have been known for a long time: DNA unzipping [8, 9], interface depinning [10], and condensation in zero-range models [11]. But, the incorrect belief persists. A necessary and sufficient condition for the existence of phase transitions in 1-d systems is hard to formulate. This question was discussed in some detail recently by Cuesta and Sanchez [12], who provided a sharper criteria for the absence of phase transitions, based on a generalized Perron-Frobenius-Jentzsch theorem. The general understanding is that singularities in the free energy come from the degeneracy of the largest eigenvalue of the transfer matrix which can occur when the conditions required for the Perron-Frobenius-Jentzsch theorem to hold are not met.

In this Letter, we discuss an example of a 1-d system that undergoes an *infinite* number of phase transitions, even though the largest eigenvalue remains non-degenerate. The singularities are robust, geometrical in origin, and come from the changes in the structure of the interaction Hamiltonian as a function of the separation between particles. This is a simple, instructive example, and it uses a different mechanism of generating singularities in the thermodynamic functions than the earlier models studied.

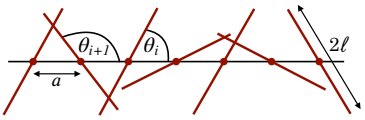


FIG. 1. A configuration of 7 rods on a line. Here, a is the spacing between rods. In the displayed configuration, the number of nearest neighbor overlaps $n_1 = 3$ and the number of next nearest overlaps $n_2 = 1$.

In its simplest version, the model consists of soft linear rigid rods of equal length 2ℓ, whose midpoints are fixed at the lattice sites of a 1-d lattice of lattice spacing a. The rods are free to rotate in the plane, as illustrated in figure 1, where a configuration of N rods is specified by a set of N angles θ_i, with $0 \leq \theta_i \leq \pi$, for $i = 1$ to N. We assume that there is an interaction between the rods, which depends on their overlap. Each overlap between a pair of nearest neighbor rods costs a constant energy U_1; between a pair of next nearest neighbors the overlap energy is U_2, and so on. Let n_r be the number of pairs of the r-th neighbor rods that overlap (see figure 1). Clearly, n_r is zero, if $r > \frac{2\ell}{a}$. The total energy of the

system is

$$\mathcal{H} = \sum_i n_i U_i \,. \tag{1}$$

This is similar to the hard-rod model that has been studied a lot in the literature, starting with Onsager [13–16]. It differs in two significant ways: the centers of the rods are fixed on a lattice, and we allow U_i to be any sign (attractive or repulsive soft-cores). A somewhat similar model of non-spherical molecules whose centers are fixed at equi-spaced points along a line, but orientations can change, was studied in [14].

Let $\mathcal{F}(\frac{\ell}{a} = \kappa, \beta)$ denote the free energy per rod of this system, in equilibrium, at inverse temperature β. We will show that $\mathcal{F}(\kappa, \beta)$ is an analytic function of β, as expected, but has a non-analytic dependence on κ. In fact, there are infinitely many transitions: as κ is varied, $\mathcal{F}(\kappa, \beta)$ is singular at every positive integer values of κ, for all β. The singularities remain unchanged irrespective of the sign of U_i, whether the interaction is repulsive or attractive. We will show that there are also other singularities at some non-integer values of κ. For example, the probability distribution of orientations changes qualitively when κ is changed across $\frac{1}{\sqrt{2}}$.

For simplicity of presentation, we begin with the simple case: $U_1 = \infty$. This is the case of hard-rods, where no nearest-neighbor overlaps are allowed, thus $n_i = 0$ for all $i \geq 1$. Then, without loss of generality, we may assume $U_i = 0$ for all $i \geq 2$, which corresponds to only nearest neighbor hard-core interactions. In this case, let $\mathcal{F}_1(\kappa)$ denote the free energy per site in the thermodynamic limit (due to hard-core interactions β is irrelevant and hence omitted). Then, using the transfer matrix technique, $\mathcal{F}_1(\kappa) = -\log \Lambda(\kappa)$, where $\Lambda(\kappa)$ is the largest eigenvalue of the integral equation

$$\Lambda(\kappa)\psi_\kappa(\theta) = \int_0^\pi \frac{d\theta'}{\pi}\; T_\kappa(\theta, \theta')\psi_\kappa(\theta')\,, \tag{2}$$

with $\psi_\kappa(\theta)$ being the associated eigenvector. The transfer matrix $T_\kappa(\theta', \theta)$ has matrix elements 0 or 1 depending on whether a pair of nearest neighbor rods with angles (θ', θ) overlap or not.

We will show below that this system shows three types of singularities: (i) $\mathcal{F}_1''(\kappa)$ is discontinuous at $\kappa = \frac{1}{2}$, (ii) for κ near 1, say $\kappa = 1+\varepsilon$, with $|\varepsilon| \ll 1$, $\mathcal{F}_1'(\kappa)$ diverges as $\log(|\varepsilon|)$, and (iii) for $\frac{1}{\sqrt{2}} < \kappa < 1$, the probability distribution of orientations $P_\kappa(\theta)$ has square-root singularities as a function of θ, which are not present for lower values of κ.

The numerical verification of these analytical results is shown in figures 2-4, obtained by numerically diagonalizing the transfer matrix, using 1000 grid points for the integartion range of $\theta = [0, \pi]$. In figure 2, $\mathcal{F}'_1(\kappa)$ is exactly zero for $\kappa < \frac{1}{2}$, and nonzero for $\kappa > \frac{1}{2}$, initially increasing linearly. Near $\kappa = 1$, it has a sharp peak. In figure 3, $\mathcal{F}'_1(\kappa)$ shows a nearly linear dependence on $\log|\kappa - 1|$.

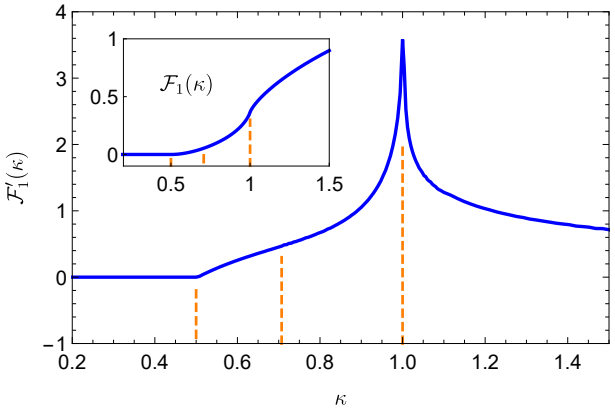


FIG. 2. First derivative of the free energy $\mathcal{F}_1'(\kappa)$ for hard-core nearest neighbor interaction between rods ($U_1 = \infty$). The inset shows the monotonic increase of $\mathcal{F}_1(\kappa)$ as a function of κ.

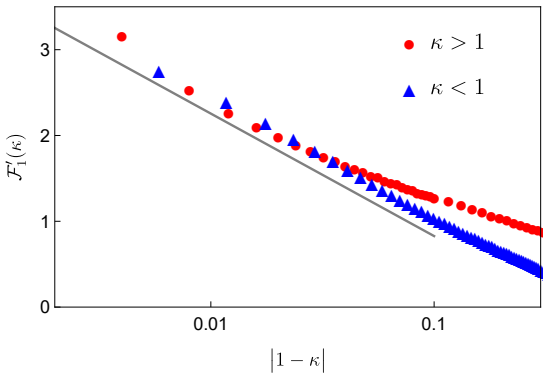


FIG. 3. Logarithmic divergence of the first derivative of the free energy $\mathcal{F}_1'(\kappa)$ near $\kappa = 1$, for $U_1 = \infty$.

We determine the probability distribution of orientations $P_\kappa(\theta)$ from the eigenvector $\psi_\kappa(\theta)$ of the transfer matrix. This is plotted in figure 4. For $\kappa < \frac{1}{2}$, all angles are equally likely, and $P_\kappa(\theta)$ takes a constant value π^{-1}. For $\frac{1}{2} < \kappa < \frac{1}{\sqrt{2}}$, $P_\kappa(\theta)$ has a non-trivial dependence on θ when $|\cos\theta| > \frac{1}{2\kappa}$, but the derivative $P'_\kappa(\theta)$ remains finite. In the range $\frac{1}{\sqrt{2}} < \kappa < 1$, $P_\kappa(\theta)$ has a square-root cusp singularity, when $\sin\theta = \kappa$. There is no clear signature of this singularity in the functional dependence of $\mathcal{F}_1(\kappa)$ on κ.

The source of these singularities is geometric in nature, and can be seen most simply in the structure of the transfer matrix. This is illustrated figure 5. Here the shaded regions in the θ-θ' plane correspond to values of (θ, θ') where the rods intersect, and the matrix element is 0, whereas the plain regions correspond to non-intersecting rods, and the matrix element is 1. The equation of the

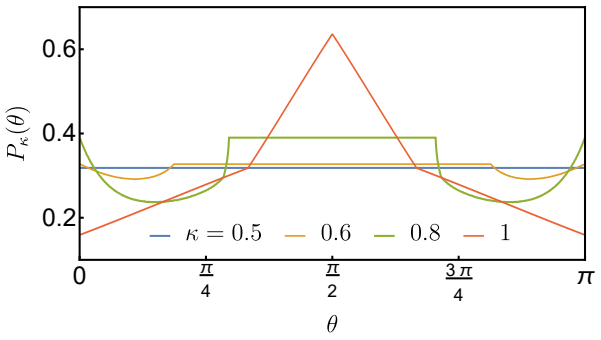


FIG. 4. Probability distribution of the orientation of the rods generated from the eigenvector $\psi_\kappa(\theta)$ associated to the largest eigenvalue of the transfer matrix.

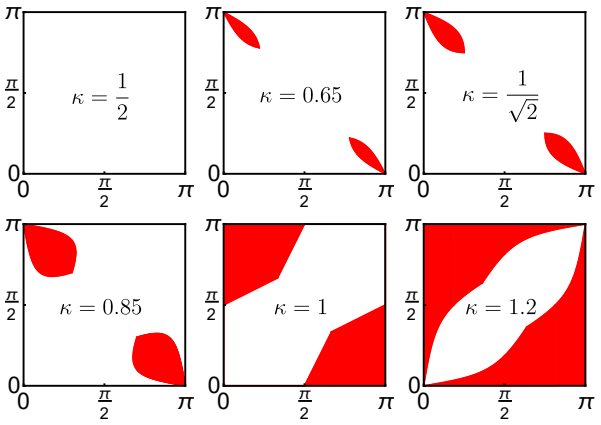


FIG. 5. The transfer matrix $T_\kappa(\theta', \theta)$ on the θ-θ' plane, for different values of κ. The shaded regions denote (θ, θ') values where the rods overlap, and $T_\kappa = 0$. In the plain regions rods do not overlap and $T_\kappa = 1$.

boundary of the shaded region is easily written down from simple geometry (see supplementary material for details). As κ is increased, the shaded regions grow in size, and the eigenvalue of the transfer matrix decreases. For $\frac{1}{\sqrt{2}} < \kappa < 1$, the slope of the boundary of the shaded region becomes infinite or zero at some points. When $\kappa = 1$, the boundary becomes a set of straight lines. For $\kappa > 1$, the two shaded patches, which are disjoint when $\kappa < 1$, merge into a single connected shaded region. We will show that precisely these topological changes in the structure of the available phase space lead to the singularities in the free energy function $\mathcal{F}_1(\kappa)$.

Let us first discuss the singularity at $\kappa = \frac{1}{2}$. For $\kappa < \frac{1}{2}$, no overlap is possible, and the rods can orient freely without any cost of energy. The associated transfer matrix $T_\kappa(\theta', \theta) = 1$ for all angles, and there are no shaded regions. The largest eigenvalue is $\Lambda(\kappa) = 1$ and the corresponding eigenvector $\psi_\kappa(\theta) =$ constant. As κ is increased beyond $\frac{1}{2}$ the nearest neighbor interaction sets in. If we define $\kappa = \frac{1}{2} + \varepsilon$, then it is easily seen that for small $\varepsilon > 0$,

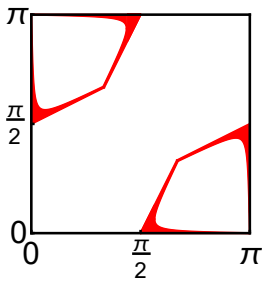


FIG. 6. The picture shows the matrix $\Delta T = T_{1-\varepsilon} - T_1$, for $\varepsilon = 0.02$ on the θ-θ' plane. In the shaded region $\Delta T = 1$, whereas in the plain region it is 0. The area of the shaded region varies as $\varepsilon \log \frac{1}{\varepsilon}$, for small ε.

the area of the shaded regions in the θ-θ' plane grows as ε^2. Then, treating the shaded regions as perturbation, the first order perturbation theory immediately gives

$$\Lambda(1/2 + \varepsilon) = 1 - C\,\varepsilon^2 + \text{ higher order in } \varepsilon. \qquad (3)$$

We find that the constant $C = \frac{32}{3\pi^2}$ (details in the supplementary material). Thus, at $\kappa = \frac{1}{2}$, the second derivative of the free energy $\mathcal{F}_1''(\kappa)$ with respect to κ is discontinuous.

We now discuss the singularity at $\kappa = 1$. For this value, the boundary of the excluded region in the θ-θ' plane becomes a set of straight lines (see figure 5). Then, the transfer matrix $T_\kappa(\theta', \theta)$ can be exactly diagonalized by converting the integral eigenvalue equation (2) into a second order differential equation. The details are given in the supplementary material. We find that the largest eigenvalue of the transfer matrix for $\kappa = 1$ is given by $\Lambda(1) = \left[3\sqrt{2}\arcsin(\frac{1}{3})\right]^{-1}$.

For κ near 1, if we write $\kappa = 1 - \varepsilon$ and define $\Delta T = T_{1-\varepsilon} - T_1$, then, to the first-order in ε, the change in the eigenvalue $\Lambda(\kappa)$ equals $\langle\psi_1|\Delta T|\psi_1\rangle$, where $\psi_1(\theta)$ is the eigenvector of the transfer matrix corresponding to the largest eigenvalue at $\kappa = 1$. This change is shown in figure 6. The curved boundary of the disallowed region near $(\theta, \theta') \equiv (0, \frac{\pi}{2})$ tends to a hyperbola, and as ε tends to zero, the area of the the shaded region in figure 6 tends to zero, but only as $\varepsilon \log \frac{1}{\varepsilon}$. Moreover, the eigenvector $\psi_1(\theta)$ is positive everywhere, with the ratio between its maximium and minimum values remaining finite. This implies that the change in the matrix element has the same qualitative dependence on ε as the area of the shaded regions. Therefore, we conclude that

$$\Lambda(1-\varepsilon) = \Lambda(1) + K_1\varepsilon\log\frac{1}{\varepsilon} + K_2\varepsilon + \text{ higher order terms}, \qquad (4)$$

where K_1 and K_2 are positive constants. A similar argument holds for negative ε and the details are given in the supplementary material.

We now discuss the singularity at $\kappa = \frac{1}{\sqrt{2}}$. For this we consider the range $\frac{1}{\sqrt{2}} < \kappa < 1$, and define $\theta_0 = \sin^{-1}\kappa$.

Then, as long as the angle of a rod $\theta \in [\theta_0, \pi - \theta_0]$, it can be easily seen, that there is no overlap with its neighbor for any angle θ' of the latter. On the other hand, if θ is outside this interval, the rods can intersect, if θ' lies in the intervals $[\phi_1, \phi_2]$ and $[\pi - \phi_2, \pi - \phi_1]$, with the expression for ϕ_1 and ϕ_2 given in the supplementary material. The important point is that the length of the intervals $|\phi_2 - \phi_1|$ varies as $\sqrt{\theta_0 - \theta}$ for $\theta \to \theta_0$. Then, from the eigenvalue equation 2, we see that

$$\psi_\kappa(\theta) = K_3 - K_4 \int_{\phi_1(\theta)}^{\phi_2(\theta)} \psi_\kappa(\theta') d\theta', \tag{5}$$

where K_3 and K_4 are functions of κ only. Using this fact that $\psi_\kappa(\theta')$ is bounded by non-zero constants, both from above and below, we see that, for θ approaching θ_0 from below

$$\psi_\kappa(\theta) \approx K_3 - K_5 \sqrt{\theta_0 - \theta}, \tag{6}$$

where K_5 depends only on κ. This shows that $\psi_\kappa(\theta)$ has a cusp singularity at $\theta = \theta_0$. As the probability density $P_\kappa(\theta)$ is proportional to $\psi_\kappa(\theta)^2$, it also has a cusp singularity for $\theta = \arcsin \kappa$.

Our above arguments can be readily generalized to the case of soft rods ($U_1 \neq +\infty$), but keeping $U_i = 0$ for $i > 1$. The matrix ΔT only gets multiplied by a factor $(1 - e^{-\beta U_1})$. In fact, one can even determine the exact eigenvalues of the transfer matrix at $\kappa = 1$, for an arbitrary pair-potential U_1. This is given by (see supplementary material)

$$\Lambda(1) = \frac{(1 - e^{-\beta U_1})}{3\sqrt{2}} \left[\arctan \frac{(1 - e^{-\beta U_1})}{\sqrt{2}(2 + e^{-\beta U_1})} \right]^{-1}. \tag{7}$$

For soft pairwise interactions, overlaps between pairs of rods beyond the nearest neighbors are allowed. In the case, where such overlaps cost a non-zero amount of energy, *i.e* $U_i \neq 0$ for $i > 1$, one can treat these pair-interactions U_i, as perturbations to the problem with only non-zero U_1. Noting that the overlap region in the (θ_j, θ_{j+i})-plane, for $i > 1$, again has a similar hyperbolic shape, we see that at all integer values of $\kappa = i$ the largest eigenvalue $\Lambda(\kappa)$ has singularities of the form $U_i(i - \kappa) \log |\frac{1}{\kappa - i}|$.

In figure 7, we present evidence of these additional transitions from Monte Carlo simulations. We took $U_i = 1$ for all i. Clearly, we have no long-range correlations in the system, and $\langle \theta \rangle = \frac{\pi}{2}$, for all κ. A signature of the transitions can be seen in the variance of the angle defined by $\langle M^2 \rangle = \frac{1}{N} \langle \left[\sum_i (\theta_i - \frac{\pi}{2}) \right]^2 \rangle$. The variance clearly shows a singularity at all integer values of κ. Also, the positions of the singularities do not depend on the value of β, as long as it remains nonzero.

The reason why the conditions for the applicability of the van Hove theorem are not met is quite clear. As the van Hove theorem demands, the matrix elements are

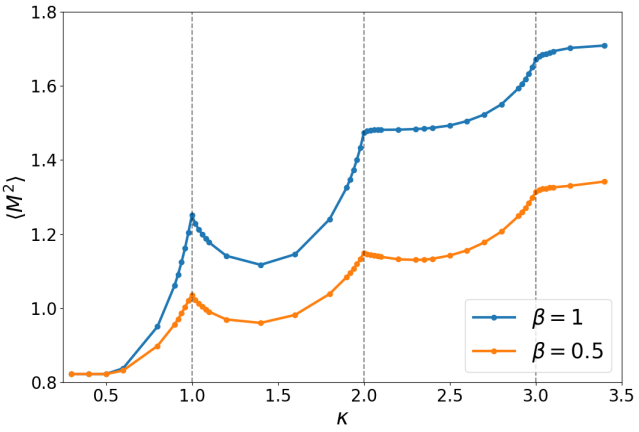


FIG. 7. Variance of the angular distribution of rods generated from Monte Carlo simulations of a system of 100 rods and averaged over 10^6 sample configurations.

analytic functions of β; however, in our case they are non-analytic (in fact discontinuous) functions of the control parameter κ. This non-analyticity is generic to all hard-core (or soft-core) models, and is at the root of the singular behavior found in the problem discussed here. Note that analyticity of the interaction potential as function of distance is not required for a well-behaved thermodynamic limit.

We note that the free energy $F(\kappa, \beta)$ is a non-convex function of κ (see inset of figure 2). Here, κ is a parameter that specifies the number of rods per unit length in the system, and convexity of the free energy as a function of density is a fundamental property, which is essential for thermodynamic stability. In our model, the spacing between particles is fixed and can not be changed. Hence a convex envelope construction, *à la* Maxwell, is not possible, and convexity is not assured. In fact, if the spacing between rods is allowed to vary, then the free energy has no singularities, in agreement with all the previous studies of this model [14–16].

Additionally, we note that in our system, for all finite κ, the correlation length remains finite, and the largest eigenvector remains non-degenerate. Moreover, the behavior of the free energy here is different from the familiar first order phase transitions, where the correlation length remains finite at the transition point, and the first derivative of the free-energy is discontinuous. In our case, the first derivative is *divergent* at the transition points.

Are the points of non-analyticity of the free energy in our system also *phase transition points* between distinct phases, or are they similar to the fluid-fluid transition (*e.g.* the liquid-gas transition), where a non-analyticity in the free energy occurs along a line within the same fluid phase? To answer this question, we consider a particular observable quantity in the equilibrium state: the fraction of i-th neighbor rods that overlap, as an order parameter, which is proportional to $\frac{\partial \mathcal{F}}{\partial U_i}$. This is exactly zero

for $\kappa \leq i$, and non-zero otherwise. This shows that distinct values of $\lfloor \kappa \rfloor$ ($\lfloor \cdot \rfloor$ denotes floor function) correspond to thermodynamically distinguishable distinct phases of the system. Of course, these phases could be further split using additional criteria, *e.g.* by the behavior of the distribution of angles.

It is easy to construct other models which show similar behavior. For example, consider a chain of Ising spins σ_i, placed on a lattice of uniform spacing a. The Hamiltonian of the system is $H = -\sum_{(i,j)} J(r_{ij})\sigma_i\sigma_j$, where $J(r)$ is a distance-dependent exchange interaction $J(r)$, and r_{ij} is the distance between the sites i and j. If we choose, $J(r) = 1 - r$, for $0 < r < 1$, and zero for $r > 1$, there is no long-range order in the problem. However, as the lattice spacing a is varied, the free energy becomes a non-analytic function of a, at all integer values of $\frac{1}{a}$, following the same reasoning as in our model.

In summary, we have discussed a mechanism of phase transitions, which is simple, but has not been sufficiently emphasized in the past. We have illustrated this mechanism with the example of a model of soft rods on a lattice in 1-d with short range interactions, which shows an infinite number of phase transtitions. The model differes from the well-studied models of the past only in the aspect that the centers of rods are placed on a regular lattice, and the distance between them cannot change, except as a global parameter. One would expect similar behavior to occur for objects of different shapes, like crosses, or T- or Y-shapes. The singularities will also occur in higher dimensions. We have studied the system of soft rods in 2-dimensions, which shows similar phase transitions, at $\frac{1}{a} = \sqrt{m^2 + n^2}$, where m and n are any integers. These will be reported in a future publication [17].

[1] R. A. Minlos and G. M. Natapov, Theoretical and Mathematical Physics **24**, 697 (1975).
[2] L. van Hove, Physica **16**, 137 (1950).
[3] D. Ruelle, *Statistical Mechanics: Rigorous Results* (World Scientific, 1999).
[4] D. Ruelle, Communications in Mathematical Physics **9**, 389 (1968).
[5] F. J. Dyson, Communications in Mathematical Physics **12**, 91 (1969).
[6] J. Fröhlich and T. Spencer, Communications in Mathematical Physics **84**, 87 (1982).
[7] L. Landau, E. Lifshitz, and L. Pitaevskij, *Statistical Physics: Part 2 : Theory of Condensed State*, Landau and Lifshitz Course of theoretical physics (Oxford, 1980).
[8] C. Kittel, American Journal of Physics **37**, 917 (1969).
[9] T. Dauxois, M. Peyrard, and A. R. Bishop, Phys. Rev. E **47**, R44 (1993).
[10] S. T. Chui and J. D. Weeks, Phys. Rev. B **23**, 2438 (1981).
[11] G. M. S. S. Grosskinsky and H. Spohn, Journal of Statistical Physics **133**, 267 (2003).
[12] J. A. Cuesta and A. Sánchez, Journal of Statistical Physics **115**, 869 (2004).
[13] L. Onsager, Ann. N. Y. Acad. Sci. **51**, 627 (1949).
[14] L. M. Casey and L. K. Runnels, J. Chem. Phys. **51**, 5070 (1969).
[15] Y. Kantor and M. Kardar, Phys. Rev. E **79**, 041109 (2009).
[16] P. Gurin and S. Varga, Phys. Rev. E **83**, 061710 (2011).
[17] J. Klamser, S. Saryal, T. Sadhu, and D. Dhar, in preparation **xx** (2018).

Supplemental material for: Multiple singularities of the equilibrium free energy in a one-dimensional model of soft rods

Sushant Saryal,[1] Juliane U. Klamser,[2] Tridib Sadhu,[3,4] and Deepak Dhar[1]

[1] *Indian Institute of Science Research and Education, Pashan, Pune, India.*
[2] *Laboratoire de Physique Statistique, Département de physique de l'ENS, Ecole Normale Supérieure, PSL Research University, Université Paris Diderot, Sorbonne Paris Cité, Sorbonne Universités, UPMC Univ. Paris 06, CNRS, 75005 Paris, France.*
[3] *Tata Institute of Fundamental Research, Mumbai 400005, India.*
[4] *Collège de France, 11 place Marcelin Berthelot, 75231 Paris Cedex 05, France.*

We present some of the algebraic details of derivations, and additional results from Monte Carlo simulations. To be specific, we give detailed expressions of the overlap region, an analysis of the singularities, and an exact diagonalization of the transfer matrix. The results from Monte Carlo simulations are about the probability distribution of the orientation of a rod at different values of κ.

PACS numbers: 05.40.Jc, 02.50.Cw, 87.10.Mn

I. THE STRUCTURE OF THE TRANSFER MATRIX

We discuss the transfer matrix T_κ when there is only nearest-neighbor coupling between rods, of strength U_1. The matrix elements $T_\kappa(\theta', \theta)$ have the value $\exp(-\beta U_1)$, if the adjacent rods with orientations θ and θ' overlap, and 1 otherwise. The matrix has the obvious symmetries

$$T_\kappa(\theta, \theta') = T_\kappa(\pi - \theta, \pi - \theta')\,, \tag{1a}$$
$$T_\kappa(\theta, \theta') = T_\kappa(\pi - \theta', \pi - \theta)\,. \tag{1b}$$

Therefore, it is sufficient to specify the matrix elements of T_κ only for the range $\theta \in [0, \frac{\pi}{2}]$.

For $\kappa < \frac{1}{2}$, there are no overlaps. If $\frac{1}{2} < \kappa \leq \frac{1}{\sqrt{2}}$, an overlap of the nearest neighbor rods is possible, but only if $\cos\theta < \frac{1}{2\kappa}$ and $\theta^{'} \in [\theta_{min}, \theta_{max}]$ (see figure 1a) where

$$\theta_{min}(\theta) = \pi - \arctan\left(\frac{\sin\theta}{\kappa^{-1} - \cos\theta}\right)\,, \tag{2a}$$
$$\theta_{max}(\theta) = \pi + \theta - \arcsin\left(\frac{\sin\theta}{\kappa}\right)\,. \tag{2b}$$

For $\frac{1}{\sqrt{2}} \leq \kappa \leq 1$, we get $T_\kappa(\theta', \theta) \neq 1$ if $\sin(\theta) \leq \kappa$, and $\theta' \in [\theta_{min}, \theta_{max}]$, where θ_{min} has different expressions for different ranges of the orientation θ of the right rod (see figure 1b). We get, for any θ

$$\theta_{max} = \pi + \theta - \arcsin\left(\frac{\sin\theta}{\kappa}\right)\,. \tag{3}$$

On the other hand, for θ_{min}, we get, if $\theta \in [0, \arccos\left(\frac{1}{2\kappa}\right)]$, then

$$\theta_{min} = \pi - \arctan\left(\frac{\sin\theta}{\kappa^{-1} - \cos\theta}\right)\,, \tag{4a}$$

whereas, if $\theta \in [\arccos\left(\frac{1}{2\kappa}\right), \arcsin(\kappa)]$, then we get

$$\theta_{min} = \arcsin\left(\frac{\sin\theta}{\kappa}\right) + \theta\,. \tag{4b}$$

For $\kappa > 1$, the elements $T_\kappa(\theta', \theta) \neq 1$ if $\theta^{'} < \theta_{min}$ or $\theta^{'} > \theta_{max}$, where θ_{max} has different expressions for different ranges of θ (see figure 1c). We get, for any θ,

$$\theta_{min} = \theta - \arcsin\left(\frac{\sin\theta}{\kappa}\right)\,. \tag{5}$$

On the other hand, if $\theta \in [0, \arccos\frac{1}{\kappa}]$, then

$$\theta_{max} = \arctan\left(\frac{\sin\theta}{\cos\theta - \kappa^{-1}}\right)\,, \tag{6a}$$

if $\theta \in [\arccos\frac{1}{\kappa}, \arccos\frac{1}{2\kappa}]$, then

$$\theta_{max} = \pi + \arctan\left(\frac{\sin\theta}{\cos\theta - \kappa^{-1}}\right)\,, \tag{6b}$$

and if $\theta \in [\arccos\frac{1}{2\kappa}, \frac{\pi}{2}]$, then

$$\theta_{max} = \theta + \arcsin\left(\frac{\sin\theta}{\kappa}\right)\,. \tag{6c}$$

The shape of the boundary of the overlap regions θ_{max} and θ_{min}, for different ranges of κ, is given in figure 2.

II. EXACT DIAGONALIZATION FOR $\kappa = 1$

When $\kappa = 1$, the boundary of the overlap region is a set of straight lines and the associated transfer matrix $T_\kappa(\theta, \theta')$ is sketched in figure 3. This makes the calculation of the eigenvalue and associated eigenvector simple. The eigenequation is

$$\int_0^\pi \frac{d\theta^{'}}{\pi} \psi_\kappa(\theta^{'}) T_\kappa(\theta^{'}, \theta) = \Lambda\, \psi_\kappa(\theta). \tag{7}$$

From (1b) we see that the eigenvector has the symmetry $\psi_\kappa(\theta) = \psi_\kappa(\pi - \theta)$. Considering this we write

$$\psi_\kappa(\theta) = \begin{cases} \psi_\kappa^{(1)}(\theta) & \text{for } 0 < \theta \leq \frac{\pi}{3}\,, \\ \psi_\kappa^{(2)}(\theta) & \text{for } \frac{\pi}{3} < \theta \leq \frac{\pi}{2}\,. \end{cases} \tag{8}$$

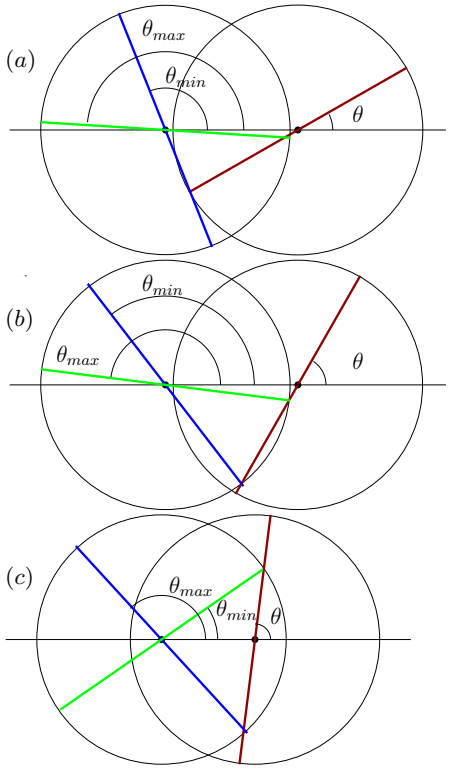


FIG. 1. Overlap criteria for a pair of nearest neighbor rods with orientation (θ', θ) for values of κ in the range (a) $\frac{1}{2} \leq \kappa < \frac{1}{\sqrt{2}}$, (b) $\frac{1}{\sqrt{2}} < \kappa < 1$, and (c) $\kappa > 1$. Overlap occurs for angle $\theta^{'} \in [\theta_{min}, \theta_{max}]$, except in the last case where overlap is for angles $\theta^{'} \in [0, \theta_{min}]$ or $\theta' \in [\theta_{max}, \pi]$.

Further, we define

$$\mathcal{N} = \int_0^{\frac{\pi}{2}} \frac{d\theta^{'}}{\pi} \psi_\kappa(\theta^{'}) \,.$$

Now, if we define $\psi_\kappa^{(1)}(\theta = \frac{\pi x}{3}) = P(x)$, and $\psi_\kappa^{(2)}(\theta = \frac{\pi}{2} - \frac{x\pi}{6}) = Q(x)$ for $0 \leq x \leq 1$, then the eigenvalue equation becomes

$$\mathcal{N} + \frac{1}{6}\int_0^x dy Q(y) + e^{-\beta U_1}\frac{1}{6}\int_x^1 dy Q(y) + e^{-\beta U_1}\frac{1}{3}\int_0^1 dy P(y) = \Lambda P(x)\,, \tag{9a}$$

$$\mathcal{N} + \frac{1}{6}\int_0^1 dy Q(y) + \frac{1}{3}\int_x^1 dy P(y) + e^{-\beta U_1}\frac{1}{3}\int_0^x dy P(y) = \Lambda Q(x)\,, \tag{9b}$$

with

$$\mathcal{N} = \frac{1}{3}\int_0^1 dx P(x) + \frac{1}{6}\int_0^1 dx Q(x)\,. \tag{9c}$$

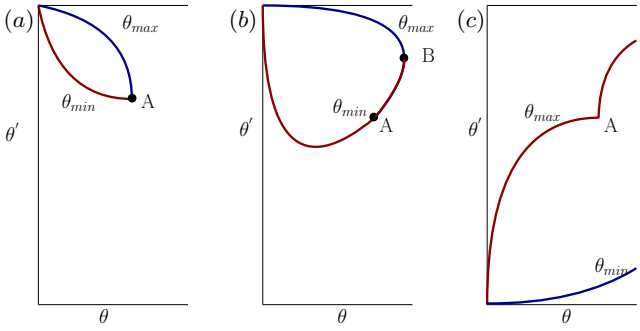


FIG. 2. The shape of the boundary of the overlap region in the transfer matrix for values of κ in the range (a) $\frac{1}{2} \leq \kappa < \frac{1}{\sqrt{2}}$, (b) $\frac{1}{\sqrt{2}} < \kappa < 1$, and (c) $\kappa > 1$. Only the range $\theta < \frac{\pi}{2}$ is shown; the rest of the region can be constructed using the symmetry (1a, 1b). The point A denotes $\theta = \arccos\frac{1}{2\kappa}$ and B denotes $\theta = \arcsin\kappa$.

These integral equations can be converted into the following coupled differential equations

$$\Lambda\frac{dP}{dx} = \left(1 - e^{-\beta U_1}\right)\frac{Q(x)}{6}\,,$$
$$\Lambda\frac{dQ}{dx} = -\left(1 - e^{-\beta U_1}\right)\frac{P(x)}{3}\,.$$

Solutions of these equations are given by

$$P(x) = \frac{N}{\Lambda}\left((1 + e^{-\beta U_1})\cos kx + \sqrt{2}\sin kx\right)\,, \tag{10a}$$
$$Q(x) = \frac{N}{\Lambda}\left(2\cos kx - \sqrt{2}(1 + e^{-\beta U_1})\sin kx\right)\,, \tag{10b}$$

where

$$\Lambda = \left(1 - e^{-\beta U_1}\right)/3\sqrt{2}k\,, \tag{10c}$$
$$k = \arctan\left(\frac{1 - e^{-\beta U_1}}{\sqrt{2}(2 + e^{-\beta U_1})}\right)\,. \tag{10d}$$

Note that there is an infinite spectrum of eigenvalues. Other eigenvectors, and eigenvalues, including the anti-symmetric ones can also be determined similarly.

III. ANALYSIS OF THE SINGULARITIES

A. Singularity near $\kappa = \frac{1}{2}$

When $\kappa \leq \frac{1}{2}$, the elements of the transfer matrix

$$T_\kappa(\theta', \theta) = 1 \qquad \text{for all } \theta \text{ and } \theta'\,. \tag{11}$$

The largest eigenvalue for this matrix is $\Lambda = 1$ and the corresponding eigenvector $\psi_{\frac{1}{2}}(\theta) = 1$. All other eigenvalues are zero. From a first order perturbation theory,

where κ is varied around $\kappa = \frac{1}{2}$, the corresponding change in the largest eigenvalue is given by

$$\begin{aligned}\Delta\Lambda &= \int_0^\pi \frac{d\theta}{\pi} \int_0^\pi \frac{d\theta'}{\pi} \psi_{\frac{1}{2}}(\theta) \Delta T(\theta,\theta') \psi_{\frac{1}{2}}(\theta') \\ &= \langle \psi_{\frac{1}{2}} | \Delta T | \psi_{\frac{1}{2}} \rangle \,, \end{aligned} \tag{12}$$

where ΔT denotes the corresponding change in the transfer matrix. If we write, $\kappa = \frac{1}{2} - \varepsilon$, with positive and small ε, the transfer matrix will remain the same, *i.e.* $\Delta T = 0$, and therefore $\Delta\Lambda = 0$. However, if we write $\kappa = \frac{1}{2} + \varepsilon$, with positive and small ε, the corresponding change in the eigenvalue is

$$\Delta\Lambda = \left(e^{-\beta U_1} - 1\right) \Delta A \,, \tag{13a}$$

where $\Delta A = A(\kappa = \frac{1}{2} + \varepsilon) - A(\kappa = \frac{1}{2})$ is the change in the overlap region, which is given by

$$\Delta A = 2 \int_0^{\arccos \frac{1}{2\kappa}} \frac{d\theta}{\pi} \int_{\theta_{min}(\theta)}^{\theta_{max}(\theta)} \frac{d\theta'}{\pi} \,. \tag{13b}$$

To evaluate this change for $\varepsilon \to 0$ we see

$$\arccos \frac{1}{2\kappa} \simeq 2\sqrt{\varepsilon} \,,$$

and consequently

$$\begin{aligned}\theta_{min} &\simeq \pi - \theta(1+4\varepsilon) + \theta^3 \,, \\ \theta_{max} &\simeq \pi - \theta(1-4\varepsilon) - \theta^3 \,. \end{aligned}$$

Using these in the equation (13a, 13b), we get

$$\Delta\Lambda = \frac{16\varepsilon^2}{\pi^2} \left(e^{-\beta U_1} - 1\right) \,. \tag{14}$$

Then, the free energy per site is given by

$$\mathcal{F}(\kappa,\beta) = \begin{cases} 0 & \text{for } \kappa = \frac{1}{2} - \varepsilon \,, \\ -\frac{16\varepsilon^2}{\pi^2} \left(e^{-\beta U_1} - 1\right) & \text{for } \kappa = \frac{1}{2} + \varepsilon \,. \end{cases} \tag{15}$$

Therefore, at $\kappa = \frac{1}{2}$ the free energy has a discontinuous second derivative.

B. Singularity near $\kappa = 1$

The structure of the excluded region for $\kappa = 1 - \varepsilon$, with $\varepsilon > 0$, is shown in figure 4. We show here that the shaded area in this plot varies as $\varepsilon \log \frac{1}{\varepsilon}$.

As the transfer matrix has the symmetry (1a, 1b), the change in area ΔA is four times the area of the shaded region in figure 4. One of its boundary is a straight line $\theta' = \frac{1}{2}\theta + \frac{\pi}{2}$. To show that asymptotic shape of this boundary near $(0, \pi/2)$ is a hyperbola, we introduce the re-scaled coordinates (ξ, η) using

$$\xi = \frac{\theta}{\sqrt{\varepsilon}} \,, \qquad \eta = \frac{\theta_{min} - \left(\frac{\pi}{2} + \frac{\theta}{2}\right)}{\sqrt{\varepsilon}} \,. \tag{16}$$

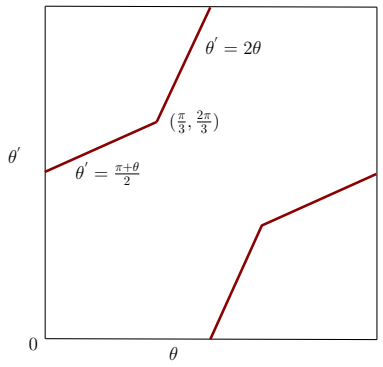


FIG. 3. The transfer matrix at $\kappa = 1$, with straight line boundaries of the overlap region.

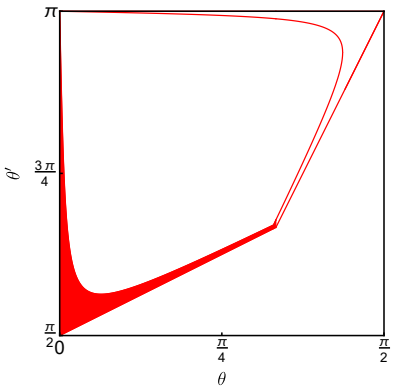


FIG. 4. The shaded area is one fourth of the change in area ΔA in the transfer matrix as κ is decreased from 1 by an amount 0.02 (see figure 6 in the *Letter*).

Writing the equation (4a) in terms of this scaled coordinates, and solving in the limit $\varepsilon \to 0$, we get a scaled hyperbolic curve $\eta\,\xi = 1$. This implies, that to the leading order in small ε, the curved boundary of the shaded region in figure 4 follows $\eta = \frac{1}{\xi}$. Then, the area of this shaded region is $\varepsilon \int \eta \, d\xi$, where the upper limit of the integral varies as $\frac{1}{\sqrt{\varepsilon}}$. Therefore, we find that the area varies as $\varepsilon \log \frac{1}{\varepsilon}$. Keeping the exact pre-factors in our calculation, we get for small ε,

$$\Delta A \simeq 4 \left(\varepsilon \ln \frac{\pi^2}{6} - \varepsilon \ln \varepsilon + \varepsilon \right) \,. \tag{17}$$

IV. PROBABILITY DISTRIBUTION OF THE ORIENTATIONS OF A ROD

The probability distribution of the orientations of a rod shows a complex dependence on the angle θ and the parameter κ. The results of a simulation on a system of 100 rods and averaged over 10^6 sample configurations is shown in figure 5. For $\kappa \leq \frac{1}{2}$, where the rods do not interact, the distribution is uniform. As κ is increased

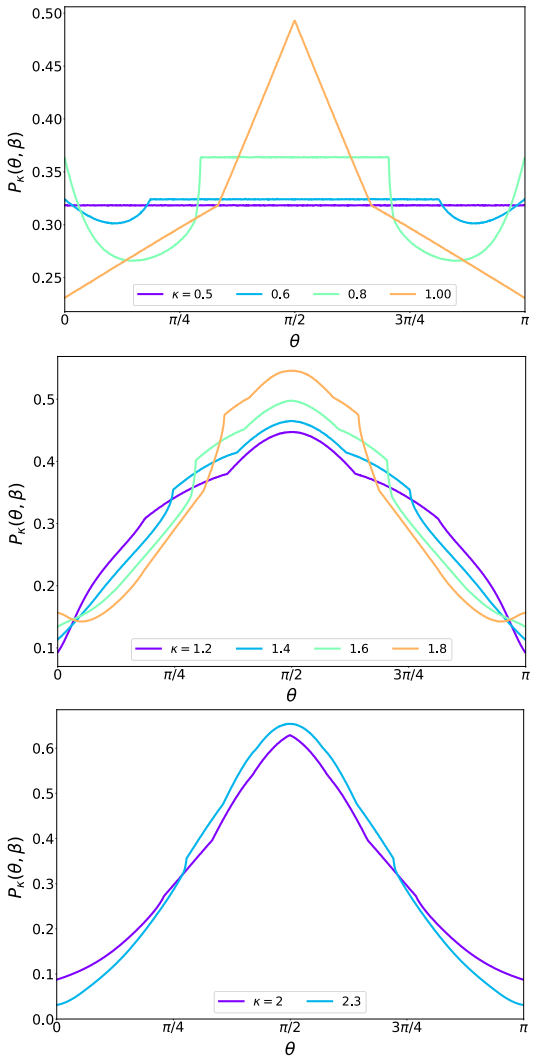


FIG. 5. Probability distribution of orientation of a rod measured in a Monte Carlo simulation of $N = 100$ rods with $\beta U_i = 1$ for all $i \geq 1$. The curves corresponds to different values of κ indicated at the bottom panel of each figure.

above $\frac{1}{2}$, the distribution function shows a discontinuous first derivative when $\cos\theta = \frac{1}{2\kappa}$. This derivative discontinuity becomes a cusp singularity for $\kappa > \frac{1}{\sqrt{2}}$. The two symmetrically located cusps move in position with increasing values of κ and merge at $\kappa = 1$. At this value, a new pair of singularities develop, and for the entire range $1 < \kappa < 2$, there are in total four singularities in the distribution function. At $\kappa = 2$, two of these singularities merge, but an additional pair of singularities emerge. This can be observed in figure 5. We find that whenever κ crosses an integer multiple of $\frac{1}{\sqrt{2}}$, a new pair of cusp singularities develop, and then move towards each other as κ is varied.

In the main text, we discussed the characterization in terms of the fractional number of k-th neighbors that

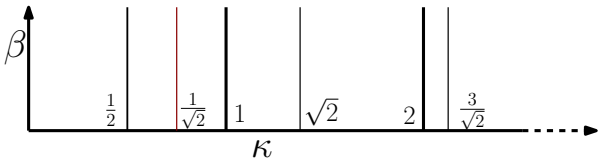


FIG. 6. A schematic phase diagram showing the different phase transition lines in the κ-β plane, when all U_i are equal. All lines are parallel to the β-axis.

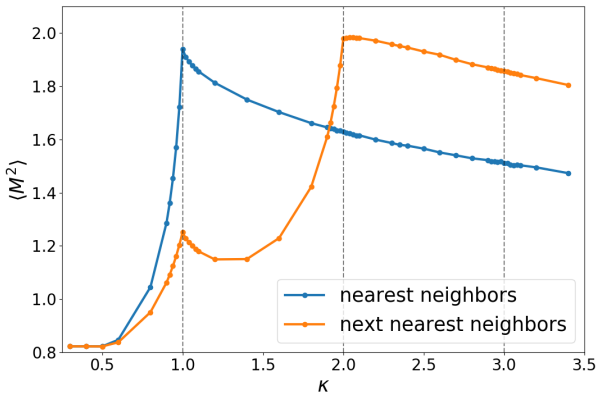


FIG. 7. Variance of the angle $\langle M^2 \rangle = \frac{1}{L}\langle\left[\sum_i(\theta_i - \frac{\pi}{2})\right]^2\rangle$ for a system of rods with only nearest neighbor interactions and another system with upto next nearest neighbor interaction.

overlap directly. We can consider a finer characterization of the phases, by also using the number of cusps in the orientation distribution. If we do this, then one gets phase transitions whenever κ is an integer multiple of 1 or $\frac{1}{\sqrt{2}}$. A schematic of such a phase diagram is drawn in figure 6.

The singularities can also be seen in the fluctuations. In figure 7, we show the numerical result for the variance of the orientations of a rod. Here we compare two cases: one with only U_1 non-zero, and the second with only U_1 and U_2 non-zero. In the first case, the singularity appears only at $\kappa = 1$, while in the second case, there is an additional singularity at $\kappa = 2$, but no detectable singularity at $\kappa = 3$.

A.17 Publication 3: A kinetic-Monte Carlo perspective on active matter

Invited publication for JCP Special Topic on Chemical Physics of Active Matter. Preprint available: Juliane U. Klamser, Sebastian C. Kapfer, and Werner Krauth, *A kinetic-Monte Carlo perspective on active matter*, arXiv:1812.06308 (2018).

Bibliography

[1] N. Goldenfeld and L. P. Kadanoff. Simple Lessons from Complexity. *AAAS*, **284** (87–89), 1999. v

[2] R. B. Laughlin and D. Pines. The Theory of Everything. *Proc. Natl. Acad. Sci. USA*, **97** (28–31), 2000. v

[3] P. W. Anderson. More Is Different. *Science*, **177** (393–396), 1972. v

[4] P. M. Chaikin and T. C. Lubensky. *Principles of Condensed Matter Physics* . Cambridge University Press, 1995. vi, 28, 29, 41

[5] V. N. Ryzhov, E. E. Tareyeva, Yu D. Fomin, and E. N. Tsiok. Berezinskii–Kosterlitz–Thouless transition and two- dimensional melting. *Phys.-Usp.*, **60** (857-885), 2017. 4, 26, 30, 44, 45, 46, 47

[6] J. M. Kosterlitz. Kosterlitz–Thouless physics: a review of key issues. *Rep. Prog. Phys.*, **79** (026001), 2016. vi, viii, 26, 30, 44, 127

[7] M. J. Allen, V. C. Tung, and R. B. Kaner. Honeycomb Carbon: A Review of Graphene. *Chem. Rev.*, **110** (132-145), 2010. vi

[8] L. D. Landau and E. M. Lifshitz. *Statistical Physics, Part 1* . Butterworth-Heinemann, 1980. vi, viii, 2, 10

[9] L. van Hove. Sur L'intégrale de Configuration Pour Les Systèmes De Particules À Une Dimension. *Physica*, **16** (137-143), 1950. viii, 28, 126, 133

[10] J. A. Cuesta and A. Sánchez. General Non-Existence Theorem for Phase Transitions in One-Dimensional Systems with Short Range Interactions, and Physical Examples of Such Transitions. *J. Stat. Phys.*, **115** (869-893), 2004. vi, viii, 15, 126, 128, 132, 133, 134, 138, 151

[11] Etienne Bernard. *Algorithms and applications of the Monte Carlo method : two-dimensional melting and perfect sampling* . PhD thesis, Université Pierre et Marie Curie, Hal Id: tel-00637330, 2011. vi, 26, 27, 28, 29, 30, 32, 33, 36, 38, 40, 43, 46, 75

[12] E. P. Bernard and W. Krauth. Two-Step Melting in Two Dimensions: First-Order Liquid-Hexatic Transition. *Phys. Rev. Lett.*, **107** (155704), 2011. 2, 27, 46, 63, 71, 75, 111

[13] S. C. Kapfer and W. Krauth. Two-Dimensional Melting: From Liquid-Hexatic Coexistence to Continuous Transitions. *Phys. Rev. Lett.*, **114** (035702), 2015. vi, 2, 27, 29, 34, 38, 43, 46, 62, 63, 71, 75, 76, 77, 94, 98, 122, 160

[14] M. C. Marchetti, J. F. Joanny, S. Ramaswamy, T. B. Liverpool, J. Prost, Madan Rao, and R. Aditi Simha. Hydrodynamics of soft active matter. *Rev. Mod. Phys.*, **85** (3):1143 – 1189, 2013. vi, 13, 15

[15] D. Needleman and Z. Dogic. Active matter at the interface between materials science and cell biology. *Nat. Rev. Mat.*, **2** (17048), 2017. vi

[16] J. Riskin. *The Restless Clock: A History of the Centuries-Long Argument over What Makes Living Things Tick* . University of Chicago Press, 2018. vii

[17] I. Buttinoni, G. Volpe, F. Kümmel, G. Volpe, and C. Bechinger. Active Brownian motion tunable by light. *J. Phys.: Condens. Matter*, **24** (284129), 2012. vii, 19

[18] I. Buttinoni, J. Bialké, F. Kümmel, H. Löwen, C. Bechinger, and T. Speck. Dynamical Clustering and Phase Separation in Suspensions of Self-Propelled Colloidal Particles. *Phys. Rev. Lett.*, **110** (238301), 2013. 17, 19, 26, 64, 74, 122

[19] J. Deseigne, O. Dauchot, and H. Chaté. Collective Motion of Vibrated Polar Disks. *Phys. Rev. Lett.*, **105** (098001), 2010. vii, 17, 19, 122

[20] P. W. Anderson, G. Yuval, and D. R. Hamann. Exact Results in the Kondo Problem. II. Scaling Theory, Qualitatively Correct Solution, and Some New Results on One-Dimensional Classical Statistical Models. *Phys. Rev. B*, **1** (4464-4473), 1970. viii, 125

[21] E. Peierls. Bemerkungen über Umwandlungstemperaturen. *Helvetica Physica Acta Suppl.*, **7** (81-83), 1934. viii, 28

[22] D. Ruelle. Statistical mechanics of a one-dimensional lattice gas. *Commun. Math. Phys.*, **9** (389-410), 1968. viii, 126, 127, 133

[23] J. Fröhlich and T. Spencer. The phase transition in the one-dimensional Ising Model with $1/r^2$ interaction energy. *Commun. Math. Phys.*, **84** (87-101), 1982. viii, 126, 133

[24] D. Chowdhury and D. Stauffer. *Principles of Equilibrium Statistical Mechanics* . *WILEY-VCH Verlag*, 2000. 2, 3, 5

[25] J. J. Binney, N. J. Dowrick, A. J. Fisher, and M. E. J. Newman. *The Theory of Critical Phenomena - An Introduction to the Renomalization Group* . *clarendon Press Oxford*, 1992. 2, 4

[26] Nigel Goldenfeld. *Lectures on Phase Transitions and Critical Phenomena* . *Westview Press*, 1992. 2

[27] Mehran Kardar. *Statistical physics of fields* . Cambridge University Press, 2007. 4, 128

[28] A. Z. Patashinskii and V. L. Pokrovskii. 2nd order phase transitions in a Bose fluid. *Sov. Phys. JETP*, **19** (677-691), 1964. 4

[29] A. Z. Patashinskii and V. L. Pokrovskii. BEHAVIOR OF ORDERED SYSTEMS NEAR THE TRANSITION POINT. *Sov. Phys. JETP*, **23** (292-297), 1966.

[30] L. P. Kadanoff. SCALING LAWS FOR ISING MODELS NEAR T_c^*. *Physics*, **2** (263-272), 1966.

[31] M. E. Fisher. The theory of equilibrium critical phenomena. *Rep. Prog. Phys.*, **30** (615), 1967.

[32] K. G. Wilson. Renormalization Group and Critical Phenomena. I. Renormalization Group and the Kadanoff Scaling Picture. *Phys. Rev. B*, **4** (3174-3183), 1971.

[33] K. G. Wilson. Renormalization Group and Critical Phenomena. II. Phase-Space Cell Analysis of Critical Behavior. *Phys. Rev. B*, **4** (3184-3205), 1971.

[34] K. G. Wilson and M. E. Fisher. Critical Exponents in 3.99 Dimensions. *Phys. Rev. Lett.*, **28** (240-243), 1972.

[35] K. G. Wilson. Feynman-Graph Expansion for Critical Exponents. *Phys. Rev. Lett.*, **28** (548-551), 1972.

[36] A. Z. Patashinskii and V. L. Pokrovskii. *Fluctuation Theory of Phase Transitions* . Oxford: Pergamon Press, 1979. 4

[37] C. Domb and M. S. Green. *Phase transitions and critical phenomena 1* . Academic Press London, 1972. 6, 126

[38] R. P. Feynman. *Statistical Mechanics: A Set of Lectures*, volume 7. The Benjamin/Cummings Publishing Company, 1972. 6

[39] L. Berthier and G. Biroli. Theoretical perspective on the glass transition and amorphous materials. *Rev. Mod. Phys.*, **83** (587-645), 2011. 6

[40] N. G. Van Kampen. *Stochastic Processes in Physics and Chemistry*, volume **3** . Elsevier, 2007. 7, 13, 14, 99, 128

[41] D. Mukamel. Phase Transitions in Nonequilibrium Systems . *arXiv:cond-mat/0003424v2*, 2000. 8, 12

[42] W. Krauth. *Statistical Mechanics: Algorithms and Computations* . Oxford University Press, 2006. 8, 82, 87, 160, 162

[43] M. Suzuki and R. Kubo. Dynamics of the Ising Model near the Critical Point. I. *J. Phys. Soc. Jpn.*, **24** (51-60), 1968. 8

[44] P. Garrido, J. L. Lebowitz, C. Maes, and H. Spohn. Long-range correlations for conservative dynamics. *Phys. Rev. A*, **42** (4), 1990. 9

[45] S. Katz, J. L. Lebowitz, and H. Spohn. Phase transitions in stationary nonequilibrium states of model lattice systems. *Phys. Rev. B*, **28** (3), 1983. 10

[46] S. Katz, J. L. Lebowitz, and H. Spohn. Nonequilibrium Steady States of Stochastic Lattice Gas Models of Fast Ionic Conductors. *J. Stat. Phys.*, **34** (3-4), 1984. 10

[47] G. Junot, G. Briand, R. Ledesma-Alonso, and O. Dauchot. Active versus Passive Hard Disks against a Membrane: Mechanical Pressure and Instability. *Phys. Rev. Lett.*, **119** (028002), 2017. 10, 75, 111

[48] A. P. Solon, Y. Fily, A. Baskaran, M. E. Cates, Y. Kafri, M. Kardar, and J. Tailleur. Pressure is not a state function for generic active fluids. *Nat. Phys.*, **11** (673), 2015. 10, 75, 111, 123

[49] L. F. Cugliandolo, J. Kurchan, and L. Peliti. Energy flow, partial equilibration, and effective temperatures in systems with slow dynamics. *Phys. Rev. E*, **55** (3898), 1997. 10

[50] L. Cugliandolo and J. Kurchan. Thermal properties of slow dynamics. *Physica A*, **263** (242-251), 1999. 10

[51] A. P. Solon, J. Stenhammar, R. Wittkowski, M. Kardar, Y. Kafri, M. E. Cates, and J. Tailleur. Pressure and Phase Equilibria in Interacting Active Brownian Spheres. *Phys. Rev. Lett*, **114** (198301), 2015. 10, 21, 75, 111, 113, 116, 123

[52] J.-F. Rupprecht and J. Prost. A fresh eye on nonequilibrium systems. *Sience*, **325** (6285), 2016. 10

[53] T. Taniguchi and E. G. D. Cohen. Onsager-machlup theory for nonequilibrium steady states and fluctuation theorems. *J. Stat. Phys.*, **126** (1), 2007. 11

[54] M. Baiesi, C. Maes, and B. Wynants. Fluctuations and Response of Nonequilibrium States. *Phys. Rev. Lett.*, **103** (010602), 2009. 11

[55] U. Seifert and T. Speck. Fluctuation-dissipation theorem in nonequilibrium steady states. *Europhys. Lett.*, **89** (1), 2010. 11

[56] C. Jarzynski. Equilibrium free-energy differences from nonequilibrium measurements: A master-equation approach. *Phys. Rev. E*, **56** (5), 1997. 12

[57] C. Jarzynski. Nonequilibrium Equality for Free Energy Differences. *Phys. Rev. Lett.*, **78** (14), 1997. 12

[58] G. Gallavotti and E. G. D. Cohen. Dynamical Ensembles in Nonequilibrium Statistical Mechanics. *Phys. Rev. Lett.*, **74** (14):2694 – 2697, 1995. 12

[59] G. Gallavotti and E. G. D. Cohen. Dynamical Ensembles in Stationary States. *J. Stat. Phys.*, **80** (5-6), 1995. 12

[60] M. R. Evans. Phase transitions in one-dimensional nonequilibrium systems. *Braz. J. Phys.*, **30** (42-57), 2000. 12

[61] R. A. Blythe. An introduction to phase transitions in stochastic dynamical systems. *J. Phys. Conf. Ser.*, **40** (1-12), 2006.

[62] H. Hinrichsen. Non-equilibrium critical phenomena and phase transitions into absorbing states. *Adv. Phys.*, **49** (815-958), 2000. 12, 13

[63] K. A. Takeuchi, M. Sano, T. Sasamoto, and H. Spohn. Growing interfaces uncover universal fluctuations behind scale invariance. *Sc. Rep.*, **1** (1-34), 2011. 13

[64] G. Popkin. The physics of life. *Nature*, **529** :16–18, 2016. 13, 17

[65] Sriram Ramaswamy. The Mechanics and Statistics of Active Matter. *Annual Review of Condensed Matter Physics*, **1** (323 - 345), 2010. 16

[66] C. Bechinger, R. Di Leonardo, H. Löwen, C. Reichhardt, G. Volpe, and G. Volpe. Active particles in complex and crowded environments. *Rev. Mod. Phys.*, **88** (045006), 2016. 21

[67] A. Doostmohammadi, J. Ignés-Mullol, J. M. Yeomans, and F. Sagués. Active nematics. *Nat. Com.*, **9** (3246), 2018. 13

[68] I. D. Couzin and J. Krause. Self-organization and collective behavior in vertebrates. *Adv. Study Behav.*, **32** , 2003. 16

[69] Y. Katz, K. Tunstrøm, C. C. Ioannou, C. Huepe, and I. D. Couzina. Inferring the structure and dynamics of interactions in schooling fish. *Proc. Natl. Acad. Sci. USA*, **108** (46):18720–18725, 2011. 16

[70] M. Ballerini, N. Cabibbo, R. Candelier, A. Cavagna, E. Cisbani, I. Giardina, V. Lecomte, A. Orlandi, G. Parisi, A. Procaccini, M. Viale, and V. Zdravkovic. Interaction ruling animal collective behavior depends on topological rather than metric distance: Evidence from a field study. *Proc. Natl. Acad. Sci. USA*, **105** (4):1232–1237, 2008. 17

[71] H. P. Zhang, A. Be'er, E.-L. Florin, and H. L. Swinney. Collective motion and density fluctuations in bacterial colonies. *Proc. Natl. Acad. Sci. USA*, **107** (13626), 2010. 17

[72] V Schaller, C. Weber, C. Semmrich, E. Frey, and A. R. Bausch. Polar patterns of driven filaments. *Nature*, **467** (73), 2010. 17

[73] Y. Sumino, K. H. Nagai, Y. Shitaka, D. Tanaka, K. Yoshikawa, H. Chaté, and K. Oiwa. Large-scale vortex lattice emerging from collectively moving microtubules. *Nature*, **482** (448), 2012. 17

[74] I. Theurkauff, C. Cottin-Bizonne, J. Palacci, C. Ybert, and L. Bocquet. Dynamic Clustering in Active Colloidal Suspensions with Chemical Signaling. *Phys. Rev. Lett.*, **108** (268303), 2012. 17

[75] J. Palacci, S. Sacanna, A. P. Steinberg, D. J. Pine, and P. M. Chaikin. Living Crystals of Light-Activated Colloidal Surfers. *Sience*, **339** (6122):936–940, 2013. 17, 19, 122

[76] A. Bricard, J. Caussin, N. Desreumaux, O. Dauchot, and D. Bartolo. Emergence of macroscopic directed motion in populations of motile colloids. *Nature*, **7** (503), 2013. 17, 122

[77] Tamás Vicsek, András Czirók, Eshel Ben-Jacob, Inon Cohen, and Ofer Shochet. Novel Type of Phase Transition in a System of Self-Driven Particles. *Phys. Rev. Lett.*, **75** (6): 1226–1229, 1995. 17, 18

[78] Vijay Narayan, Sriram Ramaswamy, and Narayanan Menon. Long-Lived Giant Number Fluctuations in a Swarming Granular Nematic. *Sience*, **317** (105), 2007. 17

[79] S. Dey, D. Das, and R. Rajesh. Spatial Structures and Giant Number Fluctuations in Models of Active Matter. *Phys. Rev. Lett.*, **108** (Marchetti), 2012. 17

[80] M. E. Cates and J. Tailleur. Motility-Induced Physe Separation. *Annu. Rev. Condens. Matter Phys.*, **6** (219), 2015. 17, 19, 21, 23, 24, 25, 60, 74

[81] Howard C. Berg. *E. coli in Motion* . Springer-Verlag New York, 2003. 18, 21

[82] A. Sokolov, I. S. Aranson, J. O. Kessler, and R. E. Goldstein. Concentration Dependence of the Collective Dynamics of Swimming Bacteria. *Phys. Rev. Lett.*, **98** (158102), 2007. 19

[83] J. Tailleur and M. E. Cates. Sedimentation, trapping, and rectification of dilute bacteria. *Europhys. Lett.*, **86** (60002), 2009. 19

[84] J. Palacci, C. Cottin-Bizonne, C. Ybert, and L. Bocquet. Sedimentation and Effective Temperature of Active Colloidal Suspensions. *Phys. Rev. Lett.*, **105** (088304), 2010.

[85] M. Enculescu and H. Stark. Active colloidal suspensions exhibit polar order under gravity. *Phys. Rev. Lett.*, **107** (058301), 2011. 19

[86] P. Galajda, J. Keymer, P. Chaikin, and R. Austin. A Wall of Funnels Concentrates Swimming Bacteria. *J. Bacteriol.*, **189** (23), 2007. 19

[87] M. B. Wan, C. J. Olson Reichhardt, Z. Nussinov, and C. Reichhardt. Rectification of Swimming Bacteria and Self-Driven Particle Systems by Arrays of Asymmetric Barriers. *Phys. Rev. Lett.*, **101** (018102), 2008.

[88] D. Dell'Arciprete G. Ruocco V. Iebba R. Di Leonardo, L. Angelani, S. Schippa, M. P. Conte, F. Mecarini, F. De Angelis, and E. Di Fabrizio. Bacterial ratchet motors. *Proc. Natl. Acad. Sci. USA*, **107** (21), 2010.

[89] L. Angelani, R. Di Leonardo, and G. Ruocco. Self-Starting Micromotors in a Bacterial Bath. *Phys. Rev. Lett.*, **102** (048104), 2009. 19

[90] B. ten Hagen, S. van Teeffelen, , and H. Löwen. Brownian motion of a self-propelled particle. *J. Phys.: Condens. Matter*, **23** (194119), 2011. 20

[91] P. Romanczuk, M. Bär, W. Ebeling, B. Lindner, and L. Schimansky-Geier. Active brownian particles. *Eur. Phys. J. Special Topics*, **202** (1-162), 2012. 20

[92] É. Fodor, C. Nardini, M. E. Cates, J. Tailleur, P. Visco, and F. van Wijland. How Far from Equilibrium Is Active Matter? *Phys. Rev. Lett*, **117** (038103), 2016. 20, 21, 50, 102, 121

[93] J. Tailleur and M. E. Cates. Statistical Mechanics of Interacting Run-and-Tumble Bacteria. *Phys. Rev. Lett.*, **100** (218103), 2008. 20, 21, 121, 123

[94] M. J.Schnitzer. Theory of continuum random walks and application to chemotaxis. *Phys. Rev. E*, **48** (4), 1993. 21, 23

[95] M. E. Cates and J. Tailleur. When are active Brownian particles and run-and- tumble particles equivalent? Consequences for motility-induced phase separation. *Europhys. Lett.*, **101** (20010), 2013. 21

[96] A. G. Thompson, J. Tailleur, M. E. Cates, and R. A. Blythe. Lattice models of nonequilibrium bacterial dynamics. *J. Stat. Mech.*, **2011** (P02029), 2011. 21

[97] Y. Fily and M. C. Marchetti. Athermal Phase Separation of Self-Propelled Particles with No Alignment. *Phys. Rev. Lett.*, **108** (235702), 2012. 21, 23, 25, 26, 49, 74, 122

[98] G. S. Redner, M. F. Hagan, and A. Baskaran. Structure and Dynamics of a Phase-Separating Active Colloidal Fluid. *Phys. Rev. Lett.*, **110** (055701), 2013. 21, 22, 23, 25, 26, 49, 74, 122

[99] J. Bialké, H. Löwen, and T. Speck. Microscopic theory for the phase separation of self-propelled repulsive disks. *Europhys. Lett.*, **103** (30008), 2013. 21, 87

[100] J. Stenhammer, A. Tiribocchi, R. J. Allen, D. Marenduzzo, and M. E. Cates. Continuum Theory of Phase Separation Kinetics for Active Brownian Particles. *Phys. Rev. Lett.*, **111** (145702), 2013. 23, 25

[101] R. J. Allena J. Stenhammar, D. Marenduzzo and M. E. Cates. Phase behaviour of active Brownian particles: the role of dimensionality. *Soft Matter*, **10** (1489), 2014. 21, 23, 25

[102] Roland G. Winkler, Adam Wysocki, and Gerhard Gompper. Virial pressure in systems of spherical active Brownian particles. *Soft Matter*, **11** (6680), 2015. 21, 75, 111

[103] Y. Fily, S. Henkes, and M. C. Marchetti. Freezing and phase separation of self-propelled disks. *Soft Matter*, **10** (2132), 2014. 21, 25, 124

[104] C. Sandford, A. Y. Grosberg, and J. Joanny. Pressure and flow of exponentially self-correlated active particles. *Phys. Rev. E*, **96** (052605), 2017. 21, 117, 123

[105] Demian Levis, Joan Codina, and Ignacio Pagonabarraga. Active Brownian equation of state: metastability and phase coexistence. *Soft Matter*, **13** (8113), 2017. 21, 75, 111, 123

[106] L. F. Cugliandolo, P. Digregorio, G. Gonnella, and A. Suma. Phase co-existence in bidimensional passive and active dumbbell systems. *Phys. Rev. Lett.*, **119** (268002), 2017. 21, 74, 123, 124

[107] T. Speck, J. Bialké, A. M. Menzel, and H. Löwen. Effective Cahn-Hilliard Equation for the Phase Separation of Active Brownian Particles. *Phys. Rev. Lett.*, **112** (218304), 2014. 25, 26, 49, 121, 122, 123

[108] P. Digregorio, D. Levis, A. Suma, L. F. Cugliandolo, G. Gonnella, and I. Pagonabarraga. Full Phase Diagram of Active Brownian Disks: From Melting to Motility-Induced Phase Separation. *Phys. Rev. Lett.*, **121** (098003), 2018. 26, 74, 111, 122, 123, 124

[109] Leticia F. Cugliandolo. Advanced Statistical Physics: Phase Transitions . Université Pierre et Marie Curie – Paris VI, Laboratoire de Physique Théorique et Hautes Energies, October 24 2017. 26

[110] Leticia F. Cugliandolo and Giuseppe Gonnella. Phases of active matter in two dimensions. unpublished lecture notes: Active Matter and Non-Equilibrium Statistical Physics, Les Houches summer school 2018 (August 27 - September 21). 26

[111] N. D. Mermin and H. Wagner. Absence of Ferromagnetism or Antiferromagnetism in One- or Two-Dimensional Isotropic Heisenberg Models. *Phys. Rev. Lett.*, **17** (1133-1136), 1966. 26, 27, 28

[112] N. D. Mermin. Crystalline Order in Two Dimensions. *Phys. Rev.*, **176** (250-254), 1968. 26, 27, 28, 29, 30

[113] B. J. Alder and T. E. Wainwright. Phase Transition in Elastic Disks. *Phys. Rev.*, **127** (359-361), 1962. 27, 28, 29, 31, 45

[114] L. Tonks. The Complete Equation of State of One, Two and Three-Dimensional Gases of Hard Elastic Spheres. *Phys. Rev.*, **50** (955), 1936. 28

[115] L. D. Landau, E. M. Lifshitz, and L. P. Pitaevskij. *Statistical Physics: Part 2* . Oxford, 1980. 28, 126

[116] E. Peierls. Quelques propriétés typiques des corps solides. *Annales de l'IHP*, **5** (177-222), 1935. 28

[117] L. D. Landau. On the theory of phase transitions. *Zh. Eksp. Teor. Fiz.*, **7** (19-32), 1937. 28

[118] C. C. Grimes and G. Adams. Evidence for a Liquid-to-Crystal Phase Transition in a Classical, Two-Dimensional Sheet of Electrons. *Phys. Rev. Lett.*, **42** (795-798), 1979. 29, 45

[119] C. A. Murray and D. H. Van Winkle. Experimental observation of two-stage melting in a classical two-dimensional screened Coulomb system. *Phys. Rev. Lett.*, **58** (1200-1203), 1987. 29, 45

[120] B. Jancovici. Infinite Susceptibility Without Long-Range Order: The Two-Dimensional Harmonic "Solid". *Phys. Rev. Lett.*, **19** (20-22), 1967. 30

[121] Fluctuations and Physical Properties of the Two-Dimensional Crystal Lattice. Y. imry and l. gunther. *Phys. Rev. B*, **3** (3939–3945), 1971.

[122] B. Gavish and Y. Imry. Static and dynamic structure factors for interdimensional systems. II. Layered crystals. *J. Chem. Phys.*, **65** (139-146), 1976. 30

[123] S. Asakura and F. Oosawa. On Interaction between Two Bodies Immersed in a Solution of Macromolecules. *J. Chem. Phys.*, **22** (1255-1256), 1954. 31

[124] M. Hasenbusch. The two-dimensional XY model at the transition temperature: a high-precision Monte Carlo study. *J. Phys. A: Math. Gen.*, **38** (5869-5883), 2005. 31

[125] J. Fröhlich and T. Spencer. The Kosterlitz–Thouless transition in two-dimensional abelian spin systems and the Coulomb gas. *Commun. Math. Phys.*, **81** (527-602), 1981. 32

[126] U. Wolff. Collective Monte-Carlo updating for spin systems. *Phys. Rev. Lett.*, **62** (361–364), 1989. 32

[127] J. M. Kosterlitz and D. J. Thouless. Long range order and metastability in two dimensional solids and superfluids. (Application of dislocation theory). *J. Phys. Condens. Matter*, **5** (L124-L126), 1972. 32, 33, 34, 35

[128] J. M. Kosterlitz and D. J. Thouless. Ordering, metastability and phase transitions in two-dimensional systems. *J. Phys. C*, **6** (1181-1203), 1973. 32, 33, 34, 35, 110

[129] V. L. Berezinskii. Destruction of Long-range Order in One-dimensional and Two-dimensional Systems having a Continuous Symmetry Group I. Classical Systems . *Sov. Phys. JETP*, **32** (493), 1971. 32

[130] V. L. Berezinskii. Destruction of Long-range Order in One-dimensional and Two-dimensional Systems Possessing a Continuous Symmetry Group. II. Quantum Systems. . *Sov. Phys. JETP*, **34** (610-616), 1972. 32

[131] R. Gupta, J. DeLapp, G. G. Batrouni, G. C. Fox, C. F. Baillie, and J. Apostolakis. Phase Transition in the 2DXY Model. *Phys. Rev. Lett.*, **61** (1996-1999), 1988. 34, 35

[132] D. J. Bishop and J. D. Reppy. Study of the Superfluid Transition in Two-Dimensional ^{4}He Films. *Phys. Rev. Lett.*, **40** (1727-1730), 1978. 34

[133] W. Janke. Logarithmic corrections in the two-dimensional XY model. *Phys. Rev. B*, **55** (3580-3584), 1997. 34

[134] J. L. Cardy. *Scaling and renormalization in statistical physics* . Cambridge, UK: Univ. Pr. (1996) 238 p. (Cambridge lecture notes in physics: 3), 1996. 35

[135] A. Jaster. Computer simulations of the two-dimensional melting transition using hard disks. *Phys. Rev. E*, **59** (2594-2602), 1999. 35, 45

[136] A. Jelić and L. F. Cugliandolo. Quench dynamics of the 2d XY model. *J. Stat. Mech.*, **2011** (P02032), 2011. 36

[137] A. Patrascioiu and E. Seiler. Different perspective of the Kosterlitz-Thouless phase transition. *Phys. Rev. Lett.*, **60** (875-878), 1988. 36

[138] E. Domany, M. Schick, and R. H. Swendsen. First-Order Transition in an xy Model with Nearest-Neighbor Interactions. *Phys. Rev. Lett.*, **52** (1535-1538), 1984. 37

[139] A. Jonsson, P. Minnhagen, and M. Nylén. New critical point for two dimensional XY-type models. *Phys. Rev. Lett.*, **70** (1327–1330), 1993. 37

[140] P. Minnhagen. The two-dimensional Coulomb gas, vortex unbinding, and superfluid-superconducting films. *Rev. Mod. Phys.*, **59** (1001-1066), 1987. 37

[141] A. C. D. van Enter and S. B. Shlosman. First-Order Transitions for n-Vector Models in Two and More Dimensions: Rigorous Proof. *Phys. Rev. Lett.*, **89** (285702), 2002. 38

[142] K. J. Strandburg. Two-dimensional melting. *Rev. Mod. Phys.*, **60** (161-207), 1988. 38, 45, 110

[143] J. G. Dash. History of the search for continuous melting. *Rev. Mod. Phys.*, **71** (1737-1743), 1999. 38

[144] B. I. Halperin and D. R. Nelson. Theory of Two-Dimensional Melting. *Phys. Rev. Lett.*, **41** (121-124), 1978. 38, 41, 42, 43, 44, 110

[145] D. R. Nelson and B. I. Halperin. Dislocation-mediated melting in two dimensions. *Phys. Rev. B*, **19** (2457), 1979.

[146] A. P. Young. Melting and the vector Coulomb gas in two dimensions. *Phys. Rev. B*, **19** (1855-1866), 1979. 38, 42, 43, 44, 110

[147] D. S. Fisher, B. I. Halperin, and R. Morf. Defects in the two-dimensional electron solid and implications for melting. *Phys. Rev. B*, **20** (4692-4712), 1979. 38

[148] S. T. Chui. Grain-Boundary Theory of Melting in Two Dimensions. *Phys. Rev. Lett.*, **48** (933-935), 1982. 46

[149] S. T. Chui. Grain-boundary theory of melting in two dimensions. *Phys. Rev. B*, **28** (178-194), 1983. 46

[150] H. Kleinert. Disclinations and first order transitions in 2D melting. *Phys. Lett. A*, **95** (0375-9601), 1983.

[151] T. V. Ramakrishnan. Density-Wave Theory of First-Order Freezing in Two Dimensions. *Phys. Rev. Lett.*, **48** (541-545), 1982. 38

[152] D. R. Nelson and R. A. Pelcovits. Momentum-shell recursion relations, anisotropic spins, and liquid crystals in $2 + \epsilon$ dimensions. *Phys. Rev. B*, **16** (2191–2199), 1977. 39

[153] K. Bagchi, H. C. Andersen, and W. Swope. Computer Simulation Study of the Melting Transition in Two Dimensions. *Phys. Rev. Lett.*, **76** (225-258), 1996. 42, 45, 110

[154] K. Zahn, R. Lenke, and G. Maret. Two-Stage Melting of Paramagnetic Colloidal Crystals in Two Dimensions. *Phys. Rev. Lett.*, **82** (2721-2724), 1999. 43, 110

[155] B. Zheng S. Z. Lin and S. Trimper. Computer simulations of two-dimensional melting with dipole-dipole interactions. *Phys. Rev. E*, **73** (066106), 2006. 44, 45, 46

[156] U. Gasser, C. Eisenmann, G. Maret, and P. Keim. Melting of Crystals in Two Dimensions. *Chem. Phys. Chem.*, **11** (963-970), 2010. 44

[157] J. V. José. *40 Years of Berezinskii–Kosterlitz–Thouless Theory* . WORLD SCIENTIFIC, 2013. 44

[158] R. J. Birgeneau and P. M. Horn. Two-Dimensional Rare Gas Solids. *Science*, **232** (329-336), 1986. 45

[159] W. F. Brinkman, D. S. Fisher, and D. E. Moncton. Melting of Two-Dimensional Solids. *Sience*, **217** (693-700), 1982. 45

[160] C. J. Guo, D. B. Mast, R. Mehrotra, Y. Z. Ruan, M. A. Stan, and A. J. Dahm. Evidence in Support of Dislocation-Mediated Melting of a Two-Dimensional Electron Lattice. *Phys. Rev. Lett.*, **51** (1461-1464), 1983.

[161] M. A. Stan and A. J. Dahm. Two-dimensional melting: Electrons on helium. *Phys. Rev. B*, **40** (8995-9005), 1989. 45

[162] R. Pindak, D. E. Moncton, S. C. Davey, and J. W. Goodby. X-Ray Observation of a Stacked Hexatic Liquid-Crystal *B* Phase. *Phys. Rev. Lett.*, **46** (1135-1138), 1981. 45

[163] S. C. Davey, J. Budai, J. W. Goodby, R. Pindak, and D. E. Moncton. X-Ray Study of the Hexatic-*B*-to-Smectic-*A* Phase Transition in Liquid-Crystal Films. *Phys. Rev. Lett.*, **53** (2129-2132), 1984. 45

[164] A. J. Armstrong, R. C. Mockler, and W. J. O'Sullivan. Isothermal-expansion melting of two-dimensional colloidal monolayers on the surface of water. *J. Phys.: Condens. Matter*, **1** (1707-1730), 1989. 45

[165] C. A. Murray and R. A. Wenk. Microscopic particle motions and topological defects in two-dimensional hexatics and dense fluids. *Phys. Rev. Lett.*, **62** (1643-1646), 1989.

[166] R. E. Kusner, J. A. Mann, J. Kerins, and A. J. Dahm. Two-Stage Melting of a Two-Dimensional Collodial Lattice with Dipole Interactions. *Phys. Rev. E*, **73** (3113-3116), 1994. 45

[167] P. Keim, G. Maret, and H. H. von Grünberg. Frank's constant in the hexatic phase. *Phys. Rev. E*, **75** (031402), 2007. 45

[168] S. Deutschländer, T. Horn, H. Löwen, G. Maret, and P. Keim. Two-Dimensional Melting under Quenched Disorder. *Phys. Rev. Lett.*, **111** (098301), 2013.

[169] T. Horn, S. Deutschländer, H. Löwen, G. Maret, and P. Keim. Fluctuations of orientational order and clustering in a two-dimensional colloidal system under quenched disorder. *Phys. Rev. E*, **88** (062305), 2013. 45

[170] A. L. Thorneywork, J. L. Abbott, D. G. A. L. Aarts, and R. P. A. Dullens. Two-Dimensional Melting of Colloidal Hard Spheres. *Phys. Rev. Lett.*, **118** (158001), 2017. 45, 46

[171] T. F. Rosenbaum, S. E. Nagler, P. M. Horn, and Roy Clarke. Experimental Observation of Continuous Melting into a Hexatic Phase. *Phys. Rev. Lett.*, **50** (1791-1794), 1983. 45

[172] S. E. Nagler, P. M. Horn, T. F. Rosenbaum, R. J. Birgeneau, M. Sutton, S. G. J. Mochrie, D. E. Moncton, and R. Clarke. Orientational order in xenon fluid monolayers on single crystals of exfoliated graphite. *Phys. Rev. B*, **32** (7373-7383), 1985. 45

[173] S. W. Koch and F. F. Abraham. Freezing transition of xenon on graphite: A computer-simulation study. *Phys. Rev. B*, **27** (2964-2979), 1983. 45

[174] F .F. Abraham. Melting Transition of Near-Monolayer Xenon Films on Graphite: A Computer Simulation Study. *Phys. Rev. Lett.*, **50** (978-981), 1983. 45

[175] A. D. Migone, Z. R. Li, and M. H. W. Chan. Melting Transition of Submonolayer Ar Adsorbed on Graphite. *Phys. Rev. Lett.*, **53** (810-813), 1984. 45

[176] A. J. Jin, M. R. Bjurstrom, and M. H. W. Chan. Thermodynamic evidence of first-order melting of Xe on graphite. *Phys. Rev. Lett.*, **62** (1372–1375), 1989. 45

[177] W. G. Hoover and F. H. Ree. Melting Transition and Communal Entropy for Hard Spheres. *J. Chem. Phys.*, **49** (3609), 1968. 45, 110

[178] J. Q. Broughton, G. H. Gilmer, and J. D. Weeks. Molecular-dynamics study of melting in two dimensions. Inverse-twelfth-power interaction. *Phys. Rev. B*, **25** (4651-4669), 1982. 45

[179] S. Prestipino, F. Saija, and P. V. Giaquinta. Hexatic Phase in the Two-Dimensional Gaussian-Core Model. *Phys. Rev. Lett.*, **106** (235701), 2011.

[180] S. Toxvaerd. Phase Transitions in a Two-Dimensional System. *Phys. Rev. Lett.*, **44** (1002-1004), 1980.

[181] K. Chen, T. Kaplan, and M. Mostoller. Melting in Two-Dimensional Lennard-Jones Systems: Observation of a Metastable Hexatic Phase. *Phys. Rev. Lett.*, **74** (4019-4022), 1995.

[182] S. Muto and H. Aoki. Crystallization of a classical two-dimensional electron system: Positional and orientational orders. *Phys. Rev. B*, **59** (14911-14914), 1999.

[183] B. K. Clark, M. Casula, and D. M. Ceperley. Hexatic and Mesoscopic Phases in a 2D Quantum Coulomb System. *Phys. Rev. Lett.*, **103** (055701), 2009. 45

[184] J. A. Zollweg and G. V. Chester. Melting in two dimensions. *Phys. Rev. B*, **46** (11186-11189), 1992. 45, 110

[185] H. Weber, D. Marx, and K. Binder. Melting transition in two dimensions: A finite-size scaling analysis of bond-orientational order in hard disks. *Phys. Rev. B*, **51** (14636-14651), 1995. 45, 110

[186] C. H. Mak. Large-scale simulations of the two-dimensional melting of hard disks. *Phys. Rev. E*, **73** (065104), 2006. 45

[187] K. Binder, S. Sengupta, and P. Nielaba. The liquid-solid transition of hard discs: first-order transition or Kosterlitz-Thouless-Halperin-Nelson-Young scenario? *J. Phys.: Condens. Matter*, **14** (2323–2333), 2002. 45

[188] V. M. Bedanov, G. V. Gadiyak, and Yu. E. Lozovik. Melting of two-dimensional crystals. *Sov. Phys. JE*, **61** (967-973), 1985. 45

[189] K. J. Naidoo, J. Schnitker, and J. D. Weeks. Two-dimensional melting revisited. *Mol. Phys.*, **80** (1-24), 1993. 45

[190] J. Lee and J. M. Kosterlitz. New numerical method to study phase transitions. *Phys. Rev. Lett.*, **65** (137-140), 1990. 46

[191] S. C. Kapfer. Two-step melting in Two Dimensions with Long-ranged and Attractive Forces . In *International Conference on Computer Simulation in Physics and beyond*, Moscow, Russia, September 24-27 2018. 46, 75

[192] M. Engel, J. A. Anderson, S. C. Glotzer, M. Isobe, E. P. Bernard, and W. Krauth. Hard-disk equation of state: First-order liquid-hexatic transition in two dimensions with three simulation methods. *Phys. Rev. E*, **87** (042134), 2013. 46, 111

[193] W. Qi, A. P. Gantaparaa, and M. Dijkstra. Two-stage melting induced by dislocations and grain boundaries in monolayers of hard spheres. *Soft Matter*, **10** (5449-5457), 2014. 46

[194] J. Russo and N. B. Wilding. Disappearance of the Hexatic Phase in a Binary Mixture of Hard Disks. *Phys. Rev. Lett.*, **119** (115702), 2017. 46

[195] J. A. Anderson, J. Antonaglia, J. A. Millan, M. Engel, and S. C. Glotzer. Shape and Symmetry Determine Two-Dimensional Melting Transitions of Hard Regular Polygons. *Phys. Rev. X*, **7** (021001), 2017. 46

[196] E. N. Tsiok, D. E. Dudalov, Yu. D. Fomin, and V. N. Ryzhov. Random pinning changes the melting scenario of a two-dimensional core-softened potential system. *Phys. Rev. E*, **92** (032110), 2015. 46

[197] E.N. Tsiok, Y.D. Fomin, and V.N. Ryzhov. Random pinning elucidates the nature of melting transition in two-dimensional core-softened potential system. *Physica A*, **490** (819 - 827), 2018. 46

[198] M. E. Cates. Diffusive transport without detailed balance in motile bacteria: does microbiology need statistical physics? *Rep. Prog. Phys*, **75** (042601), 2012. 49

[199] J. Bialké, T. Speck, and H. Löwen. Crystallization in a Dense Suspension of Self-Propelled Particles. *Phys. Rev. Lett.*, **108** (168301), 2012. 49, 122

[200] D. Levis and L. Berthier. Clustering and heterogeneous dynamics in a kinetic Monte Carlo model of self-propelled hard disks. *Phys. Rev. E*, **89** (062301), June 2014. 49, 50, 77, 78, 81

[201] J. U. Klamser, S. C. Kapfer, and W. Krauth. Thermodynamic phases in two-dimensional active matter. *Nat. Com.*, **9** (5045), 2018. 55, 64, 65, 66, 67, 70, 74, 75

[202] J. E. Mayer and Wm. W. Wood. Interfacial Tension Effects in Finite, Periodic, Two-Dimensional Systems. *J. Chem. Phys.*, **42** (4268), 1965. 67, 111

[203] M. Schrader, P. Virnau, and K. Binder. Simulation of vapor-liquid coexistence in finite volumes: A method to compute the surface free energy of droplets. *Phys. Rev. E*, **79** (061104), 2009. 67

[204] W. Mickel, S. C. Kapfer, G. E. Schröder-Turk, and K. Mecke. Shortcomings of the bond orientational order parameters for the analysis of disordered particulate matter. *J. Chem. Phys.*, **138** (044501), 2013. 68

[205] I. Petrelli, P. Digregorio, L. F. Cugliandolo, G. Gonnella, and A. Suma. Active dumbbells: Dynamics and morphology in the coexisting region. *Europhys. Lett. J. E*, **41** (128), 2018. 74, 123, 124

[206] S. C. Takatori, W. Yan, and J. F. Brady. Swim Pressure: Stress Generation in Active Matter. *Phys. Rev. Lett*, **113** (028103), 2014. 75, 111, 121

[207] Etienne P. Bernard, Werner Krauth, and David B. Wilson. Event-chain Monte Carlo algorithms for hard-sphere systems. *Phys. Rev. Lett.*, **80** (056704), 2009. 75

[208] Alan J. Mckane. *Stochastic Processes in Encyclopedia of Complexity and Systems Science*, volume 8766-9783. Springer, 2009. 99

[209] R. Kubo, M. Toda, and N. Hashitsume. *Statistical Physics II, Nonequilibrium Statistical Mechanics* . Springer-Verlag Berlin Heidelberg New York, 1991. 99

[210] S. N. Majumdar, A. Rosso, and A. Zoia. Time at which the maximum of a random acceleration process is reached. *J. Phys. A: Math. Theor.*, **43** (115001), 2010. 102

[211] K. Mallick. Some exact results for the exclusion process. *Journal of Statistical Mechanics: Theory and Experiment*, **2011** (P01024), 2011. 110

[212] C. Alba-Simionesco, B. Coasne, G. Dosseh, G. Dudziak, R. Radhakrishnan K. E. Gubbins, and M. Sliwinska-Bartkowiak. Effects of confinement on freezing and melting. *J. Phys.: Condens. Matter*, **18** (6), 2006. 110

[213] J. Lee and K. J. Strandburg. First-order melting transition of the hard-disk system. *Phys. Rev. B*, **46** (11190), 1992.

[214] A.Jaster. The hexatic phase of the two-dimensional hard disk system. *Phys. Lett. A*, **330** (120), 2004.

[215] C. H. Mark. Large-scale simulations of the two-dimensional melting of hard disks. *Phys. Rev. E*, **73** (065104), 2006.

[216] Y. Peng, Z. Wang, A. M. Alsayed, A. G. Yodh, and Y. Han. Melting of Colloidal Crystal Films. *Phys. Rev. Lett.*, **104** (205703), 2010. 110

[217] Alexandre Solon. *Physique statistique de la matière active* . PhD thesis, Université Paris Diderot (Paris 7) - Sorbonne Paris Cité - École Doctorale "Physique en Île-de-France", HAL Id: tel-01238464, 2015. 117

[218] U. M. B. Marconi, M. Paoluzzi, and C. Maggi. Effective potential method for active particles. *Mol. Phys.*, **114** (2400-2410), 2016. 121

[219] Y. Komatsu and H. Tanaka. Roles of Energy Dissipation in a Liquid-Solid Transition of Out-of-Equilibrium Systems. *Phys. Rev. X*, **5** (031025), 2015. 121

[220] G. Briand and O. Dauchot. Crystallization of Self-Propelled Hard Discs. *Phys. Rev. Lett.*, **117** (098004), 2016. 121

[221] J. T. Siebert, F. Dittrich, F. Schmid, K. Binder, T. Speck, and P. Virnau. Critical behavior of active Brownian particles. *Phys. Rev. E*, **98** (030601(R)), 2018. 122

[222] D. Vagberg and L. Berthier. The liquid solid transition of monodisperse active particles. In *APS March Meeting 2018, March 5–9, 2018; Los Angeles, California*, volume Abstract: Y48.00008. 123, 124

[223] R. Wittkowski, A. Tiribocchi, J. Stenhammar, R. J. Allen, D. Marenduzzo, and M. E. Cates. Scalar ϕ^4 field theory for active-particle phase separation. *Nat. Com.*, **5** (4351), 2014. 123

[224] A. P. Solon, J. Stenhammar, M. E. Cates, Y. Kafri, and J. Tailleur. Generalized thermodynamics of motility-induced phase separation: phase equilibria, Laplace pressure, and change of ensembles. *New J. Phys.*, **20** (075001), 2018. 123

[225] A. Patch, D. M. Sussman, D. Yllanes, and M. C. Marchetti. Curvature-dependent tension and tangential flows at the interface of motility-induced phases. *Soft Matter*, **14** (7435-7445), 2018. 123

[226] G. Briand M. Schindler and O. Dauchot. Spontaneously Flowing Crystal of Self-Propelled Particles. *Phys. Rev. Lett.*, **120** (208001), 2018. 124

[227] A. M. Menzel and H. Löwen. Traveling and Resting Crystals in Active Systems. *Phys. Rev. Lett*, **110** (055702), 2013. 124

[228] A. M. Menzel, T. Ohta, and H. Löwen. Active crystals and their stability. *Phys. Rev. E*, **89** (022301), 2014. 124

[229] L. Berthier. Nonequilibrium Glassy Dynamics of Self-Propelled Hard Disks. *Phys. Rev. Lett.*, **112** (220602), 2014. 124

[230] S. T. Chui and J. D. Weeks. Pinning and roughening of one-dimensional models of interfaces and steps. *Phys. Rev. B*, **23** (2438-2441), 1981. 125, 126, 131

[231] T. W. Burkhardt. Localisation-delocalisation transition in a solid-on-solid model with a pinning potential. *J. Phys. A: Math. Gen.*, **14** (L63-L68.), 1981. 125, 132, 133

[232] C. Kittel. Phase Transition of a Molecular Zipper. *Am. J. Phys.*, **37** (917-920), 1969. 125, 126, 129

[233] T. Dauxois, M. Peyrard, and A. R. Bishop. Entropy-driven DNA denaturation. *Phys. Rev. E*, **47** (R44–R47), 1993. 125, 126, 132, 133, 137

[234] M. E. Fisher. Walks, walls, wetting, and melting. *J. Stat. Phys.*, **5** (667-729), 1984. 125

[235] R. Lipowsky, Y. Chai, S. Klumpp, S. Liepelt, and M. J.I. Müller. Molecular motor traffic: From biological nanomachines to macroscopic transport. *Physica A*, 34 - 51, 2006. 125

[236] R. A. Minlos. Uniqueness of the limit Gibbs distribution in one-dimensional classical systems. *Theor. Math. Phys.*, **24** (697–703), 1975. 125

[237] D. Ruelle. *Statistical Mechanics: Rigorous Results* . World Scientific, 1999. 126

[238] F. J. Dyson. Existence of a phase-transition in a one-dimensional Ising ferromagnet. *Commun. Math. Phys.*, **12** (91-107), 1969. 126, 127, 133

[239] P. Sarkanych, Y. Holovatch, and R. Kenna. Exact solution of a classical short-range spin model with a phase transition in one dimension: The Potts model with invisible states. *Phys. Lett. A*, **381** (3589-3593), 2017. 126

[240] S. Grosskinsky, G. M. Schutz, and H. Spohn. Condensation in a zero-range process: stationary and dynamical properties. *J. Stat. Phys.*, **133** (267-278), 2003. 126

[241] T. D. Schultz, D. C. Mattis, and E. H. Lieb. Two-Dimensional Ising Model as a Soluble Problem of Many Fermions. *Rev. Mod. Phys.*, **36** (856-871), 1964. 128, 129

[242] L. Onsager. Crystal Statistics. I. A Two-Dimensional Model with an Order-Disorder Transition. *Phys. Rev.*, **65** (117-149), 1944. 129

[243] R. J. Baxter and I. G. Enting. 399th solution of the Ising model. *J. Phys. A: Math. Gen.*, **11** (2463-2473), 1978. 129

[244] J. F. Nagle. The One-Dimensional KDP Model in Statistical Mechanics. *Am. J. Phys.*, **36** (1114-1117), 1968. 129

[245] A.-L. Barabási and H. E. Stanley. *Fractal Concepts in Surface Growth* . Cambridge University Press, 1995. 131

[246] L Onsager. The effects of shape on the interaction of colloidal particles. *Ann. N. Y. Acad. Sci.*, **51** (627-659), 1949. 134, 151

[247] L. M. Casey and L. K. Runnels. Model for correlated molecular rotation. *J. Chem. Phys.*, **51** (5070-5089), 1969. 134, 152

[248] Y. Kantor and M. Kardar. One dimensional gas of hard needlesModel for correlated molecular rotation. *Phys. Rev. E*, **79** (041109), 2009.

[249] P. Gurin and S. Varga. Towards understanding the ordering behavior of hard needles: Analytical solutions in one dimension. *Phys. Rev. E*, **83** (061710), 2011. 134, 151, 152

[250] P. Dennery and A. Krzywicki. *Mathematics for physicists* . Harper's physics series. Harper and Row, 1967. 139

[251] S. Lepri, R. Livi, and A. Politi. Thermal conduction in classical low-dimensional lattices. *Phys. Rep.*, **377** (0370-1573), 2003. 154

Juliane Uta KLAMSER **10 décembre 2018**

Sujet : Transitions de phase en basse dimension à l'équilibre et hors d'équilibre

Résumé : Bien que la nature soit tridimensionnelle, il existe de nombreux systèmes dont les dimensions effectives sont inférieures, offrant une nouvelle physique. Cette thèse porte sur les transitions de phase dans les systèmes de faibles dimensions, en particulier sur les phases hors équilibre dans la matière active (MA) bidimensionnelle (2D). À la différence des systèmes passifs, les particules actives sont entraînées par de l'énergie injectée à l'échelle microscopique à partir de degrés de liberté internes, entraînant une dynamique irréversible, et donnant souvent lieu à des phases macroscopiques contrastant avec l'équilibre. Dans une première partie, ce travail propose une caractérisation quantitative des phases hors équilibre en s'appuyant sur un modèle minimal de MA. Ce modèle repose sur des particules 2D autopropulsées avec des interactions de paires. La dynamique (Monte Carlo cinétique persistante) est une variante des disques passifs et diffère des modèles bien connus de MA. Un diagramme de phase quantitatif complet est présenté, incluant la séparation de phase induite par motilité (SPIM). De plus, le scénario de fusion en deux étapes avec la phase hexatique se retrouve aussi hors équilibre. L'activité peut fondre un solide 2D et les lignes de fusion restent séparées de SPIM. La deuxième partie explore l'existence de transitions de phase dans les modèles 1D classiques avec des interactions courtes portées à température non nulle. Une idée largement partagée est que de telles transitions sont impossibles. Un contre-exemple clair est présenté où la non-analyticité de l'énergie libre émerge d'un nouveau mécanisme d'origine géométrique, établi de manière rigoureuse.

Mots clés : matière active bidimensionnelle, particules autopropulsées, séparation de phase induite par motilité, fusion en deux étapes hors équilibre, Monte Carlo cinétique persistante, transitions de phase unidimensionnelles

Subject : Low-dimensional phase transitions in and outside equilibrium

Version of Friday 1st March, 2019, 11:50

Abstract: Although nature is three-dimensional, lower dimensional systems are often effectively realized offering fascinating new physics. The subject of this thesis is phase transitions in low dimensions, with its primary focus on non-equilibrium phases in two-dimensional active matter. Unlike passive systems, active particles are driven by energy injected at the microscopic scale from internal degrees of freedom resulting in an irreversible dynamics, often giving rise to macroscopic phases in striking contrast to equilibrium. A goal is to give a quantitative characterization of such non-equilibrium phases and to capture these in simplest realizations of active matter. The thesis explores two-dimensional self-propelled particles with isotropic pair-wise interactions. The dynamics (persistent kinetic Monte Carlo) is a variant of passive disks and different from well-known models of active matter. A full quantitative phase diagram is presented including motility induced phase separation (MIPS) as seen in other active systems. Additionally, the famous two-step melting scenario with the hexatic phase extends far from equilibrium. In this non-equilibrium scenario, the activity can melt a 2D solid and the melting lines remain separated from MIPS. The second part explores a frequently debated issue of the existence of phase transitions in classical one-dimensional models with short-range interactions at non-zero temperature. A widely shared misconception is that such transitions are not possible. A clear counterexample to this belief is given where non-analyticity in the free energy emerges from a new mechanism with a geometrical origin, which is then established on a rigorous ground.

Keywords : active matter, self-propelled particles, motility-induced phase separation, non-equilibrium two-step melting, persistent kinetic Monte Carlo, one-dimensional phase transitions